

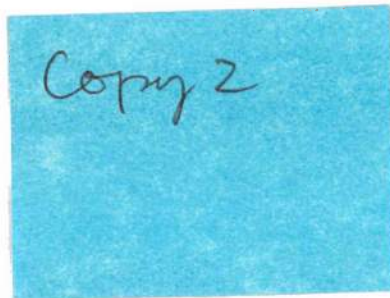


CENTER FOR MECHANICS OF SOLIDS, STRUCTURES AND MATERIALS  
DEPARTMENT OF AEROSPACE ENGINEERING AND ENGINEERING MECHANICS  
THE UNIVERSITY OF TEXAS AT AUSTIN

210 E. 24<sup>th</sup> Street, Stop C0600  
Austin, TX 78712-1221

December 21, 2013

Office of Naval Research  
875 North Randolph Street  
Arlington CA 22203-1995



Subject: Final Report  
Reference: ONR Award No: N00014-09-1-0541

Please find enclosed the final report on the above mentioned award. If you would like to receive an electronic version of the document, please let me know by e-mail ([ravi@utexas.edu](mailto:ravi@utexas.edu)) how this file may be deposited on a server (the file is about 12 Mb in size and will not transmit as an e-mail attachment).

Sincerely

A handwritten signature in black ink that reads "K. Ravi-Chandar".

Professor K. Ravi-Chandar  
Temple Foundation Professor  
Department of Aerospace Engineering and Engineering Mechanics  
The University of Texas at Austin

Mailing Address:  
210 E 24<sup>th</sup> Street, C0600, Austin, TX 78712-1221

# REPORT DOCUMENTATION PAGE

Form Approved  
OMB No. 0704-0188

The public reporting burden for this collection of information is estimated to average 1 hour per response, including the time for reviewing instructions, searching existing data sources, gathering and maintaining the data needed, and completing and reviewing the collection of information. Send comments regarding this burden estimate or any other aspect of this collection of information, including suggestions for reducing the burden, to Department of Defense, Washington Headquarters Services, Directorate for Information Operations and Reports (0704-0188), 1215 Jefferson Davis Highway, Suite 1204, Arlington, VA 22202-4302. Respondents should be aware that notwithstanding any other provision of law, no person shall be subject to any penalty for failing to comply with a collection of information if it does not display a currently valid OMB control number.

PLEASE DO NOT RETURN YOUR FORM TO THE ABOVE ADDRESS.

1. REPORT DATE (DD-MM-YYYY) 11/25/2013		2. REPORT TYPE Final Report		3. DATES COVERED (From - To) 1 February 2013 to 31 May 2013	
4. TITLE AND SUBTITLE Dynamic Response of Metal-Polymer Bilayers - Viscoelasticity, Adhesion and Failure				5a. CONTRACT NUMBER	
				5b. GRANT NUMBER N00014-09-1-0541	
				5c. PROGRAM ELEMENT NUMBER	
6. AUTHOR(S) K. Ravi-Chandar and K.M. Liechti				5d. PROJECT NUMBER	
				5e. TASK NUMBER	
				5f. WORK UNIT NUMBER	
7. PERFORMING ORGANIZATION NAME(S) AND ADDRESS(ES) The University of Texas at Austin Office of Sponsored Projects, P.O.Box. 7726 Austin, TX 78713-7726				8. PERFORMING ORGANIZATION REPORT NUMBER	
9. SPONSORING/MONITORING AGENCY NAME(S) AND ADDRESS(ES) Office of Naval Research Program Officer: Dr. Roshdy G. Barsoum 875 North Randolph Street Arlington, VA 22203-3521				10. SPONSOR/MONITOR'S ACRONYM(S) ONR	
				11. SPONSOR/MONITOR'S REPORT NUMBER(S)	
12. DISTRIBUTION/AVAILABILITY STATEMENT Approved for Public Release; distribution is unlimited.					
13. SUPPLEMENTARY NOTES					
14. ABSTRACT A series of fundamental experiments have been performed on the onset of localization under dynamic loading in tubular specimens of bare and polymer coated Al 6061-O. These experiments reveal that the onset of shear banding localization is unaffected by strain rate effects, but influenced by statistical distribution of flaws; the effect of the coating is shown to be inertial. High strain rate response of rubbers and elastomers is also examined using transient wave propagation experiments at strain rates in the range of 1000 to 10,000 per second. The potential for cathodic delamination of polyurea from steel was also considered.					
15. SUBJECT TERMS					
16. SECURITY CLASSIFICATION OF:			17. LIMITATION OF ABSTRACT	18. NUMBER OF PAGES  136	19a. NAME OF RESPONSIBLE PERSON
a. REPORT	b. ABSTRACT	c. THIS PAGE			19b. TELEPHONE NUMBER (Include area code)

## 1. Contract Information

Contract Number	N00014-09-1-0541
Title of Research	Dynamic Response of Metal-Polymer Bilayers - Viscoelasticity, Adhesion and Failure
Principal Investigator	K. Ravi-Chandar
Organization	The University of Texas at Austin

## 2. Technical Section

### 2.1. Technical Objectives

Recent discussions surrounding the high rate behavior of structural enhancements through polymer coatings have provided motivation for understanding fundamental aspects of the mechanical response of both the polymer and the metal at high pressures and high strain rates. Polymer-metal adhesion under quasi-static as well as dynamic loading conditions must also be determined through direct experiment. Thus, the main technical objectives of the program are listed below.

1. To evaluate the dynamic failure behavior of metal-polymer tubes under biaxial loading.
2. To determine the dynamic failure of metal-polymer bilayers under explosive loading
3. To determine the adhesive response of polymer-metal interfaces.
4. To develop the use of shear yielding polymers as coating materials

### 2.2. Technical Approach

#### 2.2.1. Expanding Tube Experiment for Dynamic Failure Studies under Biaxial Stretching:

Expanding ring tests have been used frequently in the characterization of high strain rate material behavior. We have used this arrangement to examine the onset of necking and fragmentation in aluminum and copper alloys and specimens coated with polyurea. Details of the experimental arrangement and results pertaining to Al 6061-O have been published (Zhang and Ravi-Chandar, 2006, 2008, Zhang et al., 2009a). In the present work, we have extended this method of generating high strain rate loading to tubular specimens, with an addition of a conical mirror imaging. This allows us to view the entire surface of the cylindrical specimen as it deforms, localizes strain and eventually fails. This scheme has been used to examine the response of tubular specimens without and with polyurea coating.

#### 2.2.2. Dynamic Failure of Metal-Polymer Bilayers under Explosive Loading

The structural and failure response of metal-polymer bilayer systems were examined using a newly developed underwater explosive loading facility; this system was built with support from a companion DURIP program. In this device, a shock wave is generated in water inside one end of a cylindrical pressure vessel by a wire explosion. This shock travels to the other end that contains the specimen placed at about 0.2 to 0.4 m from the explosion; for the dynamic failure tests, this is in the form of a plate, clamped around a circle of six inches diameter. The plate is coated with a polymer of desired thickness; therefore, both the bare metal and the metal-polymer bilayer can be tested in this arrangement. The deformation and failure response of the structure to the shock loading is monitored with a high speed camera to extract the evolution of the strain as a function of time. Numerous experiments have been performed in this configuration, but they have not provided a consistent picture of the response of the bilayer.



### *2.2.3. Adhesion of Polyurea to Metal Substrates:*

The adhesion of the coatings to steel was examined under dynamic loading in a new explosive loading device described above. The shock wave generated by an exploding wire travels to the other end that contains the specimen; for the dynamic adhesion test, this is in the form of a blister: a relatively rigid plate blocks the path of the shock, but a small opening in this plate allows the pressure to impinge on the polymer overlayer; this deforms and forms the dynamic blister. The deformation and growth of the blister are recorded with high speed camera; analysis of these images provides the strain field and the crack front variation as a function of time. These are then interpreted in terms of the energy release rate and crack velocity to develop the dynamic delamination criterion. Strain rates and delamination rates achieved in these experiments are in the range that occurs in delamination of metal-polymer bilayers. A fracture mechanics approach to accelerated life testing of cathodic delamination between steel and polyurea has been examined.

### *2.2.4. Develop the use of Shear Yielding Polymers as Coating Materials:*

We recall that Mock et al. (2006) showed that coating with other polymers, such as polyethylene was equally effective in delaying metal failure as polyurea, even when it was diced into small rectangular blocks. Therefore, we explore the use of shear yielding polymers in the metal-polymer bilayers, with polycarbonate being our first candidate. The deformation and failure response of the metal-polycarbonate bilayers was characterized in our expanding tube loading facility described above.

## **2.3. Technical Accomplishments**

We have performed a number of important experiments and analyses on the dynamic nonlinear characterization of polyurea and on the dynamic failure characterization of tubes. The deformation and failure response of polyurea and polycarbonate coated aluminum tubes have been characterized. The results have been reported at the annual review meetings and have been published in five journal articles that are attached as appendices to this report.

### *2.3.1. Expanding Tube Experiment for Dynamic Failure Studies under Biaxial Stretching:*

In this work, the electromagnetic loading device that was used for expanding metallic rings by Zhang and Ravi-Chandar (2006) has been modified for use in expanding aluminum 6061-O tubes at high strain-rates. The loading device includes a 25  $\mu\text{F}$  capacitor and a copper coil with either 6-turn (18 mm long) or 12-turn (36 mm long) winding. In these tests, the capacitor is charged to a maximum of 15 kV, corresponding to 2.8 kJ of energy, and then discharged through the coil which is held firmly in place in an epoxy mold. The tube specimen is placed outside the coil. A large, rapidly-varying current is derived from discharging of the capacitor and passed through the coil. An induced current is generated in the tube; the interaction between the drive current and induced current generates a repulsive (Lorentz) force between the solenoid and the tube specimen. As a result, the tube experiences a radial body force that causes the tube to expand in radius at high speeds. With our experimental setup, aluminum tubes of initial diameter of 30.5 mm and wall thickness of 0.5 mm can be accelerated to 200 m/s expanding velocity within about 50  $\mu\text{s}$ . This results in the development of a uniform hoop strain in the tubes at strain rates of up to  $10^4 \text{ s}^{-1}$ . The entire process of uniform deformation, emergence of strain localization, and the nucleation and growth of cracks are monitored through innovative high speed imaging schemes; in particular, the use of a conical mirror allows observation of the entire surface of the tube specimen and the consequent measurement of the strain evolution. A Cordin Model 550 high-speed camera capable of recording 32 frames is synchronized with the experiment to observe the deformation of the tube specimens; a framing rate of  $\sim 160,000$  frames per second is used in these experiments. A pattern of 2.5 mm diameter circles is electrochemically etched on the outer surface of the tube specimen; these circles provide a means of measuring the principal strains directly in the expanded tube.

We have identified the strain at the onset of localization from these experiments and have explored models to capture their statistical origin. Once again, as in the case of the ring specimens, very little strain



rate effects are observed on the onset of localization. A complete examination of the deformation and fragmentation response of aluminum tubes has been published (Zhang and Ravi-Chandar, 2010 – attached as Appendix A). In the next stage, these tubes have been coated with polyurea and polycarbonate in order to determine the influence of the polymer on the localization, failure and fragmentation response of the cylinders. Preliminary results indicate that the coating does not influence the onset of localization, but due to added mass, and the increased load carrying capability, particularly when the metal is close to failure, the overall deformation and fragmentation response is significantly altered. The results of this work have been published (Morales et al, 2011 – attached as Appendix B).

### *2.3.2. Dynamic Blister Experiments for Characterization of Dynamic Adhesive Behavior:*

The blister test is commonly used to determine the quasi-static adhesive response of thin, compliant films on stiff substrates. Since our interest is on the dynamic delamination behavior in such interfaces, we have used the shock loading method described above to explore the delamination of a polyurea coating from a steel substrate. In this experiment, a shock wave is generated in water by explosion of a copper wire by passing a large electric current; typically, the wire bursts in about 30 to 50 microseconds and generates a sharp pressure pulse, with an exponential decay and mimics an underwater explosion. This shock wave impinges on a dynamic blister arrangement and creates a propagating dynamic blister. Quantitative high-speed photographic diagnostic methods are used to determine the bulging deformation of the blister as well as the growth of the blister as a function of time. These results have analyzed to provide a characterization of the dynamic adhesion strength of the interface; however, the electromagnetic noise in the explosion interfered with the synchronization of the high speed cameras used for imaging the deformation. Reliable measurements of the response could not be obtained.

A fracture mechanics approach to accelerated life testing of cathodic delamination between steel and polyurea was examined. This required the hyperelastic behavior of the polyurea to be described by the Marlow model based on uniaxial tension and plane strain compression tests. Time-dependence was also considered but could be neglected if proper test protocols were followed in cathodic delamination tests using a strip blister specimen. The variation of J-integral with specimen geometry and loading parameter was obtained, which allowed the resistance to cathodic delamination to be expressed in terms the J-integral and the crack speeds obtained from the tests at several temperatures. The approach established that both temperature and stress can be used to accelerate the cathodic delamination, thereby providing a quantitative and rational basis for conducting accelerated testing as well as evaluating new surface treatments. These results have been submitted for publication (Mauchien and Liechti, 2013 – attached as Appendix C)

### *2.3.3. Dynamic Tensile Characterization of Polyurea:*

We have developed an experimental method by which the constitutive relations for polymers can be characterized at strain rate on the order of  $10^3$  to  $10^4$  per second. Current methods for studying dynamic properties of polymers typically focus on the use of Hopkinson bar experiments. Tensile Hopkinson bar experiments are inadequate for true quantification of high strain rate tensile constitutive relations of polymers, particularly at large stretches. In the method developed for this purpose, a gas gun is used to impact a flange and impart a known velocity to a thin strip of polyurea which is attached to that flange at one end and to a fixed clamp at the other. The dynamic stretching induced in the polymer is then imaged by high speed photography; these images allow direct measurement of the strain and particle velocity with time throughout the specimen. From the theory of nonlinear wave propagation in thin strips and appropriate material models, analytic predictions can be made for both the particle velocity and strain. The constitutive model is obtained by correlation between prediction and experiment; phenomenological models based on nonlinear viscoelasticity or viscoplasticity can be used to extract the constitutive response. This method has been used successfully to determine the response of polyurea at strain rates of about 75,000 per second. It is found that the Zhou-Clifton model of viscoplasticity, originally conceived for metals, works quite well for polyurea because of the flexibility introduced in this model incorporating both power-law and exponential behavior. The results of this work have been published (Albrecht et al,

2013 – attached as Appendix D). A biaxial variant of this method uses a membrane; in this work, the propagation of axisymmetric waves of finite deformation in polyisoprene and polyurea rubber membranes subjected to high speed impact are considered. High speed photography is used to monitor the motion and to determine the evolution of stretch and particle velocity in membranes at impact speeds of up to 160 m/s, producing a maximum stretch  $> 8$ . These experiments are used to validate the constitutive model developed through the one-dimensional experiments. The results of this work are currently under review for publication (Albrecht and Ravi-Chandar, 2013 – attached as Appendix E).

### 3. Conclusion

A series of fundamental experiments have been performed on the onset of localization under dynamic loading in tubular specimens of Al 6061-O. These experiments reveal that the onset of shear banding localization is unaffected by strain rate effects. Statistical influences on the onset of localization and the effect of propagating release waves on the further evolution of these bands as well as fragmentation have been characterized experimentally as well as through finite element simulations. The addition of a coating on the tube with polyurea or polycarbonate is shown to influence deformation mainly through the added mass effect.

Experiments have been performed on adhesion of polyurea to metal plates. Interpretation of these experiments requires high-strain rate tensile material behavior for polyurea; this is now possible, with the newly developed method for obtaining dynamic tension at strain rates of about 75,000 per second.

### References

- A.B. Albrecht, K.M. Liechti, and K. Ravi-Chandar, 2013, Characterization of the transient response of polyurea, *Experimental Mechanics*, **53**, 113-122.
- A.B. Albrecht and K. Ravi-Chandar, 2013, High strain rate response of rubber membranes, *Journal of the Mechanics and Physics of Solids*, (in revision).
- T. K. Mauchien and K.M. Liechti, A fracture analysis of cathodic delamination of polyurea from steel, submitted, *International Journal of Adhesion and Adhesives*, September 2013.
- S.A. Morales, A.B. Albrecht, H. Zhang, K.M. Liechti, and K. Ravi-Chandar, 2011, On the dynamics of localization and fragmentation: V. Response of polymer coated Aluminum 6061-O tubes, *International Journal of Fracture*, **172**, 161-185.
- H. Zhang, and K. Ravi-Chandar, 2006, On the dynamics of necking and fragmentation: I. Real-time and post-mortem observations in Al 6061-O, *International Journal of Fracture*, **142**, 183-217.
- H. Zhang, and K. Ravi-Chandar, 2008, On the dynamics of localization and fragmentation: II. Effect of geometry and ductility, *International Journal of Fracture* **150**, 3-36.
- H. Zhang, K.M. Liechti and K. Ravi-Chandar, 2009a, On the dynamics of localization and fragmentation: III. Effect of cladding with a polymer, *International Journal of Fracture*, **155**, 101-118.
- H. Zhang and K. Ravi-Chandar, 2009b, Dynamic fragmentation of solids, *Journal of Physics D: Applied Physics*, **42**, Article ID 214010.
- H. Zhang and K. Ravi-Chandar, 2010, On the dynamics of localization and fragmentation: IV. Aluminum 6061-O tubes, *International Journal of Fracture*, **163**, 41-65.

## APPENDIX A

### **On the dynamics of localization and fragmentation: IV. Aluminum 6061-O tubes**

H. Zhang and K. Ravi-Chandar

*International Journal of Fracture*, 163, 41-65, 2010



# On the dynamics of localization and fragmentation-IV. Expansion of Al 6061-O tubes

H. Zhang · K. Ravi-Chandar

Received: 31 August 2009 / Accepted: 12 November 2009 / Published online: 2 February 2010  
© Springer Science+Business Media B.V. 2010

**Abstract** In this series of papers, we investigate the mechanics and physics of localization and fragmentation in ductile materials. The behavior of ductile metals at strain rates of about 4,000–15,000 per second is considered. The expanding ring experiment is used as the vehicle for examining the material behavior in this range of strain rates. In Parts I–III, we examined the response of rings with cross-sectional aspect ratios in the range of 1–10, exhibiting a transition from diffuse necking to sheet-mode localization. In the present paper we report on experimental observations of high strain-rate expansion of Al 6061-O tubes. Through an innovative use of high-speed imaging aided with a conical mirror we determine the sequence of deformation and failure in the expanding tube. In particular, the conical mirror provides information of surface deformation on the tube. Forming limit diagrams at high strain rates are obtained from post-mortem measurement of the deformed tubes or fragments and are compared with analysis from quasi-static analysis. Numerical simulations are used to explain the experimental observations.

**Keywords** Expanding tube experiment · Ductility · Electromagnetic forming

## 1 Introduction

In this series of papers, we explore the onset of localization, the emergence of cracks and eventually fragments in ductile materials at strain rates in the range of  $\sim 10^4 \text{s}^{-1}$ . In the first three parts of this sequel, we examined the response of thin rings (Zhang and Ravi-Chandar 2006, 2008; Zhang et al. 2009). We will refer to these previous publications as Parts I, II, and III respectively. Through detailed experimental observations, measurements, models and simulations, we have established that if proper accounting is made for the statistical distribution of flaws or strength variability in the material, and if a simple power-law hardening plasticity model generalized to three-dimensions using the  $J_2$  flow theory, is implemented in a fully three-dimensional geometric model (in order to represent the possible deformation modes), then almost all aspects of the observed high strain-rate expansion and localization behavior can be captured in numerical simulations. Fracture modeling in this setting remains primitive in the sense that we used element deletion techniques; this resulted in proper scaling relationships for the fragment size, but additional effort needs to be devoted to this aspect in order to fully characterize the final aspect of high strain rate failure.

In the present paper, Part IV, we turn our attention to the dynamic failure of cylindrical specimens with the potential for generating various biaxial and plane-strain deformation paths and hence constrain the types of localization that may occur under dynamic loading.

H. Zhang · K. Ravi-Chandar (✉)  
Center for Mechanics of Solids, Structures and Materials,  
Department of Aerospace Engineering and Engineering  
Mechanics, The University of Texas at Austin, Austin,  
TX 78712-0235, USA  
e-mail: kravi@mail.utexas.edu; fracture@mail.ae.utexas.edu

Dynamic failure and fragmentation behavior of cylinders has been investigated for a long time, motivated on the one hand by the formation of fragments from explosive loading of such cylinders, and on the other hand, by the ability to form tubular (and sheet-metal) components by rapid electromagnetic forming. The pioneering work of Mott (1947) still remains one of the most important and relevant works in the area of fragmentation. Numerous other studies that followed have provided many direct observations of the process of failure and fragmentation as well as models of the fragmentation, but the fundamental ideas of Mott remain essential to the understanding and modeling of fragmentation. The main interest in such studies is the ability to predict the size and kinetic energy distribution of the fragments generated from the dynamic loading. In the area of sheet-metal forming applications, high-velocity forming has been promoted as an efficient and useful method in forming otherwise difficult to form sheet metal parts, either with or without a die backing (Plum 1995). Similar applications have also evolved in forming tubular parts. In these applications, it is the regime of uniform deformation that is of importance; the so-called "forming-limit" is the envelope in two dimensional strain-space, within which deformations remain homogeneous without the appearance of any localized deformation and all forming operations must utilize strain paths that are within this limit. There have been some conflicting reports in the literature on the effect of strain rate on the forming limit with Seth et al. (2005) suggesting that dynamic forming limits in some aluminum alloys are significantly larger than their quasi-static counterpart, while Oliveira et al. (2005) do not find such increases in the forming limit. Our interest in the present work is on both aspects of the problem—the region of uniform plastic deformation below the forming limit, as well as the generation of fragments. We will show, through careful experimental measurements and numerical simulations, that it is essential to understand the onset, growth and coalescence of localized shear bands in order to be able to understand both aspects of the problem. In order to place the present work in the proper context, we provide here a brief review of the literature on both aspects of the problem beginning with the fragmentation problem first and then following this with a discussion of the dynamic forming limit.

Wesenberg and Sagartz (1977) examined the problem of fragmentation in Al 6061-T6 cylindrical

specimens. A modified version of Niordson's expanding ring apparatus (Niordson 1965) augmented by Walling and Forrestal (1973) for application to cylinders was used. In this arrangement, a contoured copper sheet is inserted inside the cylindrical aluminum specimen and a current pulse is discharged through the copper sheet. Lorentz interaction between this current and the current induced in the aluminum specimen occurs as in the expanding ring arrangement of Niordson, resulting in an expansion of the cylindrical aluminum alloy specimen at high strain rates. Wesenberg and Sagartz used Al 6061-T6 cylinders 102 mm long, 127 mm in outer diameter and 1.27 mm wall thickness; the strain rates were in the range of  $10^4 \text{ s}^{-1}$ . A high speed framing camera was used to capture the fragmentation process. Strain localization in the form of narrow bands oriented at about  $30^\circ$  with respect to the axis of the cylinder was also observed; however, since their main interest was on fragmentation, this localization behavior was not quantified further. The strain just prior to the appearance of fractures was determined to be about 30%. Wesenberg and Sagartz collected the fragments and determined the fragment size distribution. They also solved the Mott equations for the release wave propagation numerically. Two material parameters—the yield strength and the standard deviation in the fracture strain—were used in generating the Mott model estimate of the fragment size distribution. The close correlation between the experiments and analysis obtained in their investigation implies that these two parameters are sufficient to fit the Mott model to the experimental observations. This experiment represents the first direct confirmation of the validity of the main concepts introduced by Mott in his fragmentation model.

Winter (1979) developed a method based on a gas-gun launched projectile in order to generate a rapidly increasing pressure loading on a cylindrical specimen. An elastomeric insert was placed inside the metal specimen, occupying one-half the length of the cylinder. A cylindrical nylon projectile of the same dimensions as the elastomer is then shot through the inner bore of the specimen and made to impact the stationary elastomeric insert. This geometry is reminiscent of the Taylor plug impact test; in the absence of the confining effects of the metallic specimen surrounding the polymers, both the nylon and the elastomer would begin to bulge radially, with the bulge propagating in the axial direction. However, since both polymer pieces are



confined in the metallic tube, they apply a radial loading on the specimen, with this loading moving along the axial direction. Thus, the metallic specimen experiences a bulging deformation in the central portion, at strain rates in the range of  $2\text{--}4 \times 10^4 \text{ s}^{-1}$ . These experiments were conducted in cylinders that were 17 mm in diameter and 1 mm in wall thickness. Winter observed the deformation with high speed photography and identified the formation of cracks and their axial propagation and coalescence. In particular, Winter correlated time of appearance of cracks with the overall development of strain in the tube. Grady (2006) interpreted this observation successfully through Mott's fragmentation model. Forrestal et al. (1980) developed an explosive loading technique where a fine grid patterned mesh was used to detonate a PETN charge uniformly; therefore the pressure in the cylindrical specimen evolved uniformly over the entire cylinder, unlike the propagating load in Winter's experiment. Forrestal et al. used relatively thin-walled cylinders (diameter 5 in, wall thickness 0.25;  $D/t \sim 20$ ) and demonstrated that nearly uniform strains can be developed in cylindrical specimens; furthermore, they determined that the strain at incipient fracture increased as the thickness of the cylinder increased, but did not report data on fragmentation. Even though this method of applying uniform expansion of the cylinder is very impressive, this has not been followed up by other investigators looking into fragmentation of cylinders. Mock and Holt (1983) performed experiments on the fragmentation of Armco iron and HF-1 steel; the specimens were much thicker ( $D/t \sim 3$ ). These specimens were loaded by detonation of an explosive, much like the work of Forrestal et al. (1980), but without the grid based detonation technique for ensuring uniform expansion. Mock and Holt recovered nearly all the fragments and examined them carefully; from such examination, they determined that both brittle and shear failures occurred, reflecting earlier observations of Mott. This appears to be a characteristic of thick-walled cylinders. Mock and Holt also plotted the distribution of fragment mass for the different types of fragments and suggested that an exponential distribution fit the data quite well.

While Winter examined the fragmentation of aluminum, steel, brass and other materials, Vogler et al. (2003) recreated this experiment and tested AerMet 100 steel and U-6%Nb uranium alloy; furthermore, in this work, both the projectile and the plug were

made of Lexan polycarbonate. In addition to high speed photography, direct measurements were also made of the particle velocity histories at three different points along the length of the cylindrical specimen. Vogler et al. used thick-walled cylinders with a  $D/t \sim 4$ —diameter of 12.7 mm (0.5 in) and wall thickness of 3.18 mm (0.125 in); such thick-walled cylinders fail by shear that starts at the inner wall and transitions into brittle fracture and hence the fragmentation response may not be comparable to that of thin-walled cylinders. Fragment size distribution was determined to be of the bilinear exponential form. Simulations of the fragmentation process using a hydrocode CTH indicated that the initial uniform expansion could be captured well, but the details of the fragmentation were not reproduced. The Grady–Kipp model that is based on the fracture toughness was used to get an estimate of the fragment size and appeared to predict the fragmentation behavior reasonably well.

More recently, Hiroe et al. (2008) performed an exhaustive investigation of the deformation and fragmentation behavior of 304 stainless steel, A5052 aluminum alloy, and three different low-carbon steels. The cylindrical specimens with  $D/t \sim 11$  were expanded by either a fully or partially loaded explosive charge; in addition, different types of grooves were introduced in order to steer the development of fractures and fragments; the strain rates used were in the range of  $1\text{--}5 \times 10^4 \text{ s}^{-1}$ . High-speed photography was used to reveal the emergence of cracks and fragments, but no quantitative measurements were reported from such high speed photographic observations. They also reported a combination of shear and brittle fracture; it would appear that the shear fractures begin at the inner surface regardless of the  $D/t$ , but develop brittle fractures only in thick specimens, but there is insufficient experimental information in the literature to make strong conclusions. Hiroe et al. used the Grady model to estimate the fracture energy of each recovered fragment; one would expect the fracture energy to be nearly the same from all fragments, but the experiments indicated a wide range of values for the fracture energy. Horoe et al. also modeled the experiment in AUTODYN with the Mott stochastic model and found that this had a much better correlation with the experiment. They speculated that material property changes due to shock compression prior to the large straining might influence the response of the cylinders. In another recent study, Gold and Baker (2008) used an arbitrary Lagrangian–



Eulerian code, enhanced with the Mott fragmentation model and successfully predicted the fragmentation distribution in metal shells that contain a cylindrical portion, but terminated at one end by a shaped cap; the comparison, of course, requires the back-fitting of parameters that capture the statistical distribution of flaws and strain to failure. The most promising aspect of this study is the demonstration of the ability of the Mott model to capture the fragment size distribution. Fracture and fragmentation in steel rings and cylinders was investigated by Goto et al. (2008); they used moderately thick-walled cylinders (50 mm diameter, 3 mm wall thickness for a  $D/t \sim 16.67$ ) of AeroMet100 and AISI 1080 steels. The specimens were pressure loaded by detonating a charge; this resulted in the propagation of a detonation wave along the length of the cylindrical specimen and hence nonuniform loading along the length. Real-time diagnostics included high speed photography, x-ray imaging and velocity measurements. The progressive deformation and appearance of cracking could be seen in the optical image and related to the strain at the onset of fracture. The failure strain variation was obtained from measurements on recovered fragments and indicated as histograms to show statistical variability. The failure is shown to be preceded by adiabatic shear bands emanating from the inner and outer surfaces of the cylinder. Models for the Johnson–Cook failure model were also extracted from the measurements.

Most of the experimental investigations described above used either explosives or projectile to obtain high strain rates; with the exception of the work of Forrestal et al. (1980), the radial expansion of the cylinder was nonuniform along the length of the cylinder, either because of nonuniform detonation or because of the nature of the plug development. In fact, in the projectile impact loading, regions away from the center of the cylinder do not experience significant direct loading at all. In contrast to this, the electromagnetic loading scheme is able to impose nearly uniform deformation along the length of the cylinder, as observed by Wesenberg and Sagartz (1977), and is better suited for characterization of material properties. Even before this study into fragmentation, the electromagnetic expansion of cylinders had been considered as an efficient manufacturing process; Jansen (1968) considered a hollow circular cylindrical tube made of Al 6061-O, expanded with a helical coil placed inside the tube and supplied with a discharge from a capacitor. Assuming

a linear strain-hardening response for the aluminum, Jansen determined the differential equations that govern driving force generated on the aluminum tube. The radius of the tube during expansion as well as the magnetic field between the coil and the specimen were measured directly in experiments; excellent agreement was shown between solutions to the governing equations and the measured values. The interest in Jansen's work, of course, was only in the range of uniform deformation since in applications to forming operations, one does not wish to generate nonuniform deformations or fracture; hence a highly damped circuit was used in their study that resulted in a quick reduction of the electromagnetic driving force. Takatsu et al. (1988) made a detailed model of the interaction between a flat metallic workpiece and a driving coil; the interaction creates a bulging deformation in a clamped plate and therefore a biaxial loading condition. Their study focused mainly on proper modeling of the nonlinear deformation of the plate and the geometry-dependent electromagnetic interaction between the driving coil and the deforming workpiece. Once again, attention was limited to the region prior to failure and good agreement was indicated between the numerical results and experimental measurements of the bulging deformation in an aluminum alloy. The material was modeled with a simple power-law hardening model, and included logarithmic strain-rate dependence. Once again, the onset of localization and the development of fragments were not examined. Application of electromagnetic forming appears to have had only a limited penetration into the market for reasons that are not clear. But, in recent years, there has been a resurgence of interest in electromagnetic forming.

Balanethiram and Daehn (1994) performed expanding ring experiments and suggested that "hyperplastic" behavior is exhibited at high strain rates whereby much larger strain levels are attained prior to the onset of failure. Seth et al. (2005) followed up on this study by examining the formability of sheet steel under high velocity impact; an electromagnetic launcher was used to propel sheet steel specimens against a die in order to form shapes; they concluded that the formability limit was much greater than what could be determined through quasi-static tests on the same material. However, Oliveira et al. (2005) performed similar experiments on aluminum alloy sheets and did not find support for the idea of hyperplastic deformation; they determined that the interaction between the die and

the workpiece through frictional contact may influence some forming operations and in these cases, electromagnetic forming might be beneficial. Fundamental questions regarding the forming limit under dynamic loading conditions remain unresolved and will be examined in the present work.

This paper is organized as follows: in Sect. 2 we describe the experimental arrangement of the expanding tube experiments with a particular emphasis on the use of a conical mirror for observing the entire surface of the tube specimen and the consequent measurement of the strain evolution. Experimental observations of the time evolution of homogeneous expansion, shear localization, and fracture of the tube at different expanding speeds are described in Sect. 3; these are followed by the post-mortem strain measurement for developing forming limit diagrams. The onset of shear localization, and the evaluation of the dynamic forming limit diagram are described in Sect. 4. The development of cracks and fragments are discussed in Sect. 5. Numerical simulations of the experiments are discussed in Sect. 6; these simulations utilize a  $J_2$  flow theory of plasticity in ABAQUS/Explicit and randomly distributed material defects to understand the underlying mechanisms responsible for the observed deformation, pattern of localization and the subsequent effect on fragmentation in the tube. The main conclusions are summarized in Sect. 7.

## 2 Experimental arrangement

In this work, the electromagnetic loading device that was used for expanding metallic rings in Parts I–III is used to expand aluminum 6061-O tubes at high strain-rates. The loading device includes a  $25\text{ }\mu\text{F}$  capacitor and a copper coil with either 6-turn (18 mm long) or 12-turn (36 mm long) winding. The tube specimen is placed outside the coil. In these tests, the capacitor is charged to a maximum of 15 kV, corresponding to 2.8 kJ of energy, and then discharged through the coil which is held firmly in place in an epoxy mold. This discharge generates a large, rapidly-varying current through the coil. An induced current is generated in the tube; the interaction between the drive current in the coil and induced current in the specimen generates a repulsive (Lorentz) force between the solenoid and the tube specimen. As a result, the tube experiences a radial body force that causes the tube to expand in radius at

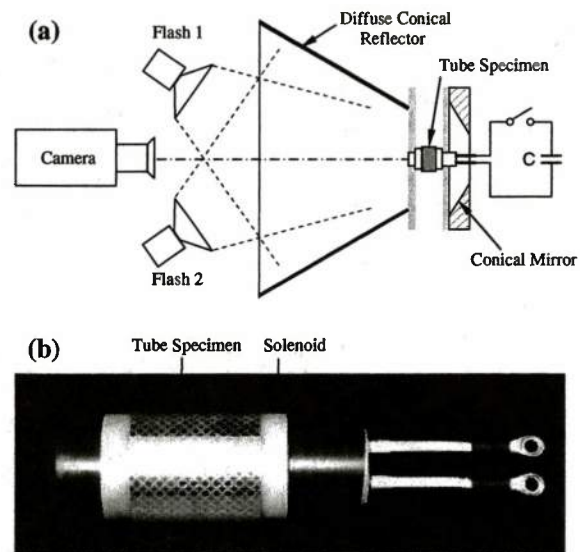
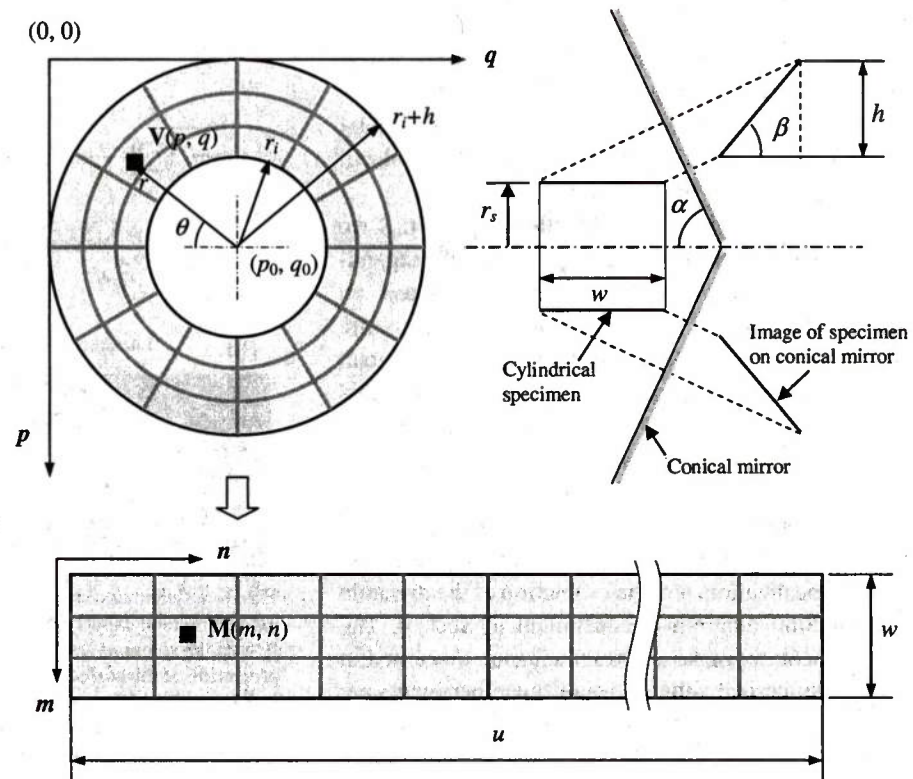


**Fig. 1** **a** Schematic diagram of the experimental setup for the expanding tube experiment. The conical mirror, placed coaxially with the solenoid and the tube specimen, provides a complete projection of the surface of the expanding cylindrical specimen; **b** photograph of the solenoid and the tube specimen; a pattern of 2.5 mm diameter circles is electrolytically etched on the outer surface of the specimen in order to facilitate strain measurements

high speeds. With our experimental setup, aluminum tubes of initial diameter of 30.5 mm and wall thickness of 0.5 mm can be accelerated to 200 m/s expanding velocity within a few  $\mu\text{s}$ . This results in the development of a uniform hoop strain in the tubes at strain rates up to  $10^4\text{ s}^{-1}$ . The entire process that consists of uniform deformation, emergence of strain localization, and the nucleation and growth of cracks is monitored through innovative high speed imaging schemes; in particular, the use of a conical mirror allows observation of the entire surface of the tube specimen and the consequent measurement of the strain evolution. A schematic diagram showing the experimental setup of the expanding tube experiment and the placement of the conical mirror is given in Fig. 1a. A Cordin Model 550 high-speed camera capable of recording 32 frames is synchronized with the experiment to observe the deformation of the tube specimens; a framing rate of  $\sim 160,000$  frames per second is used in these experiments. A carefully designed lighting configuration which includes two xenon flash lamps and a conical diffusing reflector is utilized to provide proper illumination of the tube specimen. A close-up photograph of a 12-turn solenoid is shown in Fig. 1b; the coil



**Fig. 2** A schematic diagram showing the imaging optics for the conical mirror and procedure to map the image projected on the conical mirror to the developed image of the surface of a cylindrical specimen



inside the solenoid is made of 14-gauge square cross-section copper magnet wire at a winding spacing of 3.3 mm. An aluminum specimen of the same length as the coil is mounted on the solenoid. A pattern of 2.5 mm diameter circles is electrochemically etched on the outer surface of the tube specimen; these circles provide a means of measuring the principal strains directly in the expanded tube.<sup>1</sup> Such strain measurements permit the determination of the dynamic forming limit diagrams as described in Sect. 4.2.

In the experimental setup, the conical mirror is placed behind the specimen coaxially with the cylindrical specimen; this mirror projects the complete outer surface of the specimen on the focal plane of the camera—the tube surface becomes a circular band in the camera view and is recorded along with the direct view of the tube at the center of the image. A schematic diagram showing the geometrical optics of imaging

in the conical mirror and the unwrapping procedure used to generate the completely developed surface of the cylinder are given in Fig. 2. Given the cone angle ( $2\alpha = 130^\circ$ ) of the mirror, the projected image of the tube surface can be unwrapped to a rectangular band showing a complete view of the entire tube surface. An arbitrary point  $M(m, n)$  in the unwrapped rectangular image can be traced back to the point  $V(p, q)$  in the circular image projected on the conical mirror through the following relationships:

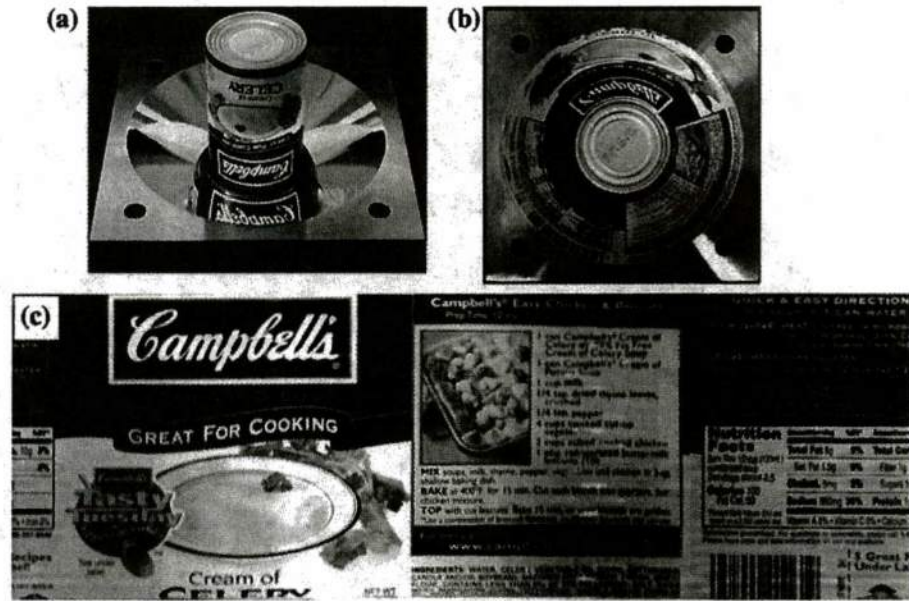
$$p = p_0 - r \sin \theta, \quad \text{and} \quad q = q_0 - r \cos \theta \quad (1)$$

where  $r = r_i + h(w - m)/w$  and  $\theta = 2\pi n/u$ .  $u$  and  $w$  are the length and width of the unwrapped image, respectively, and can be calculated through  $u = 2\pi r_s$  and  $w = h/\sin(2\pi - 2\alpha)$ , where  $r_s$  is the tube radius in the direct image of the tube and  $h$  is the tube width in the projected circular band. A simple graphical illustration of the imaging and unwrapping idea is shown in Fig. 3, where the image of a soup can observed on the conical mirror is then unwrapped to show the entire surface of the cylindrical can. Non-coaxiality of the cylinder and cone as well as deviations from axisymmetric deformations of the cylinder will

<sup>1</sup> This method is commonly used in the determination of quasi-static forming limit diagrams. The marking equipment and stencils were obtained from The LECTROETCH Company (<http://www.lectroetch.com/index.html>). Oliveira et al. (2005) and Thomas et al. (2007) used this technique to investigate dynamic forming limit diagrams.



**Fig. 3** Example of imaging with the conical mirror. **a** Overview of the conical mirror arrangement; **b** coaxial view of the soup can projected on the conical mirror; **c** unwrapped image of the surface of the soup can, obtained from the projection in (b)



lead to some errors in the unwrapped image; of course, corrections for these can only be performed with imaging with at least two cameras. This, however, is quite difficult for the dynamic problems considered here; therefore, we will restrict quantitative measurements to regions of the cylinder where the deformation may be considered to be reasonably axisymmetric. Errors in strain associated with these deviations were estimated to be  $\pm 3\%$ , which is within the range of specimen-to-specimen variability in the strain at localization.

### 3 Expanding tube experiments on Al 6061-O

Tube specimens were machined from stock Al 6061-O tubes to 15.5 mm mean radius and 0.5 mm radial thickness. Their axial lengths are either 18 or 36 mm depending on the solenoid used. For each test, a solenoid with same length as the tested tube specimen was used; this selection was used in order to produce a uniform distribution of electromagnetic force in the tube specimen. Experiments were performed on 12 tube specimens with expanding velocities in the range of 69–196 m/s, corresponding to strain rates of 4,000–12,000  $s^{-1}$ ; the experimental conditions of these specimens are listed in Table 1. A selected sequence of images from one expanding tube experiment as viewed in the conical mirror is given in Fig. 4. It should be noted that there are two views of the tube that can be seen in each of these images; first, there is a direct view of the tube as it

expands away from the solenoid that is at the center of each frame; this indicates the overall expansion of the tube in the early stages, as well as the fragmentation at later stages. In addition, the projection of the tube surface on the conical mirror can also be seen in this image; however, this can only be interpreted quantitatively after unwrapping through the conical mirror projection mapping; such unwrapped images of selected frames from this test are given in Fig. 5; these unwrapped images show the entire surface of the cylindrical tube in a plane. From the time evolution of the deformation shown here, it is easy to identify the development of strain in the two principal directions as well as the onset of localization and failure. Figure 6 shows the variation of two different measures of the hoop strain with time. First, a global measure of the strain is obtained from the direct image of the expansion of the tube; due to the slightly non-uniform expansion of the tube, this represents an average measure of the global strain. Second, the local deformation of one of the etched circles close to the middle plane of the tube surface (outlined by the white dotted square in the first frame of Fig. 5 and shown inset in Fig. 6) is used to determine the local strain in the specimen as a function of time. From these direct observations and measurements of the deformation of the expanding tube shown in Figs. 4, 5, and 6, we observe the following stages:

- The acceleration phase lasts only for about 15  $\mu s$  and in this time, the strain increases by less than

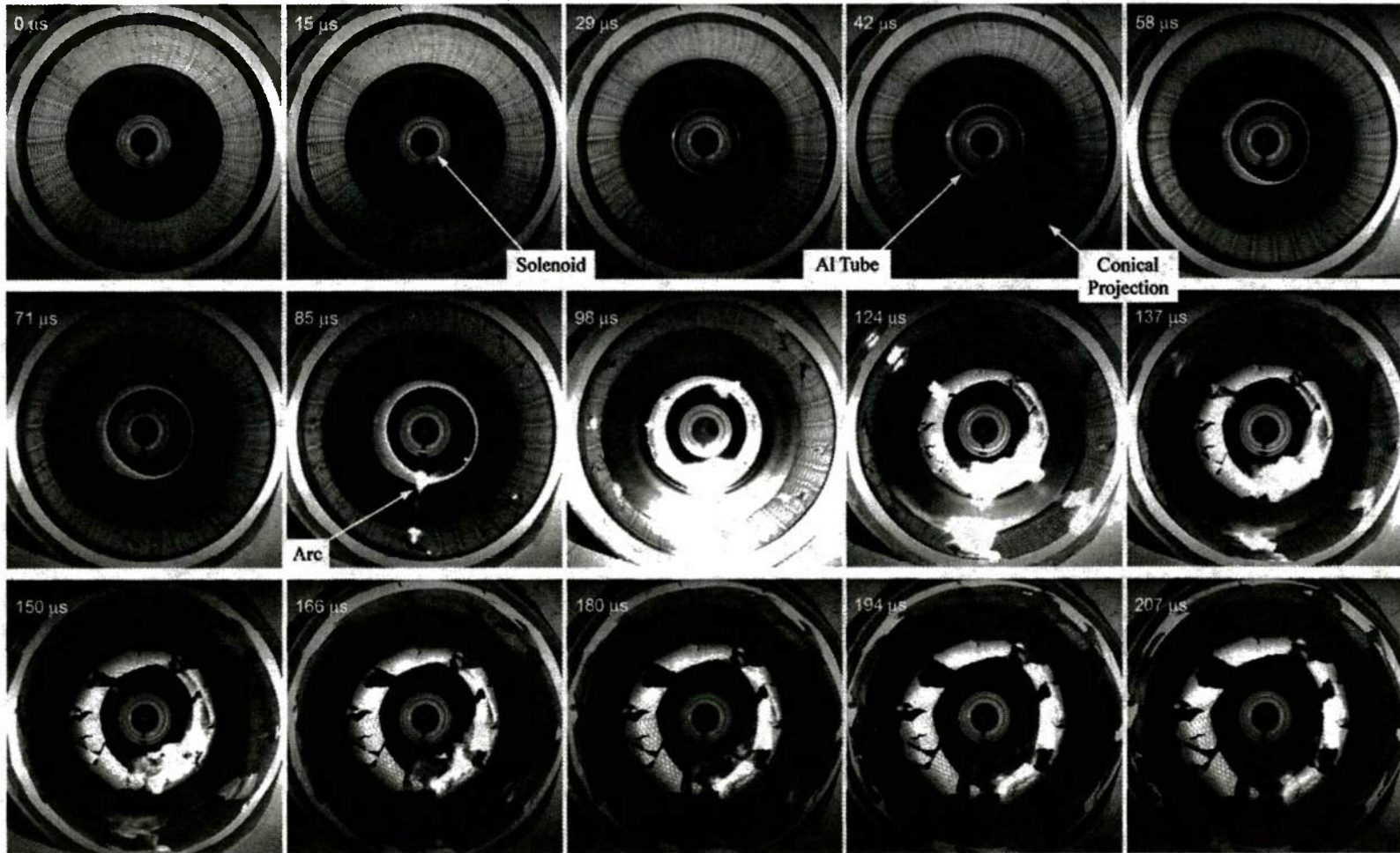


**Fig. 4** High speed images showing the expansion of an Al 6061-O tube ( $w = 36$  mm) at a speed of about 170 m/s



**Table 1** List of high speed expanding tube tests on Al 6061-O

Test number	Tube length (mm)	Solenoid (mm-turns)	Charging voltage (kV)	Tube velocity (m/s) <sup>a</sup>	Shearband angle (°)
1	18	18-6	12	69	—
2	18	18-6	12	120	54.03
3	18	18-6	13	141	53.38
4	18	18-6	14	176	51.80
5	18	18-6	14	167	50.50
6	18	18-6	14	196	51.45
7	36	36-12	12	100	—
8	36	36-12	13	116	53.73
9	36	36-12	14	156	53.65
10	36	36-12	14	146	52.23
11	36	36-12	15	171	50.27
12	36	36-12	15	170	52.51

<sup>a</sup> The steady ring expansion speed reached in the time interval 15–50  $\mu$ s is quoted. There is a brief period of acceleration for about 15  $\mu$ s and a small deceleration beyond 50  $\mu$ s

10%. In the next stage of deformation, until about 49  $\mu$ s, the tube expands nearly uniformly at a speed of about 170 m/s, corresponding to a strain rate of about  $10^4 \text{ s}^{-1}$ . Due to the effect of free boundaries at the ends of the cylindrical specimen, the tube specimen experienced a slight bulging or barreling symmetry. This bulging deformation was also observed by Thomas et al. (2007) and Thomas and Triantafyllidis (2009). During this stage, the hoop strain measured from the global expansion of the tube is similar to that measured from the local electrolytically etched marks. This stage ends when the strain in the tube reaches a critical level (to be identified later) and localization occurs. We will not consider this stage further, other than through numerical simulations in Sect. 6.

- In the second stage, localized deformations occurred nearly simultaneously at many locations on the tube surface. Direct observation of the localization bands in their early developing stage is hard due to their low optical visibility in the early stages and in part to the poor spatial resolution of the camera; however, the development of numerous localization bands is clearly indicated by the cracks that started from highly strained locations along specific directions almost immediately and also by post-mortem examinations. For example, a high magnification image of the region identified by the white dotted square labeled A in the image corresponding to 58  $\mu$ s is shown inset at the right side of Fig. 5; a blurry region is seen at the circle on the 4th column, 6th row.

In the next image, at 64.8  $\mu$ s, a crack has clearly emanated from this point and grown to over about 4 to 5 mm in length (see magnified inset of the corresponding region, labeled a). Similar localization and nucleation are identified at points labeled B (see high magnification inset image pair B-b), C and D in Fig. 5. During this stage, the tube expands at a slightly decreased average speed due to the diminution of the driving force as the tube moves farther away from the solenoid. The hoop strain measured from the global expansion still matches that from the local marks as can be verified from Fig. 6. This indicates that the deformation of the marked circle used for the local measurement is not significantly influenced by the localization; we will show in Sect. 4 that a network of uniformly distributed shear localizations is developed in this stage. This stage ends rather quickly as cracks begin to appear almost immediately.

- In the third stage of deformation, numerous cracks that developed in the last part of the second stage continue to grow along the localized bands throughout the whole width of the tube, producing complete fractures and fragments. The cracks and their orientation on the tube surface are easily identified in the unwrapped images in Fig. 5. The high magnification insets labeled A-a and B-b indicate the appearance of cracks. Nearly simultaneous nucleation of three parallel cracks can be identified in the circular region marked C-c in the images at 71.2 and 77.9  $\mu$ s; such closely space nucleation suggests that



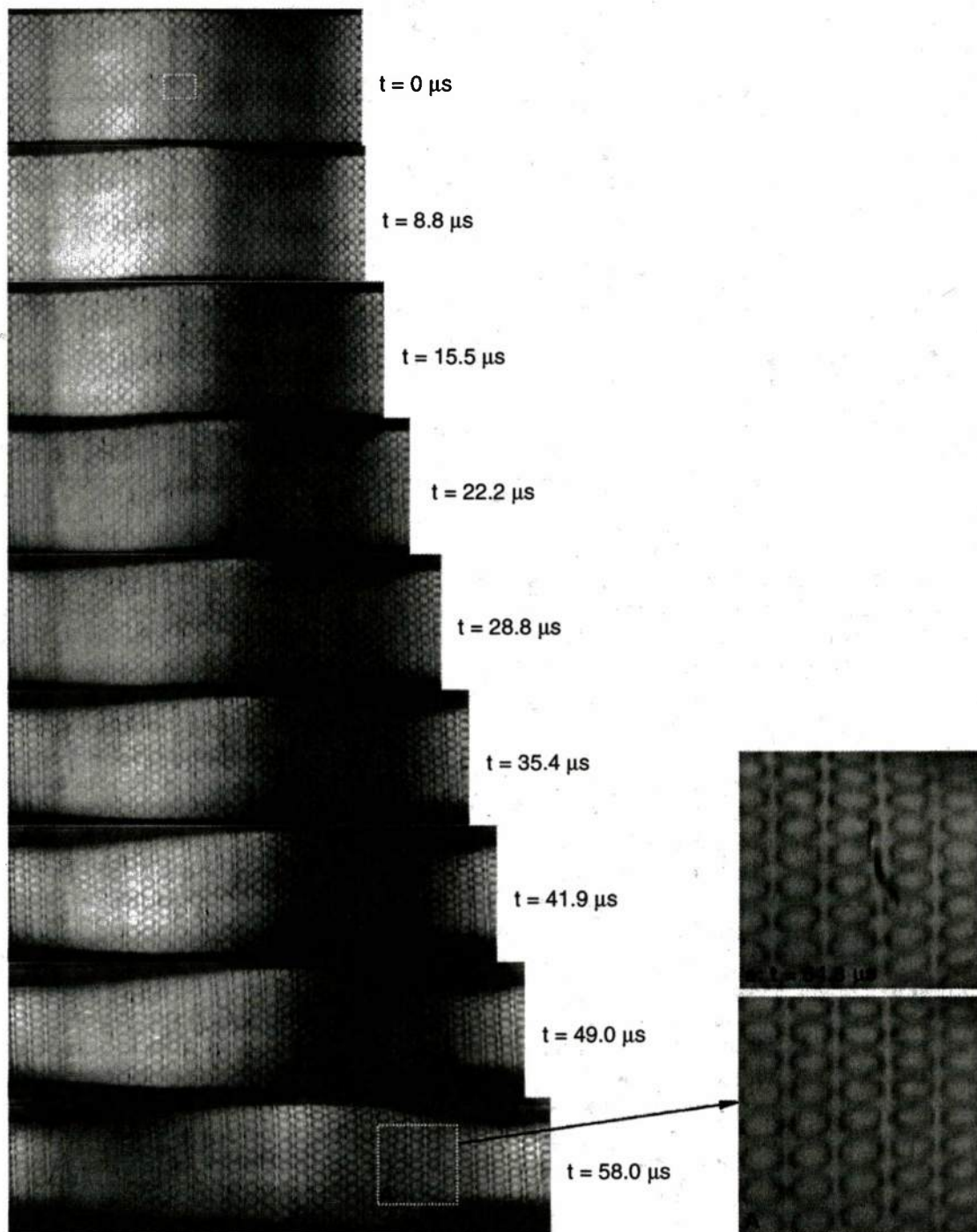


**Fig. 5** Sequence of unwrapped images from Test #10, indicating the deformation on the surface of the cylinder. Uniform deformation is observed for times less than  $49\ \mu\text{s}$ ; localization and fracture appear in the time range of  $49\text{--}85\ \mu\text{s}$ . A slight distortion of the images is observed since the expansion of the cylinder is

slightly non axisymmetric. Nucleation of new cracks and growth of multiple cracks are observed in the time range of  $49\text{--}86\ \mu\text{s}$ . Beyond this point, no new cracks are nucleated, while the cracks formed at earlier times continue to grow and create fragments

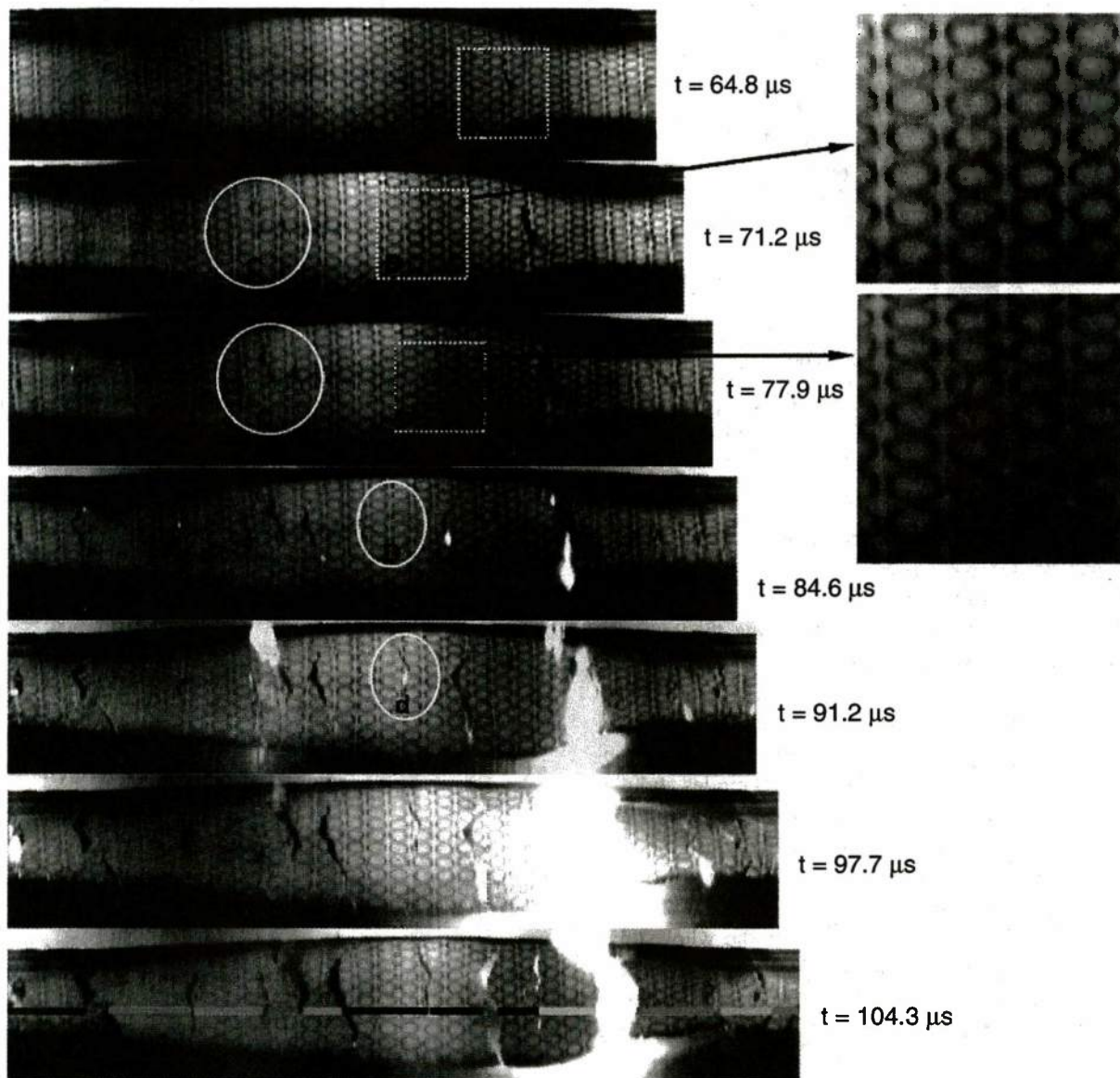
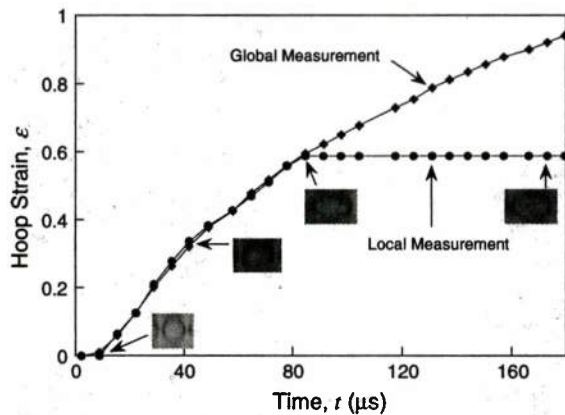


Fig. 5 continued

these were independent events. The last nucleation of crack is observed in the region marked **D-d** in the images at 84.6 and 91.2  $\mu\text{s}$ . No new cracks are nucleated beyond this time, but the cracks already nucleated continue to grow generally in the longitudinal direction, but in a zig-zag manner as the crack tracks the localization bands, and heads towards the ends of the cylinder. When the fractured surfaces separate and break electrical contact, the electric potential is still high and hence electric arcs jump

across the fragment surfaces; these are identified in Fig. 4 at 85  $\mu\text{s}$  and beyond. After this, current flow is interrupted and no further loading of the tube specimen occurs; the tubes continue to move as a result of the kinetic energy. As shown in Parts I and II with respect to the ring specimens, multiple fractures occur since unloading from each fracture diffuses through the specimen per the Mott analysis very slowly; the difference is that for the tube specimens with much larger aspect ratios, both the fracture pattern and





**Fig. 6** Variation of the hoop strain with time: the global measurement is from the average tube radius, and the local measurement is from a surface etched circle

the Mott release waves could be two dimensional, and the fragmentation process of the tube specimen is dominated by crack propagation or tearing along the localized bands. In this stage, the straining of the non-fractured regions of the tube terminates once the release waves sweeps through the entire specimen. The unloading of the specimen can be identified by the divergence between the local hoop strain as measured from the etched circles and the global strain measured from the expansion of the tube fragments on average. We label this strain  $\epsilon_d$  and will show that this strain is different from the critical strain at the onset of necking in Sect. 4. Once the release waves sweep through the whole tube specimen, fractures completed within that time produce fragments flying away from the solenoid rigidly without further straining. Statistical sampling of this strain at different locations indicated small deviations (within  $\pm 3\%$ ) in a single specimen, but not correlated to the fragment size. But as shown later in Fig. 12, there was a larger variation between specimens expanded at different speeds; however, we do not have sufficient samples to do a statistical evaluation of this.

Similar observations were made on cylindrical specimens of different lengths at different expansion speeds or strain rates. Note that these real-time observations do not provide a complete description of the deformation and failure events; the spatial resolution is not high enough to indicate precisely the strain levels at which strain localization begins to emerge. Additional

input towards this is obtained from an examination of the recovered fragments and from simulations of the expanding tube experiment. The stage of uniform deformation is easily analyzed with conventional plasticity theory and hence we will not discuss this further in this paper. The other two stages—the onset of localization and the nucleation and growth of cracks—are considered in greater detail in the next two sections.

#### 4 Onset of shear localization: dynamic forming limit of sheet metals

In this section, we examine the onset of strain localization in the expanding tube experiments described in Sect. 3 and then deduce the dynamic forming limit of sheet materials. First, we summarize the maximum tension theory that is used commonly to predict forming limit in sheets under quasi-static conditions. Next, we examine the experimental observations on strain localization and identify the deformation responsible for such localization. The dynamic forming limit is then established from the experimental measurements and compared with the quasi-static theory in order to evaluate strain rate effects on the forming limit diagram.

##### 4.1 Maximum load theory of forming limit

The constitutive response of the Al 6061-O can be represented by a power law of the form

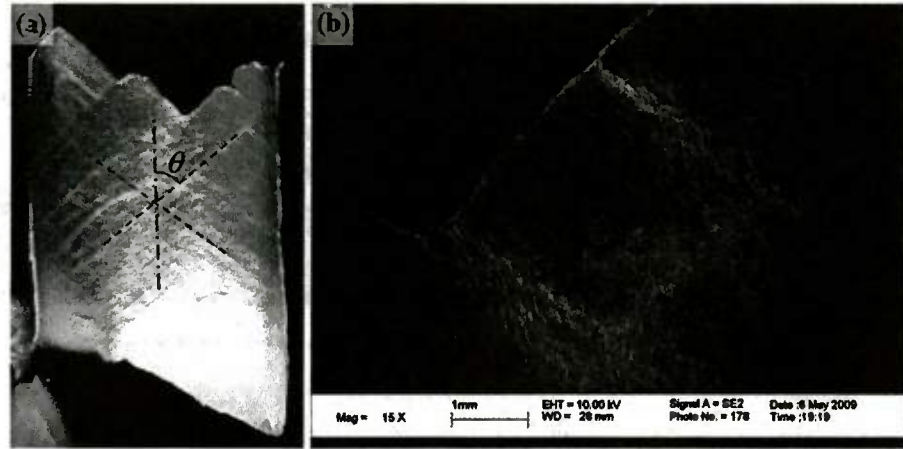
$$\sigma = k\epsilon^n \quad (2)$$

where  $k = 205 \text{ MPa}$  and  $n = 0.22$ ; the quasi-static stress-strain response of Al 6061-O is shown in Fig. 14 of Part I. This characterization was developed in a quasi-static uniaxial test in which localization in the form of a diffuse neck was observed immediately past the point of maximum load. The strain at the onset of localization or the strain at the limit load was found to be:  $\epsilon_N^{qs} = 0.22$ ; this is well predicted by the well-known Considère condition for maximum load in a bar or strip in tension where diffuse necking symmetrical about the tension axis occurs. Now we summarize the maximum load theory that is used to predict the onset of strain localization in sheets.

In large sheet materials under uniaxial tension, while diffuse necking of the type observed in bars of nearly



**Fig. 7** Post-mortem image of a typical fragment from the expanding tube test (Test #10). **a** Low magnification image showing orientation of band with respect to the hoop direction **b** Scanning electron micrograph of the region near the fracture



equi-axed cross-section is prohibited by the geometric constraint, observations show that localizations still develop, but in narrow planes oriented at an angle to the load. As in the development of the Considère condition for diffuse necking, the maximum load theory can also be used to deduce the condition for this “sheet-necking” and this analysis is briefly summarized here. Consider a region of a sheet material deforming uniformly under proportional biaxial loads  $T_1$  and  $T_2 = \alpha T_1$ . The limit load occurs when the following condition is satisfied.

$$dT_1 = t d\sigma_1 + \sigma_1 dt = 0 \quad (3)$$

For a power-law hardening material, the limit load can be shown to correspond to the strain state

$$\varepsilon_1 = \frac{n}{1+\beta} \quad \text{and} \quad \varepsilon_2 = \frac{\beta n}{1+\beta} \quad \text{or} \quad \varepsilon_1 + \varepsilon_2 = n \quad (4)$$

where  $\varepsilon_1$  and  $\varepsilon_2$  are the principal strains,  $\beta = \varepsilon_2/\varepsilon_1$  is the ratio of biaxiality of the strains and  $n$  is the strain hardening exponent. Considering the geometric constraint of the sheet localization which dictates zero extension along the shear direction, the angle of the localizations to the maximum principal loading direction is found to be

$$\theta = \frac{\pi}{2} - \frac{1}{2} \cos^{-1} \left( \frac{1+\beta}{1-\beta} \right) \quad (5)$$

For sheet materials under uniaxial tension  $\beta = -0.5$ , we get the critical strain at the onset of sheet necking  $\varepsilon_{sn} = 2n$  and the angle of the shear band  $\theta_{sn} = 54.74^\circ$  with respect to the direction of tension. Detailed accounts of localization analyses can be found in the works of Hill (1952) and Storen and Rice (1975).

The above equations are obtained in the framework of quasi-static analysis and Eq. 4 provides a limit condition when shear localization occurs in sheet materials.

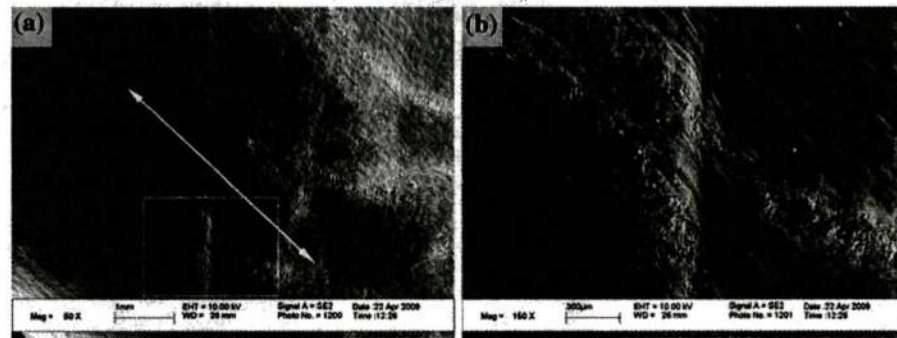
In sheet metal forming, this limit is called the forming limit, and the strain diagram presenting the limit is called the forming limit diagram (FLD). Once this limit is reached, inhomogeneities or defect in a real material will trigger localized deformation. In Part II of this series, we have shown that under dynamic loading, the geometrical and inertial effects control the propagation of localization across the cross-sectional dimension of specimens with large aspect ratios and this in turn dictates the uniform strain levels observed away from the localization. In the following sections, we will examine the forming limit of sheet materials under dynamic tension using the observations from our expanding tube experiments.

## 4.2 Experimental observations of strain localization

In this section, we examine the details of the deformation of the expanding tubes through post-mortem observations and strain measurements. Fundamentally, we aim to answer questions about when the expanding tubes reach the limit of their uniform plastic deformation, and how this instability of deformation occurs. First, we will examine the characteristics of localization of plastic deformation. Then, we will examine the forming limit diagram through measurements of the residual strains in the recovered fragments.

An optical image of one fragment from a 36mm tube specimen is shown in Fig. 7a. The hoop direction of the cylinder is indicted by the dash-dot vertical line and is the direction of the major principal strain in this specimen. The final length of the cylinder is

**Fig. 8** **a** Scanning electron micrograph showing shear deformation within the localized region **b** Higher magnification image of the region close to the etched circles



about 32 mm and is marked in the image providing a length scale for this image. Localized deformation occurs along numerous intersecting bands, making a network across the entire specimen, and the bands of such localization are visible to the naked eye under normal lighting conditions. A higher magnification scanning electron micrograph is shown in Fig. 7b to provide an enlarged view of these deformation bands. However, more detailed microscopy is required to determine the nature of the deformation along these bands as discussed in the next paragraph. Clearly, inhomogeneities or defects in the material must play a crucial role by acting as nucleation sites for triggering localized deformation. In the diffuse necking experiments discussed Parts I and II, it was possible to measure the distances between the localizations at different stages of development easily and evaluate the statistics of the localization. In contrast, in these tubes, there are so many localized bands that are closely spaced and at different stages of development, that it was difficult to extract the underlying statistics. Nevertheless, the distribution characteristics of the localization bands observed must depend on the statistical characteristics of defects in the material that triggered such localization. We will explore this through numerical simulations in Sect. 6. The angle  $\theta$  of these shear bands to the tensile loading direction is measured for the tube specimens where localization occurs and is listed in Table 1. The reported angle is an average over a large number of localizations in each specimen. It is seen that the measured angles match the angle  $\theta \sim 54.74^\circ$  predicted from Eq. 5 for uniaxial tensile loading indicating that the tube specimens are likely to be under nearly uniaxial tension conditions, at least on the time scale over which the localization appeared; furthermore, strain-rate or inertial effects

may not significantly affect the angle of development of the localization.

In order to determine the nature of the deformation localization, these bands were examined under optical and scanning electron microscope. A close view of the crossing bands can be seen in the high magnification SEM images in Fig. 8. In these images, we focused on a pair of the electrochemically etched circular marks across which the localization occurred. The double-ended arrow in Fig. 8a indicates the nominal hoop direction of the major principal strain; we observe that a band with a width in the order of about  $100 \mu\text{m}$  crosses the ellipse and that there is a dominant shearing deformation across the band. One of the fragments was sectioned in order to determine whether the localizations were necks in the thickness direction. An optical micrograph of the thickness section is shown in Fig. 9; this image indicates that the thickness remains nearly uniform (at about 0.38 mm) along the hoop direction of the cylinder except in the vicinity of cracks. In contrast, in the region where the cracks develop, significant thinning as well as cavitation are observed; clearly, the thinning is a later occurrence in this case, potentially associated with the generation of cracks. The absence of significant thickness nonuniformity corresponding to the localized bands in Fig. 9, and the shearing seen within the bands in Fig. 8 indicate that the deformation localization is in the form of in-plane shear deformations. Therefore, we will refer to them from now on as shear bands; while these shear bands are not as sharp as adiabatic shear bands observed in penetration type problems, they still represent shear localization. As in the case of the expanding rings, the residual strain in the unloaded portions of the specimen must provide a good estimate of the strain at the onset of localization; in the case, this strain is the forming limit.

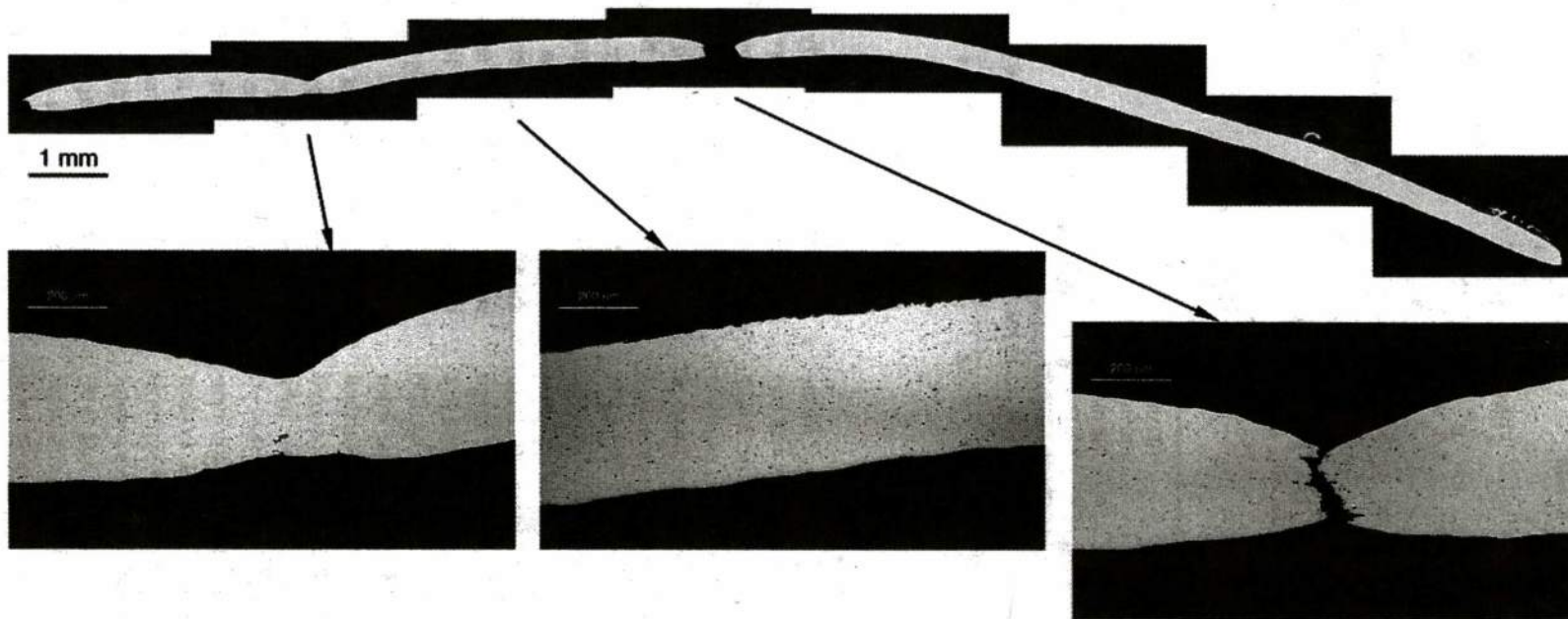
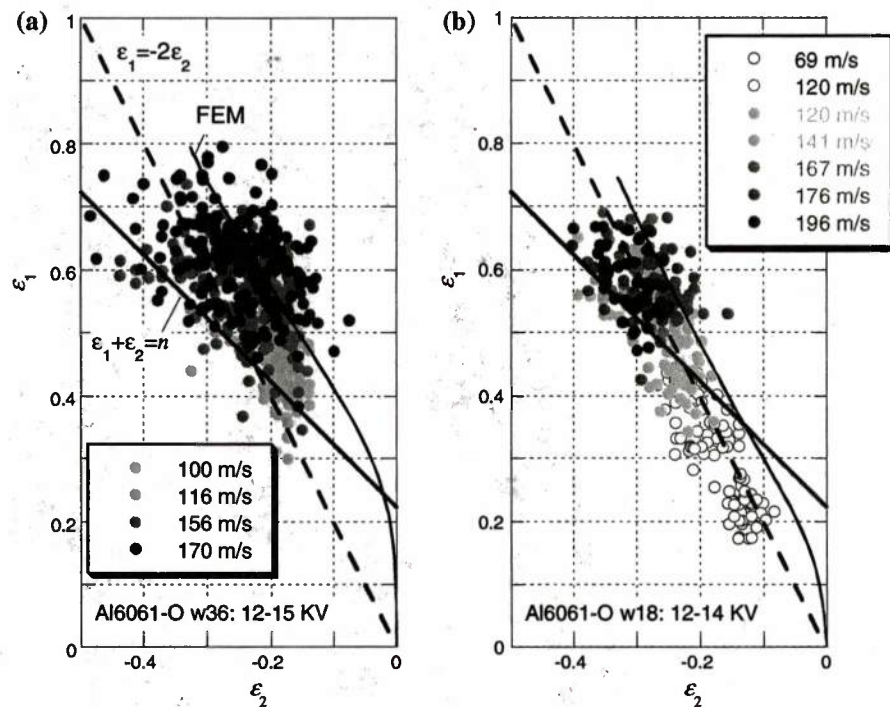


Fig. 9 Optical micrograph of a thickness section of a specimen; note that there is significant thinning in the region near the fracture, but not in other regions



**Fig. 10** Forming limit diagrams for **a** 36 mm wide tubes; and **b** 18 mm wide tubes. *Open circular symbols* correspond to principal strains measured from regions where no localization is observed, and the *filled circular symbols* correspond to regions where localization is observed. The *blue dashed line* indicates the uniaxial stress path  $\varepsilon_1 = -2\varepsilon_2$ , and the *red line* indicates the quasi-static forming limit  $\varepsilon_1 + \varepsilon_2 = n$  based on maximum tension criteria (Color figure online)



We turn next to an evaluation of the dynamic forming limit diagram. The electrochemically etched circles deform into ellipses; measurement of the major and minor axes of these ellipses provides an estimate of the maximum strains sustained by the specimen in any give experiment. We determined these principal logarithmic strains,  $\varepsilon_1$  and  $\varepsilon_2$  ( $\varepsilon_1 > \varepsilon_2$ ) from the surfaces of a large number of recovered fragments. These measured strains are plotted in the FLDs shown in Fig. 10. This corresponds to 940 measurements from 10 different tubes, expanded at strain rates in the range of  $10^3$ – $10^4$  s $^{-1}$ . The results in Fig. 10a correspond to a cylinder of 36 mm length while the results in Fig. 10b correspond to a cylinder of 18 mm length. Data from tubes expanded at different speeds are distinguished in Fig. 10 by different colors. All data were measured from regions that were close to the center of the tube where boundary influence from the free ends of the cylinder is expected to be small. The principal strains measured from regions where no localization was evident under optical microscopy are plotted as open symbols while the strains measured from regions where a shear band intersected the ellipse are plotted as filled symbols. There is quite a bit of scatter in the data presented; there are two sources for this scatter. First, these local

measurements, particularly the minor principal strains, are influenced by the curvature of the specimen, systematically to larger values. Second, the strains measured in places where a shear band intersects the etched marking do not take into account the distortion provided by the shear band. Nevertheless, these estimates of the principal strains are a meaningful measure of the state of strain in the fragments. Besides the measured data, two theoretical lines are also indicated in Fig. 10: the blue dashed line corresponds to a state of uniaxial stress, with  $\varepsilon_1 = -2\varepsilon_2$ , and the red solid line indicates the theoretical forming limit for sheet materials given in Eq. 4. The main observations from these FLDs are described below.

- It is clear that most of the measured data fall in the region  $\varepsilon_1 > -2\varepsilon_2$ , but far away from the plane-strain condition ( $\varepsilon_2 = 0$ ). While one might have expected that due to inertial constraint that the deformation might be close to a plane strain state, particularly in the middle of the cylinder, this apparently is not the case; most of the data are spread around the deformation path indicating a uniaxial stress loading experienced by these tubes. Compared to the data of 18 mm tubes, the loading path of the 36 mm tubes trends more towards the plane

strain region although it is still far from it; we will return to a discussion of the strain state later through numerical simulations.

- For the 18 mm wide tubes, the expanding velocities are in the range of 69–196 m/s. No localization is observed in the tube expanded at 69 m/s; both non-localized and localized regions are observed in the tube expanded at 120 m/s. For the tubes expanded at speeds higher than or equal to 141 m/s, the surface is covered with numerous shear bands. For the 36 mm long tubes, shear localization is evident through out the surface of all tested tubes with expanding velocities in the range of 100–170 m/s.
- The boundary between the open symbols representing uniform straining and the filled symbols representing the formation of shear bands indicates the dynamic forming limit diagram. For the 18 mm tubes, the data for the non-localized circles and the localized circles are separated roughly by the line corresponding to the quasi-static forming limit (Eq. 4); for the 36 mm tubes, even though there are no data that correspond to non-localized deformation, the majority of the data of the localized circles on the tested tubes are immediately above the predicted forming limit. It is clear that this dynamic forming limit boundary is rather well predicted by Eq. 4, with the high strain rates that the tubes experienced exhibiting little influence on the onset of shear localization and hence on the forming limit. This result is analogous to the onset of diffuse localization in expanding rings that was reported in Parts I and II.
- The measurements above show that uniform deformation of the tubes terminates and localization occurs at a critical strain  $\varepsilon_{sn}=2n$ , which is the major strain at the crossing point of the uniaxial tensile loading path and the forming limit line; for the Al 6061-O tubes,  $\varepsilon_{sn}=0.44$ . Note, however, that this strain is lower than the diverging strain  $\varepsilon_d$  defined with respect to the average global strain in Fig. 5. The fact that even after the occurrence of localization, the local strain in the specimen averaged over the length of the circular marks (about 2.5 mm) follows the global strain measured over the entire diameter of the expanding cylinder suggests that a uniformly distributed localization must have occurred after the critical strain. This is supported by the observation of the network of shear bands shown in Fig. 7a.

We now have a clear picture of the evolution of shear localization in the cylindrical specimens under dynamic loading and will explore this and other aspects of strain localization further in Sect. 6 through numerical simulations.

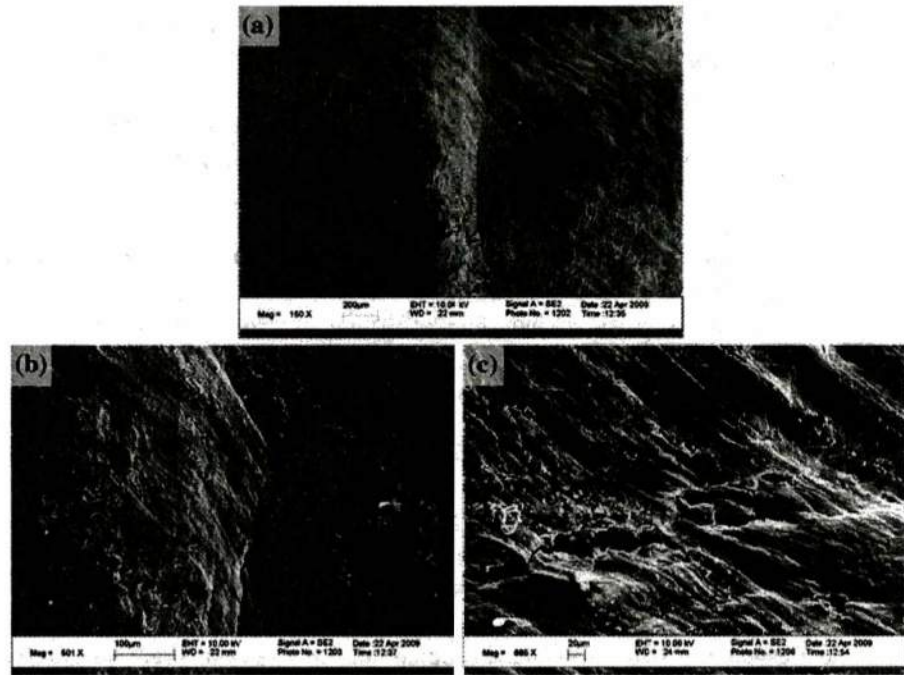
## 5 Onset of fracture, unloading and fragmentation

Next, we examine the onset of fracture and the generation of fragments. The fractured edges of the fragment shown in Fig. 7 appear to always follow along on one of the shear bands, clearly indicating that the localization precedes fracture development. In fact, cracks are seen to nucleate at intersections of the shear bands as illustrated in Fig. 11a; details of the crack nucleation are shown in Fig. 11b and c. It is evident that void growth and coalescence within the intersecting shear band is the primary mechanism of crack initiation and growth even at strain rates in the range of  $10^4 \text{ s}^{-1}$ . From the thickness measurements near the fractures in Fig. 9, and using plastic incompressibility, we infer that the failure strain is around unity (while the strain at onset of localization  $\sim 0.44$ ).

The global and local measures of the hoop strain are plotted as functions of time in Fig. 12 for three 36 mm tubes expanded at different velocities: 116, 156, and 170 m/s. The local strain is measured from high speed images of an etched circle at a similar position to that shown in Fig. 4 around the middle plane of each tube. For the tube expanded at 116 m/s, the tube expanded to a final diameter of about 49.7 mm, corresponding to an average strain of 0.47 *without* fragmenting. The energy from the applied loading is completely dissipated in the plastic deformation process and all straining as well as rigid motion of the specimen stops at the end of the experiment. Even though the global and local strain measures are completely in agreement, the whole surface of this specimen is completely covered with shear bands. Post-mortem examination of the tube did not show any optically visible nucleation of cracks. For the tube expanded at 156 m/s, the tube fragmented into seven large pieces and a number of smaller pieces; the onset of cracking is indicated in Fig. 12 by an asterisk at the appropriate time. Almost immediately following this time, the local measure of strain takes on a constant value suggesting an unloading of the specimen; the fragments retain significant kinetic energy and continue to move out radially. This behavior can be



**Fig. 11** Scanning electron micrographs indicating a nucleation of microcracks near intersections of shear bands and **b** and **c** details of the growth and coalescence of microcracks to form the crack



understood in terms of Mott's idea of "release waves" (Mott 1947) although it needs to be reinterpreted for this two-dimensional problem that includes crack extension; we will develop this idea more completely in the next paragraph. For the tube expanded at 170 m/s, a similar behavior is observed, with the final strain in the fragments being just a little bit larger; in this case there were nine major fragments and a number of smaller pieces.

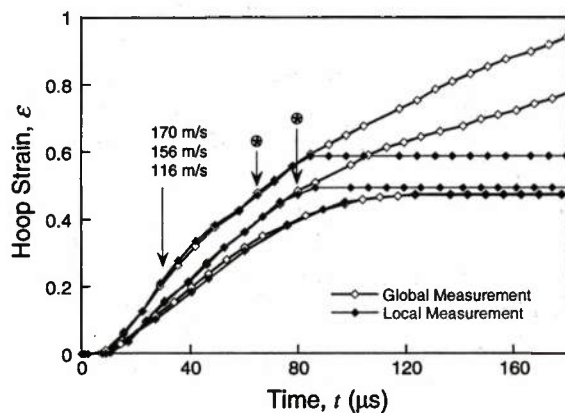


**Fig. 12** Variation of hoop strain with time for 36 mm tubes expanded at different speeds: the global measurement is from the average tube radius, and the local measurement is from a surface etched circle

Consider that the first crack nucleates at the point A as shown schematically in Fig. 13; the unloading wave that results from nucleation of this crack will diffuse away from the crack in a manner that is similar to the Mott release wave in the thin rings. The region so unloaded is indicated by the shaded region in Fig. 13; within this unloaded region, there can be no further nucleation of cracks. However, since the regions within the shaded regions still retain their velocity in the radial direction and hence significant kinetic energy, they continue to concentrate stress near the crack

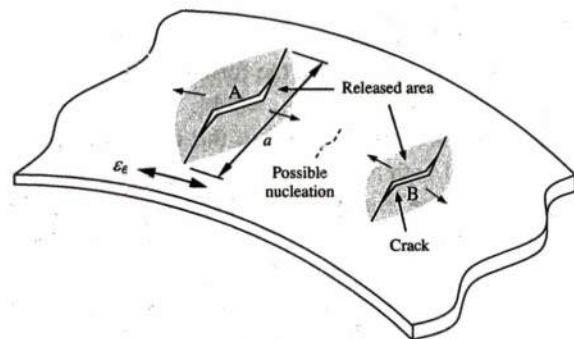


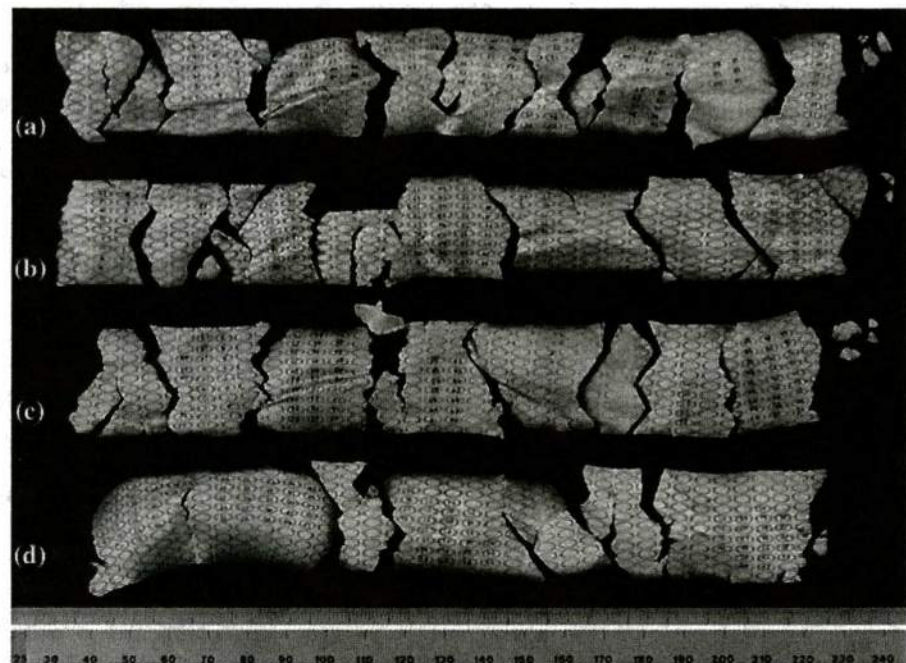
**Fig. 13** Schematic diagram of the Mott release waves from crack nucleation and growth in the expanding tube. The red arrow indicates the propagation of the release wave; the gray shaded region enveloped by the release wave (Color figure online)

tips and drive the crack dynamically. From the images in Fig. 5, we estimate that the crack speeds are typically in the range of 1,000 m/s. Hence, beyond the nucleation of cracks at the intersection of the shear bands, there is a dynamic growth of cracks involved in this fragmentation problem. This is the key difference between the ring and tube tests. Regions of the tube that are outside the released regions continue to experience higher strains and hence it is possible to nucleate other cracks, such as at the position *B* in Fig. 13; this crack behaves in a similar way, with its own release domain and crack extension. When the two release regions overlap, the portion between *A* and *B* the line segment *AB* is unloaded. Eventually, when the cracks run to the ends of the cylinder or into each other, a stress-free fragment but possibly moving with significant radial kinetic energy is created. This can be seen in Fig. 12, where the radius as a function of time of the fragments continues to increase. Hence, the process of fragment development in the tubes—nucleation of cracks at intersections of shear bands, growth of cracks, unloading through release waves—appears to be very similar to that observed in rings although there are detailed differences due to some aspects of crack propagation. Nevertheless, the nucleation of cracks and propagation of release waves suggests that statistical aspects

must be of importance in governing the development of fragments.

Detailed examination of the fragmentation, based both on the real-time observations of the entire surface of the cylinder and post-mortem evaluations of the fragments, reveals statistical information regarding the nucleation and growth of cracks and production of fragments. In prior studies, such as those of Winter (1979), Vogler et al. (2003) and others, the absence of detailed real-time imaging information implied that fragmentation statistics could only be considered through recovered fragments or with the partial views provided by the high speed images; then the analysis is typically limited to considering the distribution of the mass of fragments. But, the two-dimensional nature of the crack growth and propagation of release waves could not be captured appropriately. Here, we are guided by real-time measurements in identifying the time sequence in which cracks were nucleated and therefore, we are able to obtain the statistical distribution of fragment sizes, suitably normalized by the Mott scale for the propagation of the release wave. In Fig. 14, images of the fragments from four different tests on the 36 mm long tubes are shown. It is clear that there are many small fragments, but from the real-time images we recognize that these formed

**Fig. 14** Fragments collected from four different tube expansion experiments  
a Test # 11, b Test # 12,  
c Test # 9, d Test # 10





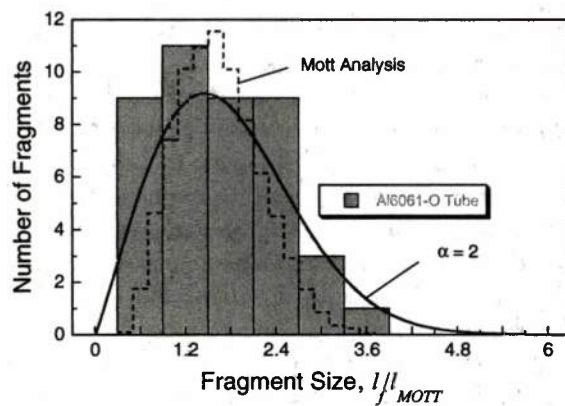


**Fig. 15** Distribution of the fragment size normalized by the Mott scaling length  $l_{MOTT}$ ; for comparison, the estimate based on Mott's statistical method is shown by the dashed line. The solid red line is the Weibull fit to the fragment distribution in thin rings from Part I (Color figure online)

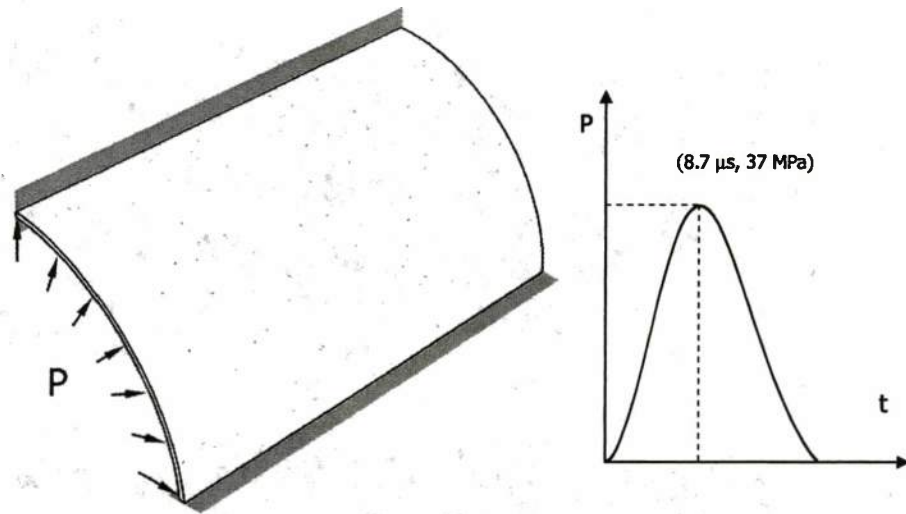
significantly later, as a result of crack interactions, and are thus not part of the early nucleation, growth, and release process. To make this clear, we identify the distance between the different cracks nucleated along the center line of the real-time image in Fig. 5 and the corresponding recovered fragments in Fig. 14, by the overlaid colored lines. This essentially ignores the crack propagation along the axial direction of the tube, but this is justified on the grounds that the statistics of fragment development is determined by the nucleation of cracks, which in turn is influenced by the propagation of the unloading waves, while the propagation of cracks along the axial direction is influenced mainly by deterministic aspects related to dynamic crack growth. The distribution of "fragment lengths" as identified above, normalized by the Mott scaling length,  $l_{MOTT} \sim 2(2\sigma_y t / (\rho \dot{\epsilon}))^{1/2}$  is plotted in Fig. 15; the strain rate  $\dot{\epsilon}$  is based on the tube velocity shown in Table 1. The distribution of fragment lengths obtained in the ring expansion experiments of Part I is also shown overlaid on this plot. In addition, the Mott estimate with  $\Delta \epsilon \sim 0.01$  is also shown in this image. These comparisons indicate that the picture of nucleation and growth of cracks, followed by the progression of the release waves and their interaction, suggested in Fig. 13 is an adequate description of the fragmentation of tubes. Of course, if the small fragments that develop later are to be included in the predictions, dynamic crack propagation and interaction will have to be included in modeling of the fragmentation process, but this is on top of the statistically determined nucleation.

## 6 Modeling and numerical simulation of localization of metal tubes

Our experimental observations reveal the following sequence of events in the fragmentation in metal tubes expanded at high speed: (i) development of a network of shear localization once the forming or critical condition is reached, (ii) dynamic nucleation of cracks at the intersections of the shear bands, (iii) dynamic growth of cracks or linking of multiple cracks in the axial direction, (iv) diffusion of release waves in the hoop direction that completely stops the continued straining of the specimen behind, and (v) the final formation of fragments. In this section, we present the results of finite element simulations that are aimed at reinforcing this understanding by quantitatively modeling the onset and growth of localization observed in the expanding tube experiments. The effect of the distribution of defects on the localization characteristics will also be discussed.

The nature of the shear band development that is revealed in the present study dictates that a three dimensional model is required in order to capture the deformations experienced by the specimen. While reduced models such as plane-strain or shell elements may be computationally cheaper, they cannot be used to represent the deformations experienced by the expanding tubular specimen. Therefore, a three-dimensional model which resembles the geometry of the 36 mm tube specimens ( $r_i = 15.25$  mm,  $r_o = 15.75$  mm, and  $w = 36$  mm) is used. On the other hand, for simplicity, we consider only a quarter segment of the tube and impose symmetry boundary conditions at planes  $\theta = 0$  and  $\theta = \pi/2$ ; this model reduction does not limit the possible deformation and localization modes observed in the experiments. Furthermore, the Mott release wave analysis indicates that as long as the simulated region is significantly larger than the scale dictated by the release process, fragment size distribution will not be affected. The model is discretized with a  $243 \times 5 \times 360$  ( $arc \times t \times w$ ) mesh using eight-node linear brick elements with reduced integration and hourglass control (C8D8R);  $f \times 100$  percent of the total elements are randomly selected as material defects to trigger localization. The tube material is taken to obey the power-law hardening model given in Eq. 2, with a  $J_2$  flow theory for 3D generalization. The elements with the material defect are assumed to possess an yield strength of 25 MPa and to exhibit no strain-hardening. Two volume fractions of the element defect are considered:

**Fig. 16** Quarter symmetry finite element model of a tube with 0.1% material defects randomly distributed in the model (indicated by the red dots). A pulse pressure is imposed on the inner surface of the tube (Color figure online)



$f = 0.001$  and  $f = 0.0001$ . We have not attempted to provide a statistical distribution for the defect material properties; while this might add more realistic features to the simulation, our main aim is to demonstrate the pattern of localization and the feasibility of fragmentation simulations. The effect of defect strength on the onset of localization has been examined by Molinari and Clifton (1987) and Estrin et al. (1997). This quarter-tube model is shown in Fig. 16, where the elements with defect ( $f = 0.001$ ) are identified by the dots. A pulse pressure loading, also shown in Fig. 16, is used to simulate the electro-magnetic driving force experienced by the tube specimen in our experiments. This pressure loading, applied on the inner surface of the tube, rises to a peak value of 37 MPa in 8.7  $\mu$ s and drops to zero at about 20  $\mu$ s. The resulting expanding velocity of the tube is about 215 m/s in the first 40  $\mu$ s, and corresponds to a strain rate of about  $10^4 \text{ s}^{-1}$ . In order to continue the simulation properly beyond the level of localization, one must impose a suitable failure criterion for the material located within the shear band; while there are a number of damage models such as the Gurson–Tvergaard–Needleman model, these are not yet fully developed to account for the material behavior within the shear band. Therefore, for the sake of simplicity, we adopted a critical strain based criterion and element deletion technique to simulate the fragmentation process. The element deletion feature in ABAQUS was used to remove elements with an effective plastic strain larger than one. We hasten to add that this is not a proper way of accounting for crack initiation and growth; however, our interest in these simulations is

capturing the early stages of the onset of shear banding localization and the unloading of the surrounding regions due to such localization. The material is assumed to follow the power-law hardening response until reaching the failure strain level; we have not introduced any strain rate effects since earlier studies in Parts I and II on this particular alloy indicated that strain rate effects are not large at rates of  $10^4 \text{ s}^{-1}$ . Also, thermal softening generated by the conversion of plastic work to heat (or from Joule heating in the specimens) is known to cause a drop in strength in some material; this has not been considered in the present simulations. A quick estimate indicates that such temperature increases are not significant enough to cause remarkable changes in the yield and flow behavior of the material. Contours of constant von Mises effective stress from the simulation with  $f = 0.001$  are displayed in Fig. 17a. The emergence of localization along characteristic directions is readily observed in Fig. 17a between 40 and 60  $\mu$ s. In order to reveal the onset of strain localization and the unloading that results from this localization more clearly, the effective plastic strain at any point, normalized by the average effective plastic strain over the entire cylinder at that time, is shown in the contour plots in Fig. 17b. From these two figures it is clear that the defect “triggers” the strain localization in the form of a narrow band and that this localization propagates along the characteristic direction until it meets the traction free surface; intersections with bands of the opposite orientation are also visible. The black regions neighboring the bands indicate that active plastic straining does not occur in these regions; this is due to the propagation



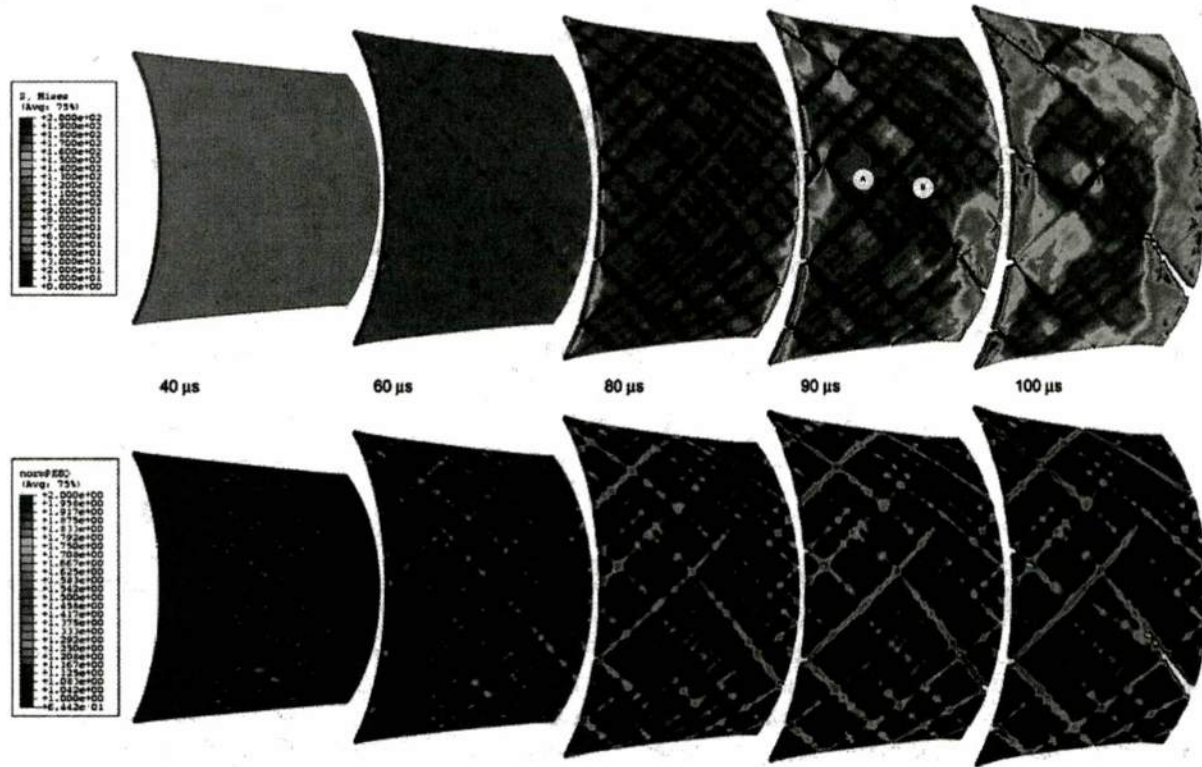


**Fig. 17** a Evolution of the von Mises effective stress as a function of time for a 36mm tube from FEM simulations. b The effective plastic strain normalized by the average plastic strain at each time step. Emergence of localization and the unloading resulting from the localization can be identified easily in this se-

quence of images. In these simulations, defects were distributed randomly, with a concentration of 0.1% by volume; the elements with defects have a reduced yield strength of 25 MPa and do not exhibit strain hardening

of the unloading from the localization. As time progresses, it is evident that further straining occurs only within the localized regions. In an effort to examine quantitatively the influence of the defect volume fraction on the emergence of localization, we plot in Fig. 18, the evolution of the hoop strain  $\epsilon^A$  at a point A which is located within a localized band as a function of the hoop strain  $\epsilon^B$  at a point B which is in the uniform region just beside the point A for two different defect volume fractions: 0.001, and 0.0001. In the early stages of the deformation, the defects do not play a significant role in the evolution of the strain; but as the critical strain level is reached, the strains within the defective region grow rapidly, forming the localization. Finally, the localization patterns obtained from these simulations are rendered in a graphic with a gray scale image of the plastic strain contours compared with an optical image of the surface of a particular

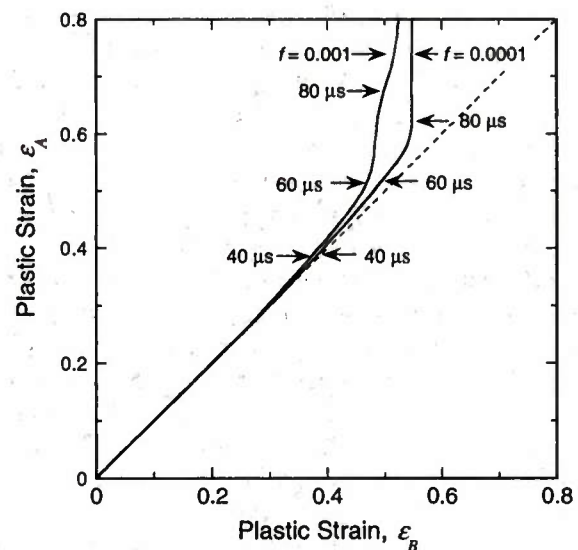


**Fig. 18** Effect of defect volume fraction on the strain at onset of localization in the tube specimens

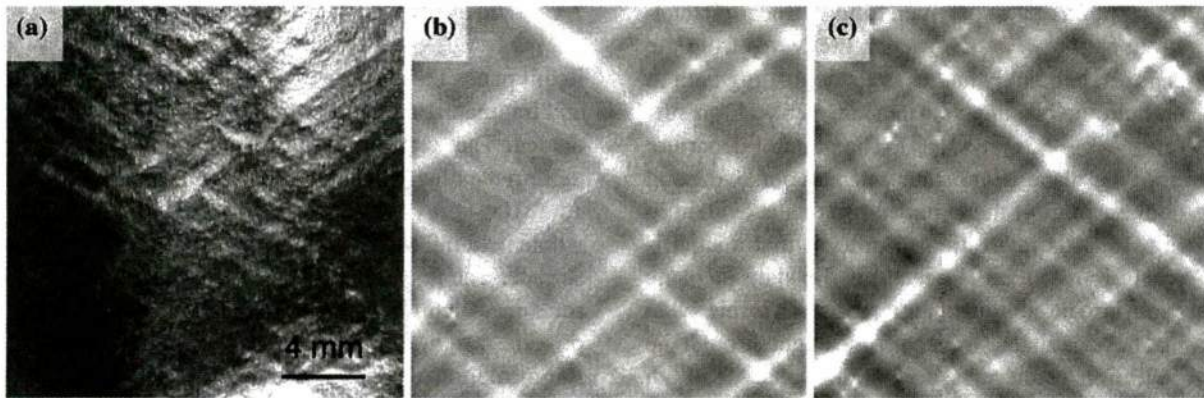


**Fig. 19** **a** Optical macrograph of the surface of a fragment observed in reflected light. Contours of effective plastic strain from FEM simulation with **b**  $f = 0.0001$  and **c**  $f = 0.001$

specimen in Fig. 19. From these results, we observe the following:

- Initially, the plastic strain evolves nearly uniformly over the entire tube as can be seen easily in Fig. 17; while there are minor perturbations in the uniformity in the vicinity of the defects, these are small and the two strain measures  $\varepsilon^A$  and  $\varepsilon^B$  appear track each other closely as shown in Fig. 18.
- Localization in the form of a large number of bands develops between 40 and 60  $\mu\text{s}$ ; this is evident from the concentration of effective plastic strains in such bands in Fig. 17b and from the rapid increase in  $\varepsilon^A$  as seen in Fig. 18. The nature of the deformation within these bands is revealed by examining the in-plane logarithmic shear strain shown in Fig. 20. The spatial variation of this strain component is a clear indication that the observed strain concentration is a shear localization within the band and not a thinning deformation (as noted earlier, this thinning deformation occurs much later in the experiments). This is very similar to the shear deformation observed in the experiments.
- For  $f = 0.001$ , the rapid increase in  $\varepsilon^A$  occurs at  $\varepsilon^B = 0.48$ ; while for  $f = 0.0001$ , this is delayed to  $\varepsilon^B = 0.55$ . This indicates an increase of the strain at onset of localization with decrease of the defect density. Note that in these simulations, the randomly distributed defects have a uniform magnitude, while in a real material both the location of the defect and the magnitude of defect will have statistical distributions. The highly simplified defects considered in these simulations are similar to those defects which

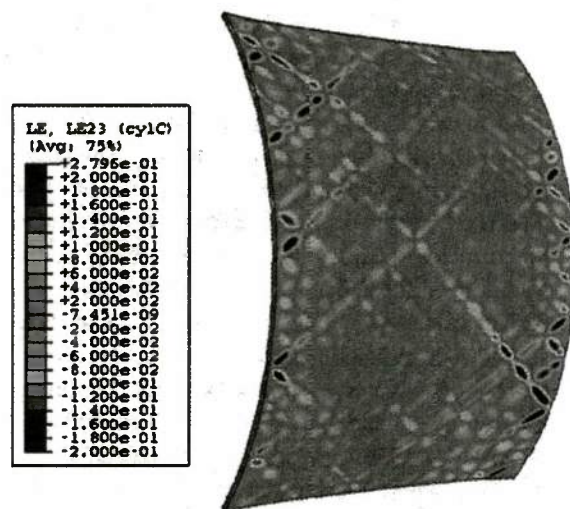


**Fig. 20** Contours of the in-plane shear strain in the tube are shown at 70  $\mu\text{s}$ . The localization of shear deformation within the bands is evident

are able to be activated in the deformation of a real material.

- These shear bands are oriented at an angle  $\theta$  with respect to the hoop direction and cross each other, making a relatively uniform network of shear bands. The angle  $\theta$  is initially about  $54^\circ$  to the tension direction and decreases slightly with maturing of the localization network. This is indicative of a nearly uniaxial stress state. The strain path followed in the simulation by a point at the central portion of the cylindrical specimen is shown in Fig. 10 for both the 18 and 36 mm cylinders by the solid blue lines. At early times, (before the arrival of the plastic waves from the ends of the cylinder), the



center point of the specimen follows a nearly plane-strain path ( $\varepsilon_2 = 0$ ); however, the waves from the ends arrive quickly and change the loading path to be quite nearly uniaxial tension, but with an offset ( $\varepsilon_2 = -0.5\varepsilon_1 + \varepsilon_{\text{offset}}$ ). The point of departure from the plane strain state will, of course, depend on the length of the cylinder and this is evident in Fig. 10. It is interesting to observe that a significantly longer tube is needed if the state of plane strain is to be continued for larger strain levels. Note that the calculated strain path goes right through the collection of the measured strain values for both cylinders, confirming that the computations are a good indication of the strain path followed by the material points during their deformation.

- The overall statistical pattern of the localization is also influenced by the volume fraction of defects. Since each shear band is triggered by one or more defects along its path, the appearance of the shear band network depends on both the number and the spatial distribution of the defects. Therefore, the simulation with a lower volume fraction  $f = 0.0001$  of defects results in a sparse distribution of the localized shear bands while a much denser distribution of shear band network is seen for  $f = 0.001$ , as shown in Fig. 19. Comparison of these simulated localization patterns with our experimental result (specimen #10) indicates that the volume fraction of defects that are triggered in the tested material is probably closer to the lower limit.
- Finally, fractures appear from the edge of the tube or at the junctions of the crossing bands and initiate the fragmentation process; unloading from these fractures terminates further development of the shear band network. This simulated process is consistent with our experimental observations on the tube expansion, but because our fracture model is based on element deletion, we do not interpret the results further quantitatively.

From the numerical simulations we can conclude that all aspects of the deformation and localization of the expanding tube experiments, with the exception of the final fracture have been captured by a simple elastic-plastic constitutive model with the appropriate inclusion of the statistics of defects within the material; it is important to emphasize, however, that a three-dimensional dynamic formulation is essential in order to be able to capture the deformation appropriately.

## 7 Conclusion

In this paper, the onset and growth of strain localization and fragmentation in Al 6061-O tubes has been investigated. The expanding tube experiment was used to deform the tube specimens at rates between 4,000 and 15,000  $\text{s}^{-1}$ . A conical mirror was used to provide the whole field information of the deformation on the tube surface. The results reveal the time-scale and length-scale in which the localization and fracture arise and provide insight into the evolution of localization and fragmentation of tubes. The main conclusions from this study are listed below.

- The tube specimens experience uniform expansion until a critical strain, followed by the nearly simultaneous nucleation of shear band localization, and eventually by fractures at the intersections of the shear bands. An approximately uniaxial stress condition is achieved in the tube specimens before the onset of localization.
- Localization develops in the form of multiple crossing shear bands at angle of about  $54^\circ$  to the tensile loading direction. The development of this network of shear bands contributes to globally uniform average deformation of the tube specimens after the onset strain of localization.
- The forming limit diagram obtained from these measurements indicates that the localization criterion developed from quasi-static considerations continue to apply in the dynamic problem.
- Statistical evaluation of fragmentation indicates that the nucleation of fragments still follows the Mott scaling; aspects associated with dynamic growth of cracks may influence further development of fragments (as well as secondary fragmentation). This latter aspect needs further investigation.
- Numerical simulations of the expanding tube indicate that the both the strain at onset of localization and the pattern of the localization bands can be controlled by statistical distribution of flaws in the material.

**Acknowledgments** This work was performed under a program entitled “Dynamic Response of Metal-Polymer Bilayers—Viscoelasticity, Adhesion and Failure” sponsored by the Office of Naval Research (ONR Grant Number N00014-09-1-0541, Program Manager: Dr. Roshdy Barsoum); this support is gratefully acknowledged.

## References

- Balanethiram VS, Daehn GS (1994) Hyperplasticity—increased forming limits at high workpiece velocity. *Scripta Met Mater* 30:515–520
- Estrin Y, Molinari A, Mercier S (1997) The role of rate effects and of thermomechanical coupling in shear localization. *J Eng Mater Tech* 119:322–331
- Forrestal MJ, Duggin BW, Butler RI (1980) An explosive loading technique for the uniform expansion of 304 stainless steel cylinders at high strain rates. *J Appl Mech* 47:17–20
- Gold VM, Baker EL (2008) A model for fracture of explosively driven metal shells. *Eng Fract Mech* 75:275–289
- Goto DM, Becker R, Orzechowski TJ, Springer HK, Sunwoo AJ, Syn CK (2008) Investigation of the fracture and fragmentation of explosively driven rings and cylinders. *Int J Impact Eng* 35:1547–1556
- Grady DE (2006) *Fragmentation of rings and shells*. Springer, Berlin
- Hill R (1952) On discontinuous plastic states, with special reference to localized necking in thin sheets. *J Mech Phys Solids* 1:19–30
- Hiroe T, Fjiwara K, Hata H, Takahashi H (2008) Deformation and fragmentation behavior of exploded metal cylinders and the effects of wall materials, configuration, explosive energy and initiated locations. *Int J Impact Eng* 35:1578–1586
- Jansen H (1968) Some measurements of the expansion of a metallic cylinder with electromagnetic pulses. *IEEE Trans Ind Gen Appl* IGA-4:428–440
- Mock W, Holt WH (1983) Fragmentation behavior of Armco iron and HF-1 steel explosive-filled cylinders. *J Appl Phys* 54:2344–2351
- Molinari A, Clifton RJ (1987) Analytical characterization of shear localization in thermoviscoplastic materials. *J Appl Mech* 54:806–812
- Mott NF (1947) Fragmentation of shell cases. *Proc R Soc Lon Ser A* 189:300–308
- Niordson FI (1965) A unit for testing materials at high strain rates. *Exp Mech* 5:23–32
- Oliveira DA, Worswick MJ, Finn M, Newman D (2005) Electromagnetic forming of aluminum alloy sheet: free-form and cavity fill experiments and model. *J Mater Proc Tech* 170:350–362
- Plum M (1995) “Electromagnetic Forming”, *Metals Handbook*, 14, 9th edition, ASM, 644–653
- Seth M, Vahnout VJ, Daehn GS (2005) Formability of steel sheet in high velocity impact. *J Mater Proc Tech* 168:390–400
- Storen S, Rice JR (1975) Localized necking in thin sheets. *J Mech Phys Solids* 23:421–441
- Takatsu N, Kata M, Sato K, Tobe T (1988) High-speed forming of metal sheets by electromagnetic force. *JSME Int J Ser III* 31:142–148
- Thomas JD, Triantafyllidis N (2009) On electromagnetic forming processes in finitely strained solids: theory and examples. *J Mech Phys Solids* 57:1391–1416
- Thomas JD, Seth M, Daehn GS, Bradley JR, Triantafyllidis N (2007) Forming limits for electromagnetically expanded aluminum alloy tubes: theory and experiment. *Acta Mater* 55:2863–2873
- Vogler TJ, Thornhill TF, Reinhart WD, Chabildas LC, Grady DE, Wilson LT, Hurricane OA, Sunwoo A (2003) Fragmentation of materials in expanding tube experiments. *Int J Impact Eng* 29:135–146
- Walling HC, Forrestal MJ (1973) Elastic-plastic expansion of 6061-T6 aluminum rings. *AIAA J* 11:1196–1197
- Wesenberg DL, Sagartz MJ (1977) Dynamic fracture of 6061-T6 aluminum cylinders. *J Appl Mech* 44:643–646
- Winter RT (1979) Measurement of fracture strain at high strain rates. *Inst Phys Conf Ser* 47:81–89
- Zhang H, Ravi-Chandar K (2006) On the dynamics of necking and fragmentation: I. Real-time and post-mortem observations in Al 6061-O. *Int J Fract* 142:183–217
- Zhang H, Ravi-Chandar K (2008) On the dynamics of necking and fragmentation: II. Effect of material properties, geometrical constraints and absolute size. *Int J Fract* 150:3–36
- Zhang H, Ravi-Chandar K (2009) Dynamic fragmentation of ductile materials. *J Phys D App Phys* 42, Article ID 214010
- Zhang H, Liechti KM, Ravi-Chandar K (2009) On the dynamics of localization and fragmentation—III. Effect of cladding with a polymer. *Int J Fract* 155:101–118



## APPENDIX B

### **On the dynamics of localization and fragmentation: V. Response of polymer coated Aluminum 6061-O tubes**

S.A. Morales, A.B. Albrecht, H. Zhang, K.M. Liechti, and K. Ravi-Chandar

*International Journal of Fracture*, **172**, 161-185, 2011.

## On the dynamics of localization and fragmentation: V. Response of polymer coated Al 6061-O tubes

S. A. Morales · A. B. Albrecht · H. Zhang ·  
K. M. Liechti · K. Ravi-Chandar

Received: 21 August 2011 / Accepted: 28 November 2011 / Published online: 22 December 2011  
© Springer Science+Business Media B.V. 2011

**Abstract** In this series of papers, we investigate the mechanics and physics of localization and fragmentation in ductile materials. The behavior of ductile metals at strain rates of about 4,000–15,000 per second is considered. The expanding ring experiment is used as the vehicle for examining the material behavior in this range of strain rates. In Parts I–III, we examined the response of rings with cross-sectional aspect ratios in the range of 1–10, exhibiting a transition from diffuse necking to sheet-mode localization. In Part IV, we reported on experimental observations of high strain-rate expansion of Al 6061-O tubes. In the present paper, we investigate the effect of polymer coatings on Al 6061-O tubes; specifically, polyurea and polycarbonate coatings are investigated as coating materials. It is demonstrated that there are two effects of the polymer coating on the overall deformation of the Al 6061-O tube specimens. First, the additional mass of the coating material results in an inertial effect; therefore, thicker coatings result in a slower overall expansion and hence for a limited impulse loading, less overall straining of the metallic specimen. Second, the flow resistance of the polymer dissipates additional energy and can prevent failure in the metallic specimen. This effect is

much more pronounced in polycarbonate, the material with a larger strength. Finally, it is demonstrated that the polymer coating does not significantly influence the dynamic forming limit of the metallic material.

**Keywords** Expanding tube experiment · Ductility · Dynamic forming limit

### 1 Introduction

Blast protection has become an important problem in many military and civilian structures. In this regard, a rather interesting phenomenon has been observed experimentally—coating metallic structural components with a layer of a compliant polymer, typically an elastomer with a glass transition temperature significantly below the use temperature, decreases the propensity of the metallic structure to fracture and fragment (Matthews 2004; Barsoum and Dudt 2009). This observation has spawned a large number of research efforts aimed at understanding and optimizing the additional impact resistance provided by such polymer-coated metal structures. In this series of papers (Zhang and Ravi-Chandar 2006 (Part I), 2008 (Part II), 2010 (Part IV); Zhang et al. 2009 (Part III)) we have explored the mechanisms and mechanics of strain localization and fragmentation using the electromagnetic ring and tube expansion experiments, with the ultimate aim of examining the effect of polymer coating. In the present paper, Part V, we turn

S. A. Morales · A. B. Albrecht · H. Zhang ·  
K. M. Liechti · K. Ravi-Chandar (✉)  
Center for Mechanics of Solids, Structures and Materials,  
Department of Aerospace Engineering and Engineering  
Mechanics, The University of Texas at Austin,  
Austin, TX 78712-0235, USA  
e-mail: kravi@mail.utexas.edu



our attention to the influence of polymer coatings on the dynamic deformation and failure of Al 6061-O cylindrical specimens subjected to rapid expansion.

The idea of coating a structure with a polymer layer to improve performance under blast loading is commercially available. Specialty Products Inc. markets the coating under the brand name of Dragonshield: “**Dragonshield BC<sup>TM</sup>** spray-applied, blast mitigating polymer represents a breakthrough in plural component polyurea technology. This product offers superior energy absorbing and fragment containment capabilities through its unique combination of high tensile strength, elongation, and strain modulus” (SPI Inc 2009). The application to armor is also described: **DRAGONSHIELD-HT<sup>TM</sup>** is a high build, fast set, polymer with a combination of physical properties which have proven to be very effective as an Energy Absorbing (EA) material. **DRAGONSHIELD-HT<sup>TM</sup>** polymer has been tested and verified as a protective material for mitigating damage caused during a blast event. When placed on the interior wall of a structure, Dragonshield effectively reduces pressure levels occupants must physically endure, while protecting them from fragmenting projectiles. This reduction in pressure also minimizes the deflection of the wall during a blast event”. The ability to spray the polyurea onto existing structures is an important aspect of this application; however, quantitative estimates of the efficiency are not available. Barsoum and Dudt (2009) provide an overview of efforts aimed at characterization of the response of polyurea/metal systems to blast and impact loading; the ability of the elastomer to withstand significant stress at high strain rates and elongations and the consequent influence on the deformation of the metal are shown to be the key factors in the improved blast resistance of the polyurea/metal system.

Three main avenues of investigations have been pursued in this regard. The first is related to the failure of the metal; ductile failure in the underlying metallic structure is typically initiated through strain localization, followed by damage processes within this localized zone. Therefore, the role of the polymer layer in delaying or inhibiting the onset of strain localization has been pursued (see Guduru and Freund 2002; Guduru et al. 2006; Xue et al. 2008; Xue and Hutchinson 2008; Zhang and Ravi-Chandar 2006, 2008, 2010; Zhang et al. 2009). The second avenue relates to the structural response of the metal-polymer bilayer systems, through experiments, analysis and numerical

simulations (McShane et al. 2008; Tekular et al. 2008; Xue et al. 2010; Amini et al. 2010a,b,c; Amini and Nemat-Nasser 2010; Roland et al. 2010). The last group of investigations is related to the constitutive characterization of the polyurea; a number of investigators have explored the dependence of the mechanical response of the polyurea on stoichiometry (Roland et al. 2007), on the strain rate (Yi et al. 2006; Amirkhizi et al. 2006; Jiao et al. 2007; Mock et al. 2009), and on the effect of confinement and pressure (Chakkarapani et al. 2006; Zhao et al. 2007; Chevillard et al. 2011). A detailed review of these efforts is provided below in order to place the current work in the proper context.

We begin with the studies on the onset of strain localization; in ductile materials strain localization is typically a precursor to material failure. The onset of localization is dependent on the geometry and loading conditions. Guduru et al. (2006), following on earlier studies of Guduru and Freund (2002) performed a perturbation analysis of the dynamic strain localization problem for a metal substrate coated with a layer of polymer under plane strain conditions. Their results predict an increase in the bifurcation strain in the presence of the coating; concomitant with this increase in the bifurcation strain is an increase in the plastic dissipation in the material. They show further that the mass, the relative strengths of the metal and the coating, and the hardening exponents of the metal and the coating play a major role in determining the magnitude of the increase in the bifurcation strain. If one uses their analysis with appropriate material parameters for an aluminum specimen coated with a polyurea of equal thickness, the increased energy absorption is negligible; increasing the coating thickness also does not appear to increase the energy absorption significantly (see Figures 8 and 9 of Guduru et al. 2006). Xue and Hutchinson (2008) performed a similar analysis of the onset of necking localization but under quasi-static biaxial loading conditions. They assumed a power-law hardening material model for the metal and a neo-Hookean model for the polymer. Their results indicated an increase in the energy dissipated in the bilayer plate (of the same mass per unit area as the metal plate) until the onset of localization; this increase depends crucially on (i) the coating thickness and (ii) the ratio of the coating modulus to the strength of the metal. For material properties corresponding to steel with a polyurea coating, Xue and Hutchinson report a potential 20% increase in energy absorption (see Figure 4 of

their paper) when the ratio of the coating modulus to the strength of the metal is larger than about 0.25 and the coating is greater than half of the thickness of the metal. Both of these analyses indicate the potential for load sharing with the polymer and therefore a delay in the onset of localization in the metal; of course, occurrence of delamination in the vicinity of the potential localization will make the metal immediately susceptible to localization. Indeed, such delamination was observed in both the quasi-static and dynamic experiments on polyurea coated metal specimens; as we reported in Fig. 3 and 8 of Part III, when the metal/polymer bilayer specimen under uniaxial tension reaches the Considère point, the metal part simply pulls away from the polyurea coating as the localization begins to form. However, in the dynamic experiments, inertial effects and the additional load carrying capacity of the unbroken polymer layer were shown to provide enhanced straining of the metal specimen in regions away from the localization—thus a new mechanism was identified in Part III for additional energy dissipation in the polymer-metal bilayer system that did not rely on the bifurcation analysis, but on the overall loading/unloading response of the bilayer specimen. We will pursue this further in the present work by performing experiments on polymer/metal bilayer tubular specimens.

A number of investigators have examined the response of polymer-coated bilayer systems under different kinds of dynamic blast and ballistic loading conditions. McShane et al. (2008) considered copper plates coated with polyurethanes with two different glass transition temperatures. These plates were subjected to spatially uniform blast loading or to loading by projectiles that was localized to the central region of the specimen. From a limited number of experiments, they concluded that on an equal mass basis, the performance of the polymer coated copper plate was at best equal to that of the bare metal specimen. They concluded that a polymer with a high modulus, high strength and a high ductility is required in order to enhance blast protection. Xue et al. (2010) report on the results of an experimental investigation as well as a numerical simulation of metal-polymer bilayers subjected to impact loading. In a comprehensive study, they subjected clamped circular plates of DH-36 steel to pressure and ballistic loading at the center. The onset of fracture or penetration (with the associated petaling of the plate) was explored through experiments and simulations. They examined a bare steel plate, a 3/16 inch (4.76 mm) steel

plate backed with a 0.44 inch (11.18 mm) thick layer of polyurea, and a sandwich configuration of two steel plates of half the original thickness, with a polyurea layer in between. It was shown that the polyurea backing provided a somewhat enhanced energy absorption capacity through an increase in the energy dissipated in the steel as well as the energy stored in the polyurea. This increase in energy was not significant at impact speeds below 200 m/s, but was about 15% for impact velocities between 200 and 300 m/s. An increase in the critical velocity at which penetration occurs was also demonstrated in these simulations. Interestingly, it was also shown that above the (increased) ballistic limit, the polyurea stored about 10% of the energy corresponding to the ballistic limit.

Amini et al. (2010a,c) also performed experiments on metal-polymer bilayers; these specimens were subjected to ballistic loads as well as blast loads. The evolution of failure was examined using high speed photography and simulated numerically. The metal plates were machined out of DH-36 steel, and the polymer coating was made out of polyurea, cast into specially designed recesses in the DH-36 specimens. The main conclusion reached by Amini et al. (2010a,b) is that when the polymer is placed on the side of the DH-36 receiving the input ballistic or blast loading, the loading is transmitted to the metal and results in failure of the metal plate, while the same polymer layer, when placed on the side opposite to the blast or ballistic loading, provides additional protection from the blast loading. It is important to recognize the inconsistency between these observations and the localization analyses which do not anticipate any differences based on the position of the coating layer relative to the loading direction. Numerical simulations and experiments were also performed by Amini et al. (2010b); Amini and Nemat-Nasser (2010) using a calibrated elastic-plastic constitutive model for the DH-36 and a viscoelastic constitutive model for the polyurea. The simulations indicated that the average effective plastic strain in the DH-36 plate decreased in comparison to the bare steel plate when the polyurea coating was placed on the backside of the specimen, but increased significantly when placed on the front side of the specimen.

Roland et al. (2010) examined the ballistic performance of a high hard steel (HHS, Mil-A-46100; thickness in the range of 5.1–12.7 mm) when coated a layer of polymers of different glass transition temperatures and thickness. The ballistic limit was found to increase



if the  $T_g$  of the coating material was close to the test temperature; this was attributed to a transition to the glassy state upon impact loading. It was also found that there is an abrupt increase in the ballistic limit in the limit of a very thin coating suggesting a possible surface effect on the deformation of the polymer. Layering of the polymer and metal was also shown to improve ballistic performance; it was suggested that this could be due to the impedance mismatch between the metal and polymer layers and the resulting break-up and attenuation of the input pulse.

The proven effectiveness of the polymer coating on delaying or preventing failure of the metal has focused attention on the constitutive behavior of polyurea, particularly in understanding its temperature, pressure (Chakkarapani et al. 2006; Zhao et al. 2007; Chevallard et al. 2011) and strain-rate dependence (Yi et al. 2006; Amirkhizi et al. 2006; Jiao et al. 2007). The effect of stoichiometry on properties has also been explored (Roland et al. 2007). The main upshot of all these investigations has been to demonstrate that while polyurea has a modulus on the order of  $10^2$  MPa at quasi-static strain rates and room temperature, at high strain rates and pressure, a glass-transition is induced and the modulus can increase to about a few GPa. Furthermore, the flow stress<sup>1</sup> of less than 10 MPa encountered at strain rates of  $10^{-3}$  s<sup>-1</sup> can increase by a factor of at least two (Roland et al. 2007) at high strain rates; however this increase in the flow stress occurs only when the stretches in the polymer are greater than  $\sim 1.5$ , at this strain level, most metallic specimens may already have failed. This suggests a possible matching of the mechanical response of the polymer with the failure strain threshold for the metallic specimens.

In this paper, we focus on performing experiments to reveal the underlying deformation of the metallic specimen without and with a polymer coating. In particular, tubular specimens under uniform radial expansion are considered; this results in either a uniaxial stress state or a uniaxial strain state depending on the dimensions of the tube. Real-time diagnostics using high-speed photography and post-mortem examinations are used to determine the deformation and failure characteristics of the metal and metal-polymer bilayer systems. The basic constitutive properties of the materials used are described in Sect. 2. The experimental arrangement is

briefly summarized in Sect. 3; most of the details have been discussed in Parts I–IV. The experimental results on the expansion of Al 6061-O tubes coated with polyurea and polycarbonate are described in Sect. 4. The dynamic forming limit diagram and the onset of strain localization in the Al 6061-O are discussed in Sect. 5. Finally, in Sect. 6, the experiments are modeled using a simple one-dimensional analytical model and then simulated as a full three dimensional problem using a finite element simulation in ABAQUS. Considerations of the design of metal-polymer bilayers for optimal energy dissipation are also presented in this section.

## 2 Constitutive properties of Al 6061-O, polyurea and polycarbonate

In this section we describe briefly the materials used in this study and their mechanical properties. The metallic specimens considered in the present work were made from extruded tubes of Al 6061-T6; subsequent to machining the specimens, they were annealed to reach the Al 6061-O condition. The quasi-static material response of the Al 6061-O was characterized in a tensile test in order to provide base-line material properties as reported in detail in Part I. The constitutive response of the Al 6061-O is taken to be a power law of the form

$$\sigma = \sigma_y (1 + \beta \epsilon_p)^n \quad (1)$$

with the material parameters obtained by fitting to the experimental response:  $\beta = 14,165$ ,  $n = 0.22$ , and  $\sigma_y = 25$  MPa. Localization in the form of a neck was observed in these uniaxial tests at the load maximum. The strain at the onset of necking localization was found to be:  $\epsilon_N^{qs} = 0.22$ . For biaxial loading conditions, the quasi-static forming limit (the strain level ( $\epsilon_1, \epsilon_2$ ) at which sheet-mode localization occurs) is described in Part IV.

Polyurea is a common elastomer that has been used to coat surfaces in a wide range of applications. The mechanical properties of the polymer are very sensitive to the stoichiometry attained in the fabrication process. The formulation of Isonate 143L (Dow Chemical) and Versalink P1000 (Air Products) in an equivalent weight ratio of 1:4 is used to produce the polyurea coating on the Al 6061-O tubes; the process of mixing the polyurea described in Section 2 of Part III was used. Coating of the tubes with polyurea is accomplished with a

<sup>1</sup> We denote the stress plateau at which the polyurea stretches to about twice its initial length as the flow stress.

two-step process. In the first step, a thick layer of polyurea is applied and in the second step the coating is machined down to achieve the desired thickness. The mixture of Isonate and Versalink is slowly poured over the aluminum tube which is mounted on a slowly rotating Teflon mandrel. Because the mixture is extremely viscous, the mixture does not drip off the sample if the rotation speed is adjusted properly. The rotation of the mandrel is continued until the polyurea solidifies completely (in about 10 min). The specimen is left to cure on the mandrel for 7 days. The mandrel is then placed in a lathe and the polyurea is gradually machined down<sup>2</sup> to the desired thickness, typically in the range of 0.3–0.5 mm. As indicated in the introduction, the quasi-static and dynamic material constitutive properties of polyurea have been examined by a number of investigators. A typical quasi-static tensile response of polyurea is shown in Figure 1 of Part III. The initial modulus of elasticity is typically around 200 MPa; beyond ~1 MPa stress level, the stiffness decreases significantly and nonlinear deformation is observed to large strain levels. After a nominal strain of ~0.5 the nominal stress remains nearly constant at about 4.4 MPa. It has been reported by Roland et al. (2007), that when the stoichiometry is adjusted slightly a stiffening can be observed for strains in the range of  $\varepsilon = 2$ –3; however, such strain levels are not attained in the coatings placed on metallic tubes because the metal fails long before reaching this strain level. A number of dynamic compressive experiments have reported significant increases in stiffness as well as stress levels corresponding to the inelastic region due to rate effects. As explained in Part III, we have found that there is far less rate dependence in tension. The amount of change is such that in simulations of tube experiments, due to the much higher stiffness of Al 6061-O, the rate dependence of polyurea can be neglected.

Polycarbonate (PC) was also considered as a coating material for the metal/polymer bilayer system. This choice was motivated by the fact that PC is a thermoplastic polymer with a shear yielding response; plastic flow occurs at a stress level of 50–80 MPa, but to logarithmic strain levels of about 0.6; in contrast, the Al 6061-O attains a stress level of about 140 MPa at a strain

level of 0.22, but strain localization occurs at this level resulting in specimen failure. Since the polycarbonate is in its glassy state at room temperature, it also exhibits a high stiffness (~2.5 GPa). Polycarbonate is modeled as an elastic-plastic material with an initial modulus of 2.5 GPa up to a strain level,  $\varepsilon = 0.25$ , after which the tangent modulus is reduced to 20 MPa. Beyond  $\varepsilon = 0.6$ , the polycarbonate is assumed to stiffen up again with a modulus equal to that of the original elastic modulus. This model does not incorporate intrinsic material softening that is typically used in constitutive models for such shear yielding polymers, but is capable of capturing the inelastic response of polycarbonate (Lu and Ravi-Chandar 1999). The polycarbonate is applied as an external coating on Al 6061-O tubes by machining a sleeve out of polycarbonate tube stock to dimensions of 16.25 mm mean radius and 0.5 mm wall thickness. A sliding fit is employed so that the sleeve can be fitted on the aluminum samples without the risk of damaging the very ductile metallic specimen. Although the polycarbonate is transparent in its stock form, once machined the surface finish becomes opaque, making it difficult to observe the electro-etched circular patterns on the metal surface. In order to overcome this problem, a staggered circular pattern is painted onto the surface of the polycarbonate sleeve by means of a stainless steel mask. The mask is aligned with the sleeve in such a way that the row and column directions of the pattern match the hoop and axial strain directions in the aluminum specimen; the separation of the painted circles in the hoop and axial directions is 1.778 and 1.015 mm respectively. These dimensions are used to measure the strain of the sample in real time; post mortem analysis is also performed on the chemically etched pattern on the aluminum in order to determine the local strains.

### 3 Experimental arrangement

In this work, an electromagnetic loading device was used for expanding Al 6061-O tubes coated with a layer of polyurea or polycarbonate; the details of construction and use of the loading device and the associated diagnostics are described in detail in Parts I and IV; here we provide a brief summary. This device includes a 25  $\mu$ F capacitor and a choice of two copper coils, with 6-turn and 12-turn windings, which are encased in epoxy. For the experiments shown in this work, two lengths of Al 6061-O tube samples were used: 18 and

<sup>2</sup> When machining a soft material such as a polyurea, to achieve a smooth surface finish, a very sharp lathe tool is essential. Minimizing the feed speed and maximizing rotational speed also aids in decreasing surface roughness.



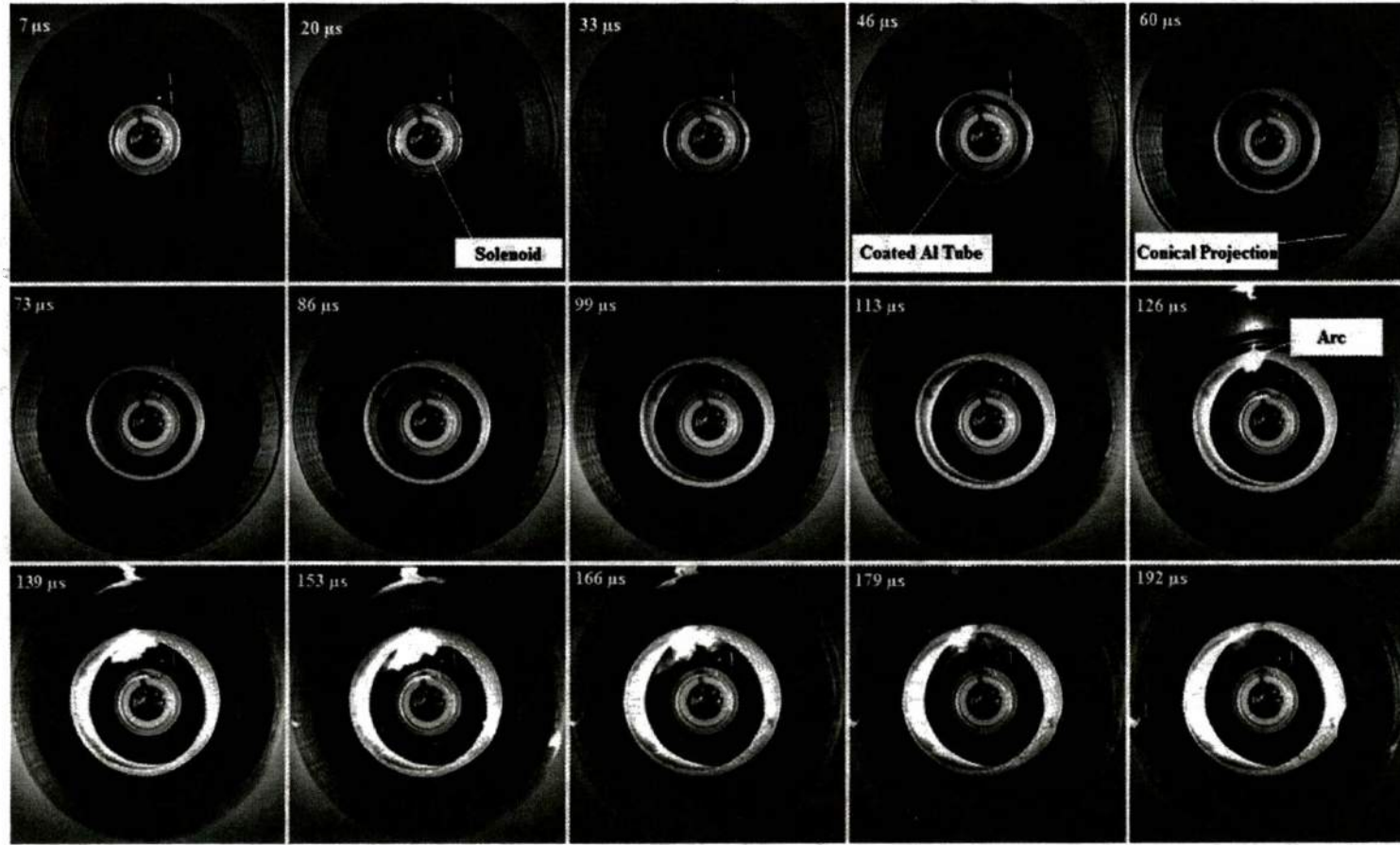


**Fig. 1** High speed images showing expansion of an Al 6061-O tube ( $w = 18 \text{ mm}$ ) with a polyurea coating, expanding at 136.1 m/s (Test PU-3)

**Table 1** List of high speed expanding tube tests on polymer coated Al 6061-O samples

Test number	Coating material	Tube length (mm)	Charge voltage (kV)	Tube thickness (mm)	Coating thickness (mm)	Expansion velocity (m/s) <sup>a</sup>	Strain rate (s <sup>-1</sup> )
PC-1	Polycarbonate	18	13	0.51	0.49	64.6	4,236
PC-2	Polycarbonate	18	14	0.50	0.50	83.3	5,462
PC-3	Polycarbonate	18	15	0.51	0.50	90.4	5,928
PC-4	Polycarbonate	18	16	0.53	0.49	82.4	5,403
PU-1	Polyurea	18	14	0.50	0.32	102.8	6,741
PU-2	Polyurea	18	15	0.50	0.32	141.3	9,266
PU-3	Polyurea	18	16	0.50	0.34	136.1	8,925
PU-4	Polyurea	36	13	0.50	0.45	81.4	5,338
PU-5	Polyurea	36	15	0.50	0.70	55	3,607
PU-6	Polyurea	36	15	0.50	0.50	101.5	6,656

<sup>a</sup> The steady ring expansion speed reached in the 15–50  $\mu$ s interval is quoted, following the procedure used in Parts I–IV

36 mm. All specimens were 30.5 mm in diameter and 0.5 mm wall thickness. A Cordin Model 550 high-speed camera is used to monitor the expansion of the samples. This camera can record 30 frames with a resolution of 1,000  $\times$  1,000 pixels; the magnification used results in a spatial resolution of 0.118 mm per pixel. The camera is synchronized with the experiment to record the event at a framing rate of  $\sim$ 150,000 frames per second; the expansion of the specimen can be followed for about 200  $\mu$ s. Two xenon flash lamps are used to illuminate the sample; a conical diffusing reflector is also employed, as per the configuration seen in Figure 1a of Part IV. In order to facilitate viewing the entire cylindrical surface of the specimen, the conical mirror arrangement described in Figure 2 of Part IV is used; the unwrapping software discussed in Part IV allows for real time measurements of strain on the entire cylindrical surface of the sample.

In order to measure the local strain from the unwrapped reflection of the sample surface observed in the conical mirror, the tube surfaces were electrolytically etched<sup>3</sup> with a pattern of circles 2.719 mm

in external diameter. The samples were then coated with their respective polymer cladding, as discussed in Sect. 2. The tube specimens are placed outside the coil—epoxy assembly. In these tests, the capacitor is charged to a maximum voltage of 16.5 kV, and then discharged through the coil, generating a rapidly alternating current; typical variation of the current with time can be found in Figure 4 of Part I. As a result of this current flowing through the coil, a current is induced in the Al 6061-O tube; the interaction between the current in the coil and that in the sample generates repulsive Lorentz forces that apply a radial body force on the specimen, causing the characteristic high speed radial expansion of the sample (note that the coil is firmly embedded in epoxy and is therefore immobile). The expansion speeds generated in these tests range from 55 to 141 m/s; for the  $\sim$ 30 mm diameter specimens, this corresponds to strain rates in the range of  $\sim$ 3,600–9,200 s<sup>-1</sup>.

#### 4 Expanding tube experiments on Al-6061-O with polymer coatings

Experiments were performed on 10 aluminum 6061-O samples, 4 using polycarbonate sleeves and 6 with polyurea coatings. The polyurea coated specimens exhibited expansion speeds of 55–141.3 m/s or strain rates of  $\sim$ 3,600–9,200 s<sup>-1</sup>. In contrast, for the same range of imposed load levels, the polycarbonate coated specimens experienced expansion of speeds of 64.6–90.4 m/s or strain rates of  $\sim$ 4,200–5,900 s<sup>-1</sup>. Table 1

<sup>3</sup> The etching is achieved by an electrolytic process. A fabric covered electrode (anode) is wetted with an electrolyte (Electrolyte solution LNC 9 by LECTROETCH). A mask with the desired pattern is laid on the anode. The aluminum specimens are then fitted onto a Teflon mandrel and slowly rolled over the mask while in contact with the cathode of the circuit. As the circuit is closed, aluminum particles migrate from the sample through the openings in the mask, to the anode, etching a pattern on the specimens. Once the etching is complete the samples are washed with Formula 1 All Purpose Cleaner by LECTROETCH.



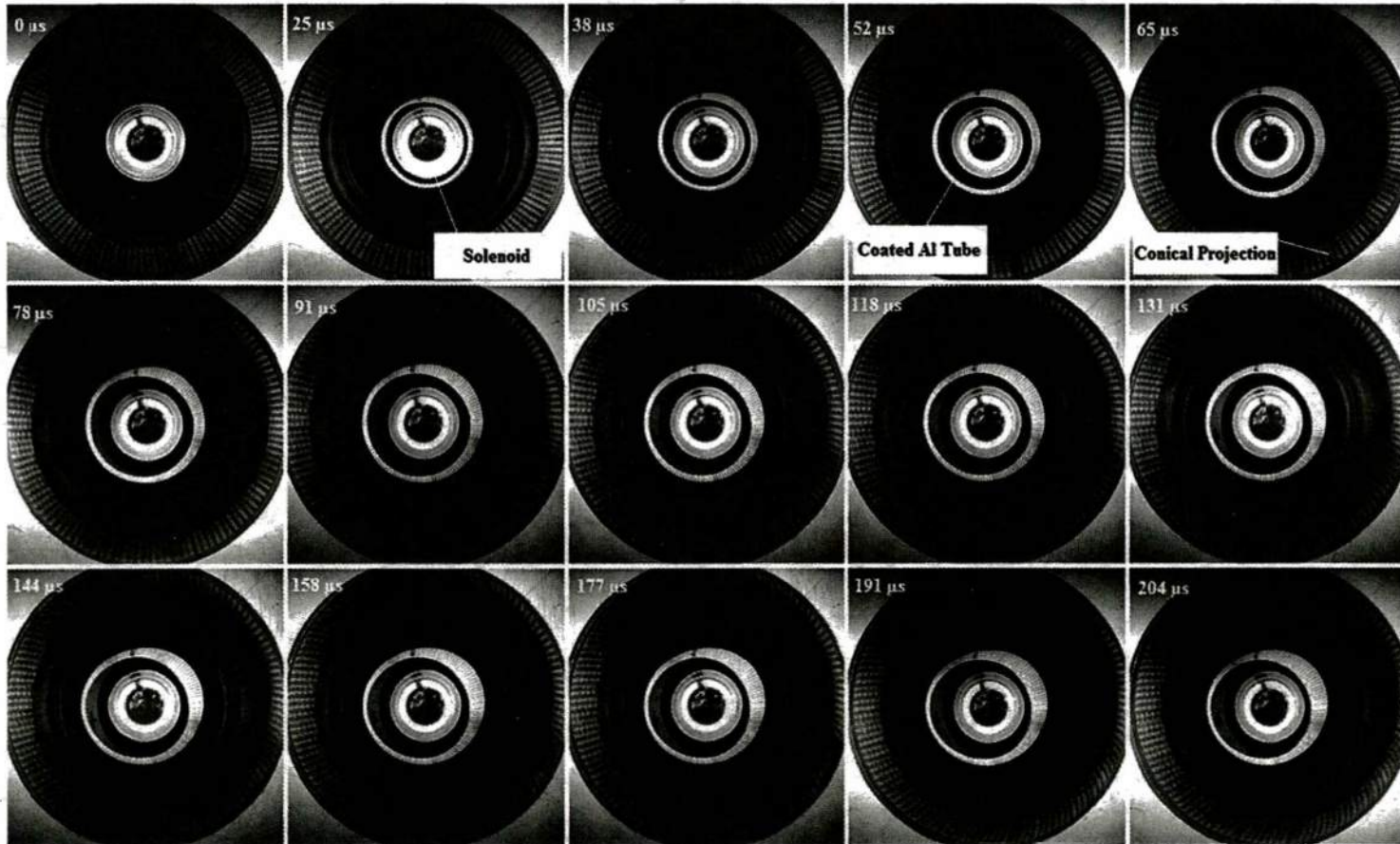


**Fig. 2** High speed images showing expansion of an Al 6061-O tube ( $w = 18$  mm) with a polycarbonate coating, expanding at 90.4 m/s (Test PC-3)

shows the experimental conditions for each of these tests. Results from twelve uncoated Al 6061-O specimens are reported in Part IV, where the expansion speeds were in the range of 69–196 m/s or strain rates of  $\sim 4,000$ – $12,000 \text{ s}^{-1}$ .

Figures 1 and 2 present two selected sequences of images from expanding tube experiments Al 6061-O tubes with polyurea and polycarbonate coatings, respectively. We will refer to these as Al/PU and Al/PC specimens. All images contain two views of the sample; at the center of each image the direct view of the expanding tube as seen in the direction of its longitudinal axis can be observed. Secondly, the reflection of the specimen surface in the conical mirror can be seen as an annular image around the direct view. This second image can be unwrapped using the conical mirror projection mapping technique discussed in Part IV, allowing for quantitative interpretation of the behavior of the specimen surface, such as the tracking of real time local strain evolution on the sample. Figures 3 and 4 show the unwrapped image sequences corresponding to the samples seen in Figs. 1 and 2, where the entire surface of the cylindrical samples can clearly be observed, albeit with some distortion arising from the barreling of the cylindrical specimen. The evolution of the hoop and axial strains, as well as the onset of fracture, can be clearly observed from these images.

Using the images from Figs. 1, 2, 3, and 4, it is possible to determine the strain evolution of the samples in two different ways. First, from the direct view, an average global strain evolution can be calculated by measuring the change in the mean radius of the sample. This measurement must be taken as an average because the expansion of the specimen is not perfectly uniform, resulting in a slight elliptical shape of the expanded tube. Second, the local hoop and axial strain evolution can be obtained by measuring the evolution of particular patterns on the specimen surfaces as a function of time. This is possible by using the unwrapped images of the events. It is worth noting that during the tests, the samples tend to barrel slightly as they expand; this means that the edges of the sample will be at a further distance from the conical mirror than the middle portions of the sample, causing a slight error in the size of the circles in the reflected image. This discrepancy induces a scaling error in the unwrapped image, affecting the measured strain. The center portion (length-wise) of the sample is affected less by this phenomenon, therefore taking the local measurements of strain here

will yield a more representative value for the local strain of the specimen. It must also be considered that the barreling of the specimen implies that the radial expansion of the center section of the tube will be greater than that of the edges. Since the average global strain is determined by measuring the variation of the sample radius at the edge closest to the camera, the obtained strain level will be smaller than that measured locally according to the above discussion; the level of the discrepancy will depend on the degree of barreling observed. Figures 5 and 6 show the evolution of average global strain and local strain for the tests presented in Figs. 1, 2, 3, and 4.

Looking at the results displayed in Figs. 1, 2, 3, 4, 5, and 6, it is possible to describe several stages in the expansion tests for both the polyurea and polycarbonate coated samples. These make evident the differences and similarities between the uses of both polymers to coat the Al 6061-O tubes. For the Al/PU specimens, the following is observed:

- The sample accelerates over the first  $20 \mu\text{s}$  of the test, to a speed of 136.1 m/s.
- From  $20 \mu\text{s}$  to  $\sim 47 \mu\text{s}$  the tube expands at a uniform speed of 136.1 m/s, corresponding to a strain rate of  $\sim 6,700 \text{ s}^{-1}$ . As observed in Part IV for the bare Al 6061-O tubes, the hoop strain increases to about 0.2, but the specimen experiences a slight bulging or barreling due to the effect of free boundaries at the ends as well as slight inhomogeneities in the electromagnetic interaction. This phenomenon starts to become evident visually after about  $20 \mu\text{s}$ .
- Due to the poor spatial resolution of the camera and the optical interference produced by the translucent polyurea coating, which is yellow and therefore darkens the reflected image of the tube surface, it is impossible to observe the localization bands in their early development directly. The first indication of their presence is the appearance of cracks on the specimen. These cracks grow in a zig-zag manner, agreeing with the observations made in Part IV.
- From  $47 \mu\text{s}$  to  $93 \mu\text{s}$  the specimen keeps expanding at a relatively constant strain rate of  $\sim 6,700 \text{ s}^{-1}$ . At  $79.5 \mu\text{s}$  a spot becomes visible in the unwrapped image as indicated by the highlighted boxes in Sequence A; this spot corresponds to the onset of localized deformation, when the hoop strain is about 0.5; high magnification images of Sequence A in Fig. 3 show the evolution of this feature in time.



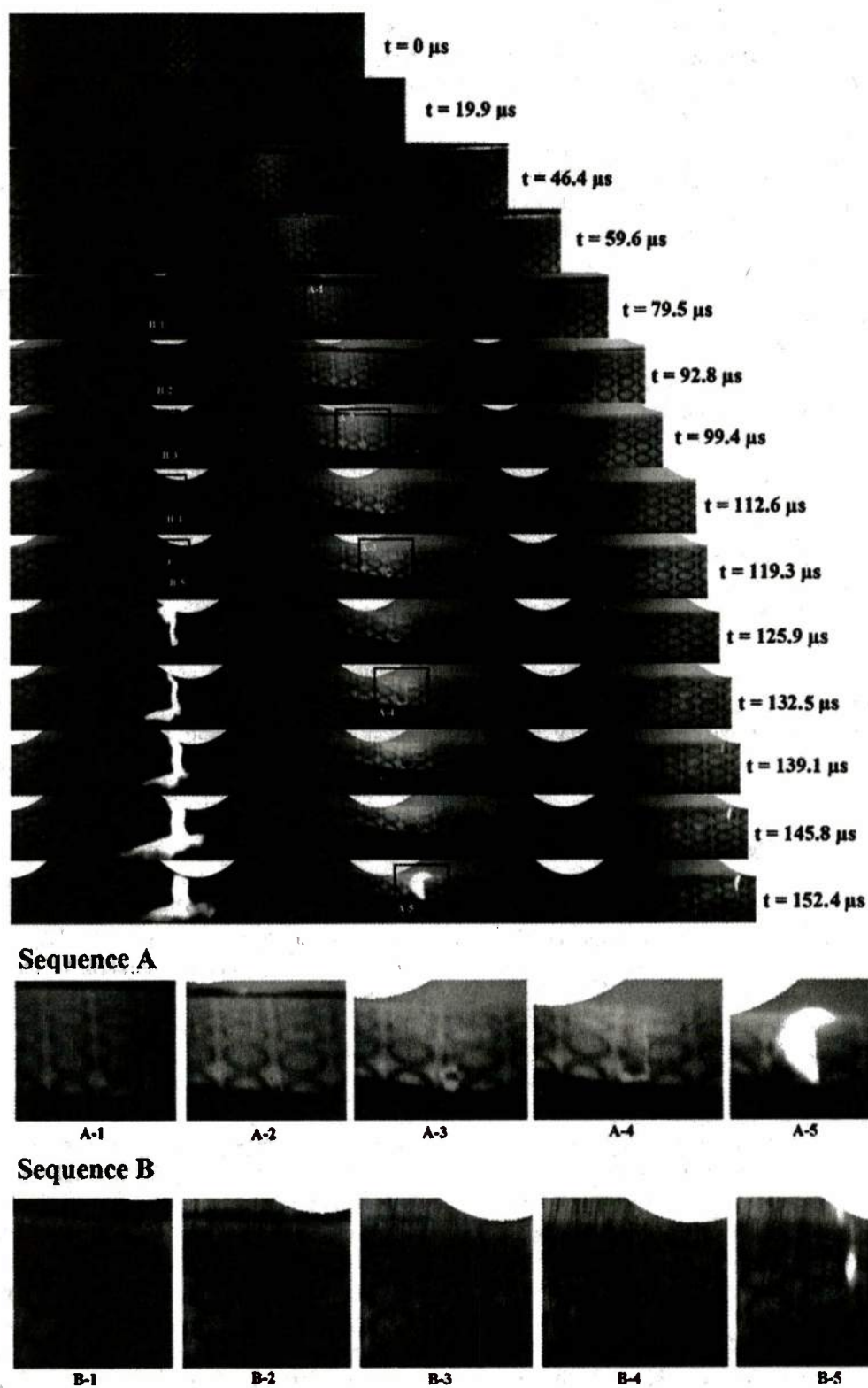


**Fig. 3** Sequence of unwrapped images for Test PU-3 indicating the deformation on the surface of the cylinder

**Fig. 4** Sequence of unwrapped images for Test PC-3 indicating the deformation on the surface of the cylinder

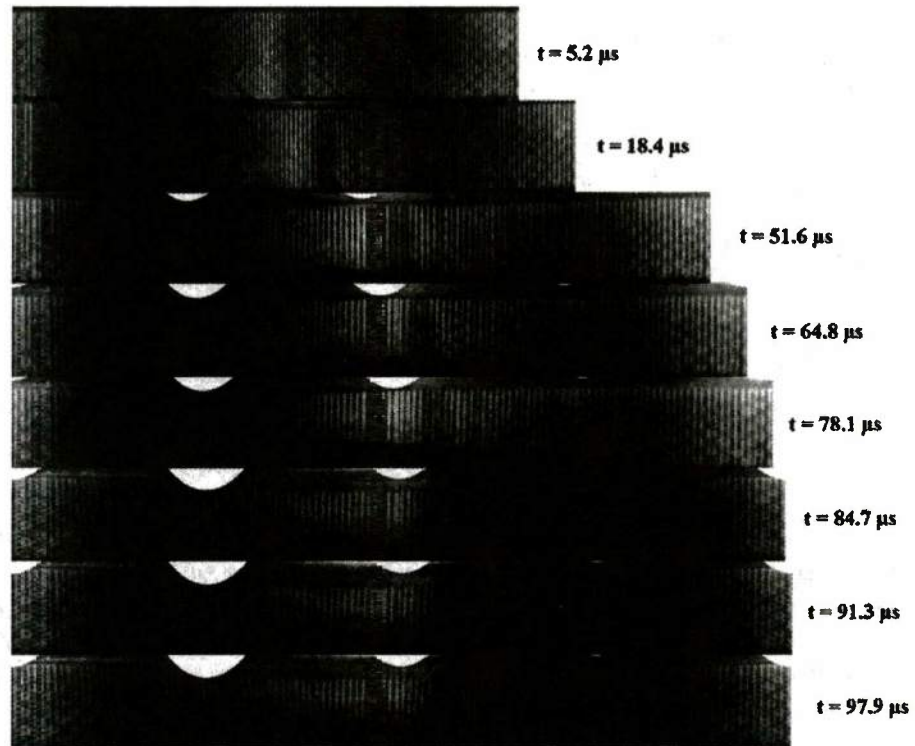
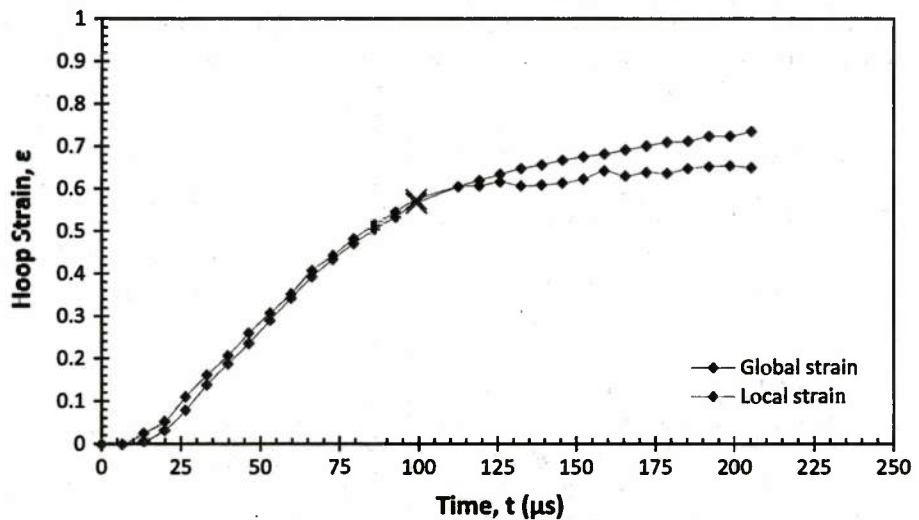


**Fig. 5** Variation of hoop strain with time for Test PU-3: the global quantity was determined by measuring the variation of average tube radius, while the local strain was obtained from measurements of the deformation of an etched circle on the sample surface. The X marks the fracture point

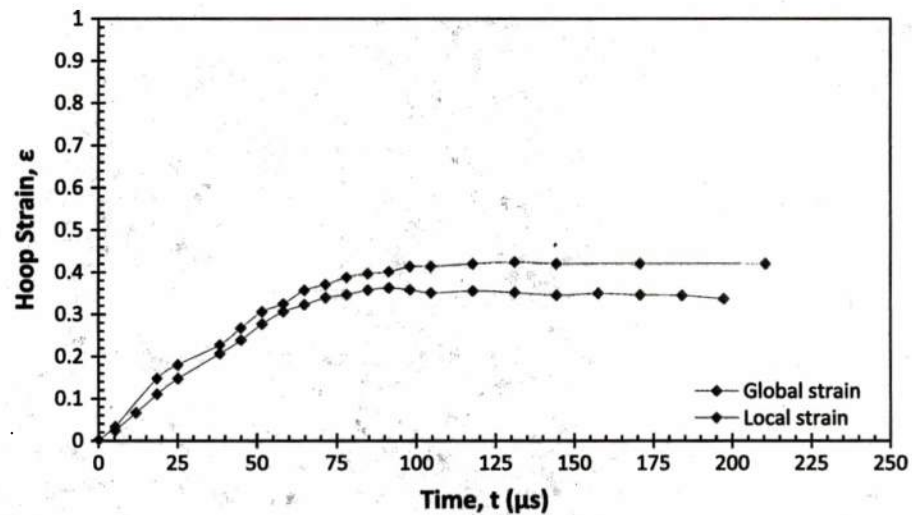


Sequence **B** shows the evolution of the first feature to produce arcing. The onset of this localized deformation is not clearly observed until 112.6  $\mu$ s due to lack of clarity in the images and obstruction by a foreign object; however, it is suspected that it initiates at about the same time as the feature observed in Sequence **A**.

- From 93  $\mu$ s to 99  $\mu$ s, the sample expansion begins to slow down, as the driving force begins to dwindle due to the increasing separation between the coil and the tube and the diminishing of the current pulse. As the tube expands, the bright spot just mentioned continues to increase in brightness. At 99.4  $\mu$ s, the first crack appears at the point where



**Fig. 6** Variation of hoop strain with time for Test PC-3: the global quantity was determined by measuring the variation of average tube radius, while the local strain was obtained from measurements of the deformation of a staggered circle pattern painted on the coating surface



this spot has been evolving; this event occurs at an average hoop strain of 0.57.

- It is evident in Fig. 5 that up until the 99.4  $\mu\text{s}$  mark, the local and global strains follow the same trend, differing only slightly in magnitude mainly as a result of the different methods of measuring both strains. The global strain is obtained from the measurement of the diameter of the sample in the direct view images (Fig. 1). Because of the nature of these images, the most well-defined boundary to measure the diameter is the inner diameter of the sample at one of the ends. The local strain however, is determined by measuring the evolution of the etched circle on the top surface of the aluminum tube (Fig. 3) at the center of the sample. This location lies on the crest of the barrel shape exhibited by the sample during expansion, while the global strain is measured at the average point of this curved shape. Both these result in the measured local strain appearing slightly greater than the measured global strain.
- From 99  $\mu\text{s}$  to 205  $\mu\text{s}$ , the specimen continues to expand at an approximately constant speed of 40 m/s. Parts of the specimen are broken into fragments; the global and local strain time histories of Fig. 5 clearly illustrate the trend—in the broken parts, where the first cracks appear, the Mott release wave begins to unload the sample, causing the fragments to stop straining; therefore, the local strain measure levels out at about 0.61. However, due to inertia, the fragments continue moving radially outward at nearly the speed that they had at the instant of fracture. Therefore the global measure-

ment of radius increases; however, this should not be interpreted incorrectly as strain in the specimen.

- Cracks begin to grow from  $\sim 112.6 \mu\text{s}$  until 152  $\mu\text{s}$ ; these are readily identified by the arcing at the crack tip that can be observed. As observed in Part IV, when the fractured surfaces separate and break electrical contact, the electric potential is still high and hence electric arcs jump across the gap between fragments. These cracks propagate very quickly across the entire length of the tube in a time interval between one to three frames, providing a lower bound crack tip speed of about 900 m/s.
- *Post mortem* analysis of the sample shows the presence of well-defined localization bands on the inside of the sample. The density and definition of these bands is uniform throughout this surface.

For the Al/PC specimen, the following observations are recorded:

- The acceleration stage for this specimen extends from 0 to 18  $\mu\text{s}$ . During this phase, the sample accelerates to a speed of 90.4 m/s. Analogous to the polyurea coated tubes, barreling is distinctly observed after 18  $\mu\text{s}$ .
- From 18 to 52  $\mu\text{s}$  the tube expands at a uniform speed of 90.4 m/s, corresponding to a constant strain rate of  $\sim 5,928 \text{ s}^{-1}$ . After 52  $\mu\text{s}$  the expansion begins to slow down, reducing gradually in speed until the expansion stops completely at 91  $\mu\text{s}$ . The average global strain at this point is 0.361; from the 91  $\mu\text{s}$  mark until the 210  $\mu\text{s}$ , when the camera stops recording the event, the diameter of the specimen

remains essentially constant. Figure 6 shows clearly how the local strain and global strain behave in the same way for this test, with the differences in the magnitude being a reflection of the method used in estimating the strain. The barreling observed for this specimen was substantial, producing a large discrepancy between the global and local strains; the maximum local strain observed is 0.423.

- Finally, it is not possible to observe the formation of localizations on the surface of the sample in real time, as the polycarbonate is even more opaque than the polyurea, making discerning even the circular patterns etched onto the aluminum samples almost impossible in the unwrapped images, much less distinguish localizations.
- *Post-mortem* analysis of the sample does not show the presence of localization bands on the inside of the sample. However, in specimen PC-4 the beginning stages of these bands are visible as we shall show later.

The evolution of deformation and failure in a 36 mm long bare Al 6061-O sample expanded by using a 15 kV discharge was reported in Part IV. From that account, certain key observations are summarized below for comparison to the polymer coated tubes:

- Initial acceleration occurred in the first 20  $\mu\text{s}$ , reaching an expansion speed of 170 m/s, or equivalently, a strain rate of  $\sim 10^4 \text{ s}^{-1}$ . Bulging was observed during expansion due to the effect of free boundaries.
- Localized deformations occurred simultaneously at many locations on the sample at a specific value of strain. Crack formation started from these localizations as indicated by real time and *post mortem* observations. Initial cracks appeared at 64.8  $\mu\text{s}$  at a strain level of  $\sim 0.46$ .
- Arcing was observed as cracks propagated and fragments began to separate. Cracks propagated in a zig-zag manner from the center of the sample to the edges and many fragments were formed.
- Complete failure of the specimen occurred in this test, resulting in fragments that continued to move away with significant kinetic energy imparted by the electromagnetic loading. The fragments travel radially outward with the velocity they possessed at the time of fragmentation.
- Finally, the observed behavior for the local and global strains matches the patterns seen in Fig. 5

for the polyurea sample. Figure 6 in Part IV shows the behavior of the uncoated aluminum sample.

Looking at the behavior of all three sample configurations, several similarities can be found. The acceleration phases of all three samples have approximately the same duration of 15–20  $\mu\text{s}$ . However, in this period of time, the bare aluminum sample accelerated to 170 m/s, while the polyurea and polycarbonate coated tubes only achieve 136.1 and 90.4 m/s, respectively, despite having equal or even greater driving force (15 kV for bare Al 6061-O and polyurea samples, and 16 kV for polycarbonate sample). The drop in expansion speed with coating can be attributed, at least partially, to the additional mass present in the composite specimens; by Newton's second law, if the same or a similar driving force is applied, the achieved acceleration will be inversely proportional to the mass variation of the samples. We will explore this further quantitatively in Sect. 6. Bulging was also observed in all samples and is to be expected as they all have the same end boundary conditions. Localization and forming of cracks appeared at 64.8  $\mu\text{s}$  in the bare aluminum sample, while in the polyurea sample localization did not appear until 99  $\mu\text{s}$  into the test; while this represents a delay in time of the onset of localization, it does not indicate a change in the strain level at the onset of localization; this will be explored further in the following paragraphs. Even more interestingly, the polycarbonate coated sample exhibited no cracking of the aluminum at all. We will examine these quantitatively in terms of the strain levels at which these events appeared.

Figures 7, 8 and 9, show the average (global) hoop strain time histories of all the polyurea and polycarbonate coated samples tested in this work, as well as the 18 mm bare aluminum samples reported in Part IV. The point at which the specimen exhibited cracking is marked by an X; the portion of the curves beyond this point is shown by a dashed line since this really does not correspond to strain, but merely radial expansion of the fragments.

- The bare Al6061-O samples (Fig. 7) fractured into fragments at strain levels in the range of 0.35–0.6, and then the fragments simply moved away radially with significant residual kinetic energy. The maximum expansion speed observed at a charge of 14 kV was 196 m/s, corresponding to a strain



**Fig. 7** Variation of hoop strain with time for uncoated Al 6061-O 18 mm tubes used in Part IV: Note the rigid body expansion observed in all the fractured specimens. The samples that did not fracture hit a plateau after the driving force was extinguished. The X marks the fracture point

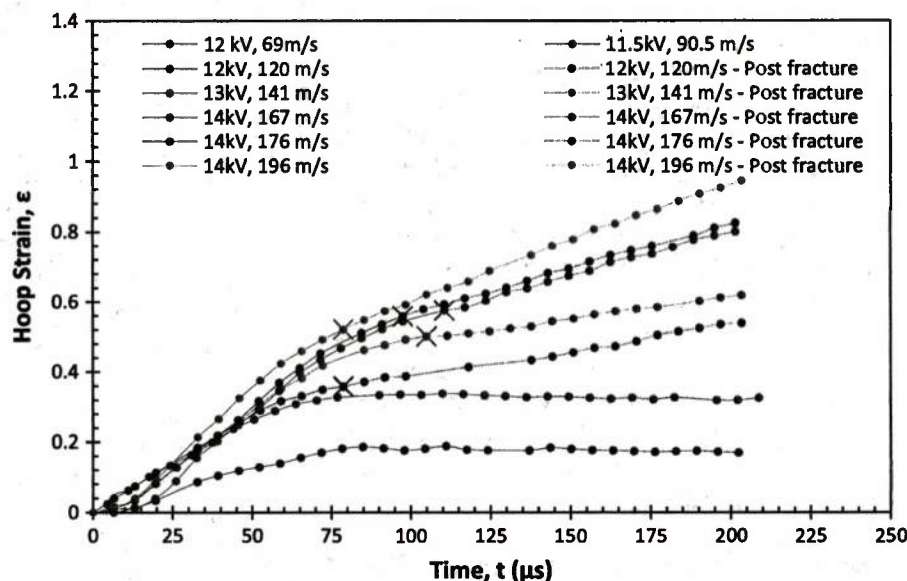
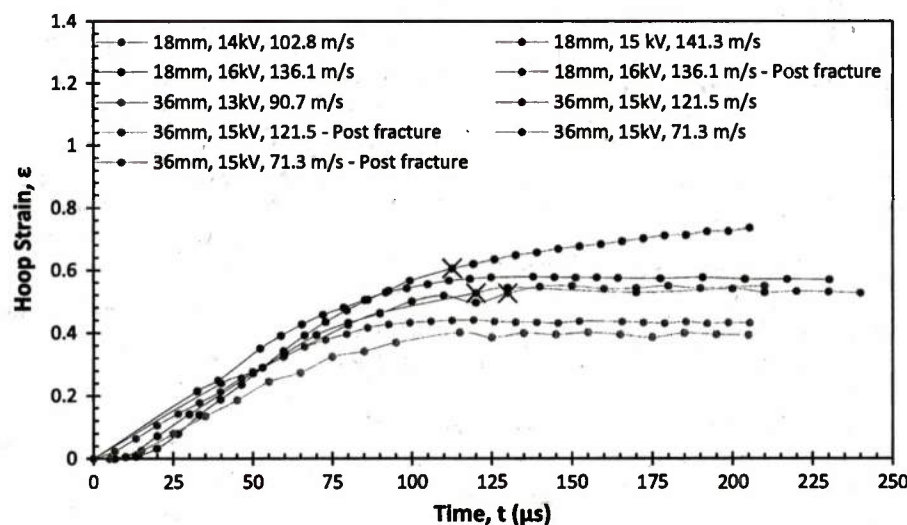


**Fig. 8** Variation of hoop strain with time for polyurea coated Al 6061-O tubes of 18 and 36 mm lengths: Note the rigid body expansion observed in all the fractured specimens. The samples that did not fracture hit a plateau after the driving force was extinguished. The X marks the fracture point



rate of  $12,800\text{s}^{-1}$ . If the charge is low enough, such as 11.5 and 12 kV, the samples do not have enough energy to reach the required localization strain, and the specimens do not fail, but decelerate and stop deforming, after straining to about 0.2–0.35.

- The polyurea coated samples (Fig. 8) exhibit a very similar response; at small charge levels, the specimens stop deforming after about  $100\mu\text{s}$ . As the loading intensity is increased, the Al/PU bilayer eventually reaches the strain threshold where the Al strain localizes and fails, with the fragments

contained within the intact polyurea. However, the Al/PU bilayer appears to withstand a larger discharge (13 and 14 kV) without reaching failure than the bare Al specimen. At higher charge voltages (15 and 16 kV), the Al specimen fractures as the strain level reaches about 0.5.

- Finally, for the polycarbonate coated samples (Fig. 9), the maximum observed expansion speed achieved at the highest discharge voltage of 16 kV was  $90.4\text{ m/s}$  corresponding to a strain rate of  $5,900\text{s}^{-1}$ ; the maximum strain reached for this case was 0.41. This level is below the strain threshold for

**Fig. 9** Variation of hoop strain with time for 18 mm long polycarbonate coated Al 6061-O tubes: Note that the samples did not fracture, hitting a plateau after the driving force was extinguished

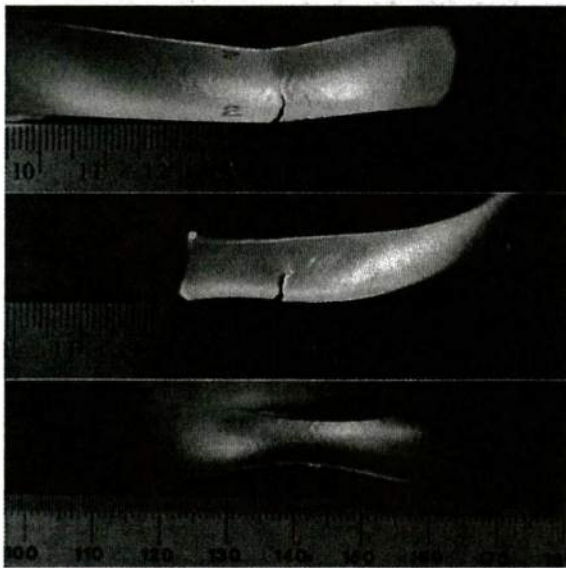
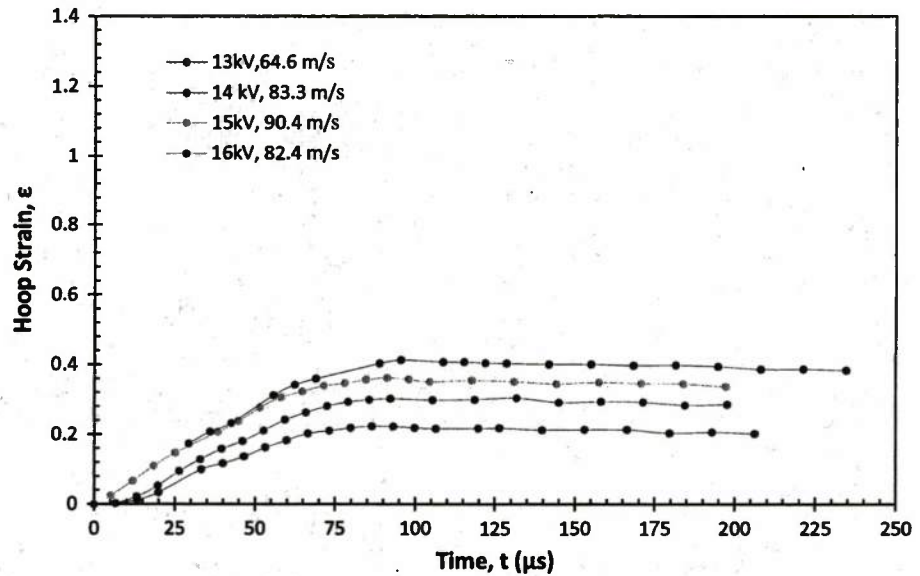


**Fig. 10** Variation of localization band intensity and distribution for different tests. The *top* image corresponds to an 18 mm long bare Al 6061-O cylinder under a 12 kV discharge, generating a expansion velocity of 120 m/s (Test 2 in Part IV). The *middle* image corresponds to Test PU-3. The *lower* image corresponds to Test PC-4. Note how in the top image, the most defined localization bands occur around the crack and become less defined as you move away from it. In the other two images, the distribution of the localization bands is uniform throughout, being a lot more defined for the Test PU-3

strain localization and hence the Al/PC specimens did not exhibit any failure, either in the metal or in the polymer.

### 5 Onset of strain localization: dynamic forming limit of sheet metals

Before proceeding to analyze the response of the polymer coated aluminum tubes, we examine the details of the deformation in the tube to identify the strain evolution and the onset of strain localization. Optical images of the inner surface of the fragments from three experiments (Test 2 of Part IV, PU-3 and PC-4) are shown in Fig. 10; localization bands are clearly visible in all specimens, but such bands are not as well developed in the Al/PC specimen. Note that the Al and Al/PU specimens are fragments, with arrested cracks visible as well, but the Al/PC specimen was cut and mounted in an inclined position in order to be able to observe the inner surface of the Al tube. Optical images of the assembled fragments of the Al and Al/PU specimen and the intact Al/PC specimen are shown in Fig. 11. Clearly, the Al specimen has fragmented into a number of pieces (Fig. 11a) and the Al/PU specimen has broken into five pieces (Fig. 11c), but the Al/PC specimen (Fig. 11b) is fully intact; neither the aluminum nor the polycarbonate exhibited any signs of failure. Identically to what was observed in Part IV, the electrolytically etched circles on the aluminum samples tested deform into ellipses (this can be observed in Fig. 11 as well); measuring the length of the major and minor axes of these ellipses allows for an estimate of the maximum strains experienced by the samples. *Post mor-*



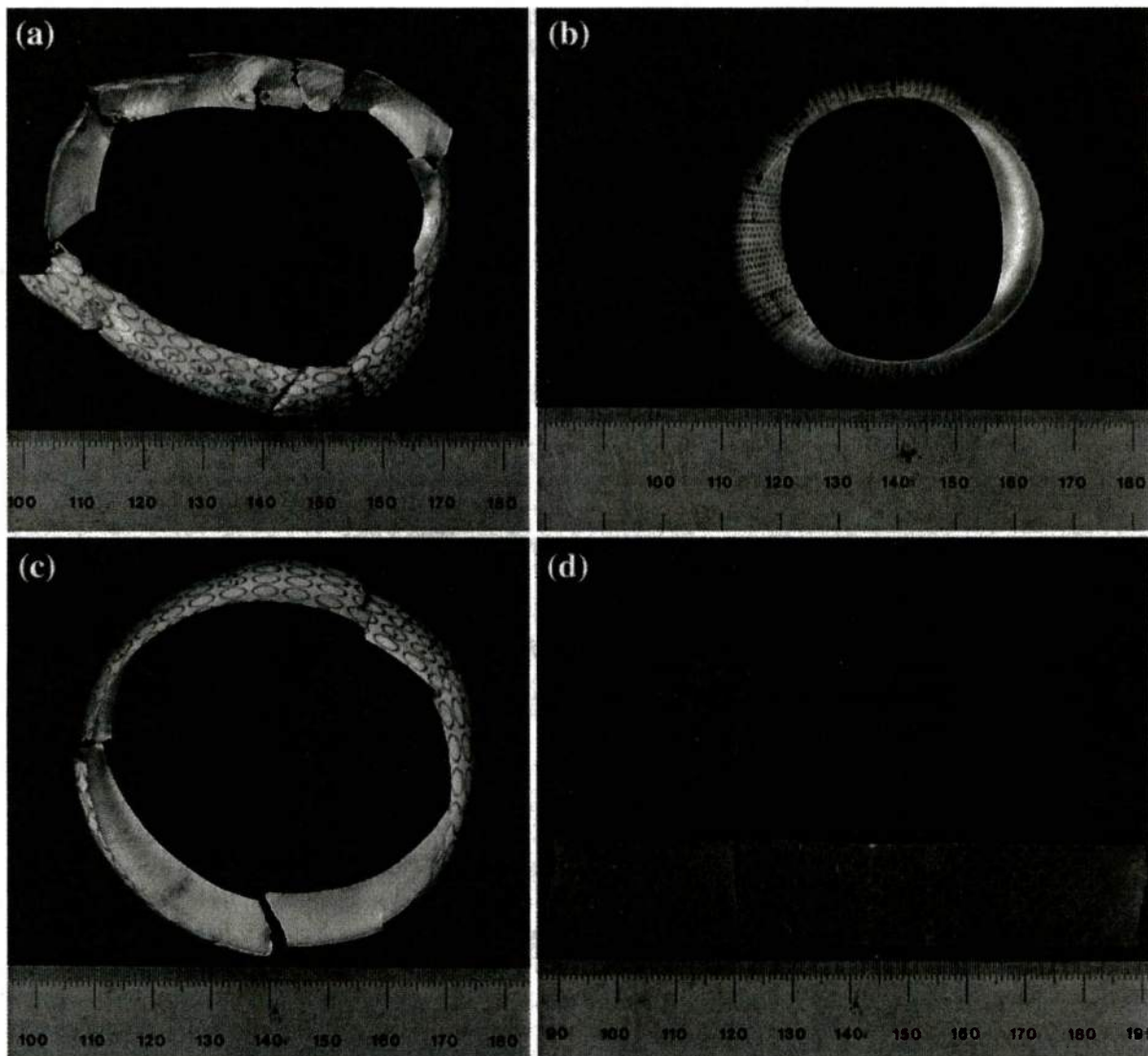


**Fig. 11** Expansion comparisons for bare Al 6061-O, polyurea coated Al 6061-O and polycarbonate coated Al 6061-O. Image a corresponds to a bare Al 6061-O tube, 18 mm long, expanded with a discharge voltage of 14 kV and attaining a radial expansion speed of 196 m/s. Image b corresponds to a polycarbonate coated Al 6061-O tube, 18 mm long, expanded with a discharge voltage of 16 kV and attaining a radial expansion speed of 82.4 m/s (Test PC-4). Finally, images c and d correspond to a polyurea coated

Al 6061-O tube, 18 mm long, expanded with a discharge voltage of 16 kV and attaining a radial expansion speed of 136.1 m/s. Note that image c shows the expanded aluminum tube and d the polyurea coating. The coating has contracted back approximately to its original dimensions, implying that the polyurea coating absorbs energy via elastic deformation. The polycarbonate coating does so in the form of plastic deformation

*tem* measurements of the ellipses were used to obtain the principal logarithmic strains,  $\varepsilon_1$  and  $\varepsilon_2$ , (where  $\varepsilon_1$  corresponds to the hoop direction  $\varepsilon_1 > \varepsilon_2$ ) from the surfaces of a large number of recovered fragments (for the Al/PC specimens, the polycarbonate coating was cut and removed in order to observe and measure the etching on the surface of the aluminum). Figures 12 and

13 show these measurements for the polyurea and polycarbonate coated specimens respectively on a forming limit diagram. Figure 12 presents data from four tests with polyurea coating on the aluminum, including both 18 and 36 mm long tubes (strain rates are in the range of  $3,600\text{--}8,900\text{ s}^{-1}$ ). Figure 13 shows data from four tests as well, but corresponding to polycarbonate coat-

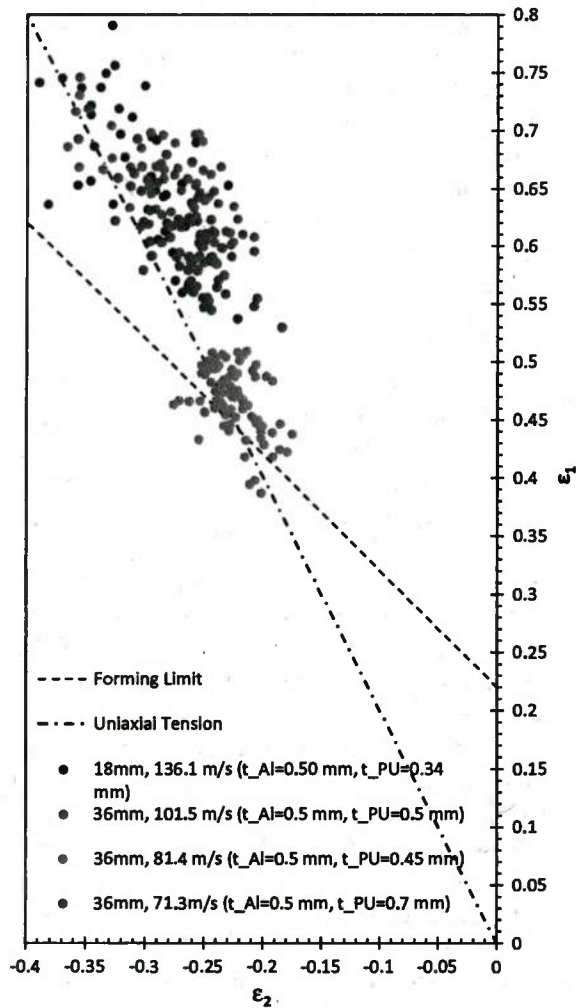


**Fig. 12** Dynamic Forming Limit diagram for Polyurea coated samples. *Open circular symbols* correspond to principal strains measured from regions where no localization is observed, and the *filled circular symbols* correspond to regions where localization is observed. The *dash-dot line* indicates the uniaxial path  $\epsilon_1 = -2\epsilon_2$ , and the *dashed line* indicates the quasi-static forming limit  $\epsilon_1 + \epsilon_2 = n$  based on the maximum tension criterion

ing, although only for 18 mm long samples (strain rates in the range of  $4,200\text{--}5,900\text{ s}^{-1}$ ).

In these figures, data from tubes expanded at different speeds are distinguished by different colors, blue corresponding to the slowest speeds and red to the highest. Additionally, strains measured from regions where no localization was evident under optical micrography are plotted as open symbols, while the strains measured from regions where a shear band was observed crossing an ellipse are plotted as filled symbols. In addition to the circles, two lines are included. The dash-dot line cor-

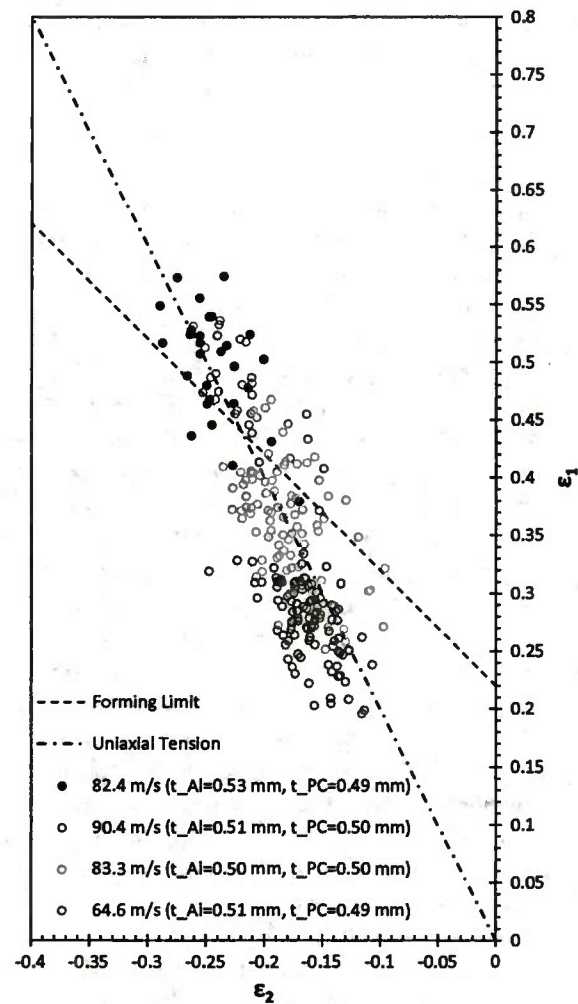


**Fig. 13** Dynamic Forming Limit diagram for Polycarbonate coated samples. *Open circular symbols* correspond to principal strains measured from regions where no localization is observed, and the *filled circular symbols* correspond to regions where localization is observed. The *dash-dot line* indicates the uniaxial path  $\epsilon_1 = -2\epsilon_2$ , and the *dashed line* indicates the quasi-static forming limit  $\epsilon_1 + \epsilon_2 = n$  based on the maximum tension criterion

responds to a state of uniaxial stress, with  $\epsilon_1 = -2\epsilon_2$ , while the dashed line represents the theoretical quasi-static forming limit for sheet materials (see Eq. (4) of Part IV). Analogous to the Al 6061-O tests in Part IV, there is considerable scatter in the data for the polyurea and polycarbonate coated samples as well. This is again caused by two reasons; first, the local measurements of strain are influenced by the curvature of the specimen to appear systematically larger, particularly the minor principal strains. Secondly, for strains measured on ellipses containing a shear band, the



distortion provided by the shear band is neglected. The main observations from these forming limit diagrams (FLDs) are described below.

- In both Al/PU and Al/PC specimens, most of the measured data fall in the region  $\varepsilon_1 \geq -2\varepsilon_2$ , following the pattern observed in Part IV for the uncoated specimens. However, for the coated specimens, the data is not spread evenly around the uniaxial stress path; the data traces a steeper line than the  $\varepsilon_1 = -2\varepsilon_2$  condition, implying that the stress state is migrating just slightly from a uniaxial stress towards a plane-strain condition ( $\varepsilon_2 = 0$ ). Furthermore, for the Al/PU coated tubes, the 36 mm samples seem to migrate<sup>4</sup> more towards the plane-strain condition than the 18 mm samples, as is expected from the observations made in Part IV. It can also be observed that the Al/PC samples (all 18 mm in length) exhibit a larger shift towards the plane strain condition than the polyurea coated specimen of the same length. This indicates that the polycarbonate coating seems to have a greater influence on the stress state of the aluminum than the polyurea.
- For the polyurea coated samples, the expanding velocities are in the range of 55–136.1 m/s. All specimens, including the ones that stopped deforming as a result of low loading levels, show shear bands throughout their surface.
- For the polycarbonate covered samples, the expanding velocities are in the range of 64.6–90.4 m/s. No localizations were observed in specimens PC-1, PC-2 and PC-3. However, the sample PC-4 showed very faint shear bands throughout its internal surface; the average local strains attained in this specimen corresponds to an average hoop strain of 0.50 and an average longitudinal strain of  $-0.24$ . The other specimens exhibit lower average local strains and do not show localization bands. It is worth noting that specimen PC-3, with a higher expansion speed of 90.4 m/s, exhibits no shear localization but has very similar average strains (average hoop strain = 0.47, average longitudinal strain =  $-0.21$ ) to the specimen PC-4, suggesting that the formation of distinguishable shear bands occurs in the range of 0.47–0.50 average hoop strain and  $-0.21$

to  $-0.24$  average longitudinal strain; these appear to be slightly above the quasi-static forming limit for the Al 6061-T6.

- Additionally it can be noted that for the polyurea covered samples, most measured circles demonstrate strain levels above or close to the forming limit for the material. Since all the samples show clear shear localization, and are located immediately above the predicted forming limit, *this is indicative that the polyurea coating does not affect the quasi-static forming limit for the aluminum* under this forming operation, and therefore the material behaves almost identically to the bare aluminum samples in Part IV.
- Finally, from the data of the polycarbonate coated samples, the forming limit does not seem to agree with the quasi-static forming limit predicted for the uncoated aluminum specimens. It is observed that there are a significant number of open symbols above the quasi-static forming limit dash-dot line in Fig. 13. This implies that the forming limit seems to have shifted upward, allowing for a larger strain level without the onset of localization. From the experimental data shown here it is difficult to determine this new forming limit exactly; however, an upward shift of the quasi-static limit by 6% strain would seem to fit better to the observed results. This may be caused by a modification of the stress state of the aluminum caused by a pressure loading applied by the polymer on the top surface of the tube and needs to be explored further.

From Table 1, and Figs. 12 and 13, it is evident that the strain levels achieved by the Al/PU samples were considerably larger than those experienced by the Al/PC, despite the fact that the charging voltages used in the tests were in the same range (13–16 kV). It can be inferred that adding a coating reduces the strain the aluminum can experience, since the acceleration of the additional mass will consume some of the energy that would otherwise be used in straining the metal. However, it can also be noted that the actual added mass from the coatings is relatively similar for both polyurea and polycarbonate, and the vast difference in the strain levels observed ( $\sim 25\%$  difference in maximum hoop strain) is due to the fact that plastically deforming the polycarbonate requires a much larger amount of energy than that needed to elastically deform the polyurea, as is expected from the material properties. This

<sup>4</sup> It is noted that plastic anisotropy could contribute to this migration; the extent of this anisotropy in extruded tubes has not been characterized, but the inertial effects are in addition to the effect of anisotropy.

higher resistance accounts for the larger effect on the stress state of the aluminum as described before. Further discussion of these results is considered in the following section through numerical modeling and simulations.

## 6 Modeling and numerical simulation

Our experimental observations demonstrate that final deformation of the tubes is dependent on the applied driving force as well as the geometric and the material properties of the coatings. In this section, we explore the underlying phenomena in order to determine the role of the polymer coating in retarding/inhibiting the deformation/failure of the metal substrate. This is accomplished first through a simple one-dimensional analysis and is then followed by a three dimensional numerical simulation.

In order to explore the influence of the polymer coating on the uniform expansion of the metal substrate, we consider a one dimensional formulation as in Parts I and III; for this case, the radial acceleration of the tube is given by Eq. (1) from Part III, reproduced below:

$$(\rho_{AL}A_{AL} + \rho_pA_p)r\ddot{r} = F(r, t) - (\sigma_{AL}A_{AL} + \sigma_pA_p) \quad (1)$$

where  $\rho_{AL}$  and  $\rho_p$ ,  $A_{AL}$  and  $A_p$ ,  $\sigma_{AL}$  and  $\sigma_p$  are the density, cross-sectional area and flow strength of the Al6061-O and the polymer, respectively.  $F(r, t)$  groups together the electromagnetic inductive terms that supply the loading to the specimen. It is clear from Eq. (1) that in contrast to the Al specimen, the Al/PU or Al/PC composite has two additional terms that resist the applied force; first, the added mass on the left hand side of Eq. (1) contributes to a decrease in the acceleration of the tube to a given load simply by increasing the inertial resistance. Both polyurea and polycarbonate are of similar density; therefore, their inertial contribution should be very similar. The second factor is the contribution from the stress in the polymer; this provides additional resistance to expansion and corresponds to the second term inside the parenthesis on the right hand side of Eq. (1). For the same cross-section of the coating, it is clear that the polycarbonate can provide a significantly larger resistance to flow than polyurea because  $\sigma_{PC} \gg \sigma_{PU}$ . Even as the modulus and flow stress of the polyurea increase with strain

rate, the stress in the polyurea may not reach levels comparable to that of polycarbonate. Clearly, we see in the experiments that the Al/PC specimens experience significantly smaller strain levels in comparison to the Al/PU specimens when subjected to the same loading conditions. It is clear that optimization of the coating can be considered by taking a polymer with a high flow stress and low density; this supports the use of polycarbonate or the hunt for another formulation of polyurea that can provide a significantly higher flow stress.

The complete response of the Al/polymer composite can only be addressed through direct numerical simulations. Such simulations have been performed to assist in understanding how inertia and strength influence the deformation and failure of the Al/polymer composite system. Furthermore, these simulations also provide some insight into how the coatings can be tailored for optimal design. In order to capture adequately the deformations experienced during the expansion of the tube, a three dimensional finite element model was used. While the full three dimensional geometry is needed to capture the deformations associated with the tube expansion, it is sufficient to look at only a quarter symmetry model of the tube as indicated in Fig. 14a. The features of the simulation are similar to that reported in Part IV for the bare Al specimens; in the present work, two modifications are made, the first to include the polymer coating, and the second to incorporate the loading as a body force, but applied only on the aluminum part, thereby mimicking the applied loading more closely. The tube geometry resembles that of the 18 mm wide tube experiment ( $r_i = 15.25$  mm,  $r_o = 15.75$  mm, and  $w = 18$  mm). The coating thickness is varied depending on the simulation. The tube is discretized with a  $243 \times 5 \times 180$  (arc  $\times t \times w$ ) mesh using eight node linear brick elements with reduced integration and hourglass control (C3D8R). 0.1% of the total number of elements are randomly selected as material defects to trigger localization. Similarly, the coating is discretized with  $251 \times t \times 180$  (arc  $\times t \times w$ ) mesh using eight node linear brick elements with reduced integration and hourglass control (C3D8R) where  $t$  depends on the thickness of the coating with an element size similar that in the tube. The tube material is taken to follow the same power law hardening model for Al 6061-O described in Part I. The material is assumed to not exhibit any softening or damage until a the logarithmic plastic strain reaches  $\epsilon_p = 1$ ; beyond this point, the



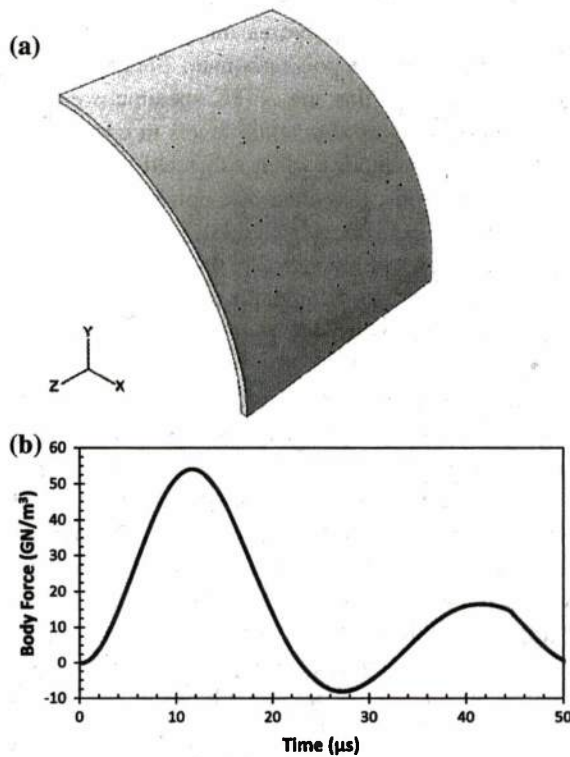


**Fig. 14** **a** Quarter symmetry finite element model of the tube with 0.1% elements with material defects. **b** Body force loading experienced by all points on the Al tube

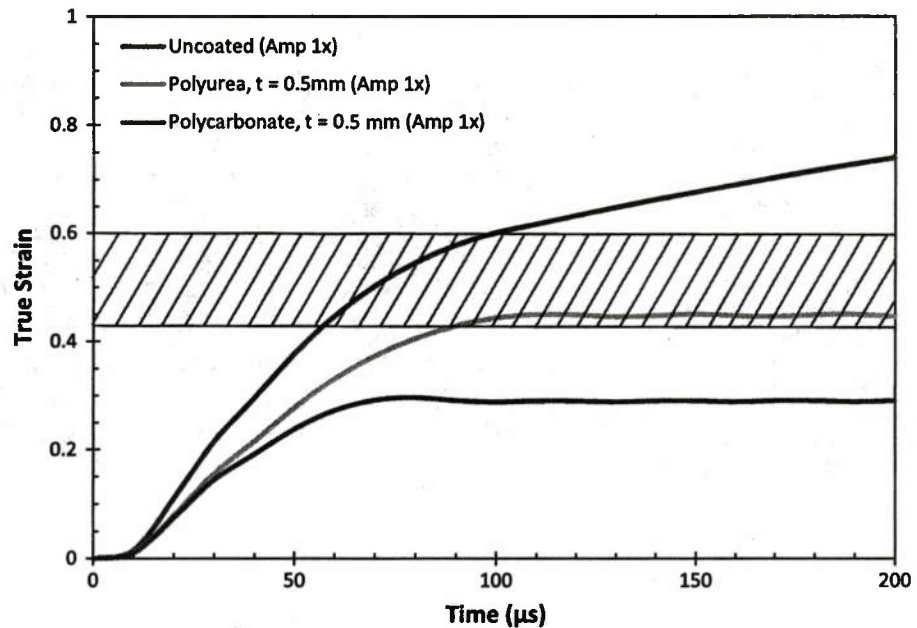
strength of the material is dropped to a small value in order to mimic failure. We note that this simple model is not a proper model of failure, but is expedient in the present work where our objective is to capture the early stages of the onset of localization and the unloading in the vicinity of the localization. The defects are assumed to possess an yield strength of 25 MPa and exhibit no strain hardening. The polyurea layer is modeled using the Marlow formulation of a hyperelastic material, calibrated based on uniaxial test data given in Part III. The polycarbonate is modeled as an elastic-plastic material with an initial modulus of 2.5 GPa up to a strain level  $\varepsilon = 0.25$ , after which it has a tangent modulus of 20 MPa. Beyond  $\varepsilon = 0.6$ , the polycarbonate is assumed to stiffen up again to a tangent modulus equal to that of the original elastic modulus. These models are described in Sect. 2. The actual densities of polycarbonate and polyurea are quite similar and have been taken to be equal ( $1,200 \text{ kg/m}^3$ ) in these simulations.

In the experiment, the aluminum tube is accelerated radially by a body force due to electromagnetic load-

ing. The amplitude of the body force is proportional to the product of the current in the solenoid and the induced current in the tube. These currents have been measured using inductive noncontact probes (see Figure 6 of Part I) and therefore a body force amplitude curve with respect to time can be created. This curve is used to specify the body force amplitude applied to the aluminum tube during the simulation. A scaling factor is used to adjust the amplitude and achieve the desired outward radial velocity. The baseline curve of the loading is shown in Fig. 14b. The baseline amplitude is the lowest amplitude that will still cause failure in the bare aluminum specimen.

We now consider the results of three simulations corresponding to Al, Al/PU and Al/PC specimens, all subjected to the same loading. The Al specimen and the polyurea and polycarbonate coatings were of the same thickness ( $t = 0.5 \text{ mm}$ ). The time evolution of the hoop strain of elements along the inner diameter at the midline of the tube is shown in Fig. 15. The localization strain level and the range of reported failure strains are also marked in this figure. As discussed in Section 4 of Part IV, sheet materials under biaxial tension, the critical necking strain is  $\varepsilon_{SN} = 2n$ . The Al-6061-O has a hardening exponent of  $n = 0.22$  so we expect localization to occur at  $\varepsilon_{SN} = 0.44$ . Failure strain is more ambiguous and as such instead of offering some specific value we have shown the typical range of maximum strain measured post mortem in failed aluminum tube samples; typical macroscopic average strain at failure has been measured to be in the range  $\varepsilon_f = 0.55 - 0.65$ . The initial velocity of expansion is 150 m/s for the bare Al specimen and  $\sim 100 \text{ m/s}$  in both polymer coated specimens. The initial expansion rate of the polymer coated specimens is slightly smaller than that of the bare aluminum; this is attributed to the added mass of the polymer as discussed above. Both the Al/PU and Al/PC specimens strained to a smaller level than the bare Al, with the Al/PC not exceeding the localization strain, while the Al/PU went just above this threshold. Contour plots of the effective plastic strain obtained from these three simulations at selected time steps are shown in Fig. 16 to examine the effect of the polymer coating. As described in Part IV, the bare Al specimen exhibits strain localization and failure (Fig. 16a); eventually the fragments fly away with significant kinetic energy; the fragments have a residual velocity of 40 m/s. The maximum strain level attained by the Al with the polyurea coat-

**Fig. 15** Variation of the hoop strain with time. The hashed region corresponds to the range of average strains at which failure occurs



ing exceeded the strain localization threshold and this simulation exhibits strain localization (Fig. 16b). The Al-tube with the polycarbonate coating, on the other hand, was unable to expand to a global strain level larger than about 0.4, due to the higher strength of the polycarbonate. The residual velocity in both cases is about  $\sim 2.5$  m/s; essentially, both the polyurea and the polycarbonate coatings stopped the expansion of the Al specimen. At the end of the simulation time, the Al specimen had fragmented into pieces each with significant kinetic energy, the Al/PU had strain localized but not fragmented, and the Al/PC specimen had contained the loading with just uniform plastic deformation over both the Al and the PC. The variation of the hoop stress in the coating with time is shown in Fig. 17. It is now easy to distinguish between the added mass effect and the increased strength effect. While both the polymers increase the mass by the same amount, it should be noted that the maximum principal stress attained by the polyurea is only about  $\sim 6$ – $8$  MPa, while the polycarbonate reached a maximum stress that is about an order of magnitude greater to  $\sim 80$  MPa. Thus, polycarbonate, with nearly the same mass as the polyurea, but with a much larger strength in the range of  $60$ – $90$  MPa, is more effective in inhibiting the failure of the Al, not by altering the localization response but simply by providing a dissipative mechanism for absorbing the energy in the Al part of the composite specimen. Around  $100 \mu\text{s}$ , when the applied loading is

terminated, dynamic oscillations of the polycarbonate can be observed<sup>5</sup> in Fig. 17.

With this understanding of the role of the polymer, we can now consider some issues related to the optimal design of polymer coatings. First, we explore the effect of varying the thickness of the polyurea coating while keeping the imposed driving force and the material strength constant. This simulation allows examination of the “added mass” effect in contrast to the previous simulations where the mass of the coating was maintained constant while varying the strength. Figure 18 shows the average true hoop strain of elements along the inner diameter at the midline of the tube for several coating thicknesses. The range of strains for onset of localization and failure in the Al are also marked in this figure. Figure 18 shows that an increase in the polyurea coating thickness results in a decrease of the expansion velocity in the early stages; all three coating thicknesses result in a rapid deceleration of the tube beyond about  $80 \mu\text{s}$ . For the two thinner coatings— $0.25$  and  $0.5$  mm—the peak strain levels exceed the localization threshold and the strain in the Al localizes along bands; however, at this point the specimen

<sup>5</sup> Note that these oscillations with an amplitude of about  $6$ – $7$  MPa can apply a compressive stress on the Al tube that is on the order of  $200$  MPa, well above compressive yield. Localized wrinkling was observed in some of the experiments; this needs to be examined more completely to explore all failure mechanisms in the Al tube.



**Fig. 16** Contour plots of equivalent plastic strain from three simulations with identical applied force. **a** Bare Al 6061-O specimen, with  $t_{AL} = 0.5$  mm; **b** Al/PU specimen with  $t_{AL} = 0.5$  mm and  $t_{PU} = 0.5$  mm; **c** Al/PC specimen with  $t_{AL} = 0.5$  mm and  $t_{PC} = 0.5$  mm. For (b) and (c), the coating has been masked, and only the strain in the Al tube is shown. The hoop stress in the coating layer was uniform at the levels indicated in Fig. 17

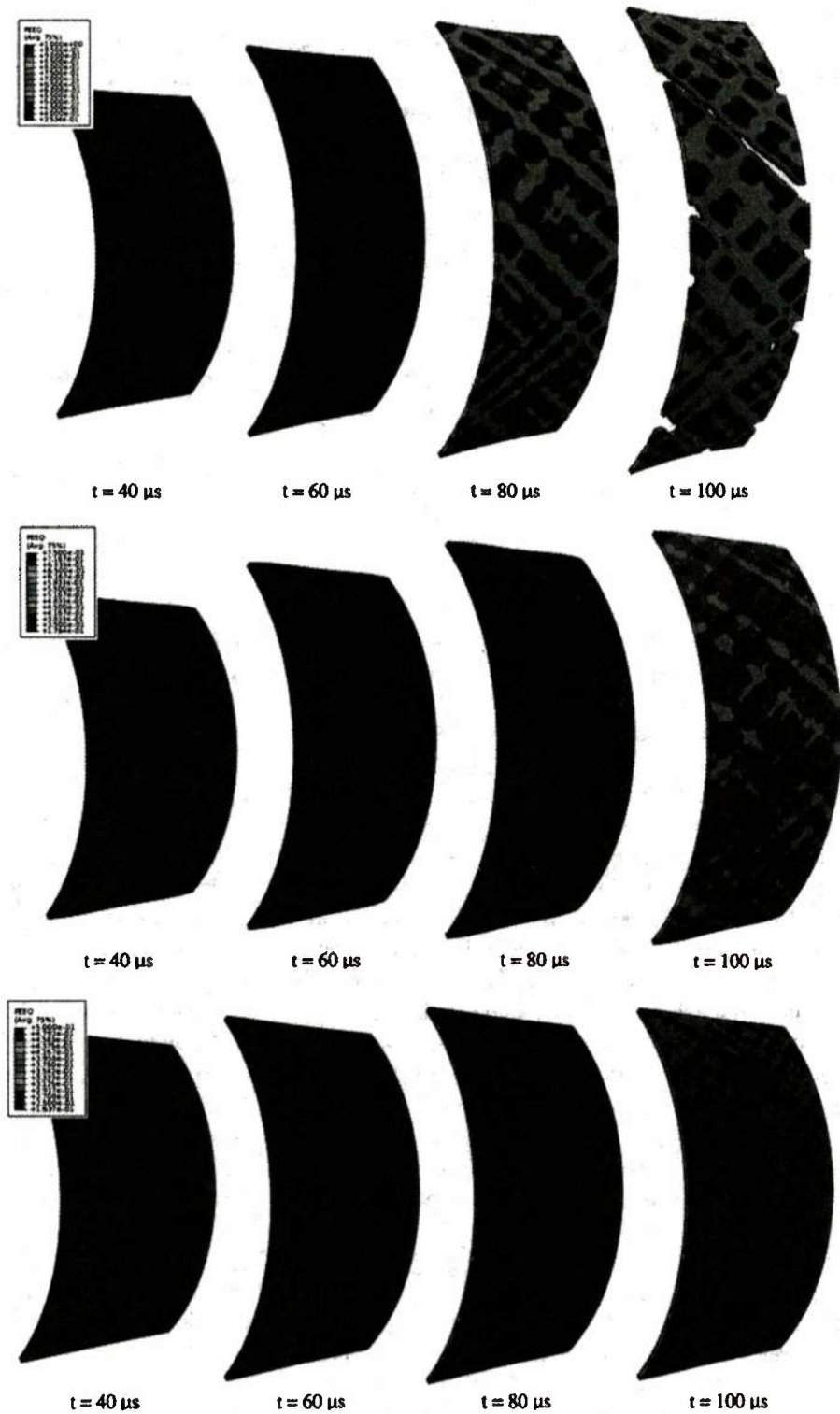


**Fig. 17** Variation of the hoop stress in the polyurea and polycarbonate coating

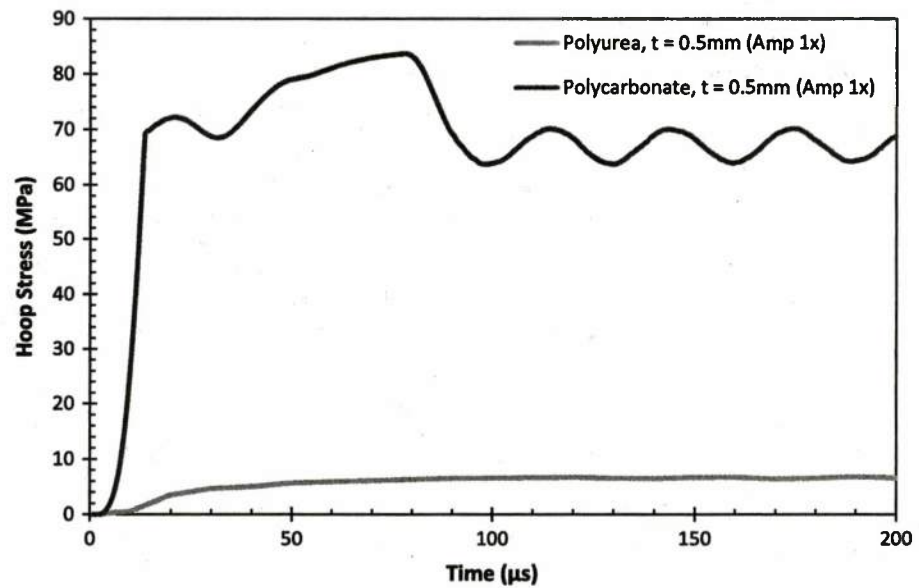
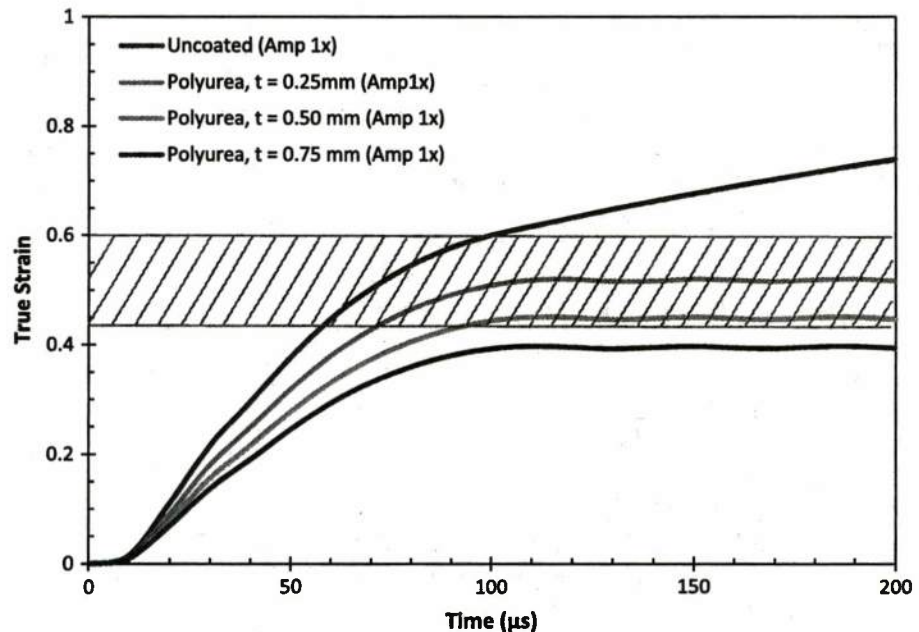


**Fig. 18** Variation of the hoop strain with time from four simulations with different thickness polyurea coatings

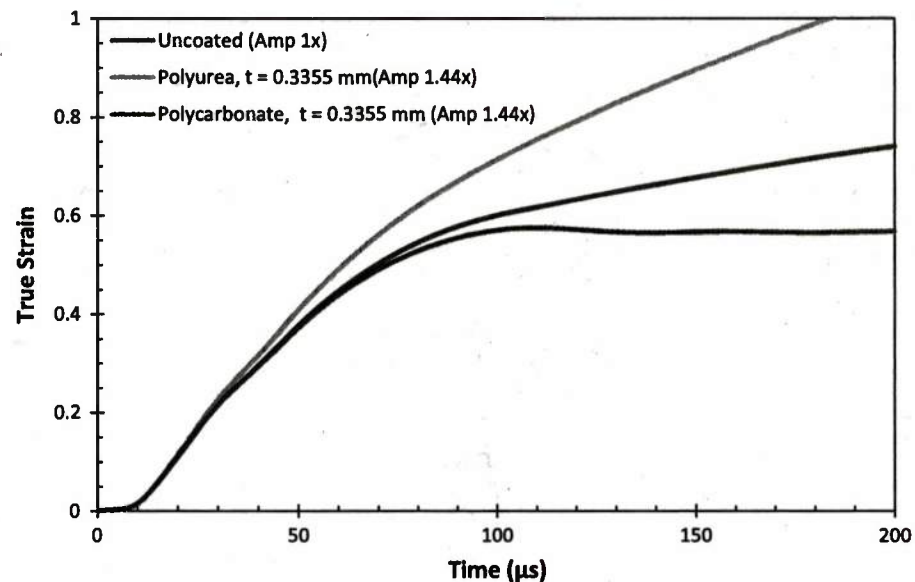


has very little kinetic energy. For the thickest coating, the resistance provided by the added mass polyurea is sufficient to stop the Al from straining even to the localization threshold. From these simulations, it is apparent that the main effect of the polyurea in providing additional resistance to the expansion of the Al/PU composite specimen is based on its mass; as the coating thickness is increased the strain is reduced to below failure strain and even below localization strain.

In the above simulations, we have maintained a constant applied force, and varied the coating materials and thicknesses; however, this approach results in an increase in the total weight of the structure. In many design scenarios, maintaining the overall weight of the structure is of critical importance. So, the following question arises: what is the consequence of designing a coated structure with the constraint of keeping the mass constant? In the last set of simulations, this was accomplished by modifying the thicknesses of



**Fig. 19** Variation of the hoop strain with time for three simulations with the same total mass and same applied loading



the polyurea and polycarbonate coatings to result in the same total mass as the bare Al specimen. Since the densities of the two polymers is nearly the same and much smaller than the Al,  $\rho_{PU} \sim \rho_{PC} \sim 0.43\rho_{AL}$ , the mass is maintained constant by reducing the thickness of the Al to  $\alpha t_{AL}$  and adding a coating of thickness  $t_p = (1 - \alpha)t_{AL}\rho_{AL}/\rho_p$ . Figure 19 shows the results of simulations in which the tube thickness was reduced to 0.35 mm ( $\alpha = 0.7$ ) and that mass was replaced with a  $t_p = 0.336$  mm coating of polyurea and polycarbonate. Since the body force is applied only to the Al part of the specimen, its magnitude was scaled to account for the reduction in driven mass and still maintain the same total force as in the 0.5 mm thick uncoated tube. In interpreting the results, it should be noted that the higher strength Al is replaced by a significantly weaker polyurea and a somewhat weaker polycarbonate. The results are clear; in comparison to the full thickness Al specimen, the Al/PU specimen experiences a greater expansion. The Al part of the specimen fragments after attaining strains of around 0.6; these fragments are, of course now contained within the polyurea, and as the polyurea expands to strain levels of around one, it is expected that the metal fragments will be slowed down; the simulations have not been performed to reach this stage. In contrast, the polycarbonate coating is sufficiently strong to resist the expansion of the metal; the strain levels still reach localization and failure threshold, but the kinetic energy of the expanding metal is nearly fully dissipated in the deformation of the poly-

carbonate. The ability of polycarbonate to carry significant hoop stress long beyond the failure of the aluminum means that this composite structure, on a per unit mass basis, is much more resistant to blast loading than either the Al or the Al/PU.

## 7 Conclusion

In this paper, the onset and growth of strain localization and fragmentation in Al 6061-O tubes coated with a layer of polymer—either polyurea or polycarbonate—has been investigated. The electromagnetic loading scheme was used to deform the tube specimens at rates between 4,000 and 15,000 s<sup>-1</sup>. A conical mirror was used to provide the whole field information of the deformation on the tube surface. The results reveal the time-scale and length-scale in which the localization and fracture arise and provide insight into the effect of polymer layers on the onset of localization and fragmentation of tubes. The main conclusions from this study are listed below.

- Nearly simultaneous nucleation of strain localization at a critical strain level is observed in the metal tube; this strain level is not significantly influenced by the presence of the polymer coating. The forming limit diagram obtained from these measurements indicates that the localization criterion developed from quasi-static considerations continue to apply in the dynamic problem.

- There appear to be two effects of the polymer coating on the overall deformation of the Al 6061-O tube specimens. First, the additional mass of the coating material results in an inertial effect; therefore, thicker coatings result in a slower overall expansion, and hence for a limited impulse loading, less overall straining of the metallic specimen. Second, the flow resistance of the polymer dissipates additional energy and can prevent failure in the metallic specimen. This effect is much more pronounced in polycarbonate, the material with a larger strength.
- Numerical simulations of the expanding tube with polymer coatings indicate that the both the inertial effect and the strength effect of the polymer may be used in slowing down the expansion of the metallic tube; if this results in a final strain below the forming limit, strain localization is not triggered.

**Acknowledgments** This work was performed under a program entitled “Dynamic Response of Metal-Polymer Bilayers—Viscoelasticity, Adhesion and Failure” sponsored by the Office of Naval Research (ONR Grant Number N00014-09-1-0541, Program Manager: Dr. Roshdy Barsoum); this support is gratefully acknowledged.

## References

- Amini MR, Nemat-Nasser S (2010) Micromechanisms of ductile fracturing of DH-36 steel plates under impulsive loads and influence of polyurea reinforcing. *Int J Fract* 162: 205–217
- Amini MR, Isaacs JB, Nemat-Nasser S (2010a) Experimental investigation of response of monolithic and bilayer plates to impulsive loads. *Int J Impact Eng* 37:82–89
- Amini MR, Amirkhizi AV, Nemat-Nasser S (2010b) Numerical modeling of response of monolithic and bilayer plates to impulsive loads. *Int J Impact Eng* 37:90–102
- Amini MR, Simon J, Nemat-Nasser S (2010c) Numerical modeling of effect of polyurea on response of steel plates to impulsive loads in direct pressure-pulse experiments. *Mech Mater* 42:615–627
- Amirkhizi AV, Isaacs J, McGee J, Nemat-Nasser S (2006) An experimentally-based viscoelastic constitutive model for polyurea, including pressure and temperature effects. *Philos Mag* 86:5847–5866
- Barsoum RGS, Dudt PJ (2009) The fascinating behaviors of ordinary materials under dynamic conditions. *AMMTIAC Q* 4:11–14
- Chakkarapani V, Ravi-Chandar K, Liechti KM (2006) Characterization of multiaxial constitutive properties of rubbery elastomers. *J Eng Mater Technol Trans ASME* 128: 489–494
- Chevallard G, Ravi-Chandar K, Liechti KM (2011) Modeling the nonlinear viscoelastic behavior of polyurea using a distortion modified free volume approach. *Mech Time Depend Mater* (published online 1 July 2011)
- Guduru PR, Freund LB (2002) The dynamics of multiple neck formation and fragmentation in high rate extension of ductile materials. *Int J Solids Struct* 39:5615–5632
- Guduru PR, Bharathi MS, Freund LB (2006) The influence of a surface coating on the high-rate fragmentation of a ductile material. *Int J Fract* 137:89–108
- Jiao T, Clifton RJ, Grunschel SE (2007) Pressure-sensitivity and tensile strength of an elastomer at high strain rates. *Shock Compr Condens Matter*, 955:707–710
- Lu J, Ravi-Chandar K (1999) Inelastic deformation and localization in polycarbonate under tension. *Int J Solids Struct* 36:391–425
- Matthew W (2004) Services test spray-on vehicle armor, *Army Times*, May 3, 2004
- McSbane GJ, Stewart C, Aronson MT, Wadley HNG, Fleck NA (2008) Deshpande vs. dynamic rupture of polymer-metal bilayer plates. *Int J Solids Struct* 45:4407–4426
- Mock W Jr, Bartyczak, Lee G, Fedderly J, Jordan J (2009) Dynamic properties of polyurea 1000. In: Elert ML et al (eds) *Shock compression of condensed matter—2009*, pp 1241–1244
- Roland CM, Twigg JN, Vu Y, Mott PH (2007) High strain rate mechanical behavior of polyurea. *Polymer* 48:574–578
- Roland CM, Fragiadakis D, Gamache RM (2010) Elastomer-steel laminate armor. *Compos Struct* 92:1059–1064
- SPI Inc (2009) URL created in 2009, accessed on 6 July 2011: <http://www.specialty-products.com/polyurea-products/Pol-yurea-Plural-Component-Coatings/dragonshield-ht-erc/>
- Tekular SA, Sbukla A, Shivakumar K (2008) Blast resistance of polyurea based layered composite materials. *Compos Struct* 84:271–281
- Xue Z, Hutchinson JW (2008) Neck development in metal/elastomer bilayers under dynamic stretching. *Int J Solids Struct* 45:3769–3778
- Xue Z, Vaziri A, Hutchinson JW (2008) Material aspects of dynamic neck retardation. *J Mech Phys Solids* 56:93–113
- Xue L, Mock W Jr, Belytschko T (2010) Penetration of DH-36 steel plates with and without polyurea coating. *Mech Mater* 42:981–1003
- Yi J, Boyce MC, Lee GF, Balizer E (2006) Large deformation rate-dependent stress-strain behavior of polyurea and polyurethanes. *Polymer*, 47:319–329
- Zhang H, Ravi-Chandar K (2006) On the dynamics of necking and fragmentation: I. Real-time and post mortem observations in Al-6061-O. *Int J Fract* 142:183–217
- Zhang H, Ravi-Chandar K (2008) On the dynamics of necking and fragmentation: II. Effect of material properties, geometrical constraints and absolute size. *Int J Fract* 150:3–36
- Zhang H, Ravi-Chandar K (2010) On the dynamics of necking and fragmentation: IV. Expansion of Al 6061-O tubes. *Int J Fract* 163:41–65
- Zhang H, Liechti KM, Ravi-Chandar K (2009) On the dynamics of necking and fragmentation: III. Effect of cladding with a polymer. *Int J Fract* 155:101–118
- Zhao J, Knauss WG, Ravichandran G (2007) Applicability of the time-temperature superposition principle in modeling dynamic response of a polyurea. *Mech Time Depend Mater* 11:289–308



## APPENDIX C

### **A fracture analysis of cathodic delamination of polyurea from steel, submitted**

T. K. Mauchien and K.M. Liechti

*International Journal of Adhesion and Adhesives*, September 2013

## **Abstract**

A fracture mechanics approach to accelerated life testing of cathodic delamination between steel and polyurea is presented. This required the hyperelastic behavior of the polyurea to be described by the Marlow model based on uniaxial tension and plane strain compression tests. Time-dependence was also considered but could be neglected if proper test protocols were followed in cathodic delamination tests using a strip blister specimen. The variation of J-integral with specimen geometry and loading parameter was obtained, which allowed the resistance to cathodic delamination to be expressed in terms the J-integral and the crack speeds obtained from the tests at several temperatures. The approach established that both temperature and stress can be used to accelerate the cathodic delamination, thereby providing a quantitative and rational basis for conducting accelerated testing as well as evaluating new surface treatments.

**Keywords:** Cathodic delamination, polymer/metal interfaces, accelerated testing, fracture mechanics.



## 1. Introduction

Cathodic delamination can be viewed as an example of environmentally assisted crack growth, an example of slow, subcritical fracture that can eventually transition to fast fracture and complete failure of the interface. The environmental or chemical aspects of the problem have been studied for a number of polymer/metal pairs [1-10], as reviewed in [11] and have the potential to be coupled with mechanical effects [11-18], thereby improving our understanding of the problem. This in turn can motivate accelerated life testing protocols and the development of new surface treatments with a view to eliminating or at least minimizing cathodic delamination in naval and automotive structures.

In the current study, we examine the potential for cathodic delamination in systems where steel is coated with polyurea, often for blast protection [19, 20]. The elements of the approach are threefold; determining the time-dependent, hyperelastic behavior of the polyurethane, conducting a stress analysis of the specimen to be used in the cathodic delamination experiment in order to obtain J-integral values as a function of crack length and conducting cathodic delamination experiments and determining the crack velocity profiles for the polyurea/steel interface as a function J-integral and temperature. The details of these steps are presented in sections 2 and 3 followed by results and discussion in section 4.

## 2. Experimental

In this section, we describe the experiments that were conducted to determine the nonlinear mechanical behavior of the polyurea and the cathodic delamination of polyurea from steel.

### *2.1. Polyurea constitutive behavior*

The polyurea considered in this study was formed by the reaction of a modified diphenylmethane diisocyanate prepolymer (Isonate 143L from Dow Chemical) with an oligomeric diamine curative (Versalink P-1000 from Air Products). A ratio of 1:4 prepolymer to curative by weight was used herein. The Versalink was heated to 50°C until its viscosity dropped sufficiently for processing. It was then degassed under vacuum at room temperature with constant stirring until no bubbles were observed. The Versalink and Isonate were then mixed under vacuum in a weight ratio of 1:4 for 5 minutes. Polyurea was poured into a rectangular sheet mold. This sheet of polyurea was then cut to prepare samples for uniaxial tension and plane strain compression tests. The cure time for the material was 2 weeks at room temperature.

The uniaxial tension specimens were strips (17.5×0.8×0.33 cm) that were gripped at each end, leaving a 5 cm gage length, and were loaded to failure in an electromechanical testing device under displacement control at various rates. The load and overall extension of the specimen were measured using the load cell and crosshead displacement sensor of the device. The engineering stress in the specimen was obtained from the load and original cross section area. A camera (Lumenera INFINITY3) was set up to measure the axial and transverse

displacements in the gage section of the specimen using horizontal and vertical lines that were marked on the specimen surface. The temperature at which the tests were conducted was 22°C.

In the plane strain compression test, polyurea sheets were compressed across their width by narrow bars (Fig. 1), which were made of ground tool steel with 0.13-cm radii to minimize stress concentrations [21]. The bars were mounted between self-aligning platens that were attached to the crosshead and base of the electromechanical loading device. The dimensions of the sheet (Fig. 1) were  $L_0 = 7.8$ ,  $b_0 = 7.8$  and  $t_0 = 0.44$  cm, while those of the bar were  $L = 1$ ,  $b = 15$  and  $h = 2.5$  cm. In order to ensure that the deformation under the bars is essentially homogeneous, the ratio of bar width to strip thickness at any instant in the test should be between 2 and 4 [22]. This choice of dimensions  $w/t_0$  satisfied this criterion initially but violated it once the true strain was  $-0.5$ . Consequently, any data outside this regime should be considered in light of this restriction. A release agent was applied to the surfaces of the polyurea as a lubricant in order to minimize friction. The load and platen displacement were measured as before and the camera was used to measure the displacement of the grips 0.5 cm from the contact surfaces. Images were recorded every 20 s. The tests were conducted in displacement control at a strain rate of  $9.2 \times 10^{-5}$  /s.

## **2.2. Cathodic Delamination**

The strip blister specimen [11] (Fig. 2) was used to characterize the resistance to cathodic delamination between polyurea and steel. The steel substrate was 11.5 cm long by 1.27 cm wide by 2.54 cm thick, with polyurea layers whose thickness  $t$  was 7.6 mm. The initial crack length  $2a_0$  was 2.54 cm. The fabrication steps were as follows: The steel surfaces were grit blasted with #50 angular steel grit at a pressure of 0.6 MPa. The adherends were then placed in an ultrasonic bath filled with methyl ethyl ketone (MEK) for 15 minutes, once to remove major debris and then again as a final cleansing. The region for the initial crack was then masked with Teflon® tape and PR-420 (PRC-DeSoto) metal primer was applied to the remainder of the steel surface and allowed to dry for 2 hours. Mold walls were applied to specimen and the gap was filled with previously evacuated polyurea to the thickness specified above. The polyurea was cured for two hours at room temperature, while the polyurea for the second layer was prepared. The specimen was then turned over and the second layer of polyurea was applied in the same way. This procedure provided two potentially different interfaces to evaluate because the primer dried for 4 hours on the second interface prior to the application of the polyurea. The interfaces were designated 2h and 4h, respectively. The assembly was allowed to cure at 22 °C for two weeks and the mold walls were removed.

For the cathodic delamination experiment itself, a 4.8 mm-diameter stainless steel dowel was inserted between the polymer and metal at both interfaces at the center of the initial crack to

provide a wedge loading to the specimen. The specimen was then allowed to relax for several hours prior to environmental exposure in order to minimize any viscoelastic effects.

The conditions for cathodic delamination were provided by placing the preloaded specimens in an artificial sea water solution [23] in an aquarium (Fig. 3) and applying a suitable electrical potential to the specimen. Air was directly injected into the artificial sea water using a Bubble Bar®, which, in conjunction with a ventilator, ensured that there was a homogeneous and sufficient supply of oxygen for the cathodic delamination reaction to occur. The artificial sea water was maintained at several temperature levels in separate tests. A potentiostat was used to maintain the metal parts of the specimen at a constant potential of -0.9 volts with respect to a standard calomel electrode (SCE). A graphite rod was used as the anode. The current flow in the tank was measured periodically throughout each experiment and remained constant at about 1 mA. The specimens were periodically removed in order to measure the crack length with vernier calipers. The measurements were made on both edges of the crack fronts and the average for each interface (2h and 4 h) was recorded as the effective crack length.

### 3. Analysis

The first part of analysis that is presented here is related to the determination of the parameters associated with the reduced polynomial [24], Ogden [25] and Marlow [26] models of hyperelastic behavior. The time dependence of the polyurea is addressed on the basis of its relaxation function [27]. It is followed by a description of the fracture mechanics analysis of the strip blister specimen with a view to determining the variation of J-integral with specimen geometry and loading parameters.

#### 3.1. Models of Polyurea Stress-Strain Behavior

The engineering stress-strain response of polyurea under uniaxial tension was obtained (Fig. 4a) at two engineering strain rates based on the local strain measurements. The initial stiff response was associated with viscoelastic effects, followed by a plateau region from 25 to 170% strain at 4 and 4.8 MPa at  $1.7 \times 10^{-4}$  and  $6.0 \times 10^{-4}$  /s, respectively. The response stiffened thereafter and the final data points were associated with failure in the gage section but close to the grips. The corresponding axial and transverse stretches are the principal stretches

$$\lambda_1 = 1 + e_a \text{ and } \lambda_2 = 1 + e_t, \quad (0.1)$$

where  $e_i$  are the corresponding engineering strains. The results are presented in Figure 4b where it can be seen that the polyurea was essentially incompressible. There was an apparent deviation from an incompressible response at large stretch values, particularly at the lower strain rate, which was most likely due to the fact that a strain marker was close to a grip. Based on this result, subsequent modeling proceeded on the assumption that the polyurea was incompressible.



### 3.1.1. Hyperelastic Behavior

The form of the reduced polynomial strain energy potential that was used here is

$$U = \sum_{i=1}^N C_{i0} (I_1 - 3)^i, \quad (0.2)$$

where  $C_{i0}$  and  $N$  are material parameters and  $I_1 = \lambda_1^2 + \lambda_2^2 + \lambda_3^2$  is the first strain invariant. Under uniaxial tension, the principal stretches are  $\lambda_1 = \lambda$ ,  $\lambda_2 = \lambda_3$ . Incompressibility requires that  $\lambda_1 \lambda_2 \lambda_3 = 1$ . Hence  $\lambda_2^2 = \lambda_3^2 = \frac{1}{\lambda}$ ,  $I_1 = \lambda^2 + \frac{2}{\lambda}$  and the strain energy potential becomes

$$U = \sum_{i=1}^N C_{i0} \left( \lambda^2 + \frac{2}{\lambda} - 3 \right)^i \quad (0.3)$$

The engineering stress can be computed from  $T_{ua} = \frac{\partial U}{\partial \lambda}$ , so that

$$T_{ua} = 2 \left( \lambda - \frac{1}{\lambda^2} \right) \sum_{i=1}^N i C_{i0} \left( \lambda^2 + \frac{2}{\lambda} - 3 \right)^{i-1} \quad (0.4)$$

For plane strain compression, the principal stretches are  $\lambda_1 = \lambda$ ,  $\lambda_3 = 1$ . In this case, incompressibility leads to  $\lambda_2 = \frac{1}{\lambda}$ ,  $I_1 = \lambda^2 + \frac{1}{\lambda^2} + 1$  and the strain energy potential becomes

$$U = \sum_{i=1}^N C_{i0} \left( \lambda^2 + \frac{1}{\lambda^2} - 2 \right)^i. \quad (0.5)$$

For plane strain compression, the engineering stress component in the loading direction is

$$T_{ps} = 2 \left( \lambda - \frac{1}{\lambda^3} \right) \sum_{i=1}^N i C_{i0} \left( \lambda^2 + \frac{1}{\lambda^2} - 2 \right)^{i-1} \quad (0.6)$$

The Ogden form of the strain energy density function is

$$U = \sum_{i=1}^N \frac{2\mu_i}{\alpha_i^2} \left( \lambda_1^{\alpha_i} + \lambda_2^{\alpha_i} + \lambda_3^{\alpha_i} \right), \quad (0.7)$$

where  $\mu_i$  and  $\alpha_i$  are material parameters. Similar steps were taken to obtain expressions for the strain energy density function and engineering stress-stretch relations under uniaxial tension and plane strain compression. Under uniaxial tension, the strain energy density function and stress-stretch relations become

$$U = \sum_{i=1}^N \frac{2\mu_i}{\alpha_i^2} \left( \lambda^{\alpha_i} + 2\lambda^{-\frac{\alpha_i}{2}} - 3 \right) \text{ and } T_{ua} = \frac{1}{\lambda} \sum_{i=1}^N \frac{2\mu_i}{\alpha_i} \left( \lambda^{\alpha_i} - \lambda^{-\frac{\alpha_i}{2}} \right). \quad (0.8)$$

In plane strain compression they become

$$U = \sum_{i=1}^N \frac{2\mu_i}{\alpha_i^2} \left( \lambda^{\alpha_i} + \lambda^{-\alpha_i} - 2 \right) \text{ and } T_{ps} = \frac{1}{\lambda} \sum_{i=1}^N \frac{2\mu_i}{\alpha_i} \left( \lambda^{\alpha_i} - \lambda^{-\alpha_i} \right) \quad (0.9)$$

The basis for the Marlow model for incompressible materials is the assumption that the first invariant is sufficient to characterize the response of the material under any stress state. The material behavior is then completely determined by a single test. The Marlow form can be derived exactly from the uniaxial tension engineering stress-strain curve  $T_T(e)$  as

$$U(I_1) = \int_0^{\lambda_T(I_1)-1} T_T(e) de, \quad (0.10)$$

where  $\lambda_T(I_1)$  is determined from the relation  $I_1 = \lambda_T^2 + \frac{2}{\lambda_T}$  reflecting uniaxial tension and incompressibility. In plane strain compression, the normal stress in the direction of loading can be derived from the strain energy density function

$$T_{ps}(\lambda_{ps}) = \frac{\partial U(I_{1ps})}{\partial \lambda_{ps}}, \quad (0.11)$$

where  $I_{1ps} = \lambda_{ps}^2 + \frac{1}{\lambda_{ps}^2} + 1$ . As a result

$$T_{ps}(\lambda_{ps}) = T_T(\lambda_T(I_{1ps}) - 1) \cdot \frac{\partial}{\partial I_{1ps}} (\lambda_T(I_{1ps})) \cdot \frac{\partial}{\partial \lambda_{ps}} (I_{1ps}) \quad (0.12)$$

Alternatively, we can write

$$T_{ps}(\lambda_{ps}) = \frac{\lambda_{ps} - \lambda_{ps}^{-3}}{\lambda_T(I_{1ps}) - \lambda_T(I_{1ps})^{-2}} T_T(\lambda_T(I_{1ps}) - 1), \quad (0.13)$$

thereby demonstrating how the uniaxial stress-strain response can be used to predict the response under other conditions.

### 3.1.2. Time Dependent Behavior

The viscoelastic behavior of polyurea was defined using the power law shear data that had been obtained in a previous study [27].

$$\mu = \mu_r + \frac{\mu_g - \mu_r}{\left(1 + \frac{t}{\tau_0}\right)^n}, \quad (0.14)$$

with the glassy modulus  $\mu_g = 1$  GPa, the rubbery modulus  $\mu_r = 10$  MPa, the relaxation time  $\tau_0 = 3.16 \times 10^{-5}$  s and the power law exponent  $n = 0.14$ . For compatibility with ABAQUS, this data was converted to a nine-parameter Prony series fit:

$$g(t) = g_\infty + \sum_{i=1}^9 \bar{g}_k^p e^{-t/\tau_k}, \quad (0.15)$$

where  $\tau_k$  are time constants,  $g_\infty$  and  $\bar{g}_k^p$  are dimensionless constants, normalized by  $\mu_g$ .

### 3.2. Fracture Analysis of the Strip Blister Specimen

In view of the nonlinearly elastic response of the polyurea, the crack analysis was carried out with the finite element code ABAQUS. The model accounted for a symmetric half of the full length of the specimen and the central crack of length  $2a$ . A plane strain formulation was used in the finite element analysis and the dowel was modeled as a rigid and frictionless circular cylindrical surface. The polyurea was initially given the hyperelastic stress-strain properties that were discussed earlier. Subsequent analyses accounted for the time dependence of the polyurea. The steel was taken to be linearly elastic with Young's modulus and Poisson's ratio of 200 GPa and 0.3, respectively. The thickness of the primer was so small that it did not need to be considered in the stress analysis of the specimen. The deformed shape of the specimen and the distribution of the von Mises stress with the dowel fully inserted are shown in Figure 5. The blunted crack with the highly deformed polyurea is clear to see. This was also the most highly stressed region.

The J-integral is ideally suited as a fracture parameter for nonlinearly elastic materials, so it was extracted from the finite element solutions. It was first used as a metric for determining the optimum degree of mesh refinement or convergence of the solutions from the stress analyses. The results are shown in Figure 6 where it can be seen that mesh sizes less than 1 mm provided convergent solutions. The finite element analysis was checked against previous results for the rubber considered in [11] and was in close agreement.

The variation of the J-integral with crack length as a function of pin diameter and polyurea layer thickness is shown in Figure 7. The anticipated decrease in the values of the J-integral can be seen in both cases. A linear interpolation of the 7 mm strip thickness was also considered (Fig. 7b). It accurately matched the solution for that case and validated the use of



interpolation for accounting for differences in the polyurea layer thickness from specimen to specimen.

#### 4. Results

The results that were obtained from the constitutive modeling of the polyurea are now presented, along with those that were obtained from the cathodic delamination experiments.

##### 4.1. Hyperelastic Behavior

As indicated earlier, the three models of hyperelastic behavior that were considered were the reduced polynomial and those attributed to Ogden and Marlow. A fit of the experimental data for the uniaxial tension test carried out at a strain rate of  $6.0 \times 10^{-3} \text{ s}^{-1}$  is plotted (Fig. 8) along with the behavior of two sets of parameters associated with the reduced polynomial and the Ogden models in addition to the Marlow model. The parameters for the reduced polynomial models of order 3 and 5 were obtained from a built-in fitting routine in ABAQUS and the uniaxial tension data are given in Table 1.

Table 1: Reduced Order Polynomial Models for Polyurea

	$C_{10}$ (MPa)	$C_{20}$ (MPa)	$C_{30}$ (MPa)	$C_{40}$ (MPa)	$C_{50}$ (MPa)
3 <sup>rd</sup> order	1.23	-0.031	0.00052	-	-
5 <sup>th</sup> order	1.846	-0.144	0.00769	-0.000184	1.64363E-06

A similar procedure was adopted for determining the parameters of the Ogden model. The results appear in Table 2 for two and four-term fits.

Table 2: Ogden Models for Polyurea

Model	i	$\mu_i$ (MPa)	$\alpha_i$
2	1	0.00218	6.08
	2	4.90	-1.39
4	1	-21.469	6.2316
	2	4.533	6.193
	3	4.004	-1.167
	4	33.905	-12.482

The responses obtained from the reduced polynomial model were the closest that could be obtained within a five-term approximation. Nonetheless, they were in least agreement with the measured response across all three models. The four-term Ogden model performed much better than the two-term one and in fact provided an excellent representation of uniaxial tension response. Nonetheless the four term representation was extremely sensitive to slight changes in the  $\alpha_i$  exponents. The Marlow model provided an excellent fit.

The next step was to examine the performance of all the models against the data obtained from the plane strain compression tests (Fig. 9) at a nominal strain rate of  $9.17 \times 10^{-5} \text{ s}^{-1}$ , which was the lowest rate considered. There are two parts to Figure 9: The first is a two dimensional analysis of the plane strain compression test with the principal stretches  $\lambda_1 = \lambda$ ,  $\lambda_2 = \frac{1}{\lambda}$  and  $\lambda_3 = 1$  that were used in the analyses in Section 3. The engineering stresses for each of the material models were given by Equations (3.6, 3.9 and 3.13). In ABAQUS, this set of conditions is known as “planar compression”. The analytical results are compared (Fig. 9a) with the data and numerical results for each material model. Within each material, the results were all self-consistent with the slight exception of the four-term Ogden model. However, none of the results were in agreement with the measurements, suggesting that three-dimensional effects might be responsible. Such effects had been noted in plane strain compression testing of epoxy [21]. Accordingly a fully three-dimensional analysis of the experimental configuration was conducted. Under these conditions (Fig. 9b), the Marlow model provided the best agreement with the measured response. The ordering of the responses of the other material models was the same as it was under the two-dimensional analysis. It was interesting to note that, although the four-term Ogden model performed well at small strains, it was unable to match the measured response more closely than the two-term one.

#### **4.2. Time Dependent Behavior**

The time dependent behavior of the polyurea was considered under uniaxial tension. The basis of the model was the hyperelastic Marlow model just considered and the data at a strain rate of  $1.7 \times 10^{-4} \text{ s}^{-1}$ , which defined the long-term elastic modulus for viscoelastic effects. As indicated in the section on analysis, the time dependence was added as a scaling factor to the hyperelastic model, based on a nine-term Prony series representation (Table 3) of the relaxation function (Fig. 10a) that had been obtained at small strains [27].

The response to ramp loading under uniaxial tension is compared (Fig. 10b) with data obtained in this and another study [28]. The agreement with data was reasonable up to a strain rate of  $0.15 \text{ s}^{-1}$ . At  $14 \text{ s}^{-1}$  the results from the analysis were 25% lower than the measurements from 0.5 to 1.5 strain, otherwise they were in reasonable agreement.

Table 3: Parameters of the nine-term Prony series for polyurea

$\overline{g}_k^P$	$\tau_k$ (s)
0.94059	1.49E-06
1.31E-02	2.93E-05
1.01E-02	2.79E-04
7.62E-03	3.02E-03
5.69E-03	3.77E-02
4.17E-03	0.55586
3.01E-03	10.035
2.13E-03	236.29
1.43E-03	7521

One concern in conducting the strip blister tests was that any rate dependence in the polyurea would affect the cathodic delamination data if the relaxation of the polyurea was taking place in the time scale of the delamination experiment itself. A stress analysis was therefore conducted to examine the relaxation process. The von Mises stresses in the polyurea near the crack front, at the middle of the crack and just above the dowel pin are shown in Figure 11. This selection of locations contrasts regions undergoing different local strain rates as the dowel pin is inserted. The stresses relaxed at all three locations, most notably near the crack front where the relaxation was from 9 to 6 MPa from three hours to 6 days after insertion of the pin. This represents a 33% relaxation of the stresses and justified our test protocol allowing at least three hours of relaxation before placing the specimens in the artificial seawater environment. In fact the specimens were usually allowed to relax for more than 12 hours and the error on the J-integral was even lower.

#### 4.3. Cathodic Delamination

The results of the cathodic delamination tests are now presented for the 2h and 4h interfaces and several temperatures. Following insertion of the dowel pin under ambient conditions, the starter crack often grew and then arrested prior to placing the specimen in the artificial seawater environment. The arrested crack length was measured and, coupled with results in Figure 7b, provided an estimate of the dry toughness of the two interfaces. The values are presented in Figure 12. While there was some variability to the results, the toughness of the specimens whose primers were cured for two hours was consistently higher. The average



toughness in that case was  $2.1 \text{ kJ/m}^2$  as opposed to  $1.3 \text{ kJ/m}^2$  for primers that were cured for four hours.

The cathodic delamination tests for the specimens with primers that were cured for two hours were conducted at 21, 25, 30 and  $34^\circ\text{C}$ . The crack growth histories are shown in Figure 13a. Increasing temperature clearly accelerated the cathodic delamination and increased its extent prior to crack arrest. Interestingly, it was not possible to observe any delamination at  $21^\circ\text{C}$  over the three-day time span of these tests. The specimens with primers that had been cured for four hours were tested at 21, 25 and  $30^\circ\text{C}$ . There was delamination (Fig. 13b) at all three temperatures; increasing temperature had a similar effect as before and the amount of delamination was much larger. Least squares fits of the delamination growth histories to a power law of the form  $a = a_0 + t^n$  are also presented in Figure 13. The derivatives of these fits were used to determine the crack growth rates that appear in the delamination resistance curves (Fig. 14).

The curves representing the resistance to cathodic delamination in each case all exhibited the classic sigmoidal shape that is associated with environmentally assisted crack growth except that there was not much of a plateau region where delamination rates are independent of J-integral value and delamination growth is controlled by transport phenomena such as surface diffusion, often depending on the viscosity of the environmental species. The room temperature toughness values for the two and four-hour cured primer are shown as asymptotes to the cathodic delamination data. In all the cases that were considered, there was clear evidence of threshold behavior where delaminations arrest and establish the J-integral levels that are required to cause cathodic delamination. There was a clear discrimination in threshold levels of J-integral between curing the primer for two and four hours; the reduction in threshold values was more than half, emphasizing why the two-hour cure is the recommended one. The threshold values are summarized in Figure 15, where it can be seen that increasing the temperature consistently reduced them for both interfaces. Attempts were made to fit the data to the Arrhenius expression, but the results were inconclusive and would require more temperature levels to be considered.

Finally, a series of experiments were conducted on samples without any primer so that the bonding between the polyurea and the steel was just the intrinsic adhesion between the two materials. The resistance to cathodic delamination is shown in Figure 16 for two temperature levels. The most striking feature of the data is that the delamination rates for a given surface and temperature were independent of the J-integral value over the entire range that was considered, suggesting that delamination growth was completely controlled by transport phenomena such as interfacial diffusion. There was no threshold like behavior and the dry toughness of the interfaces was  $382 \text{ J/m}^2$ , forming a consistent upper bound for the delamination resistance curves. The data at  $23^\circ\text{C}$  was quite consistent for both surfaces. There was more variability from surface to surface in the specimens that were tested at  $30^\circ\text{C}$ , but the delamination rates were all higher than at  $23^\circ\text{C}$ . The effect of pin diameter was

already incorporated through the J-integral so all the notation does is to indicate that it was a different specimen. The delamination rates in both cases were more than a factor of 10 higher than the highest values that were experienced with the primer (Fig. 14) at J-integral levels that were generally lower. Thus the primer clearly had a beneficial effect and the mechanism of delamination growth appeared to be different with and without the primer.

## **5. Conclusions**

A fracture mechanics approach to accelerated life testing of cathodic delamination between steel and polyurea has been demonstrated. A Marlow model of hyperelastic behavior of the polyurea was the best of the models that were evaluated in uniaxial tension and plane strain compression. Time-dependence was incorporated via a relaxation function that had been determined previously under small strains. The variation of J-integral with polyurea thickness and dowel pin diameter was obtained for a range of conditions and allowed the resistance to cathodic delamination to be expressed in terms of crack speed and J-integral. The approach established that both temperature and stress can be used to accelerate the cathodic delamination, thereby providing a quantitative and rational basis for conducting accelerated testing as well as evaluating new surface treatments.

## **Acknowledgements**

This work was performed under a program entitled "Characterization of Nonlinear Viscoelastic and Adhesive Properties of Polyurea and Characterization of Polyurea-clad Metallic Structures" sponsored by the Office of Naval Research (ONR Grant Number N00014-06-1-0644, Program Manager: Dr. Roshdy Barsoum); this support is gratefully acknowledged. The authors would also like to thank John Bulluck of Texas Research International for the assistance that was provided in fabricating the cathodic delamination specimens.

## Figures

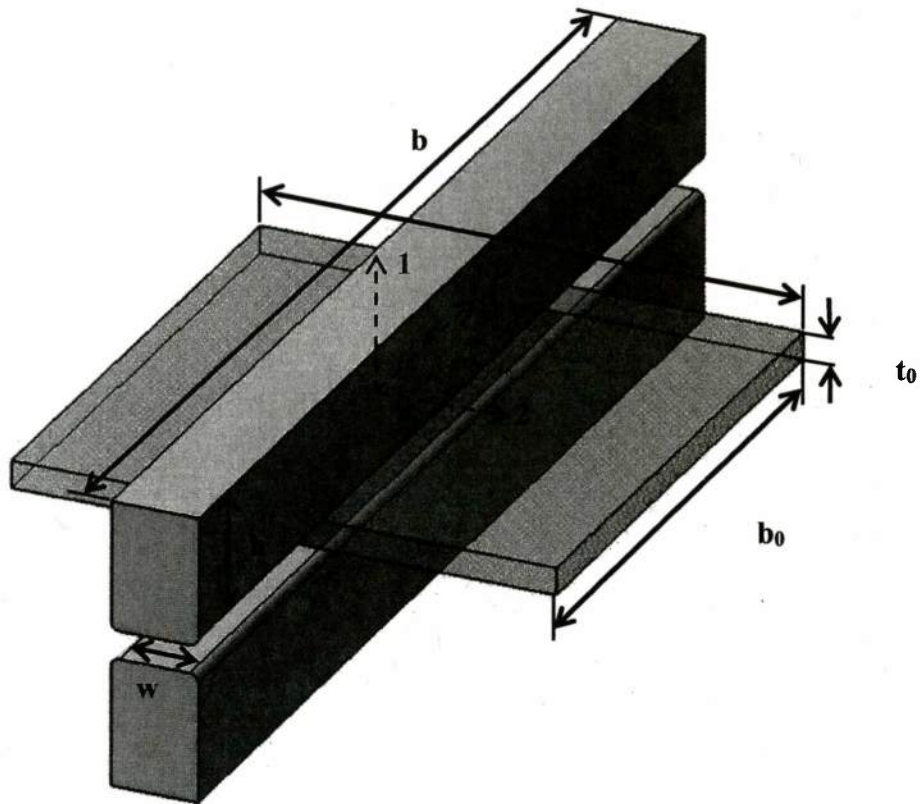


Figure 1: A schematic of the plane strain compression test and specimen. The dimensions were  $L_0 = 7.8$ ,  $b_0 = 7.8$ ,  $t_0 = 0.44$  and  $w = 1.0$  cm.



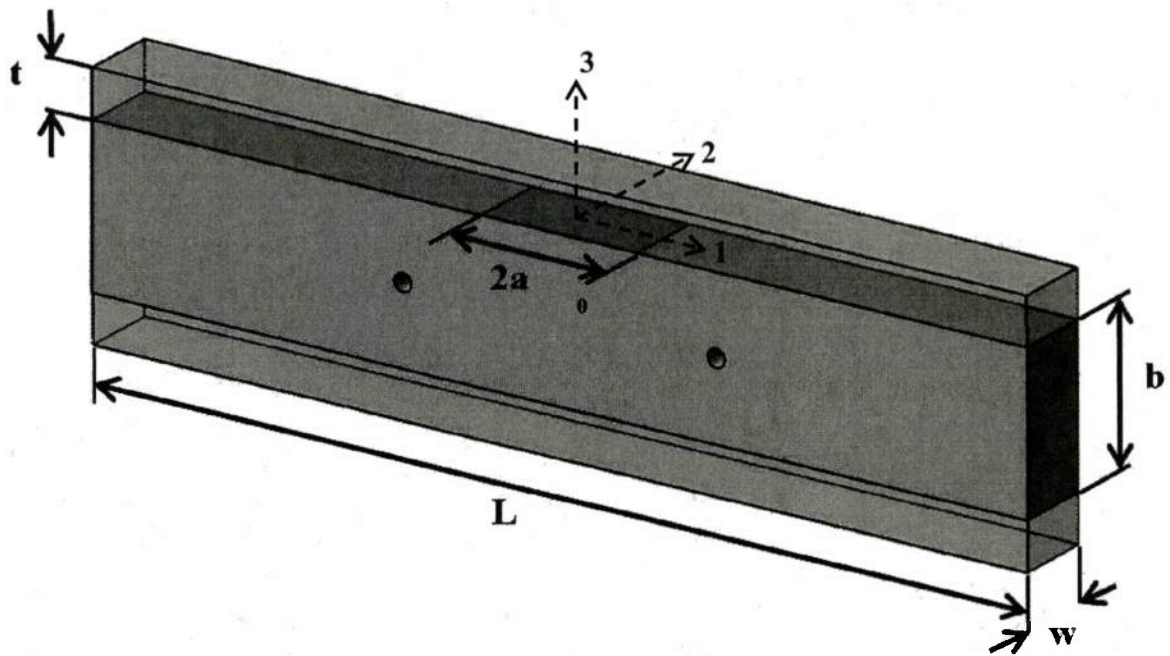


Figure 2: A schematic of the strip blister specimen with layers of polyurea bonded to steel with a primer PR-420. The dimensions were  $L=11.5$ ,  $w=1.27$ ,  $b=2.54$ ,  $t=0.76$  and  $2a=2.54$  cm.

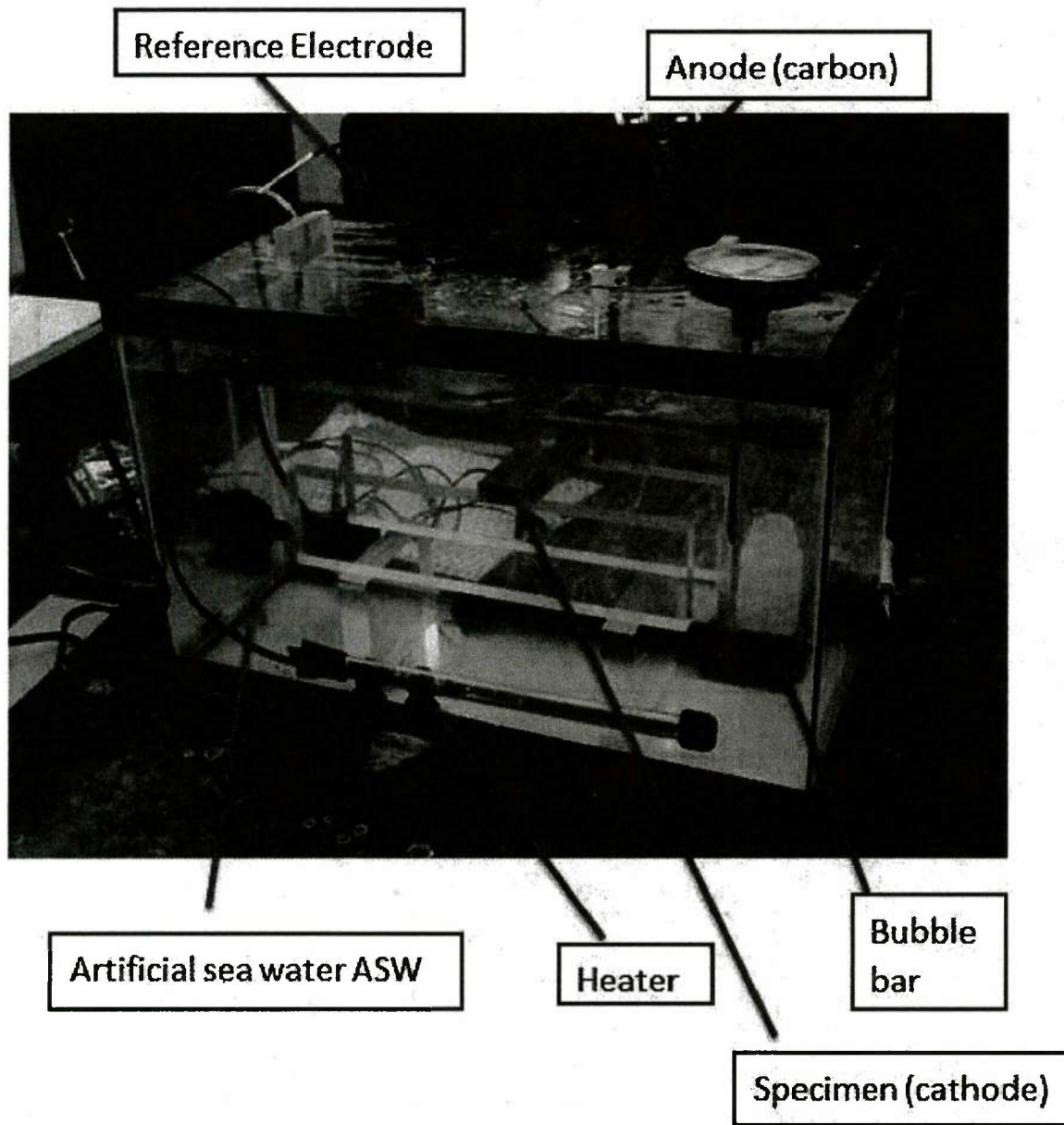
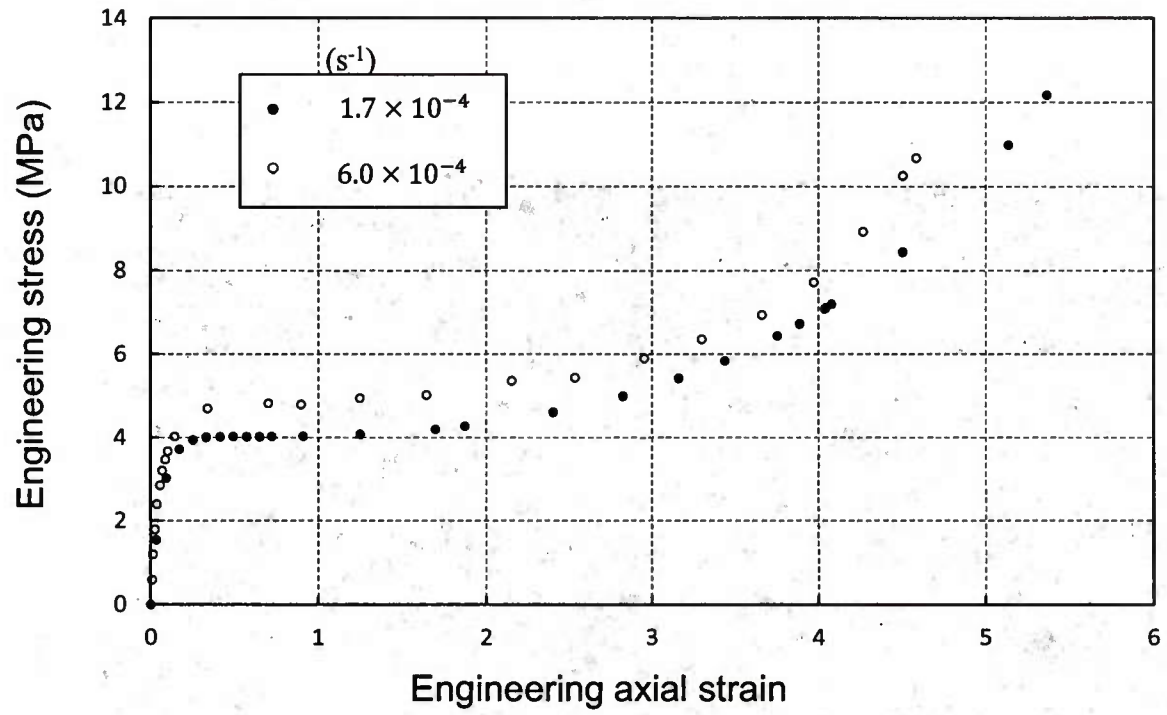
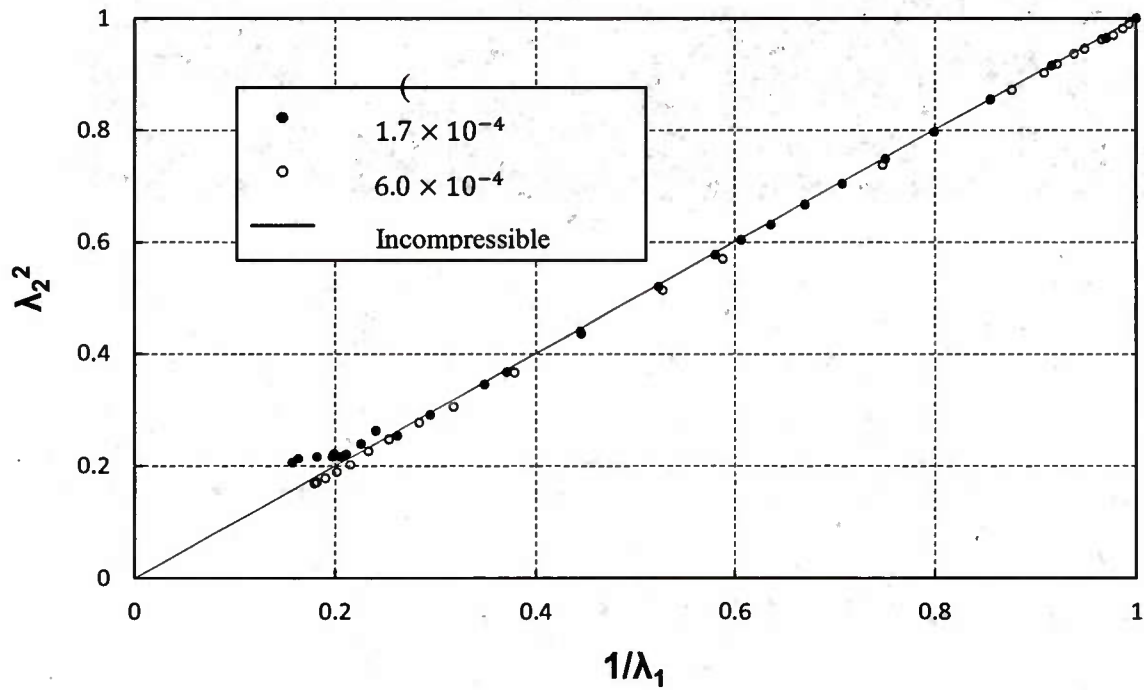


Figure 3: The apparatus for the cathodic delamination experiment.



(a)



(b)

Figure 4: The basic (a) engineering stress-strain response of the polyurea and (b) the transverse-axial stretch response, demonstrating incompressibility.



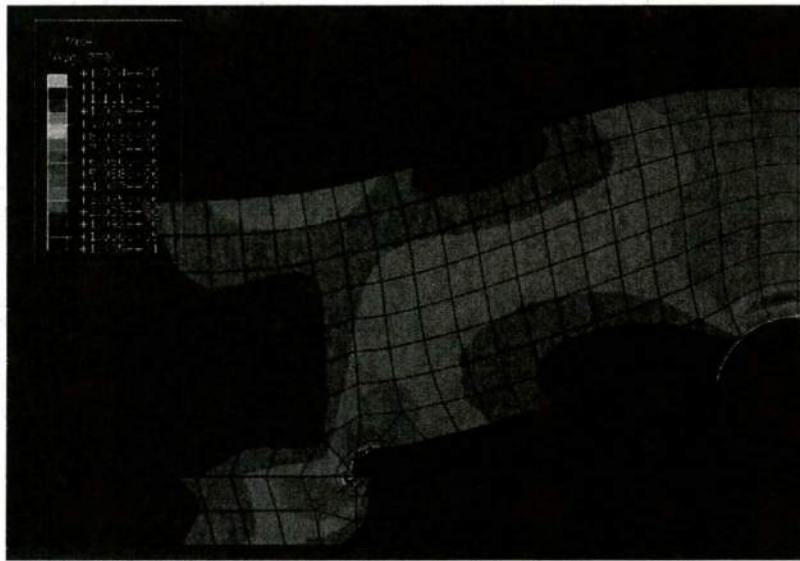


Figure 5: Deformed shape of a strip blister specimen with a dowel inserted. The distribution of Von Mises stress contours is shown.

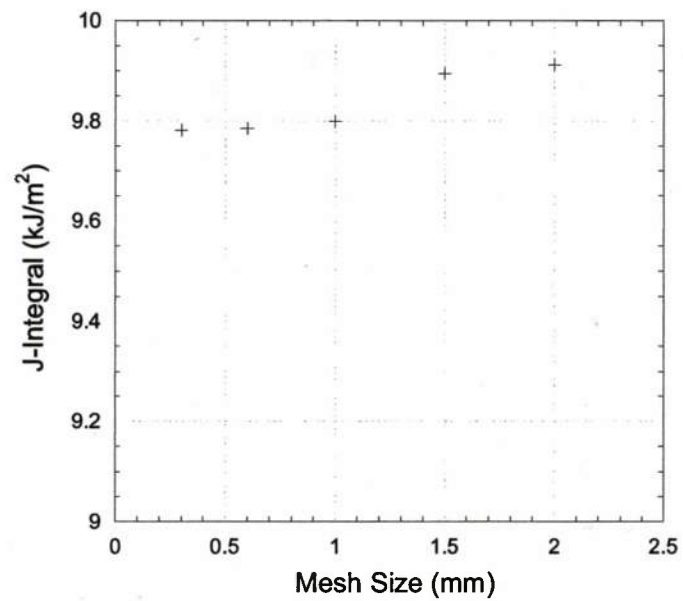
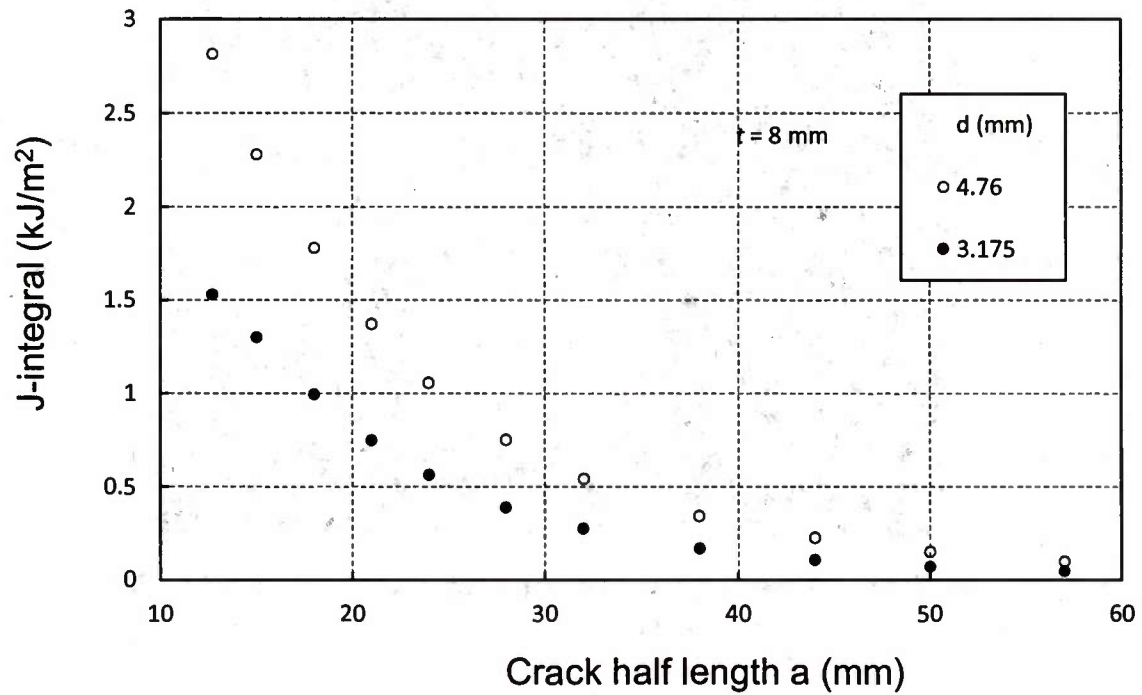
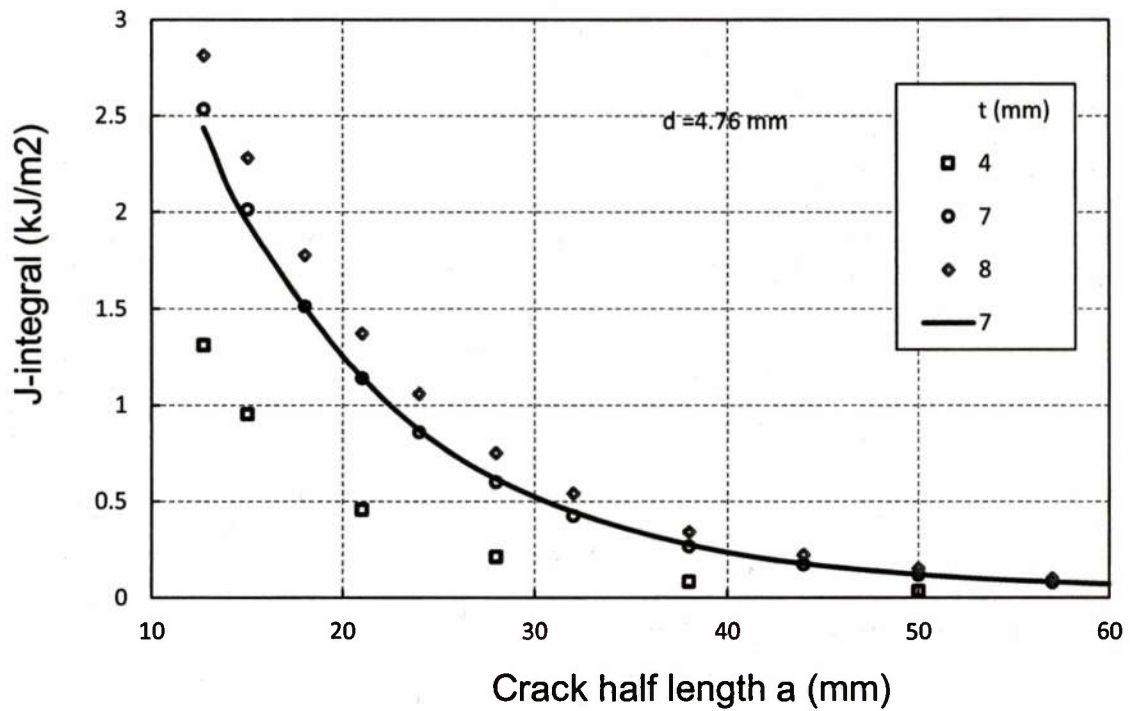


Figure 6: A mesh refinement study based on the J-integral.



(a)



(b)

Figure 7: J-integral solutions for (a) two pin diameters and (b) all strip thicknesses. The continuous curve is a linear interpolation of the result for the 7 mm strip thickness.

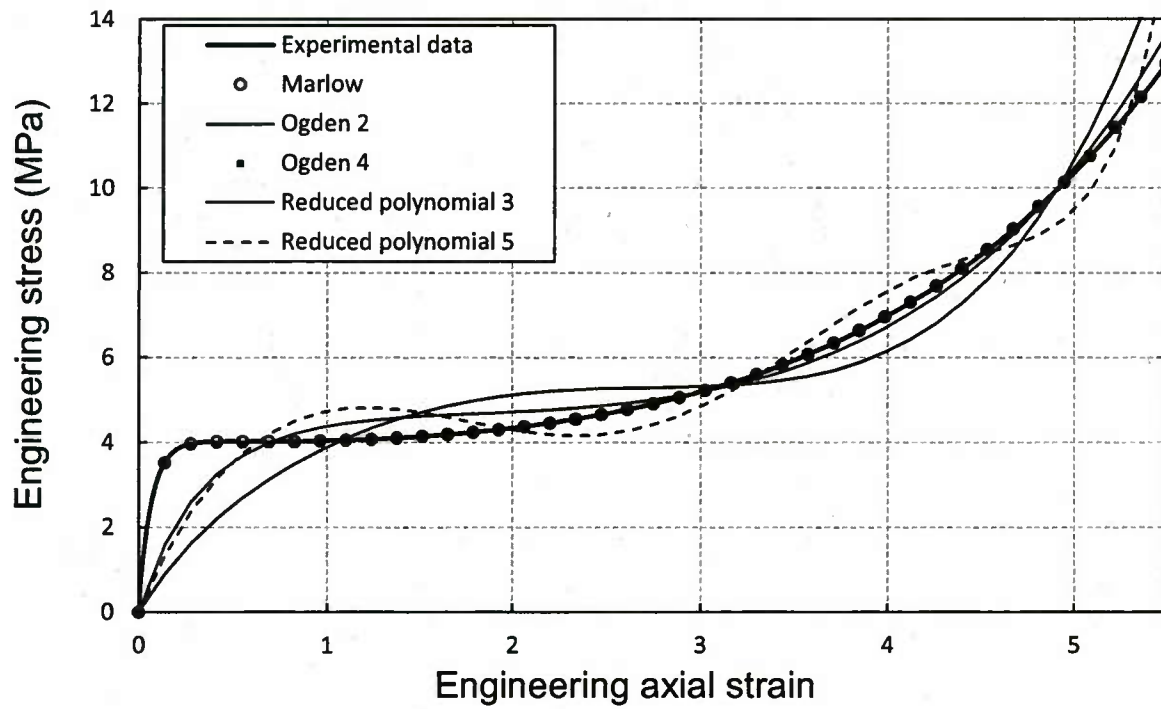
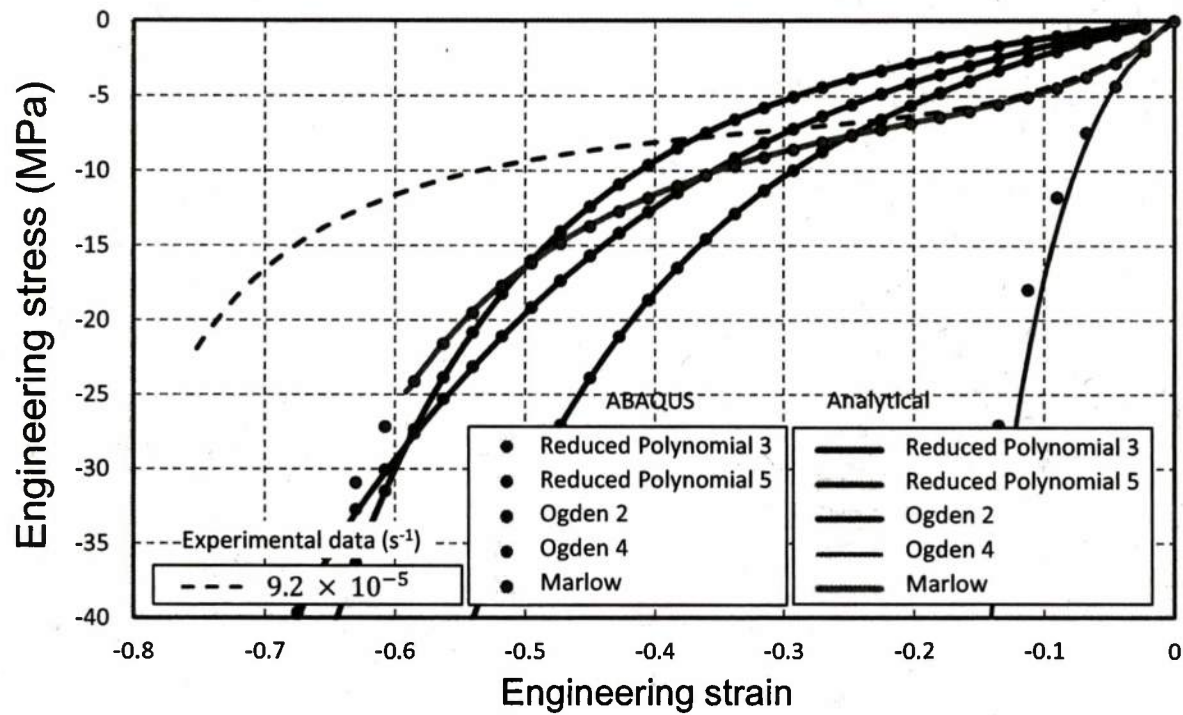
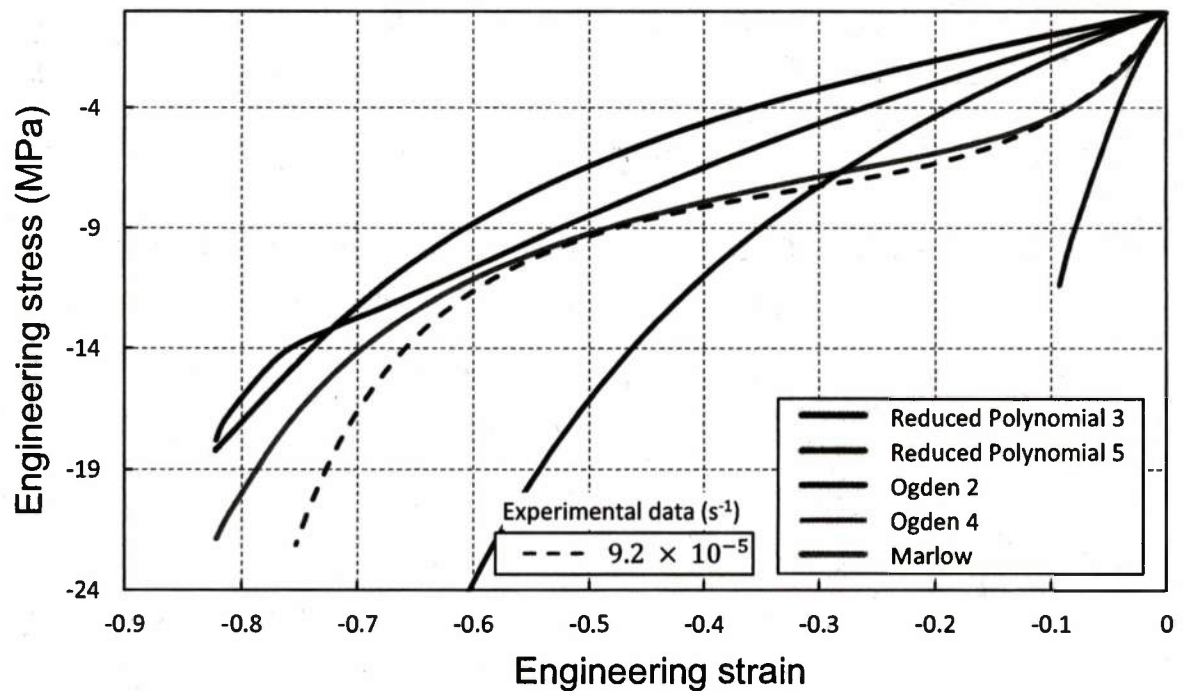


Figure 8: A comparison between the data obtained from a uniaxial tension test on polyurea and the responses obtained from various models of hyper elastic behavior.



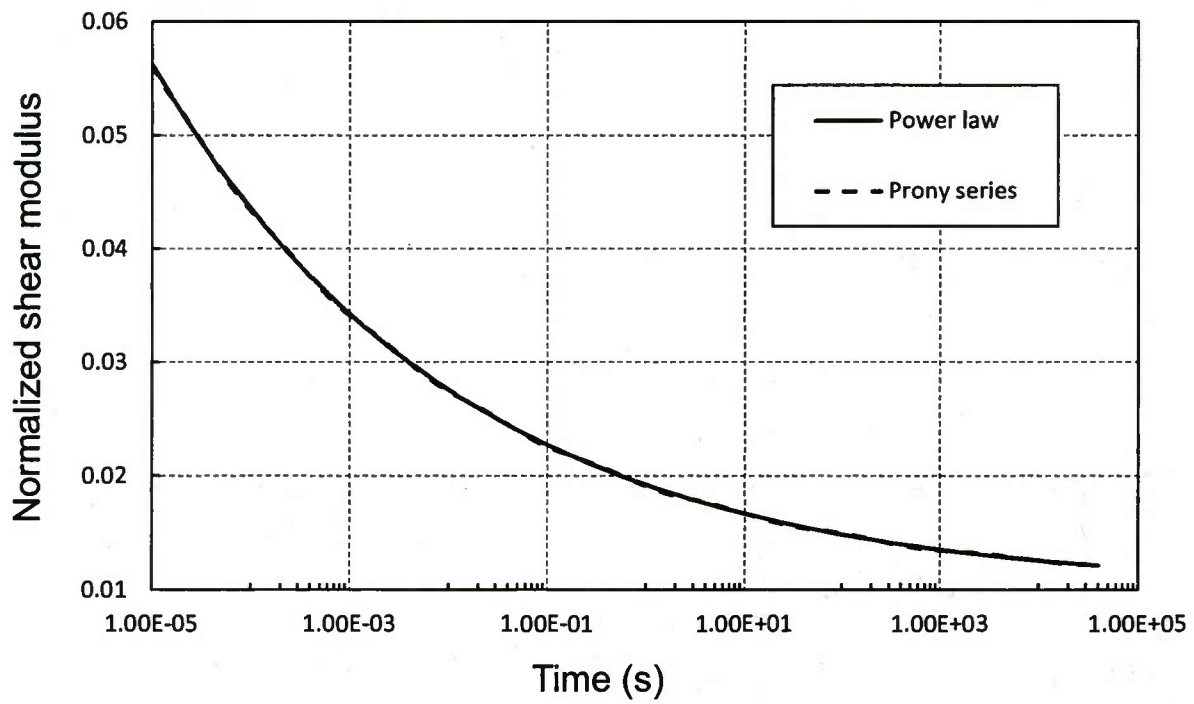


(a)

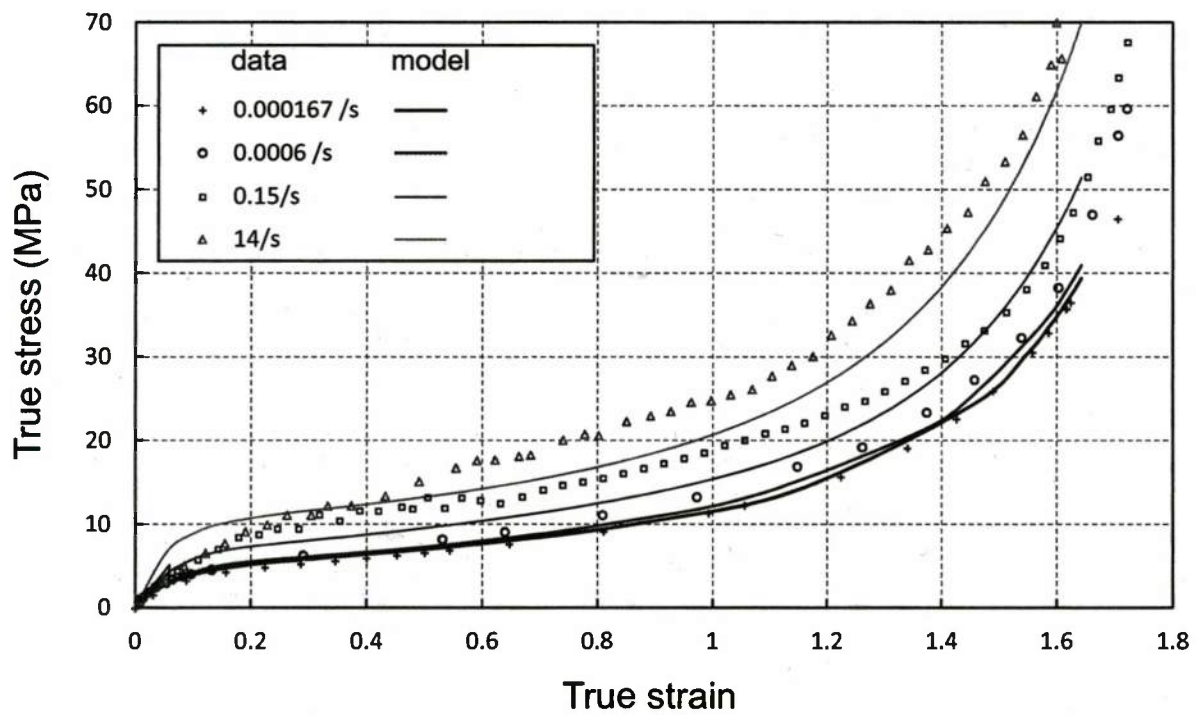


(b)

Figure 9: A comparison between the experimental data and (a) two-dimensional analytical and numerical models of plane strain compression and (b) three-dimensional numerical models.



(a)



(b)

Figure 10: The time dependent behavior of polyurea under uniaxial loading; (a) normalized relaxation function and (b) behavior under ramp loading. The data at the two highest rates is from [28].

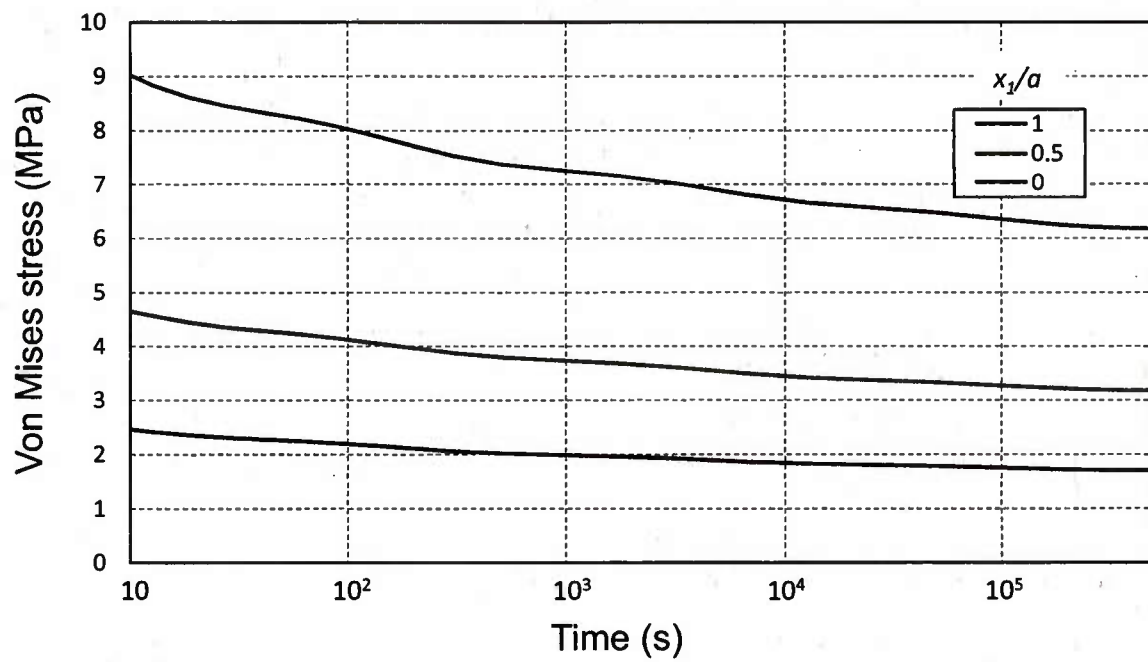


Figure 11: The relaxation behavior of the strip blister specimen at three different locations.



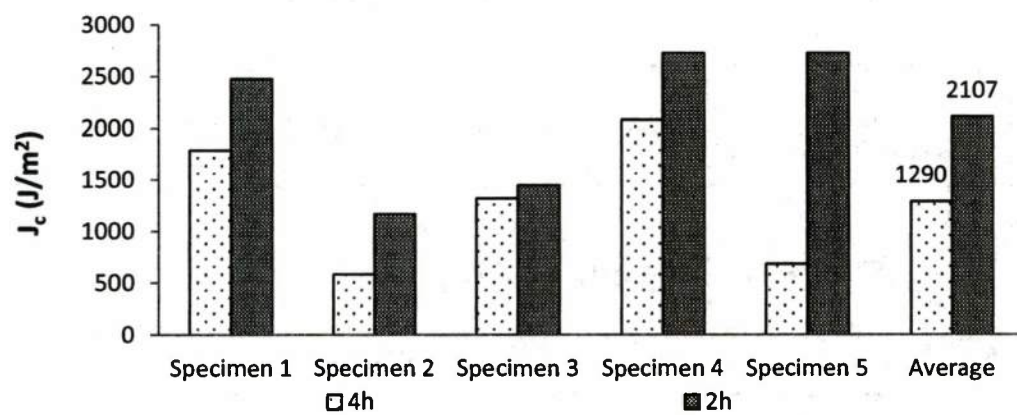
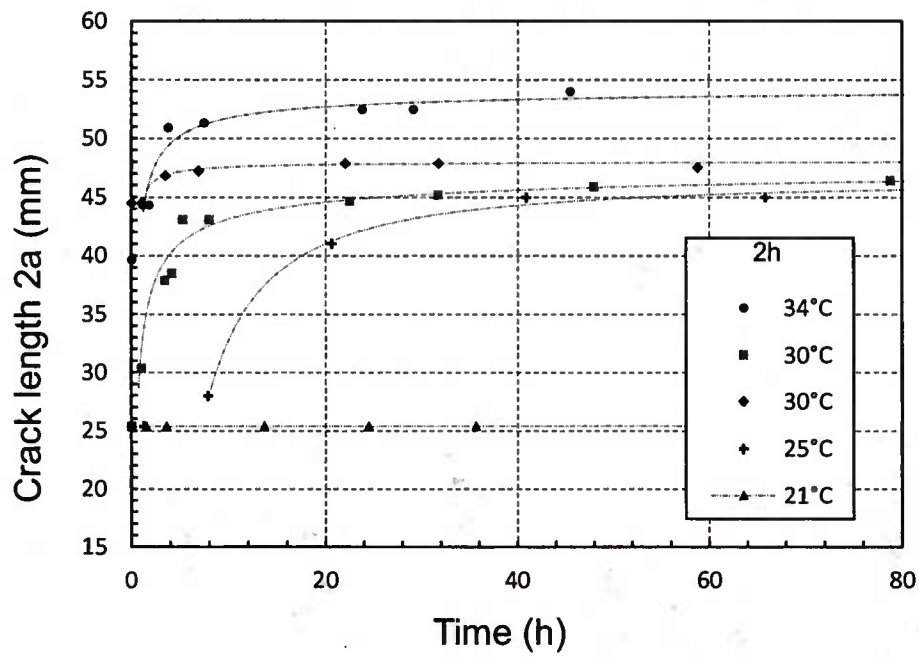
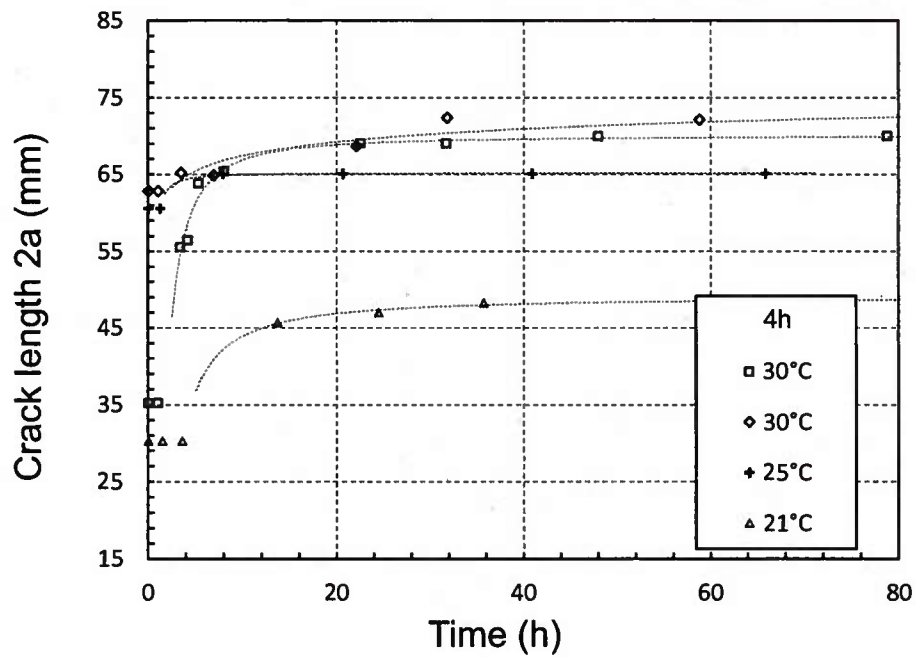


Figure 12: The dry toughness of several specimens whose PR 420 primers were cured for either 2 or 4 hours.



(a)



(b)

Figure 13: Crack growth history for the polyurea/steel strip blister. The PR420 had been allowed to cure (a) for 2 hours and (b) 4 hours before applying the polyurea.

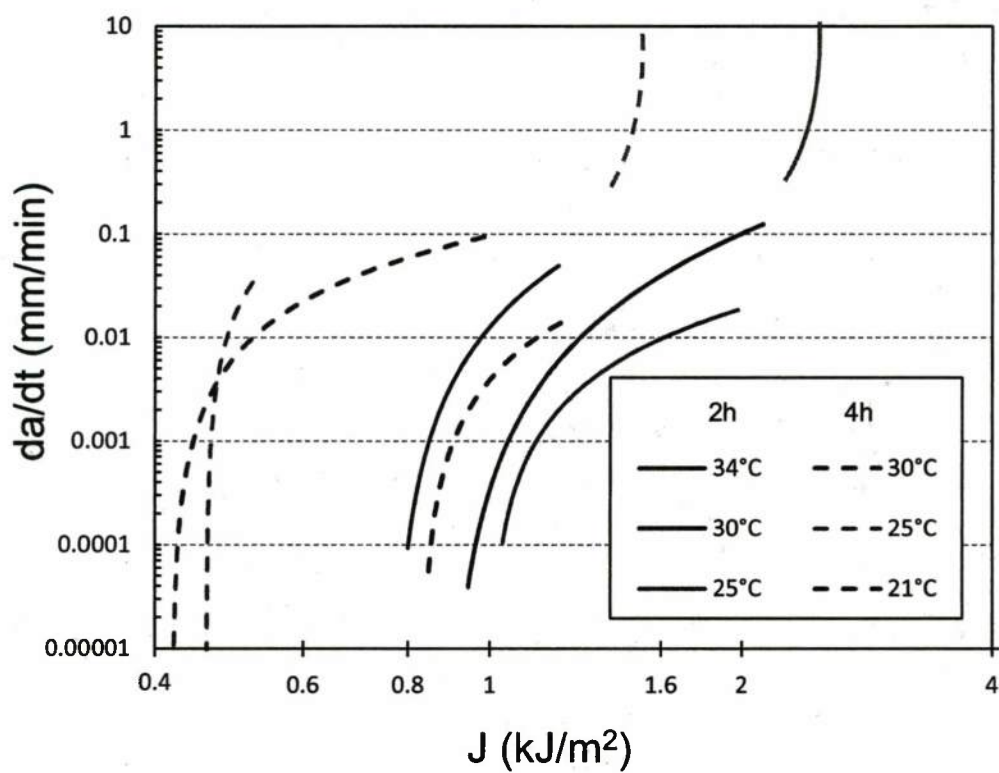


Figure 14: Resistance to cathodic delamination of a steel/polyurea interface in artificial seawater at  $-0.9$  volts relative to the standard calomel electrode.



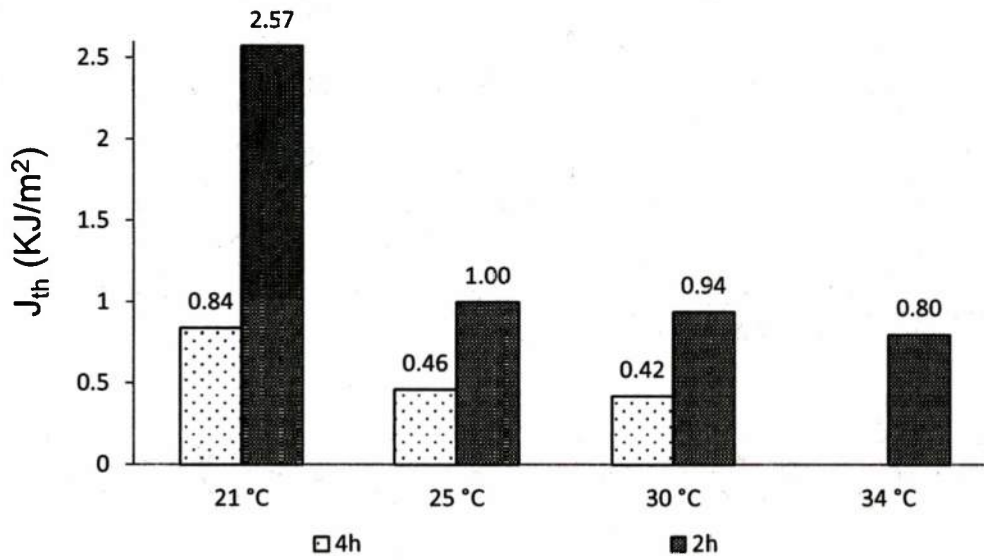


Figure 15: A summary of threshold values of J-integral for two and four-hour curing of PR420.

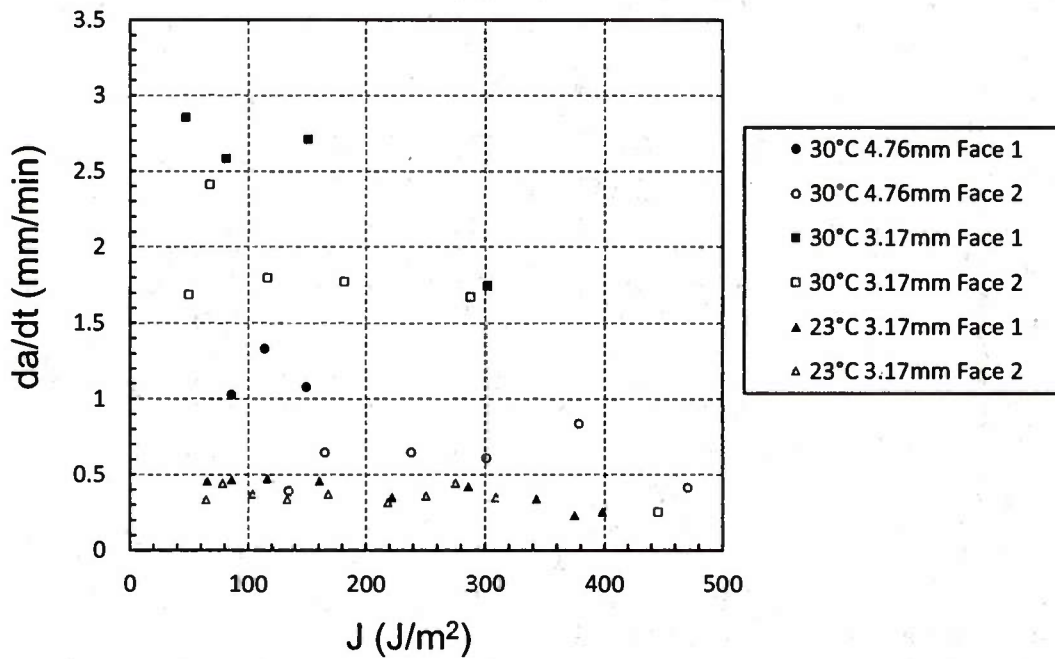


Figure 16: Resistance to cathodic delamination of a steel/polyurea interface without primer in artificial seawater at -0.9 volts relative to the standard calomel electrode.

## References

1. Leidheiser, H. and W. Wang, *Some substrate and environmental influences on the cathodic delamination of organic coatings*. Journal of Coatings Technology, 1981. **53**: p. 77-84.
2. Koehler, E.L., *The mechanism of cathodic disbondment of protective organic coatings - aqueous displacement at elevated pH*. Corrosion, 1984. **40**: p. 5-8
3. Watts, J.F. and J.E. Castle, *The application of X-ray photoelectron spectroscopy to the study of polymer-to-metal adhesion: Part 1: Polybutadiene coated mild steel*. Journal of Materials Science 1983. **18**: p. 2987-3003.
4. Watts, J.F. and J.E. Castle, *The application of X-ray photoelectron spectroscopy to the study of polymer-to metal adhesion: Part 2: The cathodic disbandment of epoxy coated mild steel*. Journal of Materials Science 1984. **19**: p. 2259-2272.
5. Dickie, R.A., J.S. Hammond, and J.W. Holubka, *Interfacial chemistry of the corrosion of polybutadiene-coated steel*. Ind. Eng. Chem. Prod. Res, 1981. **20**: p. 339-343.
6. Holubka, J.W., J.S. Hammond, J.E. DeVries, and R.A. Dickie, *Surface analysis of interfacial chemistry in corrosion-induced paint loss adhesion*. Journal of Coatings Technology, 1980. **52**: p. 63-68.
7. Stevenson, A., *The effect of electrochemical potentials on the durability of rubber metal bonds in sea-water*. Journal of Adhesion, 1987. **21**: p. 313-327.
8. Boerio, F.J., S.J. Hudak, M.A. Miller, and S.G. Hong, *Cathodic debonding of neoprene from steel*. The Journal of Adhesion, 1987. **23**(2): p. 99 - 114.
9. Boerio, F.J. and S.G. Hong, *Degradation of rubber-to-metal bonds during simulated cathodic delamination*. Journal of Adhesion, 1989. **30**(1-4): p. 119-134.
10. Kozinski, S.E. and F.J. Boerio, *Effect of an aminosilane on the cathodic delamination of adhesive bonds between neoprene and steel*. Journal of Adhesion Science and Technology, 1990. **4**(2): p. 131-143.
11. Liechti, K.M., E.B. Becker, C. Lin, and T.H. Miller, *A fracture-analysis of cathodic delamination in rubber to metal bonds*. International Journal of Fracture, 1989. **39**(1-3): p. 217-234.
12. Wang, W. and H. Leidheiser, *A mathematical-model for the cathodic delamination of organic coatings*. Abstracts of Papers of the American Chemical Society, 1984. **188**(AUG): p. 30-INDE.
13. Hamadeh, R.F., D.A. Dillard, K.M. Liechti, and J.S. Thornton, *A mechanistic evaluation of cathodic debonding of elastomer to metal bonds*. Journal Adhesion Science and Technology, 1989. **3**: p. 421-440.
14. Liechti, K.M. and W. Adamjee, *Mixed-mode cathodic delamination of rubber from steel*. Journal of Adhesion, 1992. **40**(1): p. 27-45.
15. Hamade, R.F. and D.A. Dillard, *Cathodic weakening of elastomer-to-metal adhesive bonds: accelerated testing and modeling*. Journal of Adhesion Science and Technology, 2003. **17**(9): p. 1235-1264.
16. Hamade, R.F. and D.A. Dillard, *Assessing the effects of shear, compression, and peel on the cathodic degradation of elastomer-to-metal adhesive bonds*. International Journal of Adhesion and Adhesives, 2005. **25**(2): p. 147-163.

17. Hamade, R.F., C.Y. Seif, and D.A. Dillard, *Cathodic delamination of elastomer-to-metal adhesive joints: Experimental data and empirical modeling*. International Journal of Adhesion and Adhesives, 2007. **27**(2): p. 108-121.
18. Hamade, R.F., C.Y. Seif, F. Merhij, and D.A. Dillard, *A semi-empirical model for the cathodic delamination of elastomer-to-metal adhesive joints*. Journal of Adhesion Science and Technology, 2008. **22**(7): p. 775-793.
19. Zhu, Y., K.M. Liechti, and K. Ravi-Chandar, *Direct extraction of rate-dependent traction-separation laws for polyurea/steel interfaces*. International Journal of Solids and Structures, 2009. **46**(1): p. 31-51.
20. Xue, L., W. Mock Jr, and T. Belytschko, *Penetration of DH-36 steel plates with and without polyurea coating*. Mechanics of Materials. **42**(11): p. 981-1003.
21. Liang, Y.-M. and K.M. Liechti, *On the large deformation and localization behavior of an epoxy resin under multiaxial stress states*. International Journal of Solids Structures, 1996. **33**(10): p. 1479-1500.
22. Dieter, G.E., H.A. Kuhn, and S.L. Semiatin, *Handbook of Workability and Process Design*. 2003, Ohio: American Society for Metals (ASM) International^2266
23. *Seawater*. 2012, Petco.
24. Yeoh, O.H., *Some forms of the strain energy function for rubber*. Rubber Chemistry and Technology, 1993. **66**(5): p. 754-771.
25. Ogden, R.W. *Large deformation isotropic elasticity - on the correlation of theory and experiment for incompressible rubberlike solids*. in *Proceedings of the Royal Society of London*. 1972.
26. Marlow, R.S. *A general first-invariant hyperelastic constitutive model*. in *Constitutive Models for Rubber III: proceedings of the Third European Conference on Constitutive Models for Rubber*. 2003. London: Taylor & Francis.
27. Chevillard, G., K. Ravi-Chandar, and K. Liechti, *Modeling the nonlinear viscoelastic behavior of polyurea using a distortion modified free volume approach*. Mechanics of Time-Dependent Materials, 2010: p. 1-23.
28. Roland, C.M., J.N. Twigg, Y. Vu, and P.H. Mott, *High strain rate mechanical behavior of polyurea*. Polymer, 2007. **48**(2): p. 574-578.



## APPENDIX D

### Characterization of the transient response of polyurea

A.B. Albrecht and K. Ravi-Chandar

*Experimental Mechanics*, **53**, 113-122.

# Characterization of the Transient Response of Polyurea

A.B. Albrecht · K.M. Liechti · K. Ravi-Chandar

Received: 22 April 2012 / Accepted: 30 July 2012 / Published online: 6 September 2012  
© Society for Experimental Mechanics 2012

**Abstract** The strain-rate dependent tensile response of a transparent elastomer, polyurea, is determined at stretch-rates in the range of 800 to 8000 per second. This is accomplished by measuring the spatio-temporal evolution of the particle velocity and strain in a thin strip subjected to high speed impact loading that generates uniaxial stress conditions. The observed response is modeled using a modified viscoplastic constitutive relation.

**Keywords** Impact · Nonlinear waves · Viscoplasticity

## Introduction

Blast protection has become an important problem in many military and civilian structures. There has been a large effort devoted to improving the blast resistance of metallic structural components by coating them with a layer of a compliant polymer, such as polyurea; this coating decreases the propensity of the metallic structure to fracture and fragment [1, 2]. This observation has spawned a large number of research efforts aimed at understanding and optimizing the additional impact resistance provided by such polymer-coated metal structures. A similar problem arises in transparent armor applications as well; transparency to visible and other wavelengths is essential in many applications and these transparent “ports” need to be protected against foreign object impact as well. There have been numerous studies of the dynamic failure behavior of ceramics used as transparent armor (see, for example [3, 4, 5]). Glass, laminated with alternating layers of polymers of varying thickness and fracture properties, is

also a very commonly used as transparent armor [6]. The fracture behavior of glass is rather well understood after nearly a century of investigations; however, the design of these multilayered structures, and characterization of their performance, requires experimental measurements of the properties of individual constituents of the multilayer system. In particular, while glass can be characterized as an elastic-brittle material, the rate-dependent material properties of the polymer interlayers must be characterized in order to analyze their response to high strain-rate loading; in this article, we consider the characterization of the dynamic tensile response of a transparent elastomer, polyurea. The methods, however, are quite general and are applicable for the determination of the tensile response of any material.

The split-Hopkinson bar apparatus has evolved into the most common method for dynamic material characterization (see for example, [7]); it uses a small sample in order to establish a uniform stress and strain state in the specimen, avoids detailed analysis of wave propagation through the specimen material, and therefore eliminates the need for *a priori* knowledge of the material behavior. However, the assumption of uniformity of the stress and deformation within the specimen is rather severe and limits the applicability of this technique to a certain class of materials and certain strain rates. For tension testing, the specimens are usually quite small and the strain rates obtained are typically in the range of about  $10^2$ – $10^3$  s<sup>-1</sup>; the technique is better suited for compression characterization, with strain rates reaching nearly  $10^4$  s<sup>-1</sup>. The measurement of strain-rate dependent tensile behavior of soft materials with a Hopkinson bar, particularly for large stretch levels, is fraught with difficulties; in addition to the problems arising from impedance mismatch with the loading bars that causes a very low signal to noise ratio, lateral inertia effects in the specimen and the general nonhomogeneity of the stress and deformation in this test scheme provide very restrictive conditions

A.B. Albrecht · K.M. Liechti · K. Ravi-Chandar (✉)  
Center for Mechanics of Solids, Structures and Materials,  
The University of Texas at Austin,  
Austin, TX, USA  
e-mail: ravi@utexas.edu

under which the split Hopkinson bar may be used in tension. Furthermore, for applications in many soft materials, very large stretch levels are encountered; this necessitates long duration pulses – for example, to reach a stretch of two at a strain rate of  $10^3 \text{ s}^{-1}$  a pulse duration of 2 ms is required! Recently, Youssef and Gupta [8] have developed a laser ablation based method for characterizing the high strain rate response of polyurea; in this method, the propagation of a short-duration stress pulse through the specimen is used to back out the stress strain curve at strain rates on the order of  $10^5 \text{ s}^{-1}$ ; however, due to the short duration of the loading, the peak strains attained are in the range of 2 % Youssef and Gupta [8] were able to use this method to probe the linearly elastic and viscoelastic response of polyurea.

We suggest that any test method designed to investigate the dynamic constitutive behavior of soft materials at large strain-rates to very large strain levels must deal with transient states in a hybrid or inverse approach; such an approach places no restrictions on specimen length and it is not necessary to establish uniformity of stress state or strain-rate; in addition, there is no limit to the strain level that can be attained in the test specimen. In fact, the method is quite general and could be used for any material without restrictions. This approach is explored in the present work.

This article is organized as follows. The method of manufacturing the material and the quasistatic material property of the elastomer used in this study, polyurea, are described in “Polyurea” section. The theory of nonlinear wave propagation is summarized in “Nonlinear Waves” section with the primary aim of discussing the measurements that are needed in order to characterize the material. The experimental technique is described in detail in “Experimental Technique” section. The inverse/hybrid method of extraction of the strain-rate dependent constitutive properties of the material is presented in “Results” section.

## Polyurea

Polyurea is a common elastomer that is currently being used to coat surfaces in a wide range of applications. The use of polyurea in such applications is driven by its chemical and abrasion resistance under many different environments, ease of application by spray coating, and its transparency. The name polyurea does not refer to a single chemical compound but rather to any combination of an isocyanate and a synthetic resin as long as they react to form urea linkages; therefore, there are many different formulations of polyurea used in practice. The polyurea used in the present work is formed by reaction of Isonate 143L (Dow Chemical) and Versalink P1000 (Air Products) with weight ratio of 1:4. The Versalink was first degassed at 30 °C in a vacuum of ~1 torr for 30 min with continuous stirring (typically until no bubbles were observed);

the Isonate was similarly degassed. The degassed Isonate and Versalink were mixed in a 1:4 weight ratio under vacuum for two minutes; this mixture was then vented and poured quickly onto a large steel plate to which mold release has been applied. The plate is then passed under a blade fixed approximately 1.5 mm above the surface. This process spreads the polyurea into a film of uniform thickness. The film is then allowed to cure for 7 days; the polyurea is then peeled off the plate as a single sheet and sliced into long thin strips to be used in the dynamic tension experiments. These strips are typically about 350 mm long with cross sectional dimensions of  $1.40 \pm 0.05$  mm thickness and  $5.00 \pm 0.10$  mm width.

A typical quasi-static tensile response of polyurea is shown in Fig. 1, where the nominal stress,  $\sigma$  (force per original area) is plotted against the engineering strain,  $\gamma = l/l_0 - 1 = \lambda - 1$  ( $\lambda$ , the ratio of the current length to the original length, is the stretch). This test was performed using one of the specimens from the same batch of specimens used for dynamic tensile characterization, performed at 25 °C at a strain rate of  $10^{-1} \text{ s}^{-1}$ . Repeat tests on specimens from the same batch indicated very little variability, but the differences from different batches is influenced significantly by small changes in stoichiometry (see [9], for a discussion of this variability). The initial modulus of elasticity is often taken to be around 100 to 200 MPa (see [10–13]) but the measured initial slope in this case was closer to 70 MPa.<sup>1</sup> Beyond a stress level of about ~2 MPa, (corresponding to a strain of ~0.05) the quasi-static stiffness decreases significantly and continuously, and a nonlinear stress-strain response is observed to large strain levels. After a nominal strain of ~0.6 the nominal stress remains nearly constant at about 4.4 MPa. Beyond a stretch of about 3.2, a steep increase in the stress is observed. It has been reported by Roland et al. [9] that the stretch at which this stiffening occurs can be adjusted significantly by altering the stoichiometry.

## Nonlinear Waves

We now turn to the dynamic tension testing of the polyurea described in the previous section. We illustrate the hybrid method of material characterization with a simple one-dimensional boundary-initial value problem to provide some insight as to how such a test could be performed. Consider a long thin strip of the specimen that is fixed at one end with a known velocity history imposed at the other end. This is the classic problem originally considered in the context of plastic wave propagation in metals by von Karman and Duwez [14], with the only difference being in the addition of real-time diagnostics to the measurement scheme. The propagation of the nonlinear wave into the specimen imposes a transient state

<sup>1</sup> In fact, there is never a truly linear region from which a proper elastic modulus can be extracted.



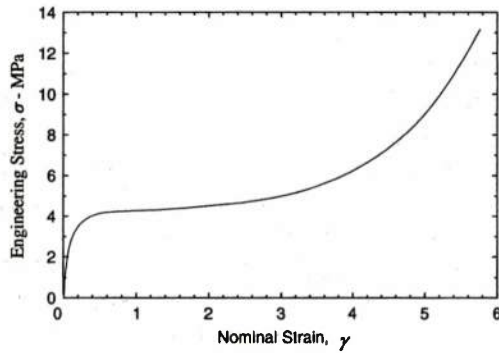


Fig. 1 Quasi-static stress-strain response of polyurea ( $\dot{\gamma} = 0.1 \text{ s}^{-1}$ )

in the specimen with a nonuniform stress, strain, and strain-rate at each material point along the length of the strip, thereby enabling the material behavior to be interrogated under a larger range of loading conditions in one test. Nonlinear one dimensional wave propagation theory provides the tools necessary to analyze this behavior and extract the material behavior through an inverse analysis.

The governing equations for the one dimensional problem are well-developed and are given here for completeness. Consider a one-dimensional semi-infinite strip of the material occupying  $0 \leq x \leq \infty$ , where  $x$  represents the position of a material point in the reference configuration. Assuming that the transverse dimensions of the specimen are small, inertia effects associated with the transverse motion are neglected. Under such conditions, the motion of material points in the strip can be represented by the one kinematic quantity,  $u(x, t)$ , the displacement in the  $x$ -direction; therefore, the current position of the material point  $x$  at any time  $t$  is given by  $y(x, t) = x + u(x, t)$ . The corresponding strain and particle velocity are given by  $\gamma(x, t) = \partial u / \partial x$  and  $v(x, t) = \partial u / \partial t$  respectively. The stretch corresponding to this strain is  $\lambda(x, t) = 1 + \gamma(x, t)$ . The governing equations of motion for this one-dimensional wave problem are obtained from the balance of linear momentum and kinematic compatibility:

$$\frac{\partial \sigma}{\partial x} = \rho \frac{\partial v}{\partial t}, \quad \frac{\partial v}{\partial x} = \frac{\partial \gamma}{\partial t} \quad (1)$$

where  $\rho$  is the mass density per unit volume (assumed to be constant as a result of the material incompressibility) and  $\sigma$  is the nominal stress (force per reference area). At the end  $x=0$  the specimen is subjected to a velocity boundary condition  $v(0, t) = v_0(t)$  in the  $x$ -direction; this generates a tensile wave propagating into the material in the  $x$ -direction. In specimens of finite length, if attention is restricted to short times such that the reflections from the other end of the specimen are not observed, and one establishes a semi-infinite specimen; on the other hand, if longer times are considered such reflections are important and in this case, the velocity boundary condition at the end  $x=L$  is  $v(L, t)=0$ . In addition, suitable initial conditions need to be specified; for example, the initial strain and

particle velocity along the specimen are prescribed:  $\gamma(x, 0) = g(x)$ ,  $v(x, 0) = h(x)$ ; such preloading can be used to examine wave propagation in prestretched specimens. The nominal stress is related to the strain and strain-rate through a nonlinear stress-strain relationship appropriate to this one-dimensional problem for the particular material and needs to be determined using an inverse or hybrid procedure. Since we wish to consider nonlinear, rate-dependent materials, a viscoplastic model is considered in terms of the true-stress and logarithmic strain. In the uniaxial state considered here, the generic form of the constitutive equation can be written as follows:

$$\tau = E(\epsilon - \epsilon_p), \quad \dot{\epsilon}_p = f(\tau, \epsilon_p) \quad (2)$$

where  $\tau = \lambda \sigma$  is the true stress,  $\epsilon = \ln(\lambda)$  is the true (logarithmic) strain,  $\epsilon_p = \epsilon - \epsilon_e$  is the plastic strain and  $E$  is the modulus of elasticity. The time rate of evolution of the plastic strain is taken to be related to the plastic strain and the true stress. The particular functional form for the evolution of plastic strain in equation (2) will vary depending on the material examined; in the present work, we evaluated the Malvern, Johnson-Cook, Bergstrom-Boyce, and Zhou-Clifton models. The above equations can be written in the form of a quasi-linear system:

$$\frac{\partial}{\partial t} \begin{Bmatrix} \epsilon \\ v \\ \epsilon_p \end{Bmatrix} + \begin{bmatrix} 0 & -e^{-\epsilon} & 0 \\ -e^{-\epsilon} C^2 & 0 & e^{-\epsilon} C_0^2 \\ 0 & 0 & 0 \end{bmatrix} \frac{\partial}{\partial X} \begin{Bmatrix} \epsilon \\ v \\ \epsilon_p \end{Bmatrix} = \begin{Bmatrix} 0 \\ 0 \\ f(\tau, \epsilon_p) \end{Bmatrix} \quad (3)$$

where  $C_0 = \sqrt{E/\rho}$  and  $C = \sqrt{(E - \tau)/\rho}$ . It should be noted that  $C_0 \sim C$  since  $\tau$  is typically very small in comparison to  $E$ . Solving for the eigenvalues of this system, it can be shown that there are three distinct characteristics, two which propagate at nearly the elastic wave speed and a third stationary characteristic along which the plastic strain evolves. The governing equations can now be written in characteristic form:

$$\begin{aligned} \dot{\epsilon}_p &= f(\epsilon_p) & \text{on } dx &= 0 \\ \mp C \dot{\epsilon} + \dot{v} \pm \frac{C_0^2}{C} \dot{\epsilon}_p \mp \frac{C_0^2}{C} f(\epsilon_p) &= 0 & \text{on } \frac{dx}{dt} &= \pm e^{-\epsilon} C \end{aligned} \quad (4)$$

In order to solve the above system, we must discretize the equations in space and time. If the particle velocity, strain, and plastic strain are known at one time step we can march that solution forward in time along the characteristics to obtain the solution at the next time step. Figure 2 shows the spatial discretization at time  $k$  and  $k+1$ . The particle

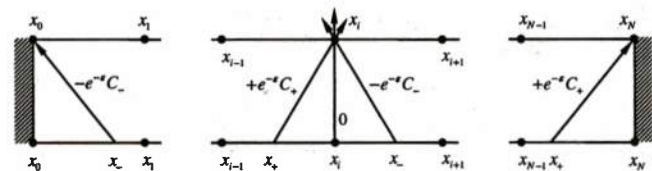


Fig. 2 Stepwise calculation by the method of characteristics

velocity, total strain, and plastic strain are known at each location  $x_i$  at time  $k$ ; quantities evaluated at time step  $k$  are indicated without a superscript. To solve for the three quantities at  $x_i$  at time  $k+1$  we march the solution at time  $k$  forward along the three characteristics; the locations of  $x_+$

and  $x_-$  from which characteristics arrive at  $x_i$  at time  $k+1$  are determined by the size of the time step and the respective wave speeds  $\frac{dx}{dt} = \pm e^{-\epsilon} C$ . Linear interpolation is used to find the necessary field quantities at each  $x_+$  and  $x_-$ . The explicit expressions for marching the solution are given below:

$$\begin{aligned}\epsilon_{pi}^{k+1} &= \epsilon_{pi} + f(\epsilon_{pi})\Delta t \\ \epsilon_i^{k+1} &= \frac{C_+ \epsilon_+ + C_- \epsilon_- - v_+ + v_-}{C_+ + C_-} + \frac{1}{C_+ + C_-} \left[ \frac{C_0^2}{C_+} \left( \epsilon_{pi}^{k+1} - \epsilon_{p+} - f(\tau_{p+}, \epsilon_{p+})\Delta t \right) + \frac{C_0^2}{C_-} \left( \epsilon_{pi}^{k+1} - \epsilon_{p-} - f(\tau_{p-}, \epsilon_{p-})\Delta t \right) \right] \\ v_i^{k+1} &= \frac{C_+ C_-}{C_+ + C_-} \left[ \epsilon_- - \epsilon_+ + \frac{v_+}{C_+} + \frac{v_-}{C_-} \right] - \frac{C_+ C_-}{C_+ + C_-} \left[ \frac{C_0^2}{C_+} \left( \epsilon_{pi}^{k+1} - \epsilon_{p+} - f(\tau_{p+}, \epsilon_{p+})\Delta t \right) + \frac{C_0^2}{C_-} \left( \epsilon_{pi}^{k+1} - \epsilon_{p-} - f(\tau_{p-}, \epsilon_{p-})\Delta t \right) \right]\end{aligned}\quad (5)$$

This is a modified form of the upwind-differencing scheme commonly used in computational fluid mechanics. Note that proper accounting of boundary conditions must be provided. Typically, the particle velocity or strain is prescribed and the other quantity is obtained from the characteristic that leaves the domain of interest as illustrated in Fig. 2.

### Experimental Technique

We now turn to a description of how the above boundary-initial value problem is implemented in the laboratory; the experimental setup is shown in Fig. 3. The test apparatus is an air gun with a 2 m long barrel. A guiding slot, along which a polycarbonate slider will travel, has been cut into half the length of the barrel. The slider is initially placed at the end of the slot and the polyurea specimen is wrapped around it as shown in the figure.<sup>2</sup> The ends of the polyurea specimen are then clamped at a distance  $L$  from the slider, typically ~180 mm. When the air gun is triggered, a hardened steel projectile is shot down the barrel toward the slider. Upon impact, the slider launches forward stretching the specimen. In order to monitor the wave propagation and make quantitative measurements of the strain and particle velocity, marker lines are drawn on the specimen. A plastic stencil was made with slots that are spaced at a uniform distance (2 mm in most cases); since the specimens were transparent,<sup>3</sup> they were dusted with a light coat of white

spray paint and then a black indelible ink maker was used to scribe lines on the specimen through the stencil. Various line thicknesses and spacing have been used; the optimum combination depends on the length of specimen that is within the field of view of the camera frame. The goal of this optimization is to achieve maximum spatial and temporal resolution while accounting for the limited number of pixels over which to resolve the image. The motion is recorded with a Photron SA1 high-speed video camera with a framing rate of 270,000 fps and a resolution of 1024×16. The typical physical region viewed in the camera is 2.18 mm high by 140 mm long, providing a resolution of 7.3 pixels/mm; in some tests, a smaller field of view (about 40 mm long) was used to improve the spatial resolution. Niemczura and Ravi-Chandar [15] have used a variant of this method to examine nonlinear elastic waves in polyisoprene rubbers.

There are a number of experimental factors that need special attention in order to minimize the measurement errors. The axial alignment of the specimen with the direction of movement of the projectile is particularly important. Small misalignments introduce a rotary wobble to the slider holding the specimen, and therefore produce twisting or kinking type out-of-plane motion that is superposed on the expected axial wave motion. Geometric imperfections of the specimens may also play a role. Variations in cross-sectional dimensions might introduce geometric dispersion of the wave and should be avoided. A last point to note is that the material itself may not be perfectly homogenous. While all the bubbles were removed by degassing the Isonate and Versalink prior to mixing, upon mixing bubbles are reintroduced and because the working time is so short it is not possible to remove them all by vacuum. There are a small number of bubbles present in the specimens. Long portions of the strips are free of the voids and specimens must be extracted from these sections.

When the high speed images are played back as a video at reduced speeds, the propagation of a tensile wave through

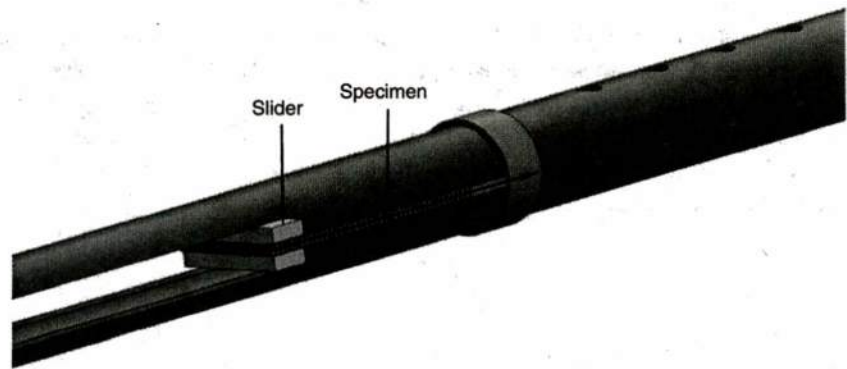
<sup>2</sup> In some later tests, the specimen was glued to the slider to prevent slippage.

<sup>3</sup> The transparency was influenced significantly by the mixing procedure; when the Versalink and Isonate were not mixed adequately, it resulted in an opaque, stiff polymer with a very small stretch to failure. By ensuring proper mixing with a stirrer, it was possible to obtain specimens that were transparent yellow in color.





**Fig. 3** Experimental arrangement for generating impact-induced tensile waves. Black lines are drawn on the specimen; the  $x$ -direction is indicated by the arrow



the specimen is easily identifiable.<sup>4</sup> In order to aid in the visual examination and quantitative interpretation of the data, a  $y$ - $t$  diagram of the particle trajectories is constructed through digital image processing: from each video image corresponding to time  $t$ , the intensity of one line of pixels corresponding to the center line of the specimen marked by the line in Fig. 3 is extracted; denote this as  $I(y, t)$ . A new image  $I(i, j) = I(y(i), t(j))$  was created in which each  $i$  corresponds to the physical  $y$ -direction in the fixed laboratory frame, while each  $j$  corresponds to the time of each video frame. Thus, the resulting picture is a streak image of the markers that indicates the particle trajectories in  $y$ - $t$  space; such a particle trajectory diagram from one experiment on the polyurea specimen is shown in Fig. 4.

The  $y$ - $t$  diagram in Fig. 4 does not show the entire length of specimen but instead focuses on the first 90 mm. The marker lines on the specimens are  $\sim 0.6$  mm wide and spaced  $\sim 0.8$  mm apart. The entire specimen is stationary and unstretched until the projectile impacts the slider at  $74 \mu\text{s}$  and imparts a particle velocity to the specimen; at this time, the left edge of the specimen begins moving to the left. The message of the impact propagates into the specimen at the appropriate wave speeds; the highest strain-rates should occur in the region nearest the point of impact. Particle velocity and strain measurements can be obtained from these images and analyzed to extract the constitutive behavior. But, before we begin this task, a couple features that are apparent in the image warrant further discussion. Along the front edge of the specimen several lines seem to just appear a short time after impact. These lines were initially sitting on the front face of the slider. Since the specimen is free to move on the slider the lines that were on the front portion of the slider simply came around the corner to the side of the slider. This can be taken into account in the analysis by considering only those marker lines that were visible in the initial image and using the measured velocity on the first of these lines as the boundary condition; the red line identified

in Fig. 4 was digitized and used as the point where the velocity boundary condition is prescribed. Also apparent in Fig. 4 are several bright regions along the front edge of the specimen; these are artifacts caused by light being reflected in different directions due to the slight wobble of the slider about its axis. This wobble can create some noise in collected data and therefore, the data analyzed in the following section was collected only from material points originally 4 mm away from the front end of the specimen.

The  $y$ - $t$  diagram of the type shown in Fig. 4 constitutes the primary diagnostic measurement in this experiment. The particle trajectories are extracted from the  $y$ - $t$  diagram by using an edge tracing algorithm to follow the left and right edges of line. This measurement provides the current position  $y(x, t) = x + u(x, t)$  of the material points at the edge of each line. From these measurements, we may calculate the strain and particle velocity throughout the specimen as a function of time. Note that this differentiation introduces errors. This error may be minimized by using a high spatial magnification with a small field of view and a high temporal sampling; it can be reduced further by a smoothing procedure that uses spline fits followed by a moving average filtering operation. It is also possible to use digital image correlation methods; however, when the strains reach the

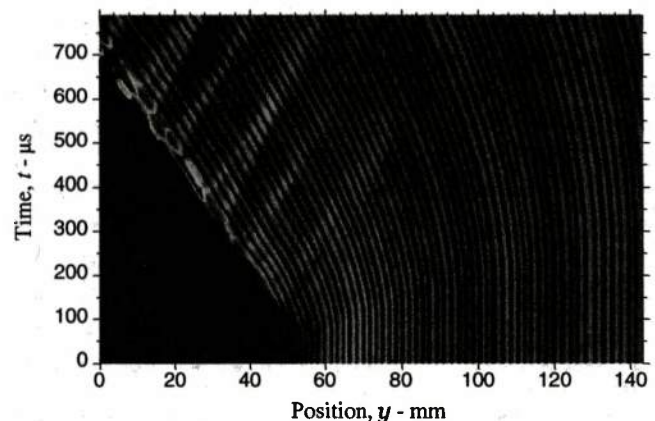


**Fig. 4** Particle trajectory diagram for Test PU-A in laboratory frame. Solid red line shows the edge trace from which the velocity boundary condition applied in simulations is extracted (Color figure online)

<sup>4</sup> See the Supplementary Material of Niemczura and Ravi-Chandar, [15] for a video of the propagation of nonlinear elastic waves in a polyisoprene rubber. The wave propagation observed in the polyurea appears to be very similar.



large levels encountered in the present experiments, the speckle patterns experience significant degradation and the correlation methods fail. It is possible to use the digital image correlation when the interest is in very high strain rates, but at small strain levels.

## Results

Numerous experiments were performed over a range of impact speeds from about 60 to 100 m/s, resulting in stretch rates over a range from 800 to 8000 s<sup>-1</sup>. One of these, Test PU-A, is described in detail in this section. Figure 5 shows the experimentally recorded particle velocity and strain histories at material points spaced 10 mm apart for Test PU-A. Figure 6 shows the corresponding particle velocity and strain profiles.<sup>5</sup> Initially, both velocity and strain are zero along the entire length. As time increases the left end of the specimen is accelerated in the negative  $x$  direction causing the particle velocity and the strain to increase near the impact end. The propagation of the strain and velocity profiles into the specimen can be seen readily in these figures and are used in the following to determine the constitutive properties of the material.

By tracing the movement of each material point to within one pixel resolution (i.e., a displacement of at least one pixel corresponding to 0.137 mm), it is observed that the fastest measurable disturbance propagates at a speed of 316 m/s. Until this characteristic (wave) arrives, a material point does not feel the effects of the velocity imposed at the left end. We take this to correspond to the elastic wave speed, and estimate the “dynamic elastic modulus” of the polyurea as  $E_d = \rho C^2$ ; this estimate of 100 MPa is to be compared to the quasi-static measurement of 70 MPa and clearly indicates the influence of the rate-dependent material behavior. Note that the strain associated with this wave is extremely small and with the resolution limits in the measurement, we could only establish the above estimate of the modulus as a lower bound. With increasing time, material points continue to accelerate and move to the left with increasing particle velocity and strain; this is the region of primary interest.

As is evident from Fig. 5, the impact event does not generate a step increase in particle velocity, but only a rapid increase to about 40 m/s in the first 50  $\mu$ s and then a more gradual increase to ~80 m/s over the next 100  $\mu$ s. Corresponding to this, the strain profiles shown in Fig. 5 indicate that the strain attains values in the range of about

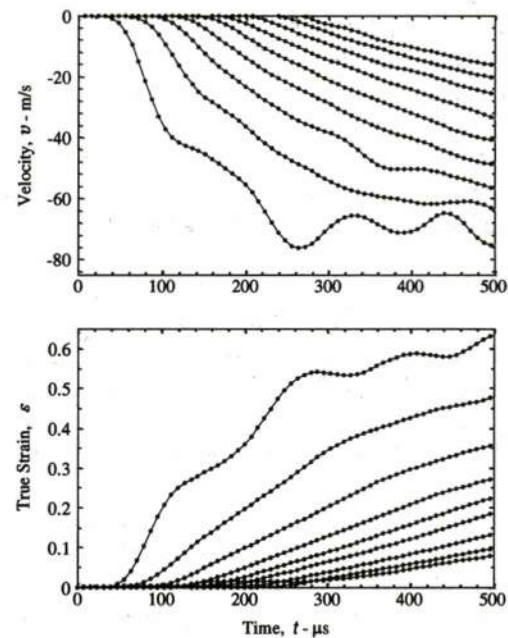


**Fig. 5** Velocity and true strain histories at material points spaced 10 mm apart for Test PU-A

0.6 at the impact point, and that the large strains move into the specimen slowly. The nonlinear nature of the wave propagation is also evident from these figures by noting that the stretch-rate and particle acceleration decrease continuously as the wave moves further into the specimen. The peak stretch-rates occur at the location of the impact and are in the range of 8000 s<sup>-1</sup>, but a few centimeters away the strain-rate has already decayed by an order of magnitude.

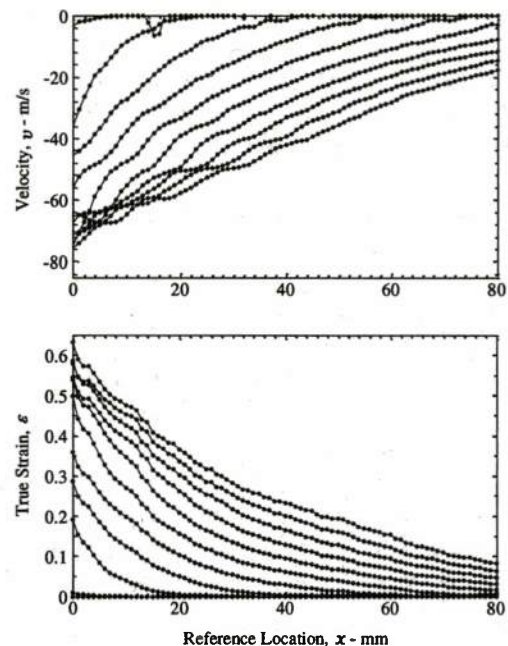


**Fig. 6** Velocity and true strain profiles along the length of the specimen every 50  $\mu$ s for Test PU-A

<sup>5</sup> It should be noted that these plots result from taking derivatives of the position data; therefore there is an inherent error from numerical differentiation that has been smoothed by a moving average filter. Furthermore, the slider interacts frictionally with the guiding slots in the barrel and provides a nonuniform boundary condition at the attachment point.

This dissipation is a manifestation of highly non-linear and rate-dependent behavior of the material.

As clearly demonstrated in the experiments above, the material experiences a wide range of stresses, strains (0–0.6), and stretch-rates (800–8000 s<sup>-1</sup>) at each location in this dynamic transient tension test. This fact makes for a very powerful test method because a single test provides experimental data for many loading conditions. Fitting a constitutive model to a single test will calibrate that model over a very large range of strains and strain-rates. Finding such a model that can accurately capture the behavior over the entire spectrum of strains and strain-rates experienced in each test does, however, prove to be quite a challenge. Many constitutive models have been proposed in the literature, covering a range of material response in metals and polymers, and are either purely empirical or motivated through micromechanical models that aim to capture the underlying deformation mechanisms. However, most of these viscoplastic models rely on the nonequilibrium or “overstress” conditions that are generated at high strain rates, where the stress rises quickly and then approaches the “equilibrium stress” as the strain evolves in time. This is motivated by the fact that the nonequilibrium response is thermally assisted. In lieu of determining the exact model that describes all of polyurea’s behavior in tension, we found one set of parameters which produced a satisfactory representation of the actual behavior in the stretch-rate range of 800–8000 per second.

Malvern [16] suggested the following phenomenological model as a means to describe the high rate behavior of strain-rate dependent materials:

$$\dot{\epsilon}_p = \dot{\epsilon}_0 \exp \left[ \frac{\tau - g(\epsilon_p)}{B} \right] \quad (6)$$

where  $g(\epsilon_p)$  is the quasi-static or equilibrium stress-strain curve for the material and  $B$  and  $\dot{\epsilon}_0$  are materials constants. This is referred to as the overstress model because the strain-rate depends on the difference between the current stress and the equilibrium stress and is supposed to model thermally activated processes.

Johnson and Cook [17] suggested a strain-rate dependent material response that can be written as follows:

$$\tau = [D_1 + D_2 \exp(D_3 \epsilon_p)] (1 + D_4 \ln \dot{\epsilon}_p) f[T] \quad (7)$$

where  $D_i$  are material parameters. This model has been calibrated for many metallic materials.

Bergstrom and Boyce [18] used a power-law creep model to fit the strain-rate dependent response of carbon black filled Chloroprene rubber, with an additional dependence on the stretch. This is written in the form:

$$\dot{\epsilon}_p = \dot{\epsilon}_0 (\lambda_{chain}^p - 1)^c \left( \frac{\tau}{g(\epsilon_p)} \right)^m \quad (8)$$

where  $\lambda_{chain}^p$  is a measure of the inelastic stretch in the chains and  $\dot{\epsilon}_0$ ,  $c$ , and  $m$  are constants.

Zhou and Clifton [19] suggested the following phenomenological model as a means to describe the high rate behavior of 1045 steel:

$$\begin{aligned} \dot{\epsilon}_p &= \frac{\dot{\epsilon}_1 \dot{\epsilon}_2}{\dot{\epsilon}_1 + \dot{\epsilon}_2}, \dot{\epsilon}_1 = \dot{\epsilon}_0 \left[ \frac{\tau}{g(k\epsilon_p, T)} \right]^m, \dot{\epsilon}_2 \\ &= \dot{\epsilon}_m \exp \left[ -\frac{ag(k\epsilon_p, T)}{\tau} \right] \end{aligned} \quad (9)$$

$$g(k\epsilon_p, T) = g_0(k\epsilon_p) \left[ 1 - \beta \left\{ \left( \frac{T}{T_0} \right)^\kappa - 1 \right\} \right] \quad (10)$$

where the function  $g_0(k\epsilon_p)$  is the quasi-static stress strain relation at a small strain-rate.<sup>6</sup>  $\dot{\epsilon}_0$ ,  $\beta$  and  $\kappa$  determine the thermal influence,  $T$  is the temperature and  $T_0$  is a reference temperature.  $m$  and  $a$  are rate-sensitivity parameters. Note that equation (9) is valid only when  $\tau > g$ ; otherwise  $\dot{\epsilon}_p = 0$ . This model has been used for representing the response of other metallic materials such as copper and aluminum alloys. The model is attractive because it combines both a power-law and exponential response and is therefore able to represent a wide range of viscoplastic materials behavior. However, we may need to modify the model to provide for stiffening when the polymer network is stretched highly.

Any one of the above phenomenological models can be introduced in the Riemann solution method described earlier to determine the particle trajectory and strain in the one-dimensional problem. The inverse method of identifying the strain-rate dependent material properties relies on comparing the calculated particle trajectory and strain variation in the specimen with the direct experimental measurements. It is essential to recognize that none of the above models pays any particular attention to the specific deformation mechanisms of the material. Simply identifying that the microscopic deformation mechanisms are thermally activated processes and hence must have an exponential or power-law form in equation (9), allows us to use models of this type for a wide range of materials. The specific material-based differences then arise in the calibration of the particular model. Through numerous trials, it was determined that except for the modified Zhou-Clifton model, none of the

<sup>6</sup> We have introduced a constant  $k$  in an effort to allow more flexibility in calibrating the measured response. The physical meaning of this is that the equilibrium response is somewhat stiffer than the quasi-static response. In this matter, we can only present a heuristic argument, since a detailed micromechanical model is not available. We suppose that the quasistatic response is attained only at extremely slow rates, when all possible configurations of the polymer chains can be sampled; in contrast, under the high strain-rate loading employed here, we conjecture that only some fraction of the possible configurations are sampled, naturally leading to a stiffer response.



other models came close to replicating the measured response of the polyurea over the range of stretch-rates (800 to 8000  $\text{s}^{-1}$ ) and strains (0–0.6). The Zhou-Clifton model, with the parameters given in Table 1, provided the best fit between the observed material behavior and the calculated response. The particle trajectories calculated using the model is compared to the experimentally observed particle trajectories in Fig. 7; for the sake of clarity, only selected lines are shown. The accuracy of the fit can be best demonstrated by considering the error in position; over the entire image, the mean position error between the measured trajectory and the calculated trajectory was within 2 pixels; we note that higher spatio-temporal resolution in the experiments could reduce this error significantly. The particle velocity and strain histories computed from the model are compared to the experimentally determined histories for the specimen PU-A in Fig. 8. A similar comparison is shown for the particle velocity and strain profiles in Fig. 9. The overall trends in the simulation appear to match reasonably well with the experimental measurements. Deviations between the simulation and experiment become pronounced only for locations far from the impact point, corresponding to later times and smaller strain rates. This suggests the possible need for multiple models for capturing the overall dynamic response. In order to highlight this, results from a second test PU-B, focusing here only on the first 10 mm from the impact point, were examined; the impact speed in this case was about 70 m/s. Comparison of the experimental velocity and true strain profiles in the first 10 mm region with the predicted response is shown in Fig. 10. It is noted that the material parameters calibrated from Test PU-A were used in generating the predictions in Fig. 10. Very good correlation is obtained between the prediction and measurements in terms of the particle velocity; somewhat larger errors arise in the strain comparisons, perhaps due to the larger gage lengths involved in the strain measurements. The spatio-temporal evolution of stretch-rate in Test PU-B is shown in the contour plot in Fig. 11; it is clear that the stretch-rate is highly nonuniform both spatially and temporally. Stretch-rates reach about 8000  $\text{s}^{-1}$ , but only over a small spatio-temporal domain. However, as pointed out earlier, this is precisely the advantage of this test method. Rather than insisting on achieving a constant stretch-rate, one single test provides a way to calibrate the model over a wide range of strains and strain rates. Similarly good fits were obtained in all the other tests performed at different impact velocities, with the same calibrated material properties.

**Table 1** Material properties for polyurea

$E$ (MPa)	$\rho$ ( $\text{kg/m}^3$ )	$\dot{\epsilon}_0$	$\dot{\epsilon}_m$	$m$	$a$	$k$
100	1200	0.1	1.0 E7	10	20	1.5

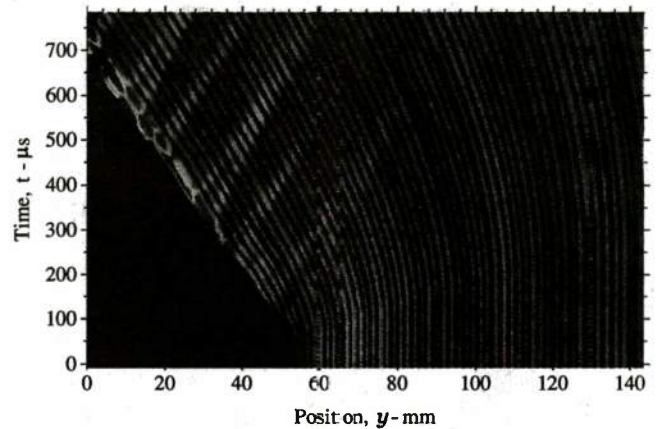


**Fig. 7** Particle trajectory diagram for Test PU-A in laboratory frame. Solid red lines show the simulated particle paths at selected locations (Color figure online)

Finally, the stress-strain paths taken by several material points are shown in Fig. 12 by the solid red lines, with the full understanding that each material point experiences a time varying stretch rate. The stress-strain responses predicted by the Zhou-Clifton model for different constant stretch-rates are shown in this figure by the blue lines; the quasi-static stress strain curve is shown by the blue dashed line. It is clear that since the stretch-rate in the experiment varies with time, the stress-strain paths taken by the material points in the experiments do not follow any one particular constant stretch-rate curve, but migrate between these curves. Also, from this comparison, for a stretch-rate of 8000  $\text{s}^{-1}$  we expect the “flow stress” to be at most three

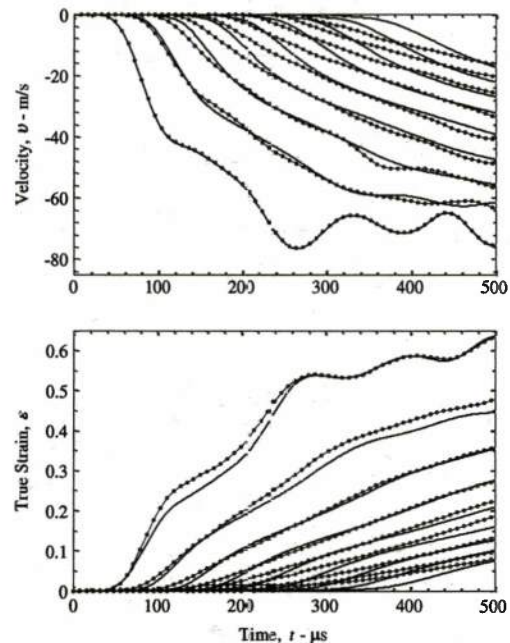


**Fig. 8** Comparison of experimental (blue) and simulated (red) velocity and true strain histories at material points spaced 10 mm apart for Test PU-A (Color figure online)



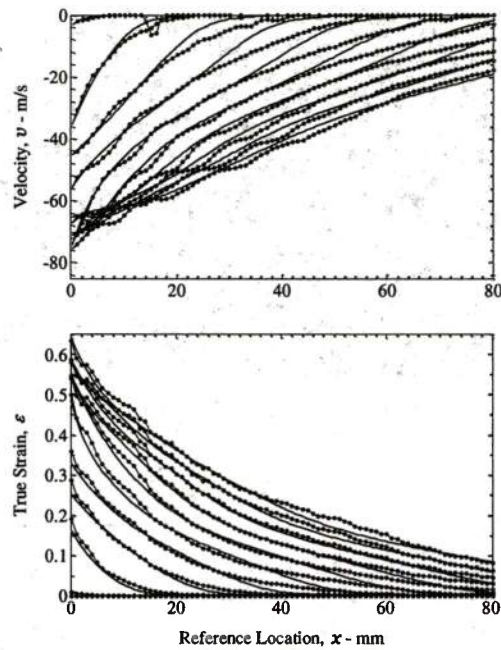


**Fig. 9** Comparison of experimental (*blue*) and simulated (*red*) velocity and true strain profiles along the length of the specimen every  $50\mu\text{s}$  for Test PU-A (Color figure online)

times that expected in quasi-static loading. We note that in their simulation of a polyurea-coated aluminum ring, Zhang et al. [20] indicated that multiplying the quasi-static stress strain curve by a factor of five was sufficient to reproduce the experimentally observed expansion of the polyurea-coated aluminum ring at a strain-rate of about  $15,000\text{ s}^{-1}$

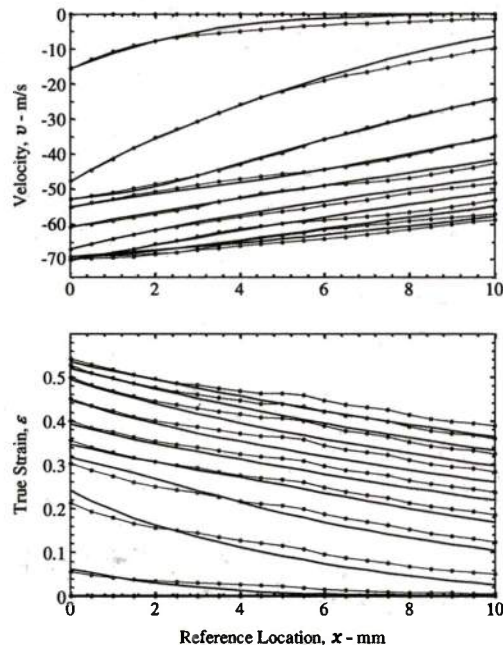


**Fig. 10** Comparison of experimental (*blue*) and predicted (*red*) velocity and true strain profiles over the first 10 mm for Test PU-B every  $50\mu\text{s}$  (Color figure online)

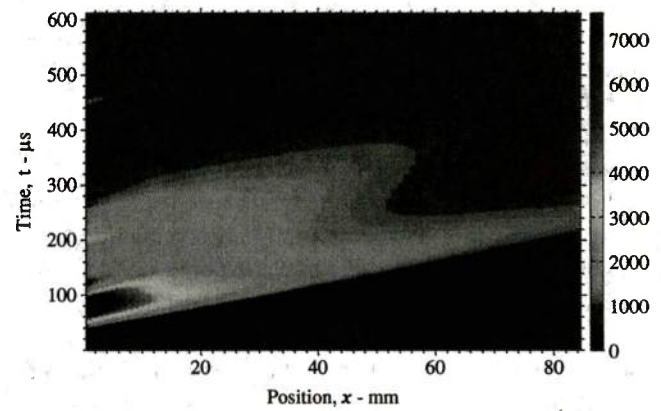


**Fig. 11** Contour plot showing the spatio-temporal variation in the stretch rate  $\dot{\lambda}$  Test PU-B

and is in the same range as the inferred stress-strain curve suggested in the present work. Based on the quality of the comparison between the experiment and the calibrated model, we can indicate that the tensile behavior of polyurea for strains below 80 % at stretch-rates in the range of  $\sim 800\text{--}8000\text{ s}^{-1}$  can be represented by the model in equation (9) with the parameters provided in Table 1.

## Conclusion

Circumventing the numerous difficulties associated with the classical split-Hopkinson apparatus, the classical experiment of von Karman and Duwez has been reconstructed with modern diagnostic instrumentation. This experiment permits the evaluation of the tensile response of materials with very few limitations. In particular, the particle velocity and strain are measured at a number of material points as a function of time; this data is then used to calibrate the Zhou-Ciffton viscoplastic material model. The high strain-rate tensile response of a transparent elastomer, polyurea, has

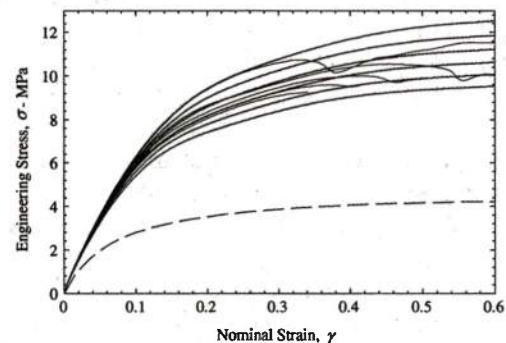


**Fig. 12** Stress-strain path predicted by the Zhou-Ciffton model for constant stretch rates ( $250, 500, 1000, 2000, 4000, 8000\text{ s}^{-1}$ ) are shown in blue. Quasi-static stress-strain response is shown by the dashed blue line. The stress-strain paths followed by material points spaced 10 mm apart in the one-dimensional impact experiment Test PU-B are shown in red (Color figure online)

been investigated to large strains as an illustrative example. The response of this material has been captured using a modified viscoplastic constitutive relation over stretch rates ranging from 800–8000  $\text{s}^{-1}$ .

**Acknowledgments** This work was performed under a program entitled “Dynamic Response of Metal-Polymer Bilayers - Viscoelasticity, Adhesion and Failure” sponsored by the Office of Naval Research (ONR Grant Number N00014-09-1-0541, Program Manager: Dr. Roshdy Barsoum); this support is gratefully acknowledged.

## References

- Mathews W (2004) Services test spray-on vehicle armor, *Army Times*, May 3, 2004
- Barsoum RGS, Dudt PJ (2009) The fascinating behaviors of ordinary materials under dynamic conditions. *AMMTIAC Q* 4:11–14
- Patel P, Gilde GA, Dehmer PG, McCauley JW (2000) Transparent armor. *AMPTIAC News* 4:1–9
- Shockey D, Bergmannshoff D, Curran DR (2008) Failure Physics of Glass during Ballistic Penetration, presentation at the 32nd International Conference & Exposition on Advanced Ceramics & Composites, January 27–February 1, 2008, Daytona Beach, FL
- Strassburger E (2009) Ballistic testing of transparent armour ceramics. *J Eur Ceram Soc* 29:267–273
- Bless S, Chen T (2010) Impact damage in layered glass. *Int J Fract* 162:151–158
- Subhash G, Ravichandran G (2000) Split Hopkinson Pressure Bar Testing of Ceramics, *ASM Handbook, Mechanical Testing and Evaluation*, Volume 8, ASM International, 497–504
- Youssef G, Gupta V (2011) Dynamic Response of Polyurea subjected to nanosecond rise-time stress waves. *Mech Time Dependent Mater*. doi:10.1007/s11043-011-9164-7
- Roland CM, Twigg JN, Vu Y, Mott PH (2007) High strain rate mechanical behavior of polyurea. *Polymer* 48:574–578
- Chakkarapani V, Ravi-Chandar K, Liechti KM (2006) Characterization of multiaxial constitutive properties of rubbery elastomers. *J Eng Mater Technol Trans ASME* 128:489–494
- Amirikhizi AV, Isaacs J, McGee J, Nemat-Nasser S (2006) An experimentally-based viscoelastic constitutive model for polyurea, including pressure and temperature effects. *Philos Mag* 86:5847–5866
- Zhao J, Knauss WG, Ravichandran G (2007) Applicability of the time-temperature superposition principle in modeling dynamic response of a polyurea. *Mech Time Dependent Mater* 11:289–308
- Qiao J, Amirikhizi AV, Schaaf K, Nemat-Nasser S, Wu G (2011) Dynamic mechanical and ultrasonic properties of polyurea. *Mech Mater* 43:598–607
- von Karman T, Duwez P (1950) The propagation of plastic deformation in solids. *J Appl Phys* 21:987–994
- Niemczura J, Ravi-Chandar K (2011) On the response of rubbers at high strain rates: I: simple waves. *J Mech Phys Solids* 59:423–442
- Malvern LE (1951) Plastic wave propagation in a bar of material exhibiting a strain-rate effect. *Q Appl Math* 8:405
- Johnson GR, Cook WH (1985) Fracture characteristics of three metals subject to various strains, strain rates, temperatures and pressures. *Eng Fract Mech* 21:31–48
- Bergstrom JS, Boyce MC (1998) Constitutive modeling of the large strain time-dependent behavior of elastomers. *J Mech Phys Solids* 46:931–954
- Zhou M, Clifton RJ (1996) Dynamic ductile rupture under conditions of plane strain. *Int J Impact Eng* 19:189–206
- Zhang H, Liechti KM, Ravi-Chandar K (2009) On the dynamics of necking and fragmentation: III. Effect of cladding with a polymer. *Int J Fract* 155:101–118

## APPENDIX E

### High strain rate response of rubber membranes

A.B. Albrecht and K. Ravi-Chandar

*Journal of the Mechanics and Physics of Solids*, in review, 2013.



# High strain rate response of rubber membranes

Aaron B. Albrecht<sup>1</sup> and K. Ravi-Chandar<sup>2</sup>

*Center for Mechanics of Solids, Structures and Materials*

*University of Texas at Austin*

*Austin, TX 78712-1221*

**ABSTRACT:** This paper investigates the propagation of axisymmetric waves of finite deformation in polyisoprene rubber membranes subjected to high speed impact. High speed photography is used to monitor the motion and to determine the evolution of stretch and particle velocity in membranes at impact speeds of up to 160 m/s, producing a maximum stretch  $> 8$ . A constitutive model is developed through a semi-inverse method correlating experimental results with simulations. The potential for formation wrinkles is also addressed.

## 1. INTRODUCTION

The challenge of modeling the constitutive behavior of rubbers and elastomers is long-standing. At present a number of phenomenological models exist that capture the quasi-static response over certain strain ranges under specific load conditions (for example, the models of Mooney-Rivlin, Ogden, Gent, Arruda-Boyce, etc). As the strain-rate is increased, however, these models are no longer adequate. Niemczura and Ravi-Chandar (2011a,b,c) building on the pioneering work of von Karman and Duwez (1949), developed a dynamic stretching experiment and found that a simple power-law type model could capture the uniaxial tensile behavior of polyisoprene rubber at strain-rates between  $500\text{-}10^4 \text{ s}^{-1}$  for stretches between one and four. In order to develop a robust description of the material behavior however, the response must be extended to larger stretches under a range of strain-rates. Such a model would likely come in the form of a description of the energy function of the material. The goal of this paper is to calibrate such a model under one loading scenario, dynamic stretching for example, and then demonstrate that the model is able to predict the behavior under other loadings such as biaxial tension. In order to validate any description of the high strain-rate behavior of rubbers and elastomers, experiments must be performed under loading conditions other than the one used for calibration of the model, and hence the need for the dynamic membrane impact test considered in the present work.

A number of studies have addressed the high strain-rate deformation of a membrane from a number of different angles. Hallquist and Feng (1979) produced some of the earliest analytical work describing the dynamic response of a Mooney-Rivlin membrane subjected to a step pressure load using a Rayleigh Ritz procedure which minimized the

---

<sup>1</sup> Present Address: California Institute of Technology, Pasadena, CA 91125

<sup>2</sup> Corresponding Author: [ravi@utexas.edu](mailto:ravi@utexas.edu)

potential energy of the deformed configuration of the membrane and obtained the shape variation with time. Early high speed imaging of dynamic membrane deformation along with prediction of transverse wave speed can be found in the work of Farrar (1984). In that study, rubber membranes were impacted with projectiles traveling at 12 m/s. The limitation on impact speed was due the assumption of small deformations in the wave propagation analysis used to predict the deflection. In this restricted case, they were able to match the recorded out of plane deflection reasonably well. Haddow et al. (1992) presented an analytical study of dynamic deformation of membranes under finite strains using the method of characteristics (MC) to model the wave propagation. This work, in which the material was assumed to obey a Mooney-Rivlin constitutive model, did not include any comparison of experimental results with their predictions. In this article, we use high speed imaging to record the large axisymmetric deformation of polyisoprene membranes subjected to normal impact with speeds in the range of 50 – 150 m/s. These experimental measurements are used to explore a constitutive model by comparing the measured kinematic quantities of deflection, strain, and particle velocity with those predicted by simulations.

The choice of material models must include the possibility of stiffening at high strains. This stiffening is observed in quasi-static tension tests and is attributed to the generation of orientation with stretching, as opposed to simply the unraveling, of the polymer chains and is expected to occur in some form at large stretches even during high strain-rate deformation. The inflection in the stress strain curve which results from this stiffening however, presents the possibility of tensile shock wave formation.

All of the above assumes axisymmetric deformation; however, during several tests wrinkles were observed in the membrane, clearly invalidating the assumed symmetry. The wrinkles initiated at the transverse wave front, and grew radially as the deformation progressed. Vermorel et al (2009) investigated the formation of these wrinkles during low speed membrane impacts. Through simulation, we explore the possible reason why wrinkles appear only in some of our tests.

This article is organized as follows: the potential constitutive models used to describe the dynamic response of the polyisoprene membrane are described in Section 2. The quasi-linear system of equations that govern axisymmetric wave propagation in a membrane is reviewed in Section 3. The method of characteristics (MC) used to solve the membrane problem is described in Section 4. The experimental setup and the diagnostic tools are described in Section 5. The response of the membrane, determined through high-speed photography, is discussed in Section 6. In Section 7, the measured response of the membrane is compared to the calculated response, and in the process the parameters of the constitutive model are extracted. The observed wrinkling is described, and underlying reasons for its formation are explored through simulations in Section 8. Finally, the key findings are summarized in Section 9.

## 2. POLYISOPRENE RUBBER

The dynamic response of polyisoprene rubber used in this work has been examined by Niemczura and Ravi-Chandar (2011a) who found that at strain rates greater than  $500 \text{ s}^{-1}$ , the rate dependence of the material saturated and therefore the uniaxial tensile behavior of material could be captured reasonably well with a simple power-law type model with the form  $\sigma = \mu \gamma^n$ . A comparison between this rate saturated power law and the quasi-static tensile behavior of rubber is shown in Figure 1 ( $\mu = 1 \text{ MPa}$ ,  $n = 0.5$ ), a recreation of Figure 7 from Niemczura and Ravi-Chandar (2011a). In an attempt to generalize this power law to multiaxial loading, it was found that the dynamic uniaxial tensile behavior can also be closely matched by a material with the Mooney-Rivlin strain energy density:

$$W = \mu_1 (I_1 - 3) + \mu_2 (I_2 - 3) \quad (1)$$

$$I_1 = \lambda_1^2 + \lambda_2^2 + \lambda_3^2 \quad (2)$$

$$I_2 = \lambda_1^2 \lambda_2^2 + \lambda_2^2 \lambda_3^2 + \lambda_3^2 \lambda_1^2 \quad (3)$$

The constants which most closely fit the uniaxial behavior indicated by Niemczura and Ravi-Chandar (2011a) are  $\mu_1 = 0.17 \text{ MPa}$  and  $\mu_2 = 0.22 \text{ MPa}$ . The biaxial Cauchy stress vs. stretch relationship for an incompressible material can then be represented as:

$$\tau_{1,2} = 2\mu_1 \left( \lambda_{1,2}^2 - \frac{1}{\lambda_1^2 \lambda_2^2} \right) + 2\mu_2 \left( \lambda_1^2 \lambda_2^2 - \frac{1}{\lambda_{1,2}^2} \right) \quad (4)$$

While the model generalized from the dynamic uniaxial properties seems like the candidate most likely to match the dynamic behavior in biaxial tension, the membrane test imparts stretches far beyond those achieved in the dynamic uniaxial tests. The maximum stretch reaches values greater than nine in a membrane test whereas it seldom exceeded four in the uniaxial tension test. Achieving these higher stretches brings the possibility of secondary stiffening observed during quasistatic tension of rubber but not dynamic tension. If there is stiffening, the Mooney-Rivlin model will not be able to capture the behavior properly. Instead we need something more similar to the quasistatic curve at larger stretches. Lopez-Pamies (2010) has developed a strain energy function that accomplishes this objective with a generalization of the Neo-Hookean material model:

$$W(I_1) = \frac{3^{1-\alpha_1}}{2\alpha_1} \mu_1 (I_1^{\alpha_1} - 3^{\alpha_1}) + \frac{3^{1-\alpha_2}}{2\alpha_2} \mu_2 (I_1^{\alpha_2} - 3^{\alpha_2}) \quad (5)$$



The uniaxial tension response of this model matches the quasistatic response of polyisoprene rubber with the following parameters:  $\alpha_1 = 0.78$ ,  $\alpha_2 = 4.12$ ,  $\mu_1 = 0.5$  MPa,  $\mu_2 = 68$  Pa. The biaxial Cauchy stress vs. stretch relationship for an incompressible material can be represented as:

$$\tau_{1,2} = \left( 3^{1-\alpha_1} \mu_1 I_1^{\alpha_1-1} + 3^{1-\alpha_2} \mu_2 I_1^{\alpha_2-1} \right) \left( \lambda_{1,2}^2 - \frac{1}{\lambda_1^2 \lambda_2^2} \right) \quad (6)$$

There are approximations with each of these models. Imposing the dynamically calibrated Mooney-Rivlin (we will refer to this as the DCMR model) model assumes that the stiffness decreases monotonically, while the Lopez-Pamies fit to the quasistatic uniaxial behavior (we will refer to this as the Q-LP model), if nothing else, will have a much lower initial stiffness than the dynamic tension tests would require. Also, with the Q-LP model, we have the possibility to create shocks due to the inflection in the stress strain curve, but we will not pursue this here.

### 3. AXISYMMETRIC WAVE PROPAGATION

The equations of motion can be written in a standard quasilinear form following the procedures outlined by Cristescu (1967). Consider an axisymmetric membrane deformed by a pressure load as shown in the free body diagram of a slice of the membrane in Figure 2. The initial geometry is defined by radial and axial coordinates,  $r_0(s_0)$  and  $z_0(s_0)$ , where  $s_0$  is the position of a material point in the initial (reference) configuration. The membrane is assumed to have an initial thickness  $h_0$ . The position of the material point in the deformed (current) configuration is denoted by  $s$ ; the deformed geometry is denoted by the current values of the radial and axial coordinates:  $r(s)$  and  $z(s)$ . The current thickness is denoted by  $h(s)$ ; it is assumed that a pressure  $P(s)$  which depends on current material coordinate  $s$ , is imposed on the membrane as well. The pressure load creates internal stresses in the membrane. The true stress in the meridional direction  $\tau_1(s)$  is indicated in the free-body-diagram in Figure 2. The meridional view free-body-diagram with a cut along the axis illustrated in Figure 3, shows  $\tau_2(s)$ , the true hoop stress. Summing the forces in the vertical and horizontal directions yields the two equilibrium equations:

$$\frac{\pi}{2} P(s) \left[ r(s+ds)^2 - r(s)^2 \right] + (\tau_1 \pi r h) \Big|_s \sin \varphi - (\tau_1 \pi r h) \Big|_{s+ds} \sin \varphi = 0 \quad (7)$$

$$2P(s)r(s)\sin\varphi - 2\tau_2(s)hds + \int_{-\frac{\pi}{2}}^{\frac{\pi}{2}} \left[ \tau_1 rh \cos\varphi \right]_s^{s+ds} \cos\theta d\theta = 0 \quad (8)$$

We can simplify both of the above equations by introducing the kinematic relations:

$\sin\varphi = -\frac{dz}{ds}$  and  $\cos\varphi = \frac{dr}{ds}$  (see Figure 3 for definition of the angle  $\varphi$ ):

$$P(s)r \frac{dr}{ds} + \frac{d}{ds} \left( \tau_1 rh \frac{dz}{ds} \right) = 0 \quad (9)$$

$$P(s)r \frac{dz}{ds} - \tau_2 h + \frac{d}{ds} \left( \tau_1 rh \frac{dr}{ds} \right) = 0 \quad (10)$$

For the dynamic problem, we should include inertia and consider the shape as well as stress to be functions of position and time:  $(s, t)$ . The resulting equations of motion are given as:

$$\rho hr \frac{\partial^2 w}{\partial t^2} = -Pr \frac{\partial r}{\partial s} + \frac{\partial}{\partial s} \left( \tau_1 hr \frac{\partial w}{\partial s} \right) \quad (11)$$

$$\rho hr \frac{\partial^2 r}{\partial t^2} = Pr \frac{\partial w}{\partial s} + \frac{\partial}{\partial s} \left( \tau_1 hr \frac{\partial r}{\partial s} \right) - \tau_2 h \quad (12)$$

Note that the substitution  $w(s, t) = -z(s, t)$  has also been made. These equations can be mapped back to the reference coordinate system and then rewritten in the standard quasi-linear form; the details are given by Cristescu (1967) and only the final result is provided here. The radius of the initially flat membrane ( $w(s_0) = 0$ ) is taken to be  $R$ ; note that for the initially flat membrane we can set  $s_0 = r_0$ . The three principal stretches in the radial, circumferential (hoop) and thickness directions can be defined from the following three relations:

$$\lambda_1 = \frac{ds}{dr_0} = \sqrt{\left( \frac{dr}{dr_0} \right)^2 + \left( \frac{dw}{dr_0} \right)^2} \quad (13)$$

$$\lambda_2 = \frac{r}{r_0} \quad (14)$$

$$\lambda_3 = \frac{h}{h_0} = \frac{1}{\lambda_1 \lambda_2} \quad (15)$$

The last of the above equations introduces the assumption that the material is incompressible i.e.,  $\lambda_1\lambda_2\lambda_3=1$  and therefore the constitutive model can be written as a function of the in-plane stretches alone, i.e.  $\tau_{1,2}=\tau_{1,2}(\lambda_1,\lambda_2)$ . The density remains constant at  $\rho_0$  and the initial pressure (atmospheric pressure) is  $P_0$ . The pertinent nondimensional parameters are listed below; a subscript of 0 refers to reference configuration while quantities without a subscript refer to current configuration.

$$\begin{aligned} \eta = \frac{r}{R} \quad \eta_0 = \frac{r_0}{R} \quad \omega = \frac{w}{R} \quad \xi^2 = \frac{P_0 t^2}{\rho_0 R h_0} \quad p = \frac{PR}{h_0} \quad p_o = \frac{P_0 R}{h_0} \\ F = \frac{\tau_1(\lambda_1, \lambda_2)}{p_0 \lambda_1^2} \quad F_1 = \frac{\partial F}{\partial \lambda_1} \quad F_2 = \frac{\partial F}{\partial \lambda_2} \end{aligned} \quad (16)$$

The four primary unknown kinematic variables – the radial and axial stretches and particle velocities – are also expressed in a non-dimensionalized form as:

$$u = \frac{\partial \eta}{\partial \eta_0} \quad v = \frac{\partial \omega}{\partial \eta_0} \quad x = \frac{\partial \eta}{\partial \xi} \quad y = \frac{\partial \omega}{\partial \xi} \quad (17)$$

Compatibility relations among these kinematic quantities can then be obtained as:

$$\frac{\partial u}{\partial \xi} = \frac{\partial x}{\partial \eta_0} \quad (18)$$

$$\frac{\partial v}{\partial \xi} = \frac{\partial y}{\partial \eta_0} \quad (19)$$

The four governing equations can then be combined to form a quasilinear system and written in the form

$$\mathbf{u}_\xi + \mathbf{A}\mathbf{u}_{\eta_0} + \mathbf{b} = \mathbf{0} \quad (20)$$

where

$$\mathbf{u}(\eta_0, \xi) = \begin{Bmatrix} u(\eta_0, \xi) \\ v(\eta_0, \xi) \\ x(\eta_0, \xi) \\ y(\eta_0, \xi) \end{Bmatrix} \quad (21)$$



$$\mathbf{A}(\mathbf{u}(\eta_0, \xi), \xi) = \begin{bmatrix} 0 & 0 & -1 & 0 \\ 0 & 0 & 0 & -1 \\ -\left(F + \frac{u^2}{\lambda_1} F_1\right) & -\frac{uv}{\lambda_1} F_1 & 0 & 0 \\ -\frac{uv}{\lambda_1} F_1 & -\left(F + \frac{v^2}{\lambda_1} F_1\right) & 0 & 0 \end{bmatrix} \quad (22)$$

and

$$\mathbf{b} = \begin{Bmatrix} 0 \\ 0 \\ b_x \\ b_y \end{Bmatrix} = \begin{Bmatrix} 0 \\ 0 \\ \frac{\lambda_1 \lambda_3 \tau_2}{\eta_0 p_0} - \frac{\lambda_2 p v}{\eta_0 p_0} - \frac{u F}{\eta_0} + \frac{u(\lambda_2 - u)}{\eta_0} F_2 \\ \frac{\lambda_2 p u}{\eta_0 p_0} - \frac{v F}{\eta_0} + \frac{v(\lambda_2 - u)}{\eta_0} F_2 \end{Bmatrix} \quad (23)$$

This quasilinear system can be solved using the MC. There are four distinct eigenvalues for this system:  $\lambda^{1,2} = \pm\sqrt{F}$ ,  $\lambda^{3,4} = \pm\sqrt{F + \lambda_1 F_1}$ . Each of these eigenvalues defines the speed of a characteristic but we see there are two different types of characteristics in this case. Let us define two wave speeds  $C_1 = \sqrt{F}$  and  $C_2 = \sqrt{F + \lambda_1 F_1}$ . For ease of interpretation, these wave speeds are given explicitly in terms of Cauchy stress, stretch, and density:

$$C_1 = \sqrt{\frac{\tau_1}{\rho_0 \lambda_1^2}} \quad (24)$$

$$C_2 = \sqrt{\frac{1}{\rho_0 \lambda_1} \left( \frac{\partial \tau_1}{\partial \lambda_1} - \frac{\tau_1}{\lambda_1} \right)} \quad (25)$$

Note that  $C_2$  is largely dependent on the tangent modulus, and therefore can be understood as the axial wave speed in a membrane (in-plane stretching).  $C_1$  depends on the Cauchy stress, and is therefore initially significantly slower than the axial wave speed; it is analogous to the transverse wave speed in a string, except that it applies to the transverse wave in a membrane; we will call this the *kink wave speed*. We examine the kink and axial wave speeds as a function of stretch for each of the proposed models. The dimensional forms of kink and axial wave speeds are given in Eqs. (24) and (25). If we first consider the DCMR model, we can plot these two wave speeds as a function of

stretch in the meridional direction. We assume a uniaxial stress state with the full understanding that the true state is somewhat different (the experiments demonstrate uniaxial tension is a reasonably good approximation). These two wave speeds are plotted for the DCMR model in Figure 4a. This material model has a stiffness which decreases monotonically with stretch and hence two wave speeds never cross each other; furthermore, the axial wave speed does not have a minimum. It is useful to note that the limiting kink wave speed indicated by this model is very close to 25 m/s. If we plot the same two wave speeds for the Q-LP model however (Figure 4b) a very different result arises: there is a minimum in the axial wave speed but there is the additional complication that the axial wave speed decreases below the kink wave speed for stretches between 2.4 and 4.3. The upshot of this analysis is that the axial wave increases the stretch thereby facilitating the propagation of the kink wave, but because higher amplitude axial waves propagate slower than higher amplitude kink waves, the kink waves catch up with the axial wave; a natural expectation is that the speed of the kink wave in an initially unstretched membrane will correspond to that stretch where the axial and kink waves have nearly the same speed. This can be written as:

$$\lambda_1 \frac{\partial \tau_1}{\partial \lambda_1} = 2\tau_1(\lambda_1, \lambda_2) \quad (26)$$

Note that, in fact, this equality is never attained in the DCMR material model, but is possible in the Q-LP model at two different stretch levels.

#### 4. NUMERICAL SOLUTION OF THE GOVERNING EQUATIONS

Each of the eigenvalues of  $\mathbf{A}$  of Eq. (20) has an associated left eigenvector which will be used to put the quasilinear system into characteristic form. Those eigenvectors are given below.

$$\lambda^{1,2} = \mp C_1 \Rightarrow l^{1,2} = \{\pm C_1 v, \mp C_1 u, v, -u\} \quad (27)$$

$$\lambda^{3,4} = \mp C_2 \Rightarrow l^{3,4} = \{\pm C_2 u, \pm C_2 v, u, v\} \quad (28)$$

“Multiplying” Eq. (20) by each of these eigenvectors produces an ordinary differential equation (ODE) which is satisfied along the respective characteristics. The result is the following set of four equations:

$$\mp C_1 v \frac{du}{d\xi} \pm C_1 u \frac{dv}{d\xi} + v \frac{dx}{d\xi} - u \frac{dy}{d\xi} + v b_x - u b_y = 0 \quad \text{when} \quad \frac{d\eta_0}{d\xi} = \pm C_1 \quad (29)$$

$$\mp C_2 u \frac{du}{d\xi} \mp C_2 v \frac{dv}{d\xi} + u \frac{dx}{d\xi} + v \frac{dy}{d\xi} + u b_x + v b_y = 0 \quad \text{when} \quad \frac{d\eta_0}{d\xi} = \pm C_2 \quad (30)$$

Note, it is not possible to define Riemann invariants or variables in this case, but nevertheless, the equations can be written in characteristic form. If  $u$ ,  $v$ ,  $x$ , and  $y$  are known at one time step we can march that solution forward in time along the characteristics to obtain the solution at the next time step. Figure 5 shows the spatial discretization at time  $k$  and  $k+1$ . The four dependent variables are known at each location  $\eta_{0i}$  at time  $k$ . To solve for the four quantities at location  $\eta_{0i}$  and time  $k+1$  we march the solution at time  $k$  forward along the four characteristics that initiate at the locations  $\eta_{01+}$ ,  $\eta_{02+}$ ,  $\eta_{01-}$ , and  $\eta_{02-}$  to arrive at the location  $\eta_{0i}$  at time  $k+1$ . Linear interpolation is used to find the necessary field quantities at time  $k$ . We are then left with the following matrix inverse problem to find the unknown quantities:

$$\begin{Bmatrix} u_i^{k+1} \\ v_i^{k+1} \\ x_i^{k+1} \\ y_i^{k+1} \end{Bmatrix} = \begin{bmatrix} -C_{1+}v_{1+} & C_{1+}u_{1+} & v_{1+} & -u_{1+} \\ C_{1-}v_{1-} & -C_{1-}u_{1-} & v_{1-} & -u_{1-} \\ -C_{2+}u_{2+} & -C_{2+}v_{2+} & u_{2+} & v_{2+} \\ C_{2-}u_{2-} & C_{2-}v_{2-} & u_{2-} & v_{2-} \end{bmatrix}^{-1} \begin{Bmatrix} x_{1+}v_{1+} - y_{1+}u_{1+} - v_{1+}b_{x1+}\Delta\xi + u_{1+}b_{y1+}\Delta\xi \\ x_{1-}v_{1-} - u_{1-}y_{1-} - v_{1-}b_{x1-}\Delta\xi + u_{1-}b_{y1-}\Delta\xi \\ -C_{2+}\lambda_{12+}^2 + x_{2+}u_{2+} - y_{2+}v_{2+} - u_{2+}b_{x2+}\Delta\xi - v_{2+}b_{y2+}\Delta\xi \\ C_{2-}\lambda_{12-}^2 + x_{2-}u_{2-} - y_{2-}v_{2-} - u_{2-}b_{x2-}\Delta\xi - v_{2-}b_{y2-}\Delta\xi \end{Bmatrix} \quad (31)$$

Note that proper accounting of boundary conditions must be provided. In the experiments performed in this work the outer radius is clamped to a rigid plate and an impact with a fast moving projectile is imposed at the center. These boundary and loading conditions will be implemented by fixing the outer edge and applying a known radial and out-of-plane velocity at some inner radius close to the center (as determined from the experimental measurement). The other quantities along the boundary are obtained from the characteristics that leave the domain of interest as illustrated in Figure 5. Note that the applied pressure is set to zero for all of our simulations. A code written in MATLAB is used to solve this boundary-initial value problem and a semi-inverse method is used to match the measured deformation with the calculated deformation and determine the suitability of constitutive models.

## 5. EXPERIMENTAL SETUP

We now turn to a description of how the above boundary-initial value problem is implemented in the laboratory. The test setup consists of the circular clamp ( $R=140$  mm) holding the specimen and an air gun. An oblique view of non-impact surface of a rubber membrane in the test apparatus is shown in Figure 6. The circular frame is cut from an aluminum block; a 305 mm (12 in) diameter O-ring is placed between the rubber and one of the aluminum plates to clamp the rubber securely and prevent slipping. The barrel of the air gun is placed at least one meter behind the surface of the specimen in order to prevent the air burst following the projectile from affecting the deformation of



the membrane; such large separation between the muzzle and the specimen provides significant challenges to aiming the projectile on the center of the membrane.

When the air gun is fired a projectile is launched from the 14.22 mm (0.56 in) diameter barrel at a velocity in the range of 50-160 m/s depending on the projectile and pressure used. A 12.7 mm (one-half inch) diameter spherical steel ball and two cylindrical nylon bullets that were custom-machined to an ogive nose were used. The benefit of the steel ball is that because of its symmetry, it creates an axisymmetric deformation, regardless of its orientation at impact. However, due to the fact that the ball is slightly smaller than the barrel diameter, much of the air pressure rushes around the ball causing two main problems. First, this excess space results in the maximum speed being limited to rather small values of around 50 m/s. Second, the extra airflow around the ball diminishes the ability to aim the projectile correctly. The ball also develops unpredictable spin travelling down the length of the non-rifled barrel which, even over the short flight distance, creates difficulty in hitting the exact center of the membrane. In contrast, the cylindrical nylon bullets were machined to provide a sliding fit in the barrel, resulting in improved ability to aim as well as increase the speed due to the tight fit and the decreased mass. The projectile, however, has the problem of rotating (tumbling) a bit during flight along axes other than the flight path which results in slightly skewed impact loading; in order to take this into account, the axial and radial motion of one set of markers on the specimen away from the point of impact was digitized and used to characterize the imposed loading.

The motion of the membrane is monitored by two Photron SA1 high-speed video cameras, one oriented perpendicular to the propagation direction of the projectile, providing a meridional view and the other recording at an oblique angle in order to obtain a projection of the membrane (as indicated in Figure 6). The oblique view allows for observation of the axisymmetry of the deformation as well as the exact location of impact. In some tests, the rim of the circular clamp obscures the initial impact and deformation of the membrane in the meridional view so the oblique view is crucial for measurement of the exact time and location of impact as well as the kink wave speed. The meridional view allows for the precise measurement of the deformed profile; in cases when the deformation remains truly axisymmetric, all the kinematic quantities of the deformation of the membrane can be determined completely from the meridional profile. The frame rate was adjusted depending on the membrane material used. The impact is typically recorded at 10,800 frames per second.

In order to quantify the deformation, Lagrangian markers are drawn on the specimen. A stencil was used to draw the circumferential lines shown in Figure 6, to permit accurate data collection. Measurement of the location of Lagrangian markings along the deformed profile allows for determination of the axial and radial displacement of the marked points; this is the principal measurement in each frame. From these measurements, the principal stretches, and the particle velocities in the radial and axial directions can be

obtained through numerical differentiation. Furthermore, tracing the motion of the Lagrangian marker closest to the ball provides an efficient way to deal with the boundary condition to be used in the simulations, and avoid the complications that arise in the area of contact with the projectile. The process of adding Lagrangian markers to the specimen warrants further detail because of some unique challenges in marking thin samples of polyisoprene rubber. First, the majority of pens and markers have difficulty transferring ink to the surface of the smooth polyisoprene rubber. The extra fine point oil-based opaque paint markers from Sharpie<sup>®3</sup> work best. The other challenge is even the slight pressure of dragging a pen tip causes stretching and wrinkling of the thin and soft rubber sheet. This hurdle is overcome by adhering an Avery<sup>®4</sup> adhesive label paper to the back of the rubber sheet to decrease the tendency to stretch and wrinkle. Even with the adhesive sheet, a very gentle touch is required to avoid the pen tip getting stuck thereby stretching and wrinkling the sheet.

## 6. EXPERIMENTAL RESULTS

Results from two experiments performed with impact speeds of 150 m/s and 160 m/s, referred to as Test A and Test B, respectively, are described to illustrate the data collection and analysis process. In the following section we will compare these experimental results with simulations. .

Both tests used a nylon bullet with an air-gun pressure of 827 kPa (120 psi). The data collection begins with images taken from the side view; a selected sequence of images from Test B is shown in Figure 7, where the meridional view and oblique view are shown as pairs<sup>5</sup>. As a result of minor misalignments in the air-gun, discussed above, the impact typically occurs slightly off center; therefore, the impact point and the time variation of the radial and out of plane locations of each Lagrangian marker are recorded. In the first image, Figure 7a, the point of impact is marked with a red 'x' symbol and the initial location of each Lagrangian marker that is tracked in subsequent frames is marked with green '+' symbol on the meridional view of the undeformed membrane. Each of these points is tracked throughout the experiment as illustrated in the subsequent frames. The tracking of the position of Lagrangian points along the evolving profile of the membrane is the primary diagnostic measurement from the membrane tests. These measurements allow calculation of the evolution of the principal stretches as well as particle velocities at the selected points in the membrane and interpolation for points in-between. Due to the rather coarse spacing of the measurement points and the difficulty in recording exact position, the raw data is fairly noisy. Applying a simple moving average filter using 5 data points, however, cleans it up significantly.

---

<sup>3</sup> Sharpie<sup>®</sup> is a registered U.S. trademark of Sanford

<sup>4</sup> Avery is a registered U.S. trademark of Avery Denison Corporation

<sup>5</sup> A video file of the oblique and meridional views of Test A is available online in the Supplementary Material of this paper.

The general features of the wave propagation in the membrane can be discerned from the images in Figure 7. As indicated in Section 3, the axial wave propagates the fastest, and with its arrival brings a radially inward movement of the circular Lagrangian markers (this can be observed easily in the video file included under Supplementary Materials). Concomitant with the axial wave is a contraction in the hoop direction that *may* manifest itself much later as a fine set of wrinkles (buckles) in the thin membrane; we will explore this in Section 8 through numerical simulations. The axial wave is followed by the slower kink wave; while the axial wave stretches the membrane and keeps the membrane in its initial plane, the kink wave brings with it a dramatic change in the out-of-plane displacement and velocity as well as the meridional stretch. It should be noted that both the axial and kink waves are nonlinear waves, and that their speeds depend on the stress/stretch state. In particular, the axial wave is expected to slow down with increasing stretch while the kink wave will increase in speed with increasing stretch. The measured principal stretches,  $(\lambda_1, \lambda_2)$  for Test A and B are plotted as a function of the normalized radial position  $\eta_0$  in Figures 8 and 9 at time increments of 275  $\mu\text{s}$ . We note that there is a small uniform initial stretch in each test which is visible in Figure 9<sup>6</sup>. The corresponding variations of the out-of-plane particle velocity,  $\dot{z}(\eta_0, t)$ , are plotted as a function of the normalized radial position  $\eta_0$  in Figure 10, at the same time increments. The arrival of the axial wave cannot be seen easily in these plots, but the approximate arrival of the kink wave is marked in each curve by an asterisk. Ahead of the kink wave, the stretch state reaches  $(\lambda_1 = 1.4, \lambda_2 = 0.9)$ , but just behind the kink wave, the meridional stretch  $\lambda_1$  jumps to a maximum of about 9 in Test A and 10 in Test B with an accompanying hoop stretch  $\lambda_2$  of 0.5 and 0.6 respectively. With progression of time, the kink wave goes towards the fixed boundary with the large stretch following the kink wave. From these measurements, it is also possible to get an estimate of the stretch rate. This data suggests a maximum stretch rate of  $10^4 \text{ s}^{-1}$  was achieved.

The out-of-plane particle velocity is zero prior to the arrival of the kink wave; immediately behind the kink wave, the particle velocity increases rapidly to that imposed by the projectile. Even though this data is noisy due to limits in experimental resolution, it appears that the out-of-plane velocity reaches a steady value behind the kink wave. The kink wave speed can be obtained from the out-of-plane velocity plots or directly from measurement of the kink position: the oblique view camera images provide a better indication of the location of the kink wave. In order to measure the Lagrangian kink wave speed properly, the time at which the kink wave reaches each concentric circle is recorded. The kink position has been plotted as a function of time for three tests in Figure 11. Test A and B are at similar speeds but the third example is at a much slower speed, a third of that of the other two. Despite the dramatic difference in impact velocity, the kink

---

<sup>6</sup> This arises from the procedure of clamping the specimen in the circular holding frame.



waves propagate with the same speed of  $\sim 25$  m/s for the first 2 ms. Beyond 2 ms the axial wave, reflected from the outer boundary, arrives at the kink front and causes deviation in the propagation of the kink wave. The initial 2 ms however demonstrates that, as predicted, the kink speed is a function of the material, not the impact speed. Recall from Figure 4 that the axial and kink wave speeds approach about 25 m/s according to the DCMR model; it would appear that the experiments approach the same limit.

The results of the impact experiments on polyisoprene can be summarized with the following observations:

- The axial wave causes significant in-plane stretching of the membrane, setting the conditions in which the kink wave develops;
- The kink wave follows in the pre-stretched membrane with increasing speed and eventually settles to a steady-state value that is independent of the impact velocity;
- The kink wave causes a very large jump in the out-of-plane particle velocity, and therefore the stretch rate;
- Behind the kink wave, the stretch increases rapidly to very high levels and may approach failure of the membrane.

One last experimental observation to consider before moving to the simulations is the possibility of wrinkling. Compressive stress in a very thin sheet can cause wrinkling and indeed, this has been observed in some of the experiments (see Figure 12 which shows that wrinkling can develop in the vicinity of the kink wave). This image shows the wrinkles at about 1 ms after their initiation so they have had some time to develop. In this test the rubber membrane was impacted at 55 m/s with the 12.7 mm ( $\frac{1}{2}$  in) diameter steel ball. The primary difference between this and the previously described tests is impact speed. Vermorel et al. (2006) studied this wrinkling phenomenon at the kink wave by using a linear elastic buckling analysis. In their tests unconstrained specimens were impacted at about 5 m/s. We examine the possibility of wrinkling through an analysis of the nonlinear membrane impact problem in Section 8.

## 7. SIMULATION RESULTS

We move now to the description of the simulations of the above described experiment. The procedure for simulating dynamic axisymmetric deformation of a membrane through the MC has been introduced in Section 4. The only steps necessary to apply that procedure to the test are to introduce dimensions, boundary conditions, and material properties. Dimensions and material density are easily measured; the boundary condition at the outer radius is fixed so there is no radial or out of plane motion. The inner radius boundary condition should, in principle, be the velocity of the impact point; however, the details of the contact zone between the projectile and the membrane cannot be easily

determined. In the simulation, it is sufficient to apply the known motion of any fixed point within the membrane. The time variation of radial and out-of-plane velocities of the impact point and a Lagrangian marker near the impact point ( $r = 16.7\text{ mm}$ ) measured in the 160 m/s test are given in Figure 13 and 14; this motion is imposed in the simulations, avoiding uncertainties associated with the state of contact between the projectile and the membrane. The material is modeled with the form of DCMR and Q-LP models discussed in Section 2.

Figure 15 shows a selected sequence of images, showing an oblique view of the simulated membrane response. For visualization, the colors in Figure 15 indicate the meridional stretch<sup>7</sup>; it is easily observed that an axial wave moves in the planar membrane, and is followed by the kink wave that brings along with it a large stretch as well as out-of-plane particle motion.

For quantitative comparison of the predictions with the experiments, the meridional profiles of the membrane obtained from the simulations with both the DCMR and Q-LP material models are plotted on the experimentally recorded images at selected time steps in Figure 16. In addition to the overall profile, the positions of the Lagrangian markers that identify the mid-width locations of the concentric circles are identified in the simulated profiles by an asterisk in order to enable visualization of the motion of reference points in comparison to that observed in the actual experiment.

These results show that while neither model captures the behavior exactly, the Q-LP based model, representing the generalization of the quasistatic stress strain behavior, deviates significantly from the experiments. There is clearly a curvature in the profile which is completely missing from the behavior predicted by the Q-LP model. With the DCMR model on the other hand, the membrane exhibits a much greater curvature than observed in the experiment. This is primarily apparent in the region with the highest stretches suggesting that the actual material does show some increase in stiffness by a greater amount than that provided in the DCMR model. One might conclude that both material models provide qualitatively reasonable results; they capture the propagation of the axial and kink waves, indicate the development of large stretches behind the kink wave, etc. However, quantitative matching requires additional features in the constitutive response.

To further examine this comparison we have plotted the profiles for the stretches, stresses, and out of plane velocity for the DCMR and Q-LP models in Figures 17 through 21. The figures containing predictions of kinematic quantities have the associated experimentally measured quantities, shown above in Figures 8-10, overlaid to facilitate direct comparison. Starting with meridional stretch, when comparing the experimental results to the predictions in Figure 17, the DCMR model predicts a result closer to the physical measurement. The Q-LP model predicts a rather sharp jump in stretch from  $\sim 2.5$

---

<sup>7</sup> A video animation of the results of this simulation is available online with the Supplementary Material for this paper.

to 5 which does not decay during the time period examined; this feature is absent from the experiment. The DCMR prediction does show a decrease in stretch around the inner boundary condition which is not seen in the experiment but it is possible that it is simply not resolved due to complications of measurements around the projectile. A similar decrease in magnitude, though of opposite sign, is seen in the DCMR predictions of circumferential stretch. This inflection is seen in the experimental data and is absent from the Q-LP simulations; however, the magnitude of hoop stretch predicted by the DCMR simulation is much larger than that measured in the experiment. While the predicted stress profiles in Figures 19 and 20 cannot be compared to experimental measurements, they do contain an illustration of the reason for the differences between the DCMR and Q-LP results. The meridional stresses are similar but the hoop stresses are dramatically different. The Q-LP model shows essentially no hoop stress whereas the DCMR model has a spike at the inner boundary which decays rapidly but to a value still nearly an order of magnitude greater than that predicted by the Q-LP model. Comparison of the predicted and measured velocity profiles does not provide any clear distinctions but the experiment does seem to exhibit a bit of the maximum velocity plateauing behavior seen in the Q-LP results. The hoop stress then is the key difference in the models and would lead us to believe that finding a model which predicts some middle ground between these two stresses is likely to produce a displacement profile very similar to that measured in the experiment. It is interesting to observe that, even with these large disparities, the kink wave speeds for both models seem to match that of the experiment reasonably well.

## 8. WRINKLING

Vermorel et al. (2006) observed wrinkling at the kink wave during 5 m/s impact of an unconstrained rubber membrane. In the image taken from a test at 55 m/s impact, shown in Figure 12, wrinkles are observed in the vicinity of the kink wave. However, in neither the 150 nor the 160 m/s impact test was significant wrinkling observed. For wrinkling to occur, a compressive stress must develop. Two variables affect the possibility of those stresses developing: impact velocity and initial stretch. If we look first to the simulations of the high speed impacts, specifically the hoop stress profiles shown in Figure 20, we note that not only was the hoop stress never negative, it never dropped below the initial stress level due to the initial stretch of the specimen for either material model.

When we simulate slower impact speeds we find a different result. We have two examples of slow speed impacts during which wrinkles form: the 55 m/s test performed in the same manner as the high speed tests described in the previous sections and the 5 m/s test performed by Vermorel et al. (2006). The 55 m/s test had a small initial stretch whereas the 5 m/s test was on an unconstrained sheet of rubber meaning there were no initial stresses in the membrane. The meridional stretch profiles for the simulation of the 55 m/s and 5 m/s are plotted in Figure 22 at time intervals of 275  $\mu$ s and 1 ms respectively. The profiles for the 55 m/s impact are similar to those observed in the high



speed simulations. The 5 m/s test however has a notably smaller maximum stretch which, is to be expected. The hoop stress profiles for each of the simulations are plotted in Figure 23. Immediately we see a different result: looking first at the 55 m/s test, it can be noticed that the hoop stress does in fact dip below the stress imposed initially, suggesting the possibility of wrinkling. Not only does the stress dip below the initial value but the DCMR model predicts that a compressive stress should develop. The Q-LP model skirts the line but because of that initial stretch, does not clearly drop into the compressive range. The 5 m/s simulation shows the same behavior of dipping below the initial stress value but since the initial stretch is negligible both material models predict compressive stresses develop in the hoop direction. We should note that as soon as these compressive stresses develop, wrinkling should occur, violating the assumption of axisymmetry and therefore invalidating the simulation results after that point. The important conclusion is that the possibility for wrinkle formation is based first and foremost on the impact speed. Clearly, an initial stretch can always be applied that will negate the chance of compressive stresses forming but similarly above a critical velocity, it is also not possible for compressive stresses to develop.

## **9. CONCLUSION**

The response of polyisoprene rubber membranes subjected to high speed impact has been considered. Through the use of high speed photography, the principal stretches and particle velocities through time were recorded for impact speeds in the range of 50-150 m/s. These measured quantities were compared to simulated results using two different constitutive models based on generalizations of the response of polyisoprene to uniaxial tension; one based on the quasi-static response and the other based on the high rate response. While neither of the generalized models captured the membrane response perfectly, the DCMR was seen to produce the closer results. A key difference between the two models was the predicted resistance to hoop deformation pointing the direction for future investigation. Wrinkling was also explored and found to be dependent on impact speed.

## **Acknowledgement**

This work was performed under a program entitled "Dynamic Response of Metal-Polymer Bilayers - Viscoelasticity, Adhesion and Failure" sponsored by the Office of Naval Research (ONR Grant Number N00014-09-1-0541, Program Manager: Dr. Roshdy Barsoum); this support is gratefully acknowledged.

## References

- Cristescu, N. 1967, Dynamic Plasticity. Amsterdam: North-Holland Pub.
- Farrar CL, 1984, Impact response of a circular membrane. *Experimental Mechanics*, **24.2**:144-49.
- Haddow JB, Wegner JL, and Jiang L, 1992, The dynamic response of a stretched circular hyperelastic membrane subjected to normal impact. *Wave Motion*, **16**:137-50.
- Hallquist JO, and Feng WW, 1975, Dynamic response of axisymmetric hyperelastic membranes, *Journal of Applied Mechanics*, **42.4**:890.
- Knowles JK, 2002, Impact-induced tensile waves in a rubberlike material. *SIAM Journal on Applied Mathematics*, **62.4** :1153.
- Lopez-Pamies O, 2010, A new  $I_1$ -based hyperelastic model for rubber elastic materials. *Comptes Rendus Mécanique*, **338.1**:3-11.
- Niemczura J and Ravi-Chandar K, 2011, On the response of rubbers at high strain rates: I: Simple waves, *Journal of the Mechanics and Physics of Solids*, **59**:423-442.
- Niemczura J and Ravi-Chandar K, 2011, On the response of rubbers at high strain rates: II: Shock waves, *Journal of the Mechanics and Physics of Solids*, **59**:443-456.
- Niemczura J and Ravi-Chandar K, 2011, On the response of rubbers at high strain rates: III: Effect of hysteresis, *Journal of the Mechanics and Physics of Solids*, **59**:457-472.
- Vermorel R, Vandenberghe N, and Villiermaux E, 2009, Impacts on thin elastic sheets. *Proceedings of the Royal Society A: Mathematical, Physical and Engineering Sciences*, **465.2103**:823-42.
- von Karman T, Duwez P, 1950, The propagation of plastic deformation in solids. *Journal of Applied Physics*, **21**, 987-994.
- Whitham, GB, 1974, Linear and Nonlinear Waves. New York: Wiley.
- Yang WH and Feng WW, 1970, On axisymmetrical deformations of nonlinear membranes. *Journal of Applied Mechanics*, **37.4**:1002

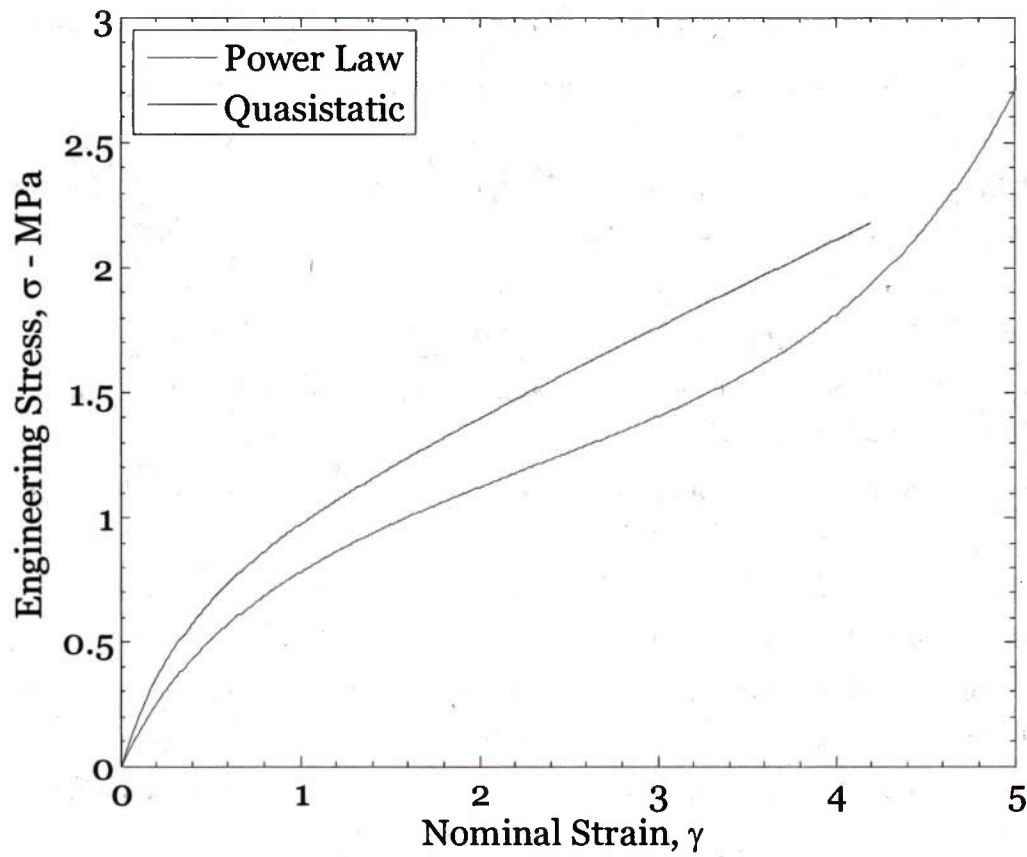


Figure 1: Comparison of the measured uniaxial tensile response of polyisoprene rubber during quasistatic loading (red) to the power law model (blue) used to capture the rate saturated behavior. (Niemczura and Ravi-Chandar 2011a)



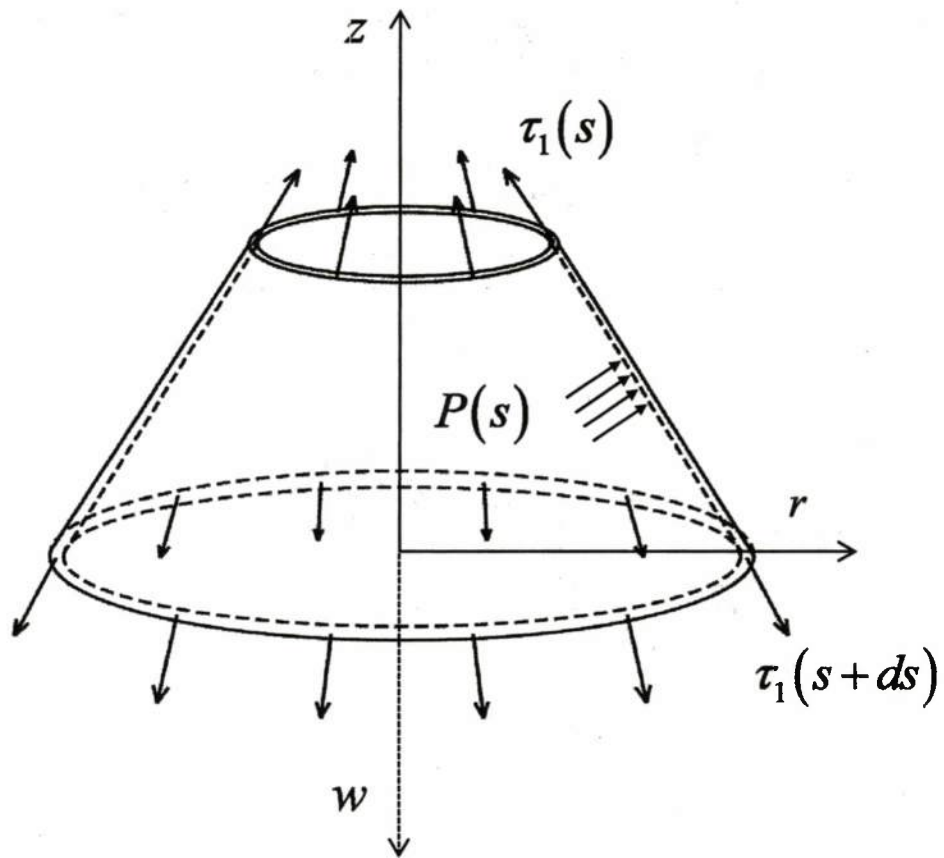


Figure 2: Free body diagram showing axisymmetric deformation of a membrane due to pressure load

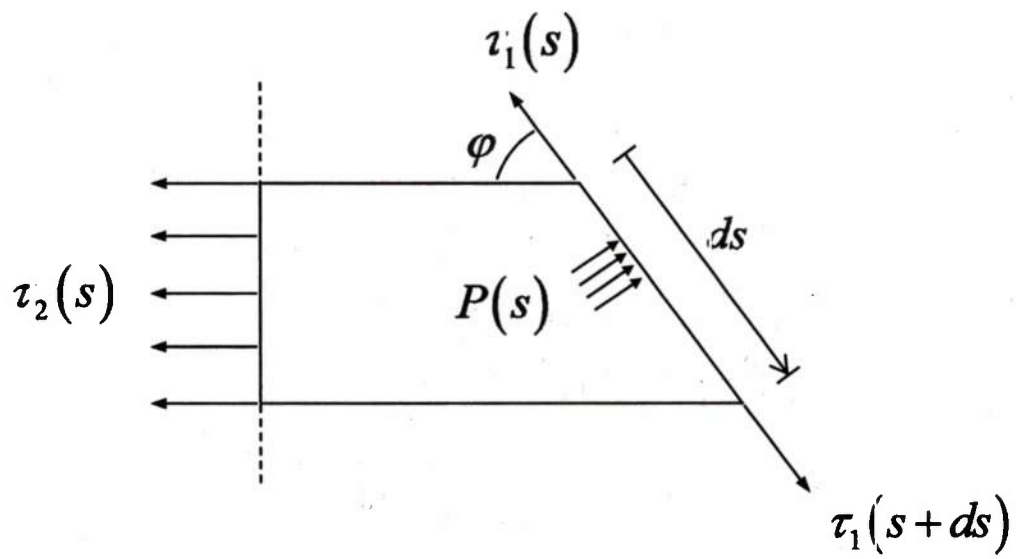


Figure 3: Meridional view of free body diagram of deformed membrane cut along vertical axis

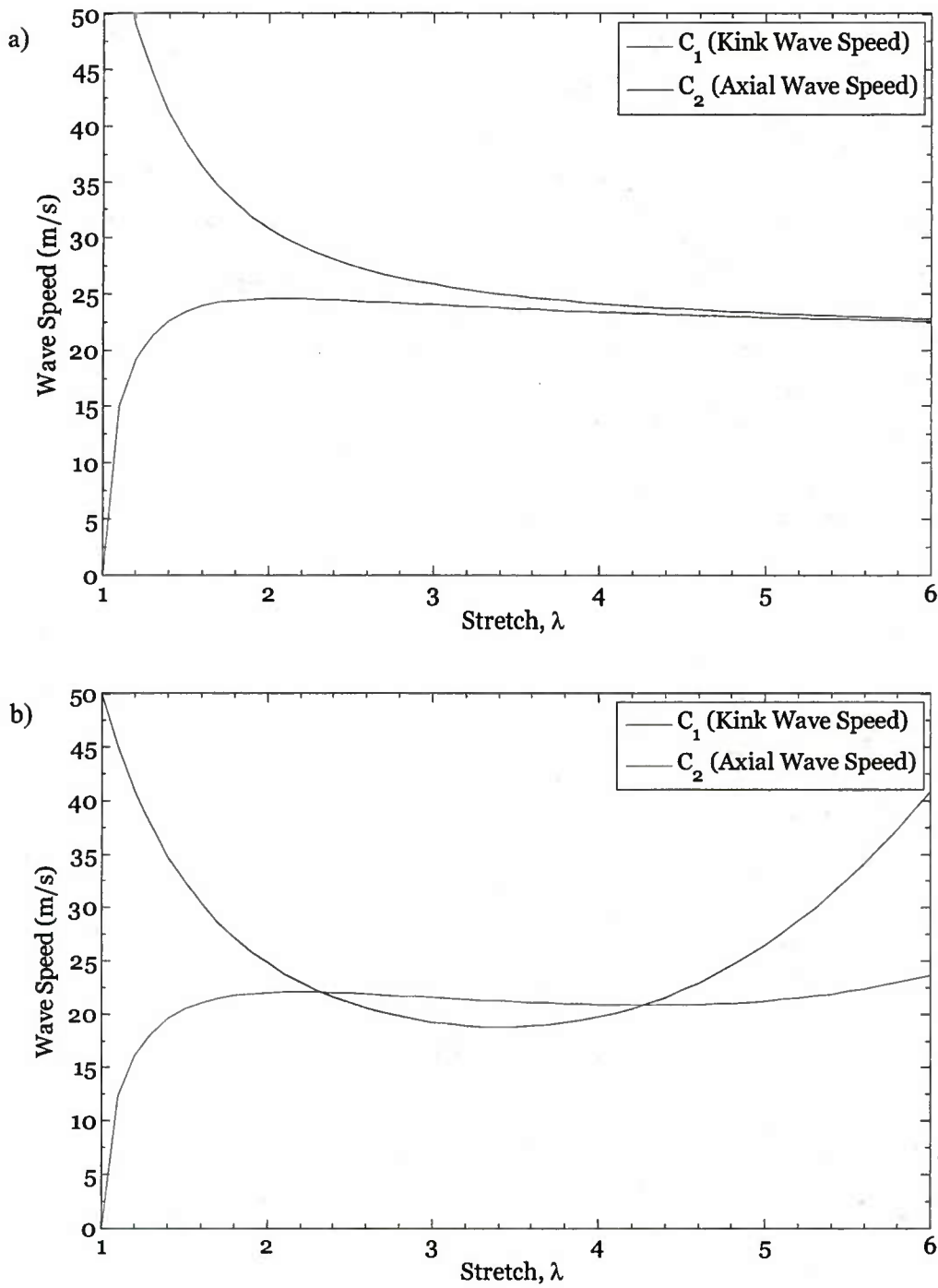


Figure 4: Kink and axial wave speed plotted as a function of stretch in uniaxial tension for a) DCMR material model and b) Q-LP material model



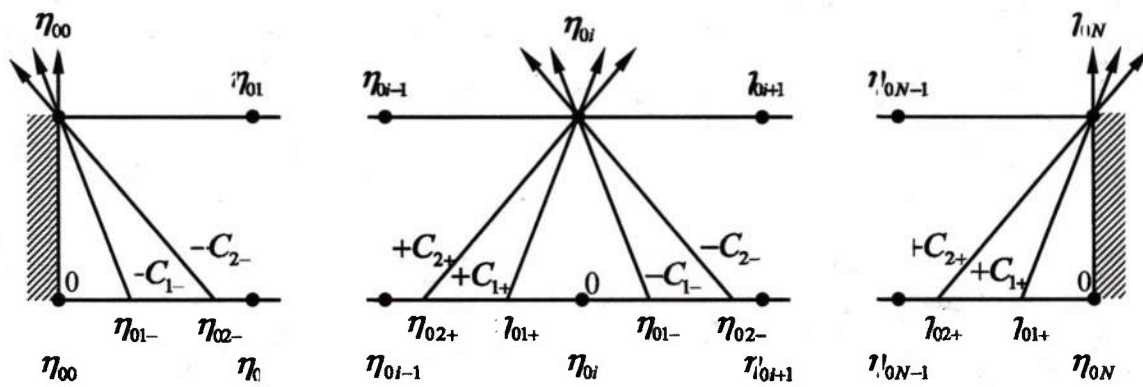


Figure 5: Stepwise calculation by the method of characteristics.

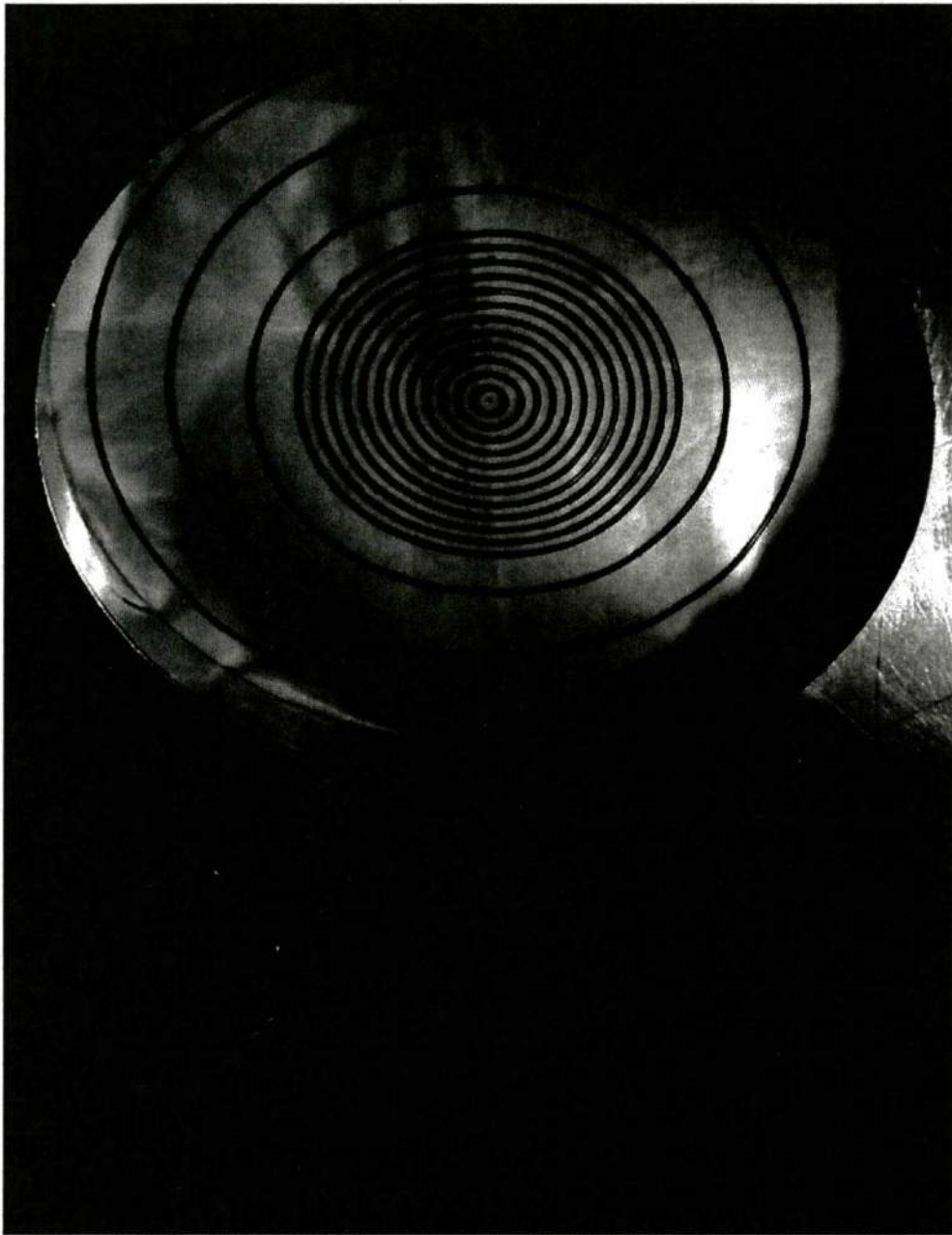


Figure 6: Oblique view of nonimpact side of rubber membrane marked with concentric circles. Inner circle spacing = 5mm

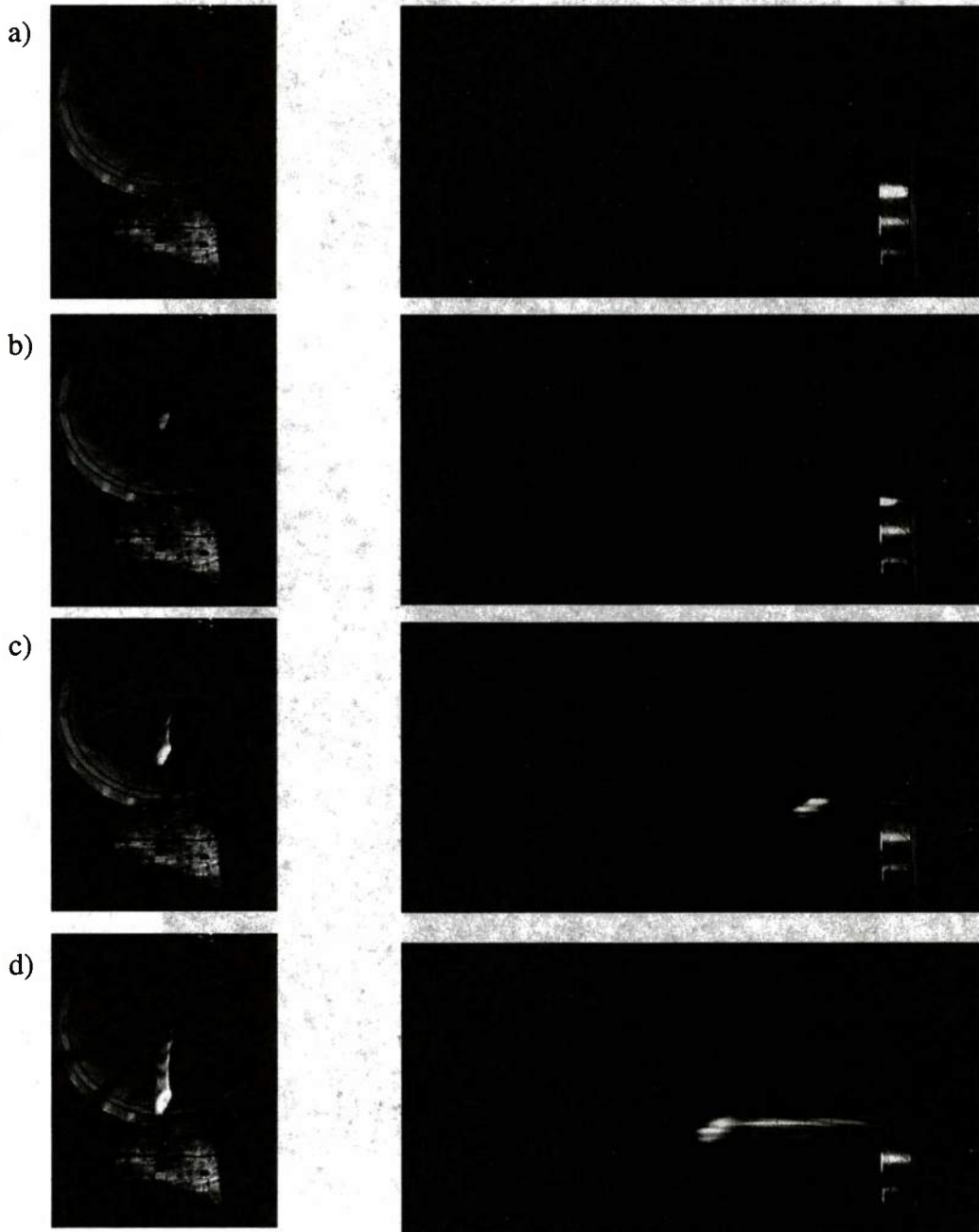


Figure 7: Evolution of membrane deformation in 160 m/s impact speed test. Impact point marked with red x in a). Location of material points tracked for measurement shown as green +'s. Time interval 463  $\mu$ s



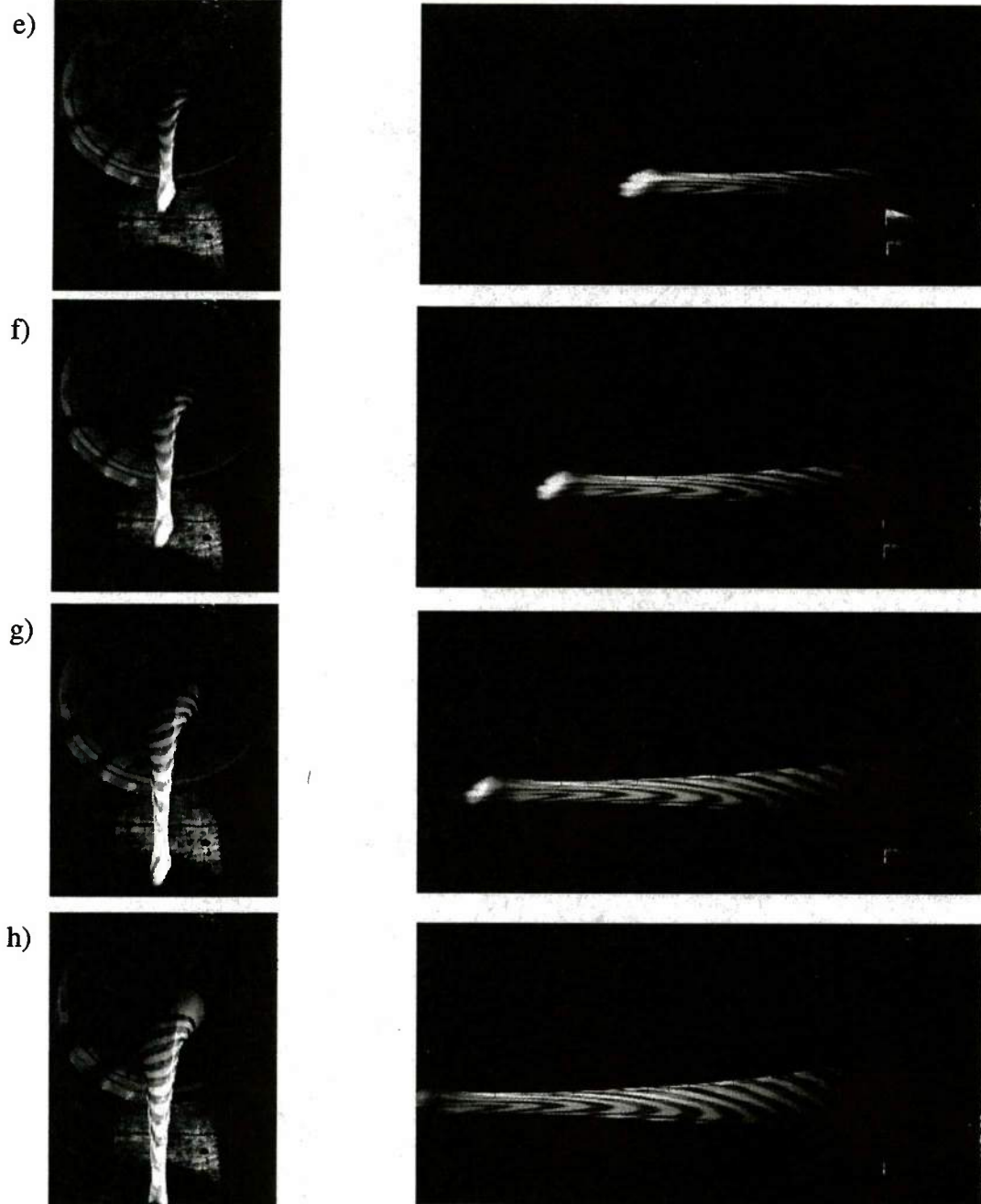


Figure 7: cont

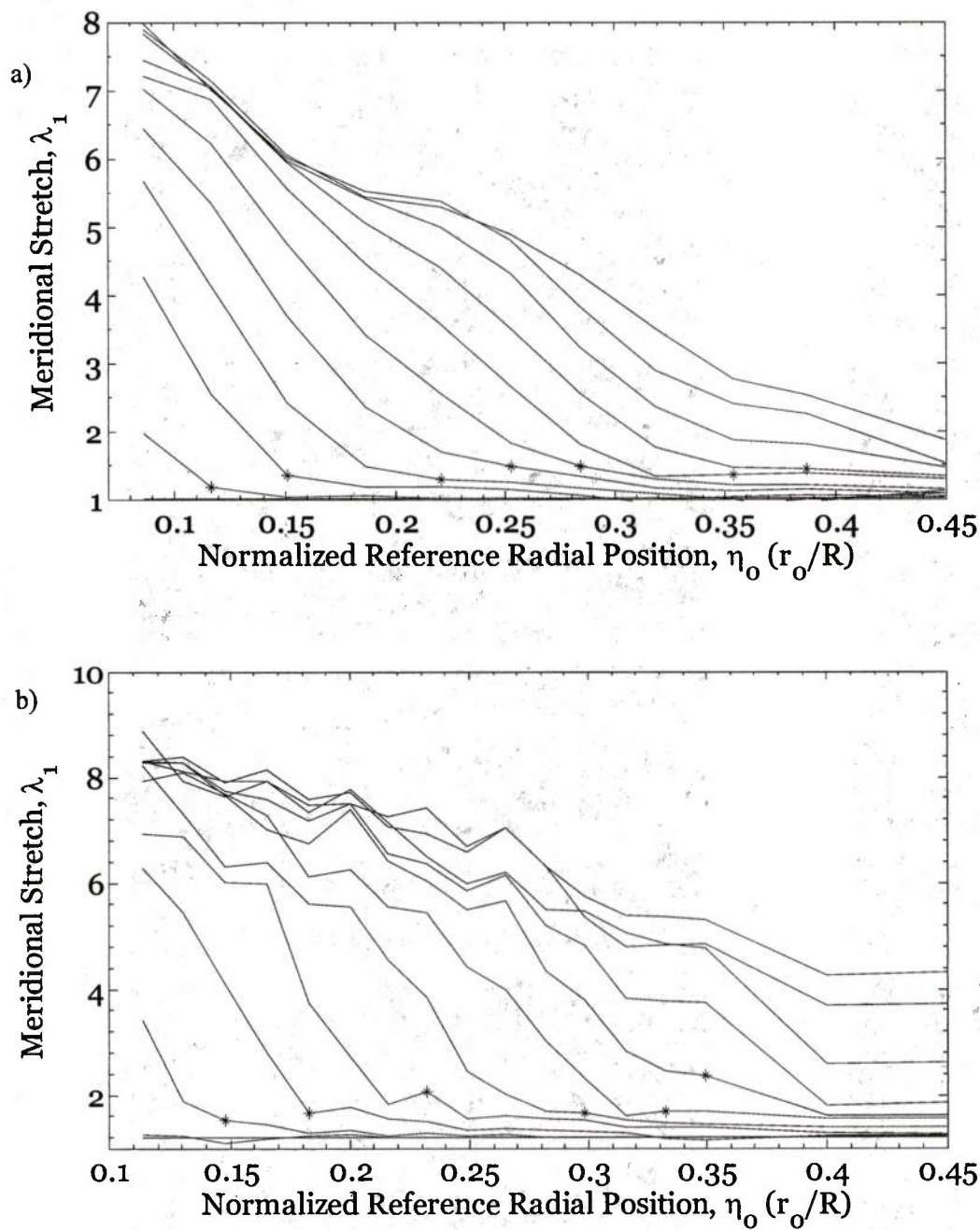


Figure 8: Measured meridional stretch profiles every 275  $\mu$ s for two different impact speeds. a) 150 m/s; b) 160 ms.

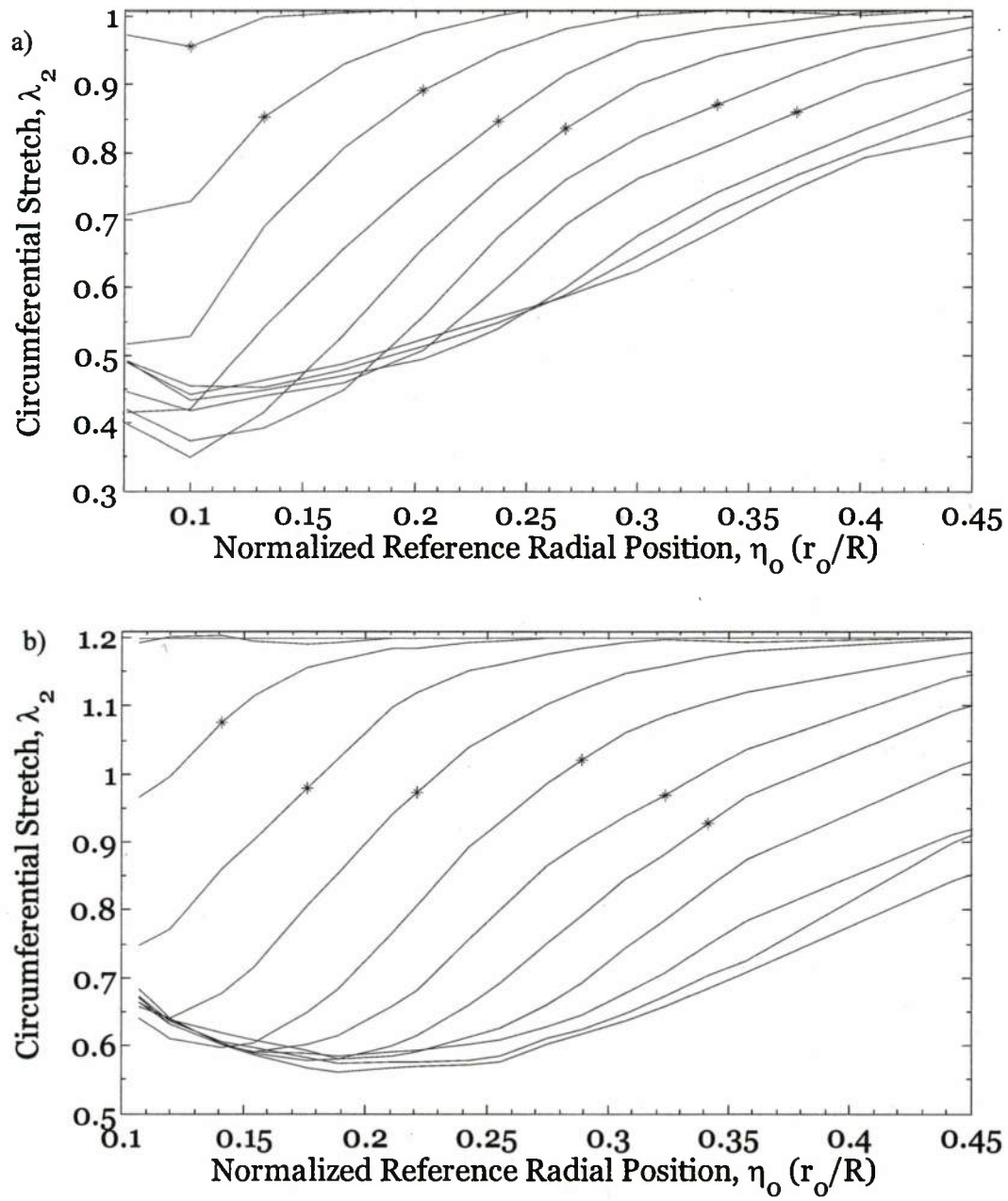


Figure 9: Measured circumferential stretch profiles every  $275\mu\text{s}$  for two different impact speeds. a) 150 m/s; b) 160 ms.



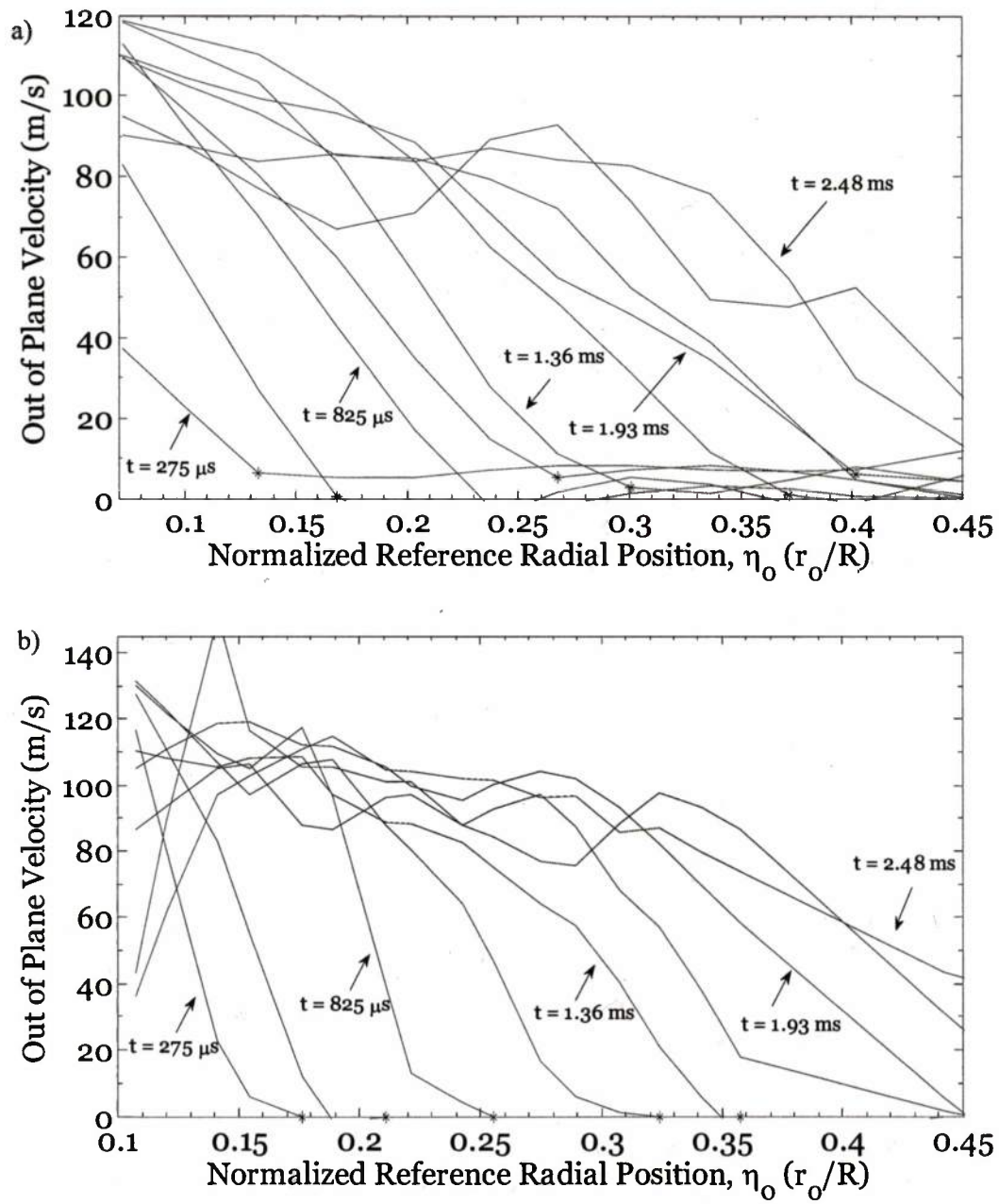


Figure 10: Measured out of plane velocity profiles every  $275 \mu s$  for two different impact speeds. a) 150 m/s; b) 160 m/s.

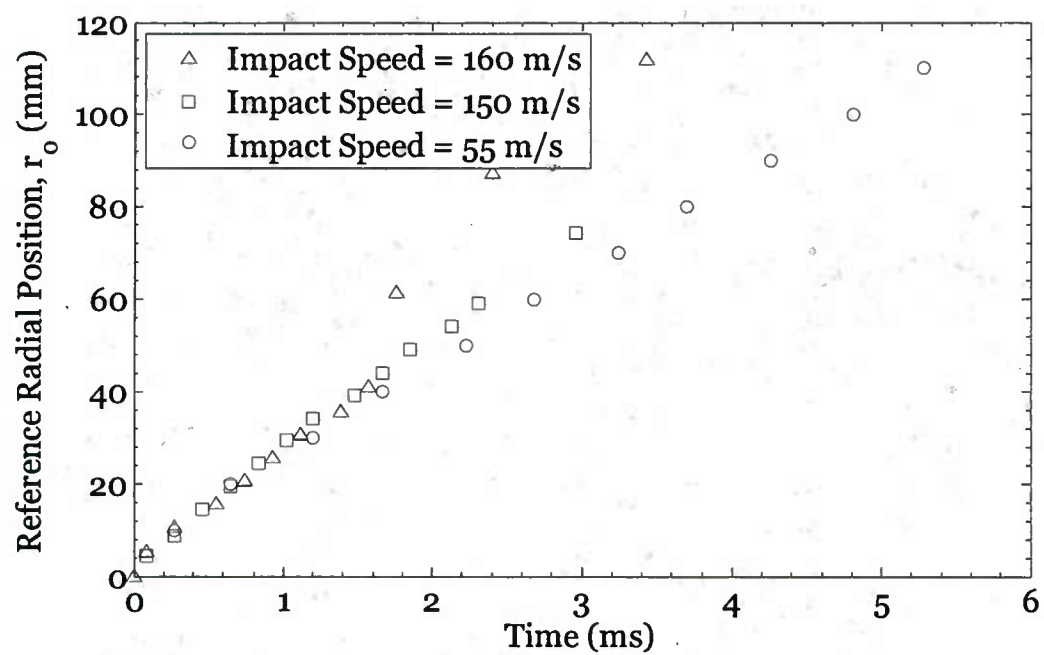


Figure 11: Comparison of measured kink wave position vs. time for three tests. Initial speed ~25m/s observed in all three tests.

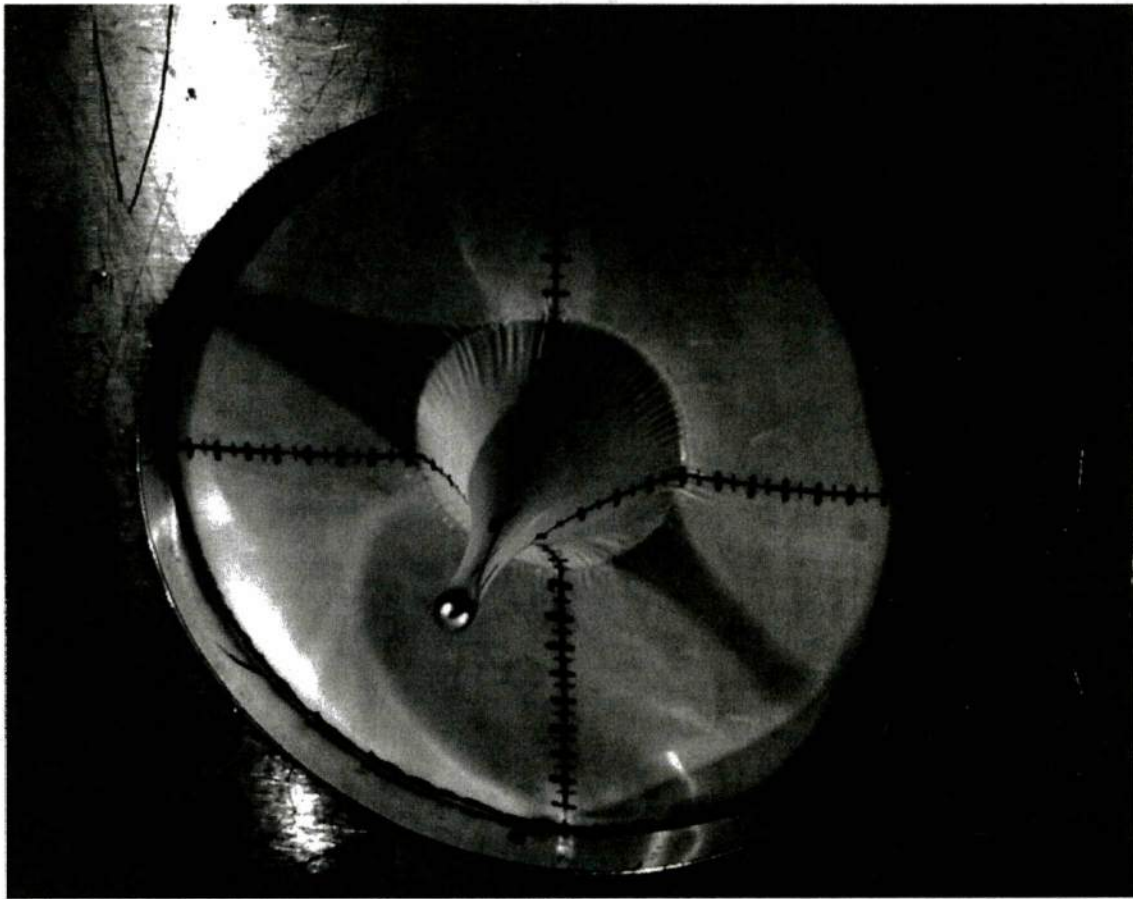


Figure 12: Oblique view of membrane, 2.3 ms after 55 m/s impact, showing the wrinkles that formed around the kink wave.



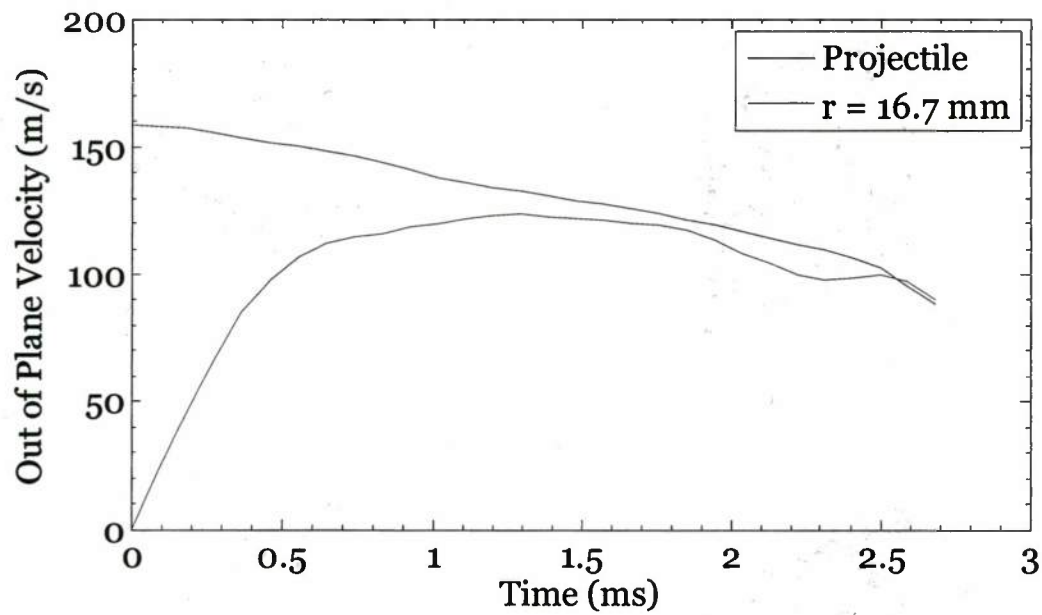


Figure 13: Measured projectile velocity and out-of-plane velocity of a material point on the membrane that is to be used as inner radial boundary condition in simulations of 160 m/s impact.

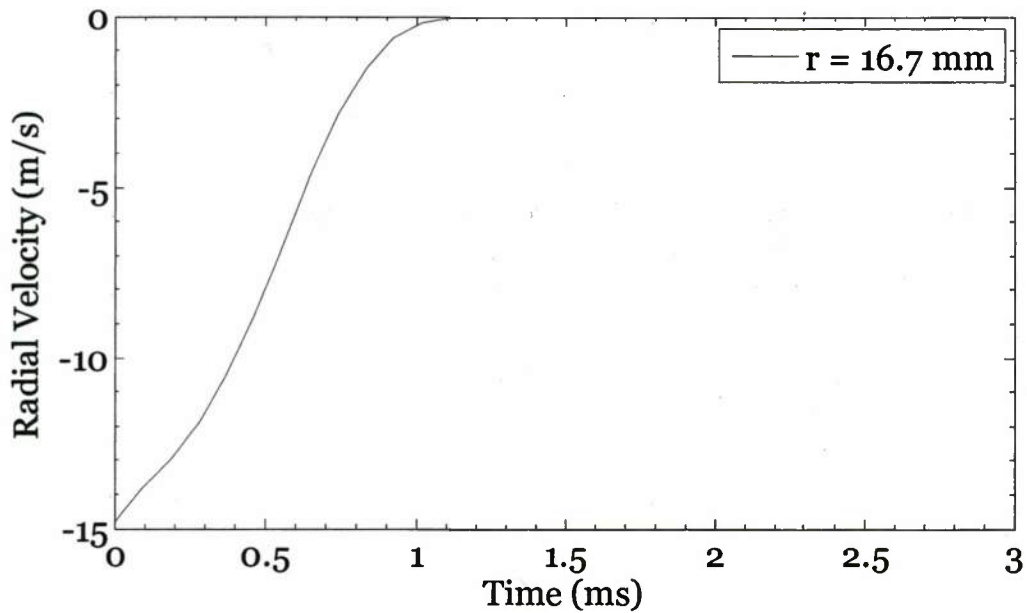


Figure 14: Radial velocity of a material point to be used as inner radial boundary condition in simulations of 160 m/s impact.

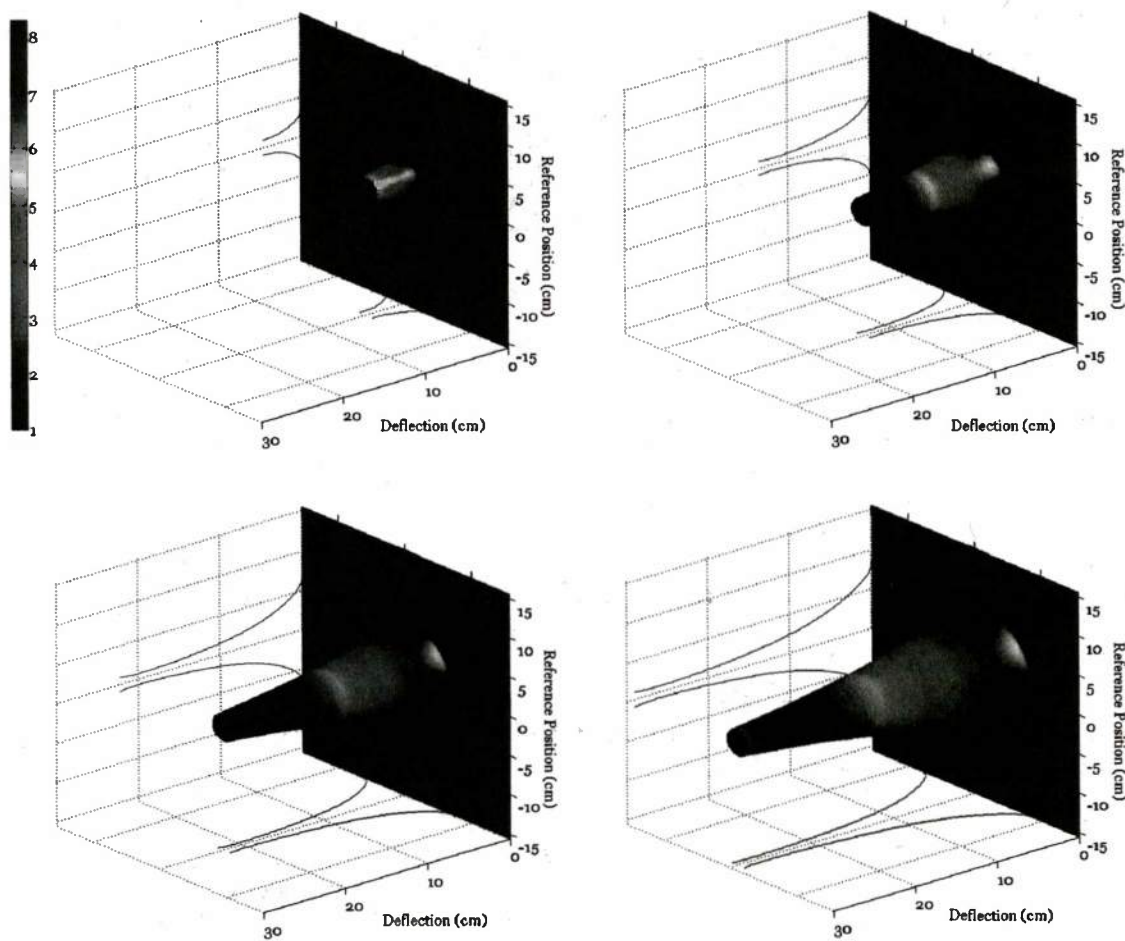


Figure 15: Oblique view of the simulation of 160 m/s impact on circular polyisoprene membrane using the DCMR material model. Color contours signify meridional stretch,  $\lambda_1$ . A video of the simulation is available in the online version under Supplementary Materials.

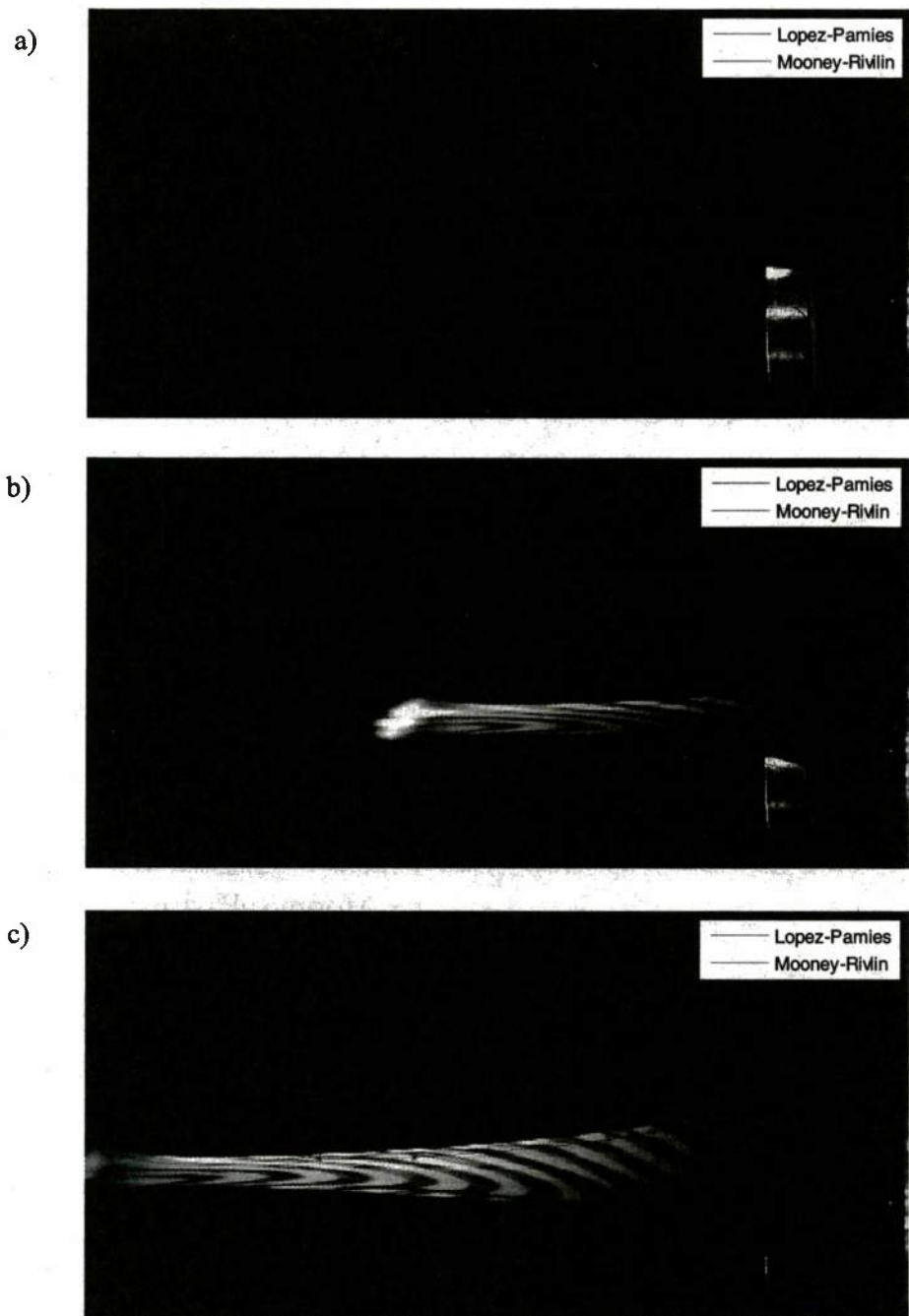


Figure 16: Predicted membrane profile overlaid on high speed images of actual deformation for 160 m/s impact test. Asterisks mark the material points at the midpoint of width for each concentric to show particle motion. a)  $t = 0$  ms; b)  $t = 1.4$  ms; c)  $t = 2.8$  ms.



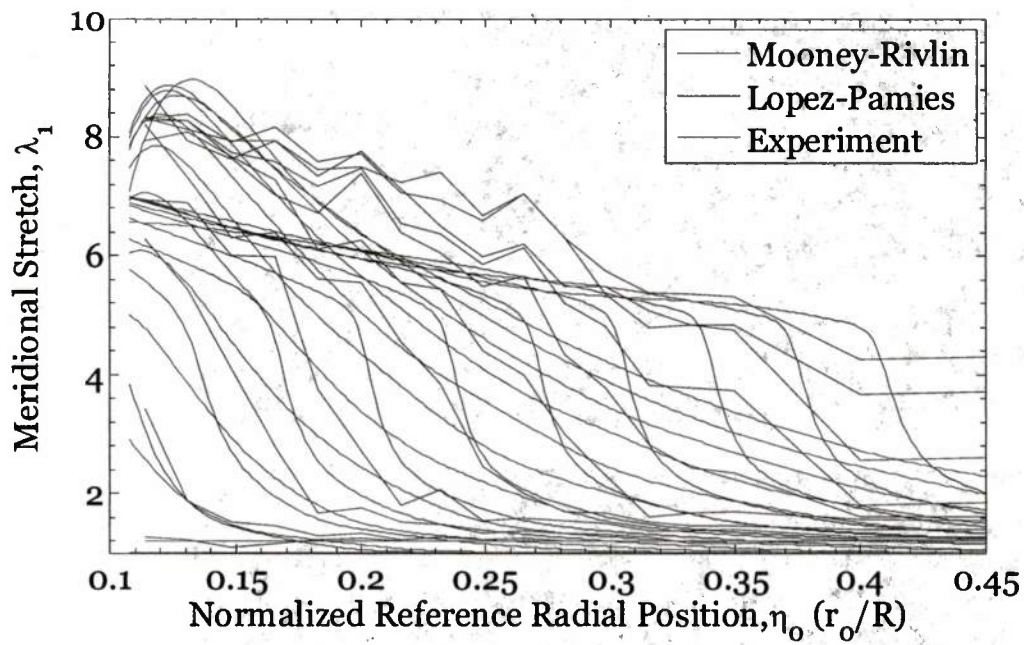


Figure 17: Comparison of meridional stretch profiles every 275  $\mu\text{s}$  predicted by DCMR and Q-LP models to experimental measurements for 160 m/s impact.

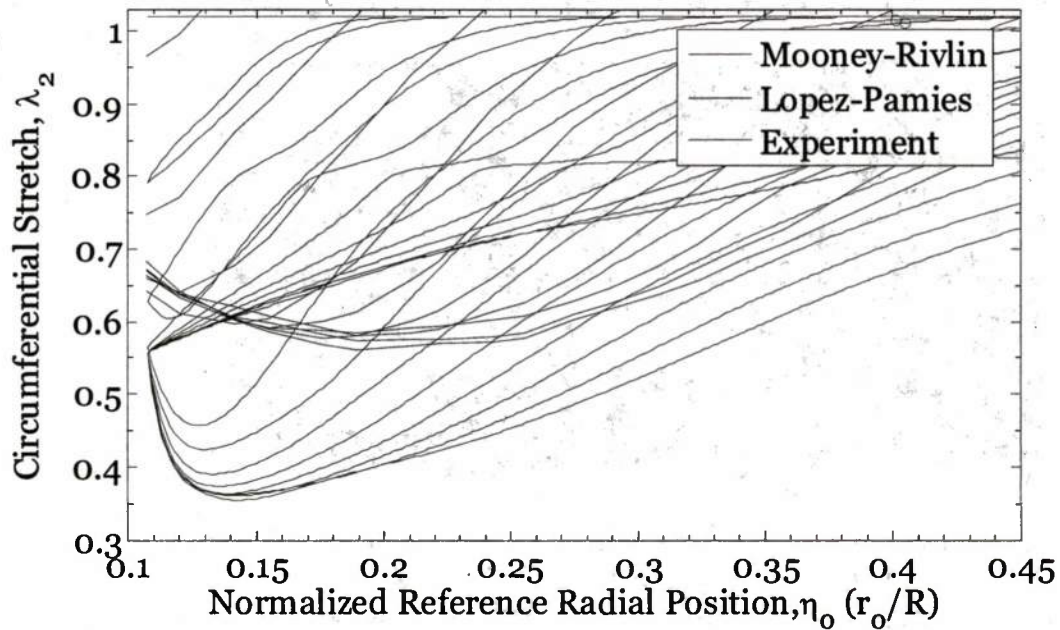


Figure 18: Comparison of circumferential stretch profiles every 275  $\mu\text{s}$  predicted by DCMR and Q-LP models for 160 m/s impact.

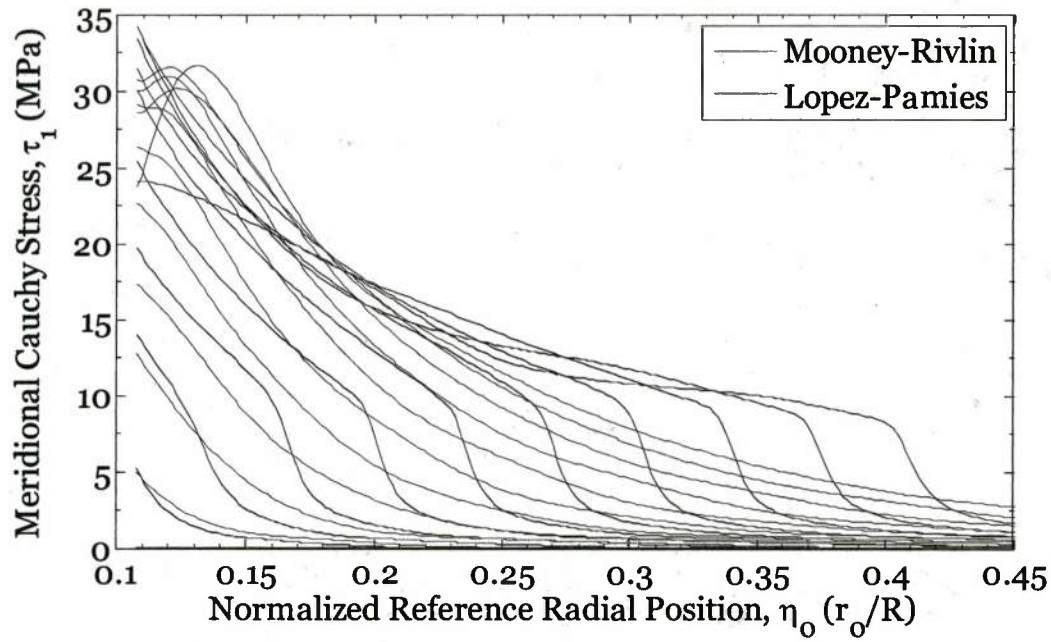


Figure 19: Comparison of meridional Cauchy stress profiles every 275  $\mu$ s predicted by DCMR and Q-LP models for 160 m/s impact.

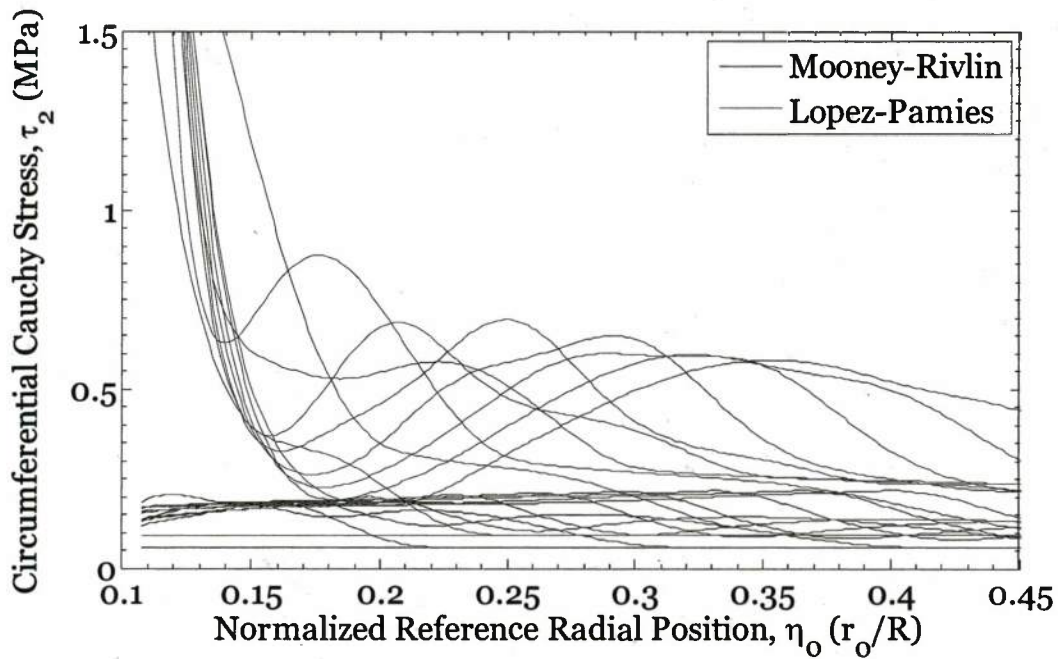


Figure 20: Comparison of circumferential Cauchy stress profiles every 275  $\mu$ s predicted by DCMR and Q-LP models for 160 m/s impact.

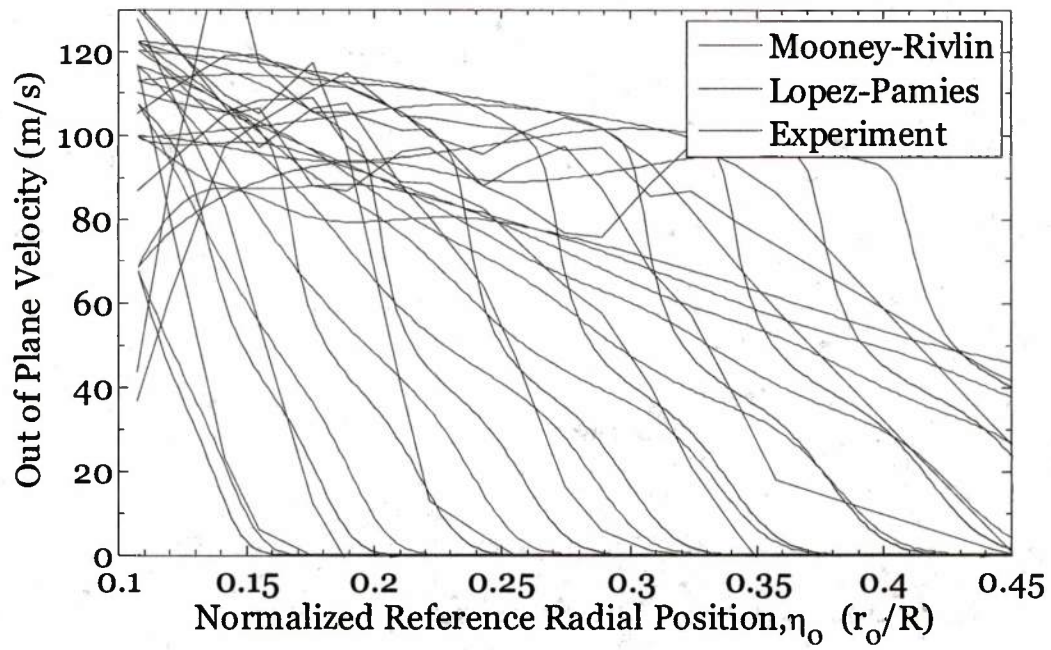


Figure 21: Comparison of out of plane velocity profiles every 275  $\mu$ s predicted by DCMR and Q-LP models to experimental measurements for 160 m/s impact.



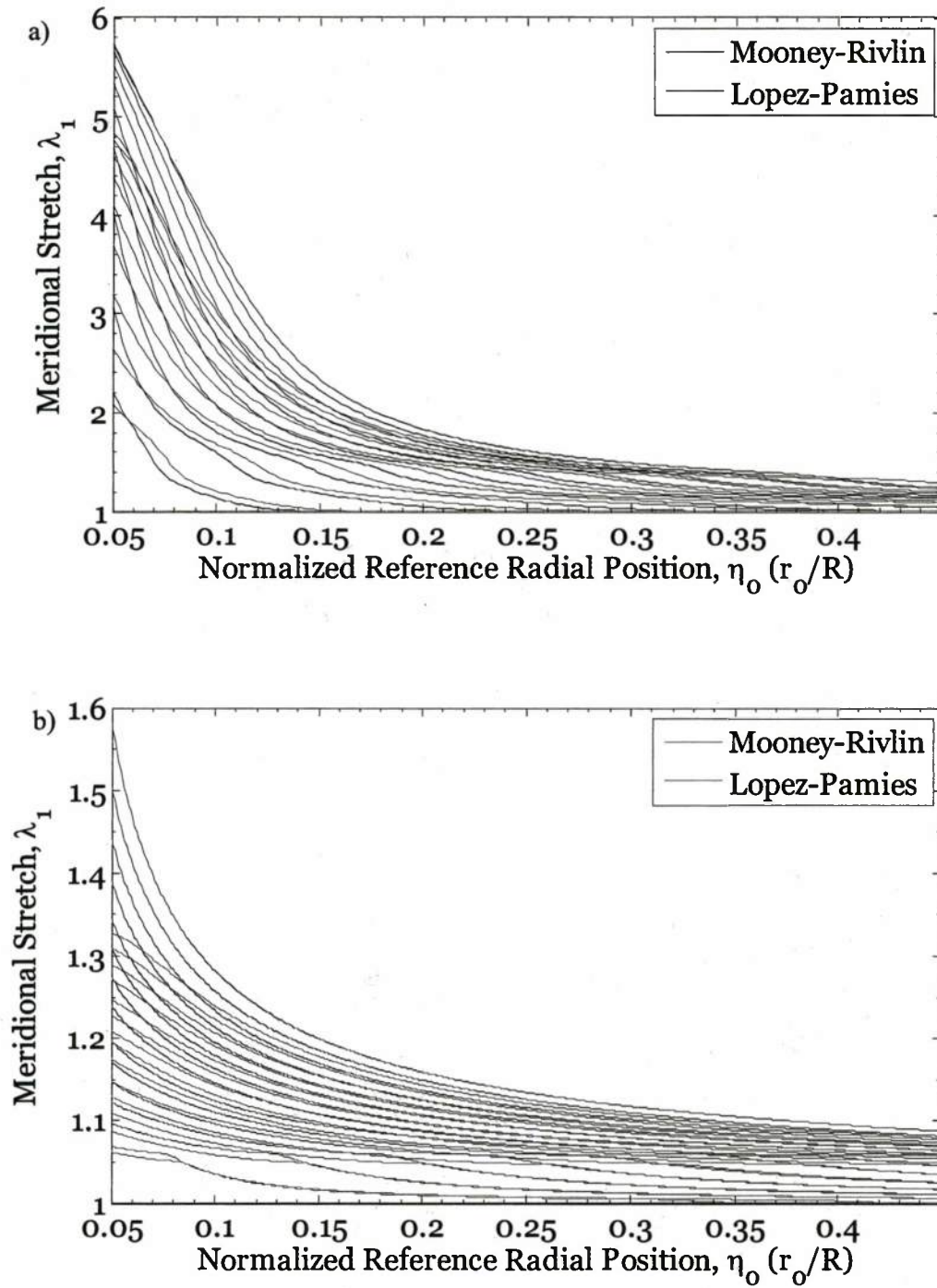


Figure 22: Comparison of meridional stretch profiles predicted by DCMR and Q-LP models. a) 55 m/s impact every 275  $\mu$ s; b) 5 m/s impact every 1 ms.

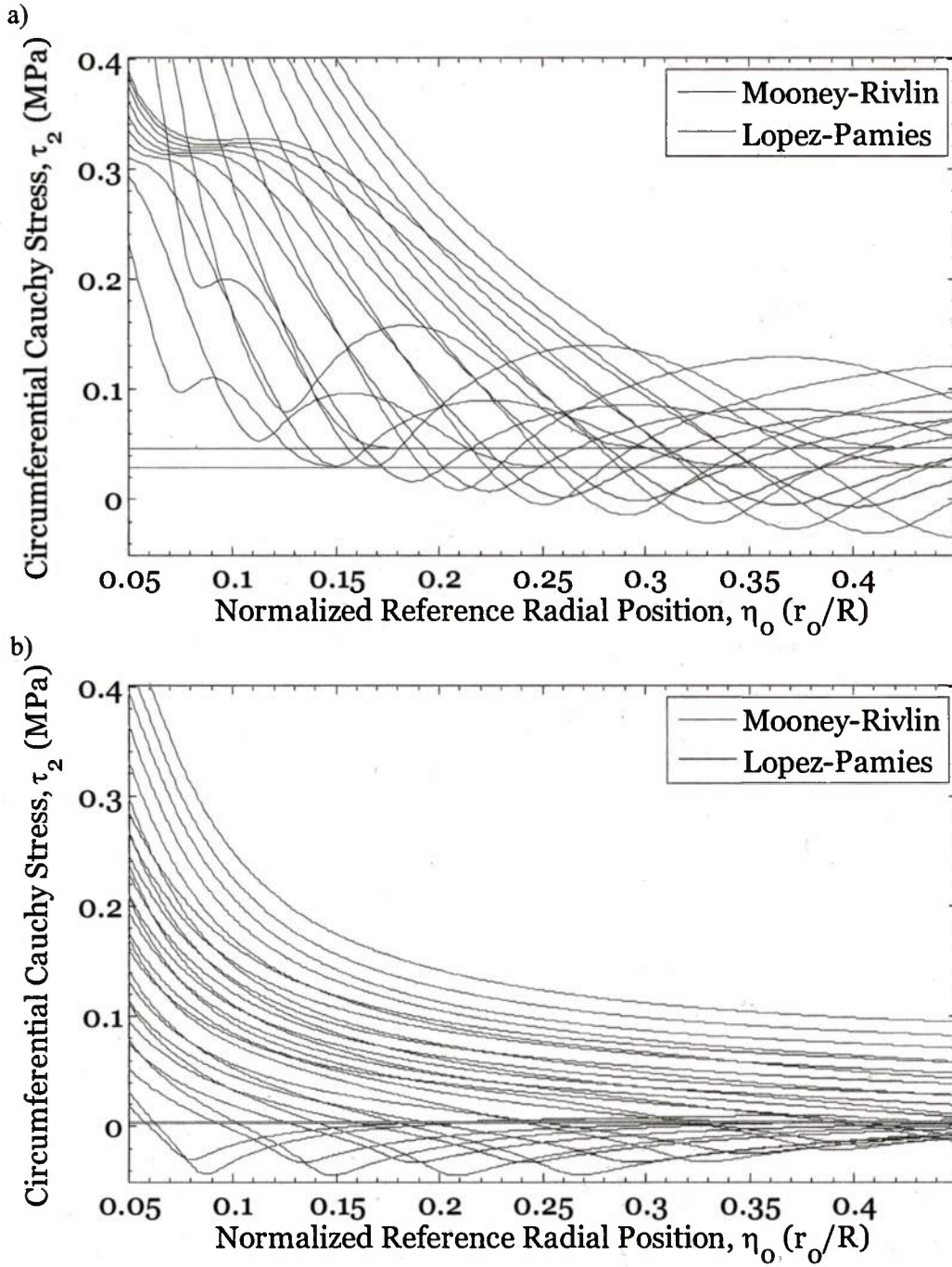


Figure 23: Comparison of circumferential Cauchy stress profiles predicted by DCMR and Q-LP models. a) 55 m/s impact every 275  $\mu$ s; b) 5 m/s impact every 1 ms.